THÈSE

PRÉSENTÉE À:

L'UNIVERSITÉ PIERRE ET MARIE CURIE

ÉCOLE DOCTORALE: Sciences Mécaniques, Acoustique, Electronique & Robotique de Paris

Par: Carlos ROSSA

POUR OBTENIR LE GRADE DE:
DOCTEUR

SPÉCIALITÉ: Mécatronique, Automatique et Robotique

A HYBRID ACTUATION SYSTEM FOR HAPTIC INTERFACES

Laboratoire des Interfaces Sensorielles et Ambiantes (CEA, LIST)

Soutenue le 02 Décembre 2013
Devant la commission d'examen formée de:

Xavier BOUTILLON	Directeur de Recherche	CNRS École polytechnique	Rapporteur
Jean-Pierre RICHARD	Professeur	École Centrale de Lille	Rapporteur
Vincent HAYWARD	Professeur	Université Pierre et Marie Curie	Examinateur
Alain MICAELLI	Directeur de Recherche	CEA LIST	Directeur de thèse
José LOZADA	Ingénieur Chercheur	CEA LIST	Co-Encadrant

ACKNOWLEDGEMENTS

Je tiens tout d'abord à exprimer mes plus vifs remerciements à José Lozada pour son encadrement, sa patience et sa disponibilité tout au long de ces trois ans. Je remercie également Alain Micaelli, mon directeur de thèse, pour la confiance qu'il m'a accordée en acceptant d'encadrer ce travail et pour ses précieux conseils. Merci enfin à Moustapha Hafez, qui m'a ouvert les portes de l'équipe du Laboratoire des Interfaces Sensorielles et Ambiantes (LISA) et pour avoir toujours encouragé mon travail.

J'exprime ma sincère gratitude aux membres du jury, M. Xavier Boutillon et M. Jean-Pierre Richard pour avoir pris le temps de rapporter cette thèse ainsi qu'à M. Vincent Hayward pour avoir accepté de l'examiner.

Nombreux sont ceux à avoir au cours de cette thèse apporté leur contribution. Je pense à toute l'équipe du LISA pour leur accueil et leur convivialité, plus particulièrement à Laurent Eck, Nicolas Guénard, Florent Souvestre et Christian Bolzmacher, pour leur soutien technique enrichissant, à Mehdi Boukallel pour son assistance, à Annick Latare pour toutes les démarches administratives, toujours sous le signe de la bonne humeur, et à Margarita Anastassova pour m'avoir patiemment accompagné dans le mystérieux monde de la psychophysique. Je remercie également Adrien Jaegy et Vincent Samy, que j'ai eu la chance d'encadrer durant leurs stages de fin d'études.

Je ne pourrais pas oublier de remercier Edouard Leroy, mon colocataire de bureau, pour les nombreux débats (pas toujours très utiles) avec lesquelles nous avons refait le monde. Je témoigne toute ma reconnaissance à Lucie Brunet, Charles Hudin, Gwénaël Changeon, Steven Strachan, Harald Zophoniasson et Sabrina Paneeeels, qui ont partagés avec moi leurs indispensables amitiés.

Enfin, ces remerciements seraient incomplets si je n'en adressais pas à l'équipe anonyme du Jeudi soir pour les agréables moments passés ensemble lors des incomptables soirées au 15 Rue de la Butte aux Cailles.

CONTENTS

LIST OF FIGURES

INTRODUCTION

VIRTUAL reality development is motivated by the necessity for human interaction with various types of simulations. Several methodologies outlining techniques for human-machine interaction have emerged since the past three decades. Conventional interfaces are basically able to give interaction feedback to the human operator under the form of visual or sonorous stimuli and are limited in conveying information on mechanical properties such as inertia, friction, compliance, rigidity, and roughness. These physical properties can be best transferred to the user by means of the haptic interaction.

Haptics refers to the modality of touch and concomitant sensory feedbacks. The origin of the term haptics is the Greek word *haptikos* meaning to contact or to touch. In human-machine interfaces, haptic effects are provided to the operator using mechanical actuators applying force, vibration, pressure, motion or other stimuli interrelated to the sense of touch. A haptic device is designed to enhance the use of virtual reality based interfaces by stimulating human kinesthesia and tactile receptors, it is therefore able to simulate immersive interaction with virtual worlds and the presence of virtual objects. Haptic devices allow operators to sense and manipulate either computer-generated environments or teleoperated tasks.

Haptic displays are an effective contribution for improving the user experience through the restoration of haptic stimuli. The improvement of human-machine interface usability by multimodal experiences provides several benefices including but not limited to decreasing learning time, enhancing productivity and comfort, and reducing error in manipulation or telerobotics tasks. The implementation of haptic interfaces involves two main domains: the simulation of complex dynamic systems in order to obtain associated haptic stimuli, and the restitution of these feedbacks to the human operator. The simulation must be connected to a haptic display so that information about forces and motions can be exchanged between the operator and the virtual environment. Therefore, the devices that effectively give the feedback to the operator must cover a wide range of forces varying ideally from zero to infinite, while maintaining stability and safety.

Usually, haptic interfaces employs electric motors in order to deliver haptic stimuli. However, haptic devices based on active actuators can convey only a limited range of haptic sensation, since for example, its ability to display the interaction with rigid virtual environments is bounded by stability issues. The state-of-the art of haptic rendering employing such actuators highlights that there is an inherent tradeoff between performance and stability. Furthermore, the simulation involving high forces and velocities can pose a potential danger to the operator if the system becomes unstable as well as provide uncomfortable feeling. On the other hand, some haptic devices are based on the use of passive actuators such as brakes or dampers. Although these actuators are stable and safe, they cannot restore any energy to the human operator, and therefore the haptic feedbak rendreded by passive interfaces are limited to the simulation of passive environments. In view of enhancing haptic interaction performance, improvement of actuation techniques is needed.

The combination of both passive and active actuation techniques in a hybrid device appears as a natural extension for haptic systems. In this context, the objective of this thesis is to develop an innovative way to enhance the user interaction quality by the improvement of the actuation performance. The work comprises the design of a mechanical actuator as well as the development of associated control laws which are independent of the virtual environment. The objective is to create an independent actuation approach able to replace conventional actuators without affecting the virtual environment or the initial characteristics of an existent haptic device.

THESIS SCOPE

The proposed actuation offers the possibility to combine the versatility of active actuators to the stability and safety of passive ones. This results in a wide-ranged torque and stable device. The actuator and the specific control laws should be independent of any application, to enable the system to be adaptable to many different haptic interfaces. This thesis deals with several issues related to development of the mechanical actuator and the of control with regard to the actuator dynamics, torque capability and stability.

The proposed actuation approach combines a commercial electric motor and two custom made magnetorheological brakes. Each brake is connected to the motor by means of an overrunning clutch to apply a torque only in a defined direction. This enables the system to be controlled without a torque feedback. A complete modelling of different brake geometries is performed in order to highlight the tradeoffs in the design of the passive actuator. From the control perspective, each actuator is treated independently. The associated control laws are able to follow a reference torque of the virtual environment using the association of the brakes and the motor while maintaining stability. The controller is able to determine the gains implemented in the environment. Then, the maximal gain sent to the motor is bounded to avoid instability. The brake compensates for the difference providing for the interaction's stability.

The main contributions of this work address the control of a hybrid actuator regardless the virtual environment model, taking into account the different characteristics of each actuator. The integral modelling and design including a magnetostatic model for the optimization of the magnetorheological brakes is developed. The proposed approach allows for the design of high transparency devices regardless the dimensions of the brake. Finally, the influence of the active/passive torque assymetry on the perception of elasticity is investigated. The objective is to identify the user's capabilities to perceive stiffness asymmetry during the interaction with virtual springs. The results drawn from this experiment can be integrated in the design of the control laws as well as in the integral design of the actuator.

THESIS OVERVIEW

This document is articulated into seven chapters organised as following.

Chapter 1 aims at identifying the main requirements in the design of high fidelity haptic devices and how conventional actuators and associated software solutions meet these concerns. An analysis of control methods used in force feedback rendering based on mechanical actuators is presented, comprising the use of active and passive actuators. The objective is to highlight their limits and advantages in human-robot interaction interfaces in order to understand how the combination of both actuator in a hybrid configuration can enhance the fidelity of such systems.

Chapter 2 presents a brief review of actuators employed in human-machine interfaces. Inspired from this configurations, several ways of coupling active and passive actuators are studied. The new actuation concept and control laws based on the use of unidirectional rotary brakes associated to a motor are introduced. Experimental results obtained from a prototype composed of a commercially available magnetorheological brake and an electric motor demonstrate the feasibility of the proposed approach.

Chapter 3 addresses the control of the hybrid actuation approach considering the torque and stability characteristics of the passive and active devices. Considering each actuator independently, the stability condition is obtained using the Nyquist stability criterion. Considering the coupled system, the global stability criterion is subsequently obtained via passivity condition analysis. The proposed controller determines the gains implemented in the virtual environement and limit the maximal gain sent to the motor in order to respect these stability criteia. The brake then compensates for the difference between the reference torque and the motor's torque.

Chapter 4 deals with the design of the passive actuator which will compose the integrated hybrid actuator. As passive actuator, a magnetorheological brake is chosen. This chapter presents a multiphysics modelling of the most current brake geometries and is intended to highlight the interdependence of the measures of performance characterising a brake suitable for high transparency force feedback devices. The extensive magnetostatic model enables the comparison of different brake configurations.

Chapter 5 presents the design of the hybrid actuator on the basis of the model developed in the previous chapter. The first part presents the optimization, fabrication and characterization of a single brake. The second part deals with the integration of two identical brakes with a DC motor form the hybrid actuator, and the implementation of stable control laws developed in Chapter 3.

Chapter 6 evaluates the use of the proposed hybrid actuator in the worst application case. It corresponds to a virtual environment exhibiting high active torques. The objective of the experiment is to determine if the combination of a powerful brake and an active actuator with lower torque capability affects the perception of elastic elements by users. The hybrid haptic device is therefore used in order to simulate virtual springs. The participation of the brake and of the motor are adjusted to generate some amount of torque asymmetry and evaluate the impact in the user's perception.

A general conclusion and perspectives of the thesis are finally presented in **Chapter** 7.

ISSUES IN THE CONTROL OF HAPTIC FEEDBACK RENDERING

1

Contents

Section 4.3 partially reprinted with permission from

©2012 Springer Berlin Heidelberg

C. Rossa, J. Lozada, and A. Micaelli. "Interaction Power Flow Based Control of a 1-DOF Hybrid Haptic Interface" Eurohaptics 2012 Conference, Lecture Notes in Computer Science, Isokoski, Poika, Springare, Jukka, vol 7283, pages 151-156, 12-15 June 2012

THIS chapter presents a literature review of control strategies employed to generate haptic rendering using mechanical actuators. The first objective is directed toward understanding what are the main requirements in the design of high fidelity haptic devices and how conventional actuators and the associated software solutions meet these concerns.

The control considerations are classified according to the nature of the actuator used to generate haptic stimuli. An analysis of the use of active and passive actuators is conducted in order to highlight their limits and advantages in human-robot interaction interfaces and to give some clues about how the combination of both actuators in a hybrid configuration can enhance the fidelity of such systems. In the same way, an analysis of control methods for hybrid actuators is subsequently presented.

1 PRELIMINARIES

A haptic interface is a robotic system intended to display reflective forces which recreate the interaction with a virtual or tele-operated environment. Their most common applications include teleoperation, steer-by-wire systems, surgical training devices, [Laycock et Day, 2003] etc. A haptic interface is composed of a mechanical device, in interaction with a human operator, and a computational unit [Srinivasan et Basdogan, 1997]. The task of the mechanical device is to apply and to measure mechanical signals using one or several electromechanical sensors and actuators. In parallel, the role of the computational unit is to drive the transducers by generating relevant signals for a particular application, in order to provide haptic rendering capabilities to the device [Hayward *et al.*, 2004].

The computational unit is used to represent environments which can be real or virtual. In a virtual environment, a mathematical model is solved computationally to find forces, displacements, velocities, acceleration, etc, as a function of a measured signal from the interface [MacLean et Roderick, 1999]. In the case of real environments, the operator uses the haptic device to command a remote manipulator. The computational unit generates haptic rendering integrating informations received from a remote site. The local operator feels as if he was somehow present in the remote scene [Cui *et al.*, 2003].

A haptic device must convey kinaesthetic stimuli from the environment to the operator with maximum transparency. Ideally, the operator should not be able to distinguish between the real world, e.g holding a real object, and the virtual world, in which the same object is simulated [Hayward et Astley, 2000][Astley et Hayward, 2000].

The virtual environment can be divided into volumes representing free space or virtual objects. The boundaries between the two are the surface of these objects. As a consequence, first of all, a haptic rendering system should be able to provide the sensation of free space. This requires a mechanical device with intrinsic characteristics that allows the user to move it about without feeling its dynamic effects [Salisbury *et al.*, 1995]. Touching a virtual sur-

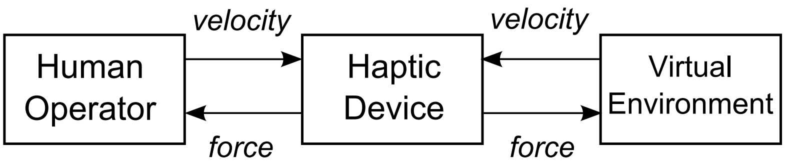

Figure 1.1: Schematic representation of a haptic interface. An human operator interacts with mechanical actuator which recreates the interaction with a virtual or teleoperated environment.

face, on the other hand, is described as the sudden transition from the free motion region to one of constrained motion. The sensation of presence of the objects is then given to the operator in the form of mechanical impedance, defined as the ratio force/vitesse, with regard to the environment characteristics including stiffness, viscosity and inertia [Adachi *et al.*, 1995] [Minsky *et al.*, 1990]. In order to cover both operation modes, an ideal haptic device has therefore no inertia and no friction, infinite bandwidth and can vary from zero to infinite output impedance while maintaining stability.

Fig. 1.1 presents a schematic representation of an human operator which interacts with a virtual environment using a haptic device. The interface basically consists of an actuator, that the operator grasps. The position of the actuator or the resultant force imposed by the operator are measured using displacement or torque transducers. The haptic sensation is generated using impedance or admittance loops based control. In *impedance control* the virtual environment calculates a force to be presented to the user in response to measured positions or velocities [Mills et Goldenberg, 1989]. In *admittance control* the user exerts a force on the haptic device, and the virtual environment reacts with the corresponding displacement in response to the measured force [Van der Linde *et al.*, 2002]. The instantaneous characteristics of the virtual environmental as either stiffness or compliance respectively, give the relationship between forces and velocities and directly specify the control loop gains.

Both for impedance or admittance control, the haptic feedback can take the form of either passive or active stimuli. Inert elements such as obstacles or damping imply passive rendering while animated (non-inert) elements that can supply some energy require active rendering [Hayward *et al.*, 2004]. Depending on the nature of the actuators employed to deliver the rendering to the operator, a haptic device can also be classified as active or passive.

Passive devices are designed to allow for a controllable dissipation of the energy provided by the human operator [Sakaguchi et Furusho, 1998] and commonly employ controllable brakes [Kikuchi *et al.*, 2007], dampers, or continuously variable transmissions actuators [Pesgens *et al.*, 2006]. They can successfully be employed to convey passive stimuli but cannot actuate as an active system [Munir *et al.*, 1999]. Active interfaces, on the other hand, can inject energy to the system via electric motors, hydraulic actuators and other mechanisms, and are able to simulate non-inert elements. However, the use of active interfaces to simulate passive environments remains a particular challenge [Mahvash et Hayward, 2003][Hogan, 1989]. Several authors have considered issues for stable haptic interaction using active actuators. They noted a critical tradeoff between the sampling rate, the simulated stiffness and the energy dissipation due to viscous friction [Diolaiti *et al.*, 2005][Colgate et Brown, 1994]. They concluded that any active device will exhibit a limited range of achievable impedance.

It is well-known that to achieve stable haptic interaction using active actuators, a threadoff between performance and stability need to be established. On the other hand, although passive actuators are stable and safe, they cannot restore any energy to the human operator. To overcoming the specific limitations of passive and active interfaces, and of enhancing the fidelity of the haptic rendering, hybrid interfaces combining passive and active actuators seem to be a natural extension of haptic interfaces. The versatility of active actuators can be combined to the stability and high torque capability of passive devices. In this thesis, we propose a new hybrid actuator concept for haptic interfaces. The identification of elements limiting the use of both active and passive actuators is a crucial point for designing this hybrid system. This is the objective of the following sections.

2 ACTIVE INTERFACES

Active interfaces present the possibility of dissipating and restoring the energy provided by the operator. However, the simulation of stiff environments can lead the system to the instability. To highlight this limitations, the following section reviews the basic definitions of passivity analysis. It is not intended to give an exhaustive description of passivity theory, but rather a limited introduction that presents some results we will need throughout this document.

2.1 STABILITY PROBLEM STATEMENT

In order to determine the limits of stability of an active haptic device, the stability condition is deduced from a continuous system in closed loop and subsequently applied to a haptic device in discrete domain.

2.1.1 PASSIVITY OF COUPLED SYSTEMS

Consider a generic operator G, which has an input signal $u(t)$ resulting in the output sigal $y(t)$. A statement of absolute system passivity is that the maximum energy in the system is always equal to or less than the initial stored energy [Brown, 1998]. Even without knowing the nature of the signals $u(t)$ and $y(t)$, it is possible to make a mathematical statement about the operator's G passivity. The operator G is passive if the following condition is respected:

$$\int u(t)y(t)dt + E\left(t_0\right) \geq 0 \tag{1.1}$$

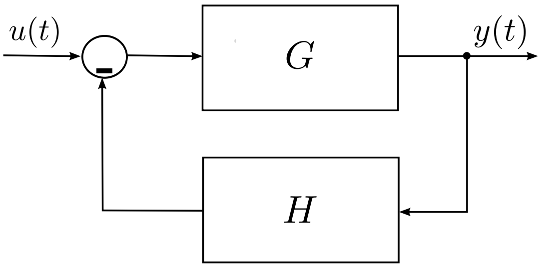

Figure 1.2: Block diagram a closed loop connection. Where G is strictly passive and H is a system to which it is connected. The imput and output of the coupled system is denoted $u(t)$ and $y(t)$ respectively.

where $E(t_0)$ is some constant that depends on the initial condisions of the system. A system that does not satisfy 1.1 is said to be active. This statement does not specify anything about energy but can match the energy definition of system passivity when $u(t)$ and $y(t)$ are complimentary effort/flow variables. In this case the product $u(t)y(t)$ is the instantaneous power of the system, G is the impedance (ratio flow/effort or effort/flow), and $E(t_0)$ is the initial stored energy into the system.

Assuming G as a linear and stable scalar passive impedance, a passive transfer can be described in the frequency domain as:

$$Re\{G(j\omega)\} \geq 0 \tag{1.2}$$

where $G(j\omega)$ is the frequency domain description of the operator G.

Consider now the block diagram of two coupled operators G and H in closed loop shown in Fig. 1.2. A stability theorem [Brown, 1998] states that if G is both input and output passive [1], a necessary and sufficient condition for coupled stability is the passivity of H. This condition will be used to determine the limits of stability of a haptic interface. The characteristic equation of the transfer function of the coupled system in closed-loop is

$$1 + G(j\omega)H = 0 \tag{1.3}$$

or more clearly:

$$G(j\omega) = -\frac{1}{H} \tag{1.4}$$

According to the Nyquist theorem, the solution to this equation is given by the intersection between the correspondent Nyquist region of the function $G(j\omega)$ and the locus of $-H$. Intersection of these loci provides the solution of (1.3) which represents the limit cycles.

---

[1] The operator G is linear and respects (1.1) with the left hand side positive and bounded away from zero.

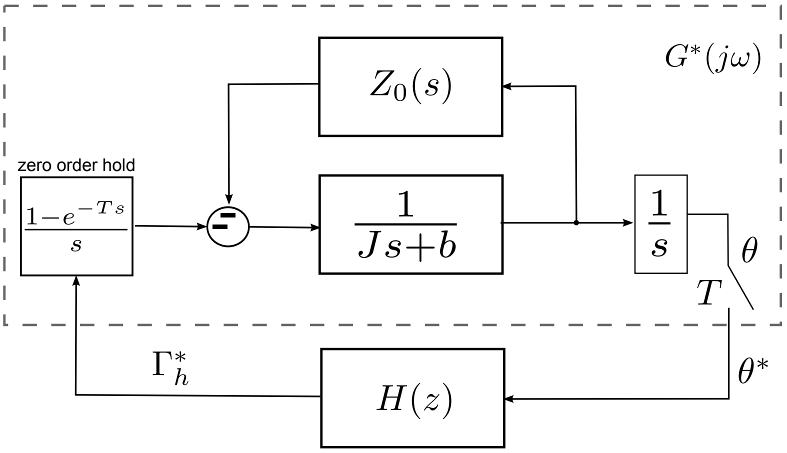

Figure 1.3: Generic control scheme of an active interface. The device has an inertia J and a damping b. The human operator is represented by the passive impedance $Z_0(s)$. The virtual environment is the discrete function $H(z)$ which calculates a reference torque Γ_h^* as a function of the measured position θ^*. The conversion discrete/continuous domain is modelled by the zero-order hold function according to a sampling rate T.

2.1.2 APPLICATION TO ACTIVE INTERFACES

Consider now the block diagram of a rotary one degree of freedom haptic device composed of a mass that has an inertia J with some viscous friction denoted b, as shown in Fig. 1.3. The position θ^* is measured and sent to the discrete function $H(z)$, which represents the virtual environment and calculates the reference torque to be presented to the operator. The torque is provided by an active actuator. A human operator interacts with the device and he is considered as a passive impedance called $Z_0(s)$ [2]. The conversion between the discrete and continuous domain is realized by a zero-order hold function (ZOH) with a sampling period T defined as:

$$ZOH(s) = \frac{1-e^{-Ts}}{s} \tag{1.5}$$

Colgate et Shenkel [Colgate et Schenkel, 1994] found a transformation that, when applied to a virtual environment $H(j\omega)$, gives a system with the same closed loop characteristics as the original. Applying the small gain theorem, a necessary condition for closed loop stability is:

$$b > \frac{T}{2}\frac{1}{1-cos(\omega T)}Re\{(1-e^{-j\omega T})H(e^{-j\omega T})\} \tag{1.6}$$

---

[2] No passive contact between the human operator and the haptic device should result in an unstable system since the operator are not able to induce undamped motion. He cannot destabilize the system by modulating limb impedance using muscular contraction or changes in posture. In everyday experience, we do not encounter instability when manipulating passive physical objects. As well, the haptic device appears to the human as an inanimate object which can only give back or absorb the energy provided by the human. The human operator is free to force undamped motion through intentional excitation, but the haptic interface will not contribute to a buildup of kinetic or potential energy.

with $0 \leq \omega \leq \omega_N$ where ω_N is the Nyquist frequency. A common implementation of a virtual wall describes it as a virtual spring which has a stiffness K mechanically coupled in parallel to a virtual damper with a damping B [Colgate *et al.*, 1993][Rosenberg et Adelstein, 1993]. The virtual environment model takes the following formulation:

$$H(z) = K + B\frac{z-1}{Tz} \tag{1.7}$$

where $z = e^{-j\omega T}$. Replacing (1.7) in (1.6), the stability condition becomes:

$$b > \frac{T}{2}\frac{1}{1-\cos(\omega T)}Re\left\{\left(1-e^{-j\omega T}\right)\left(K + B\frac{e^{-j\omega T}-1}{Te^{-j\omega T}}\right)\right\} \tag{1.8}$$

After straightforward algebraic manipulation, this relation can be reduced to:

$$b > \frac{KT}{2} - B\cos(\omega T) \tag{1.9}$$

At the Nyquist frequency ($\omega_N = (2\pi/T)/2$), the cosine-dependent term is maximized and the relation is simplified to:

$$b > \frac{KT}{2} + B \tag{1.10}$$

From this analysis we can draw that to achieve stability some physical energy dissipation is essential, and it must be larger than the total damping generated by the discrete time controller. Nevertheless, an inherent physical damping damages the transparency of the haptic rendering. It also demonstrates that for a given virtual and physical damping, the achievable stiffness depends on the sampling rate. Another important statement is that the achievable virtual damping is independent of the sampling rate.

2.2 VIRTUAL COUPLING

The virtual coupling is usually defined as a passive impedance $C(z)$ which has some damping B and stiffness K. The mapping of the forces is presented in Equation 1.11. The torques Γ_1^* and Γ_2^* are equal and opposite because they represent the force between the haptic display handle and virtual environment. The velocity output of $H(z)$ is called $\dot{\theta}_c^*$.

According to the stability criterion presented in the previous section, high control loop gains may violate the stability of the interface. However, a virtual environment can exhibit infinite stiffness in order to simulate a virtual obstacle. To maintain stability, it is essential to limit the control loop gains. That is equivalent to bound the impedance of the virtual environment. Without prior knowledge of the simulation model, a passive element placed between the device and the simulation is a potential solution to bound the impedance sent to the actuators and to decouple the design of the control from that of the virtual environment.

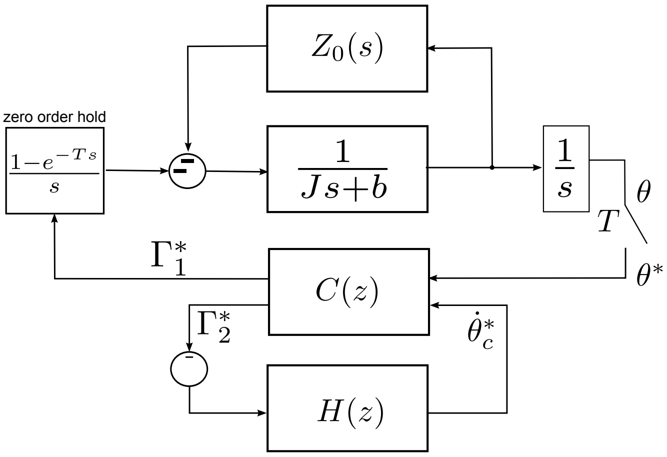

Figure 1.4: Virtual coupling implementation. The virtual coupling takes the form of a passive impedance $C(z)$ that bounds the rendered impedance to the human operator by dissipating some amount of energy. The torques Γ_2^* and Γ_1^* are the torque applied to interface and the torque sent the virtual environment after the virtual coupling. The output $\dot{\theta}_0^*$ is the recalculated velocity.

Colgate et al. [Colgate *et al.*, 1995] introduced the concept of virtual coupling. It acts as an impedance filter placed between the simulation and the device to bound the displayable impedance range for passive human operators and environments. The main idea is presented in Fig. 1.4.

$$\begin{pmatrix} \Gamma_1(z)^* \\ \Gamma_2(z)^* \end{pmatrix} = \begin{pmatrix} K+\frac{B}{T}(1-z^{-1}) & \frac{-KT}{1-z^{-1}}-B \\ -K-\frac{B}{T}(1-z^{-1}) & \frac{KT}{1-z^{-1}}+B \end{pmatrix} \begin{pmatrix} \theta(z)^* \\ \dot{\theta}_c(z)^* \end{pmatrix} \tag{1.11}$$

The virtual coupling generates haptic distortions. For example, if the virtual environment simulates an infinite stiffness, the device will instead render the impedance of the virtual coupling [Brown, 1998]. Adams and Hannaford [Adams et Hannaford, 1999] used two-port network theory to deduce optimal virtual coupling impedance values that satisfies the passivity condition.

2.3 PASSIVITY-BASED CONTROL

Even when the virtual environment is passive, the interaction with stiff virtual environments can prove to be active. This occurs because there is an inherent delay between the interface input and output due to the sampling rate. In addition, the sensors used to measure the state of the display are imperfect [Colgate *et al.*, 1995]. Another common control method used to guarantee the passivity of the device employs the so called passivity-based control scheme [Hannaford et Ryu, 2002]. The controller bounds the energy restitution of the interface to no more than the one provided by the operator.

Consider again the haptic device presented in Figure 1.3. The system is said to be passive if the operator cannot extract energy from it. The energy of the device should be inferior or equal to the energy provided by the operator. If the operator applies a torque Γ_z, this condition, $\forall t \geq 0$ is

$$\frac{1}{2}J\dot{\theta}(t)^2 \leq -\int_0^t \Gamma_z(t)\dot{\theta}(t)dt \tag{1.12}$$

where $\dot{\theta}(t)$ is the angular velocity of the device. If the system is passive, the only energy source is the torque provided by the operator. The torque applied by the interface is called Γ_h. An energy balance on the device leads to:

$$\frac{1}{2}J\dot{\theta}(t)^2 = -\int_0^t \Gamma_z(t)\dot{\theta}(t)dt - \int_0^t \Gamma_h(t)\dot{\theta}(t)dt - \int_0^t b\dot{\theta}(t)^2dt \tag{1.13}$$

The first term on the right corresponds to the physical energy dissipation. Combining (1.13) and (1.12) gives:

$$\int_0^t \Gamma_h(t)\dot{\theta}(t)dt + \int_0^t b\dot{\theta}(t)^2dt \geq 0 \tag{1.14}$$

The second term is always positive. A sufficient condition for passivity is that the energy provided by the actuator is maintained positive. Hannaford and Ruy [Hannaford et Ryu, 2002] introduced the concept of "energy observer" that can measure the energy flow in real-time. If the interface is controlled according with a sampling rate T, the energy observer is defined as [Ryu *et al.*, 2004a]:

$$E_{obs}(n) = T\sum_{k=0}^{n} \Gamma_h^* \dot{\theta}^* \tag{1.15}$$

If $E_{obs}(n)$ is negative, the interface creates energy. The passivity based control consists of dissipating some amount of energy in real time in order to respect the passivity condition given by (1.14) [Ryu *et al.*, 2004b]. While $E_{obs}(n) < 0$, using admittance control, the effective torque sent to the actuator Γ_c is recalculated as a function of the velocity and of the observed energy as:

$$\Gamma_c = \Gamma_h + \alpha\dot{\theta}^* \tag{1.16}$$

with:

$$\alpha = \frac{-E_{obs}}{T\dot{\theta}^*} \tag{1.17}$$

If $E_{obs} \geq 0$, the passivity controller is deactivated by setting $\alpha = 0$. By these means the passivity condition is respected. However, the required forces to dissipate the generated energy may exceed the actuator limits.

2.4 DISCUSSION

From a control perspective many factors have to be considered to achieve stable haptic interaction using active actuators. In particular, a direct consequence of the computational delay and loss of information due to the time-discretization introduced by the zero-order hold, is the injection of energy into the system in an amount proportional to the displayed stiffness [Gillespie et Cutkosky, 1996][Colgate *et al.*, 1993]. This phenomenon may lead to unstable or oscillatory behaviours that affect the haptic rendering. In addition, other points should be considered, such as the quantization of the measured position or force and the estimation of their derivatives using limited resolution position encoders, as well as the precision of Analog-Digital converters. As a consequence, although many virtual environments can be envisioned as passive, the combination of these factors can make the system active. If the intrinsic friction of the device is not sufficient to dissipate this energy excess, the interface may become unstable.

Therefore, much effort has gone toward enhancing stability by reducing the computation and the sampling delays which are bounded by hardware limitations [Lee et Lee, 2004] [Vasudevan *et al.*, 2007] [Sevcik *et al.*, 2007] . The main tool to provide stability for a haptic display is the control by passivation. The objective is to implement a dissipative element in the control scheme is order to satisfy the passivity condition. An usual implementation consists of increasing the virtual damping of the virtual model [Srikanth *et al.*, 2008] [Colgate et Schenkel, 1994] or even by implementing the virtual damping [Weir *et al.*, 2008].

The virtual coupling employed as dissipative element can effectively ensure the passivity of the haptic device and allows for the interaction with nonlinear virtual environments [Miller *et al.*, 2000] [Lee et Lee, 2003]. However, the maximal impedance rendered to the operator is bounded to the impedance of the virtual coupling. As well, the implementation of the so called energy observer can be used to detect unexpected active behaviour and to dissipate the created energy in order to maintain the absolute passivity condition [Ryu *et al.*, 2004a] [Ryu *et al.*, 2004b] [Kim et Ryu, 2004b] [Kim et Ryu, 2004a]. The amount of observed energy depends on the device precision and sampling rate. The dissipation may represent distortions between the virtual environment and the real rendered feedback. Moreover, from the operator perspective, this method cannot ensure the interaction's fundamental safety.

Furthemore, motors are frequently linked to reduction stages which dramatically increases the inertia and the frictions reflected to the end-effector [Nam et Park, 2007]. Furthermore, motors have to work in very different conditions from their nominal operating points in the torque-velocity plan, which increases the energy consumption. High reduction ratio improves the torque-to-weight ratio but at the same time the bandwidth, efficiency and quality of produced forces are damaged. Parasitic forces however need to be reduced to improve the transparency of the device under the smallest human-detectable force so that the operator's perception is not disturbed by the device [Mohand-Ousaid *et al.*, 2012]. This can be achieved by

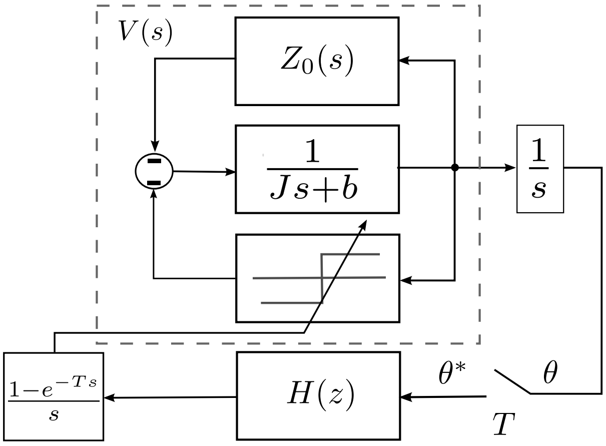

Figure 1.5: Control scheme of an passive interface. The mechanical device has an inertia J and a damping b. The human operator is the time invariant passive element $Z_0(s)$. The virtual environment $H(z)$ calculates a reference torque as a function of the measured position θ^*. The conversion discrete/continuous domain is given by the zero-order hold function according to a sampling rate T. The brake's torque is given by (1.18)

reducing its dynamic effects, for instance, compensating parasite forces with appropriated control laws [Baser *et al.*, 2012b]. In this way, the devices employ admittance control schemes, which need force transducers and some minimal detectable inertia. Admittance control provides good accuracy in free-motion but it can result in instability during the interaction with stiff environments [Ott *et al.*, 2010]. A second possibility may consist in redesigning the mechanical device by replacing, for example, reduction stages by passive actuators. In other words, let the actuator be passive rather than the control scheme. Passive actuators cannot inject energy into the system and are therefore intrinsically stable and safe.

The use of passive actuators in haptic interfaces is presented in the following section.

3 PASSIVE INTERFACES

Passive interfaces are intrinsically stable and safe. Passivity eliminates the possibility of damage or injury to the human operator and this faculty is especially desirable during the interaction involving high forces and velocities [Matsuoka et Townsend, 2001]. Furthermore, passive actuators generally possess a higher torque density and need lower power compared to active actuators [Blake et Gurocak, 2009].

Consider the block diagram of a passive force feedback device presented in Fig. 1.5. The device has an inertia J and a damping b, the operator is represented by the passive impedance $Z_0(s)$ and the virtual environment is the function $H(z)$. Consider also that the haptic rendering is provided by a brake. The torque delivered by the actuator can be interpreted as a controllable physical damping which is independent of the sampling rate. According to Karnopp's model [Cho *et al.*, 2007], if the brake is commanded to generate a torque Γ_h^*, the braking torque Γ_b is:

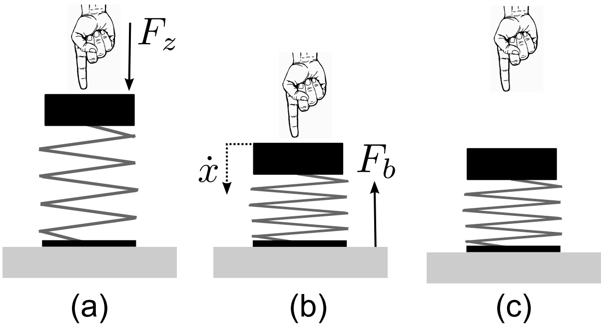

Figure 1.6: Simulation of elastic elements using only brakes: the brake provides the required stiffness only during the compression phase. In (a) the operator compresses the virtual spring with a force F_z, in (b) the device generates a force F_b against the velocity $\dot{x}$. When the operator releases the handle, it stains at the final position (c).

$$\Gamma_b = \begin{cases} -|\Gamma_h^*|\mathrm{sgn}(\dot{\theta}) & if \quad \dot{\theta} \neq 0 \\ -|\Gamma_h^*|\mathrm{sgn}(\Gamma_h^*) & if \quad \dot{\theta} = 0 \end{cases} \tag{1.18}$$

The transfer function of the passive interface is:

$$V(s) = \frac{1}{Js + b + Z_0(s)} \tag{1.19}$$

Considering the braking torque given in (1.18), the viscous friction coefficient b can be modified by the control loop gains of the virtual environment and is always positive. Thus, the according to 1.19, the haptic device appears to the human operator as a passive system which can only dissipate energy. In orther words, there is no limit for the control loops gains implemented in $H(z)$ that can led the interface to the instability. This analysis demonstrates that passive interfaces can successfully be used in order to render higher impedance than active interfaces. However, in spite of they suitable features for haptic interaction, their strictly passive behaviour impairs the ability of the device to simulate elastic elements. These implications in force feedback devices are presented in the following section.

Such actuators are intrinsically dissipative and this behaviour has some drawbacks which affects the quality of the haptic rendering. The limitations comprise the impossibility to create forces in arbitrary directions, the stick phenomenon in the simulation of unilateral contacts and the impossibility to restore energy as presented by the following examples.

Using brakes, the simulation of elastic elements can be displayed in one direction only. Consider the simulation of a virtual spring using a 1 degree-of-freedom (DOF) passive haptic interface shown in Fig. 1.6. The operator imposes the force F_z to compress the spring (a). The brake can create a reactive force F_b proportional to the displacement (b) applied against the velocity of the handle $\dot{x}$. When the user releases the handle (c), it stays at the compressed position. Moreover, during the compression phase of the spring (b) if the operator's force becomes inferior to the reference force the decompression phase of the spring can not be displayed.

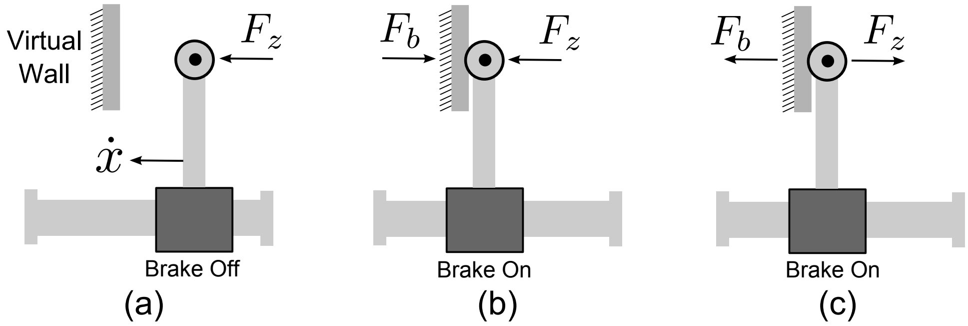

Figure 1.7: Stick phenomenon in the simulation of a virtual wall using only brakes: the operator imposes a force F_z to move the handle according to the velocity $\dot{x}$, when the virtual wall is attained, the brake applies a resistive force F_b which is always opposed to F_z.

Another limitation of passive interfaces is illustrated in Fig. 1.7. Consider now a 1-DOF device that simulates a virtual wall using a linear brake mounted on the guide-way. The human operator applies a force F_z in the direction of the wall (a). If the handle does not touch the wall, the operator should be able to move it freely. When the end-effector reaches the wall, the device generates an force F_b against the velocity of the end-effector $\dot{x}$. Due to the response time of the system, the end-effector penetrates the wall until the forces are balanced. Considering the model of the brake given by (1.18), the the braking force is always opposed to the operator's force. As a result, in (c), when the operator tries to turn back out of the wall the brake blocks the end-effector even though it should move freely in the direction of $-\dot{x}$. This behaviour can be perceived by the user as a stick phenomenon and ruins the perception of the virtual wall.

Consider now a 2-DOF passive force-feedback interface presented in Fig. 1.8 composed by two independents linear brakes, mounted on two connected guide-ways. In a multiple degrees of freedom (MDOF) device, the strict dissipative behaviour of passive actuators impairs its ability to generate forces in arbitrary directions [Colgate *et al.*, 1996] [Cho *et al.*, 2007]. The device works as follows. If both brakes are released, the end effector signalized by the black circle can move freely. If brakes 1 and 2 are activated, it is possible to display a resistive force aligned with the velocity in every possible direction.

Consider that the virtual environment simulates a frictionless triangular wall limited by the segments $\overline{ABC}$. In order to simulate a constraint along the $\overline{AB}$ segment, the brake 1 can be activated to create a reaction force F_{AB}. To simulate a constraint in the segment $\overline{AC}$ by the brake 2 with the force F_{AC}. If the operator moves the handle along the y axis, (imposing a force F_z), when the handle touches the segment $\overline{CB}$, a normal reaction force F_n can be controlled by engaging both brakes. At this point, the resultant force and the lack of friction should induce a displacement along the segment $\overline{CB}$ in the direction of the point C. Since brakes can exert a force only against the velocity, when the handle moves along the inclined segment, an undesirable tangential force F_t appears, as a consequence the normal force F_n cannot be simultaneously controlled. The brakes are consecutively engaged and turned off, and the virtual

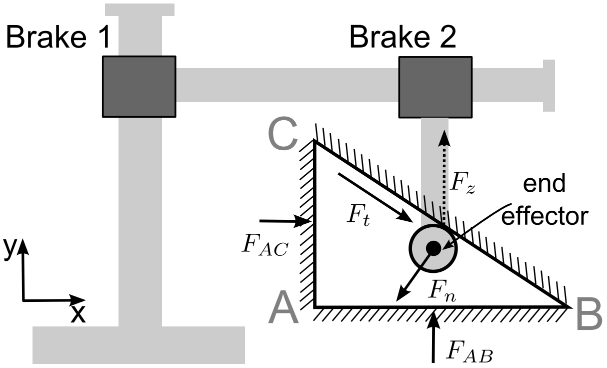

Figure 1.8: 2-DOF brake-based interface: The brake 1 can impose a resistive force against the displacement of the handle along the y axis while brake 2 can restrain the movement in the x axis. Where F_{AB} is the force generated by the brake 1 to simulate the virtual wall $\overline{AB}$, F_{AC} the force of the brake 2 normal to $\overline{AC}$. The virtual wall $\overline{BC}$ requires the force F_n which cannot be obtained by the brakes due to the tangential force F_t resulting when the operator imposes the force F_z.

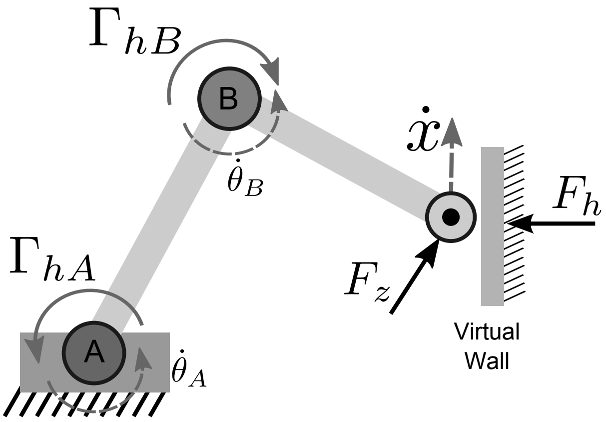

Figure 1.9: Simulation of virtual walls using passive actuators. The actuation force F_h is generated by a torque Γ_{hB} and Γ_{hA}. The resultant velocity in the joint A and B are $\dot{\theta}_A$ and $\dot{\theta}_B$ respectively. In the joint B the desired torque is opposed to the velocity. A brake can effectively produce the reference torque. However, in A the velocity and the desired torque have the same directions. Using only brakes, the desired force F_h cannot be achieved.

wall is rendered under the form of small steps, certainly perceived by the user. To deal with this issues, Colgate et al. [Colgate *et al.*, 1996] proposed the concept of nonholonomic joints which are perceptually smooth along any direction in the configuration space.

A similar effect can be observed using the two link manipulator presented in Fig. 1.9. Each joint A and B is equipped with a brake. The virtual wall is simulated by generating the force F_h with the precise combination of the torque Γ_{hA} in the joint A and Γ_{hB} in the joint B according to the Jacobian transformation. Given the operator's force F_z, the resultant velocity of the end effector is $\dot{x}$. The rotational velocities in each joint are $\dot{\theta}_A$ and $\dot{\theta}_B$ respectively. In the joint B, the induced velocity is opposed to the desired torque. As a consequence, a brake can effectively produce the desired torque. Conversely, since $\mathrm{sgn}(\Gamma_{hA}) = \mathrm{sgn}(\dot{\theta}_A)$ the brake cannot be employed in A. Therefore, the virtual wall cannot be simulated using only brakes.

These examples demonstrate that to accurately display any virtual environment, the haptic device should have the possibility to restore energy. The combination of active and passive actuators is presented in the next section.

4 HYBRID INTERFACES

Hybrid actuators have been shown as an efficient way for achieving high performance in haptics over the past 20 years. Several application of hybrid actuators for haptic rendering are available in the literature including the development of rotary knob for in-vehicle control [Badescu *et al.*, 2002] [Chapuis *et al.*, 2007], the combination of electro-rheological brake and ultrasonic motor [Chapuis *et al.*, 2006], surgical devices [Gonenc et Gurocak, 2012] [Samur *et al.*, 2008], and telerobotics systems [Walker *et al.*, 2009] (the respective mechanical configurations will be presented in **Chapter** 2). Hybrid interfaces comprising passive and active actuators are a natural extension of haptic devices. The energy restitution can be assured by the active actuator while the passive one provides for the interaction's stability and high torque capability.

From a control perspective, three main control approaches can be distinguished. The first uses the active actuator to display the forces of the virtual environment, while the passive actuator provides for the interaction's stability appliying a controllable damping. The second method employs the passive actuator to display the reflective forces, and the active one compensates for its inherent frictions. In the last one, both actuators can be combined to display reflective forces.

An and Kwon [An et Kwon, 2002] describe the design of a 1-DOF joystick composed of a motor/brake actuator pair. The system allows for the simulation of virtual walls, virtual damping and real objects without stability issues involved using high torque motors only. They demonstrated that the combination of active and passive actuators can effectively improve the achievable impedance range of the device. Chen and Liao [Chen et Liao, 2009] develop an assistive knee brake for a rehabilitation device where the brake is used to control the resistive force during the lowering of the leg while the motor applies an active torque for facilitating the folding over phase.

Kwon and Song [Kwon et Song, 2006] developed a 2-DOF hapic device comprising magnetorheological brakes and motors in each link. They concluded that when brakes are employed, the direction of the reflective force depends on the force imposed by the operator. This occurs because the brake can exert a force only against the motion. When brakes and motors are linked, the effort of the brake and the motor can be easily added to impose a resistive force, but at the same time, if the end-effector is released, the brake naturally blocks the motor. Conti and Khatib [Conti et Khatib, 2009] propose a system combining a brake, a spring and a motor

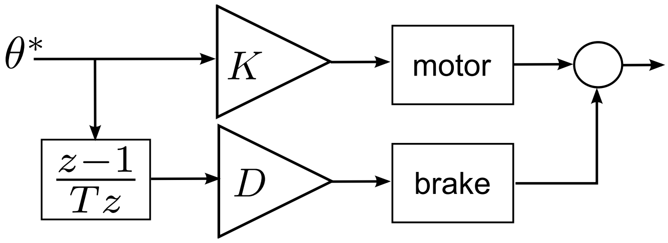

Figure 1.10: Actuation based on the motor. The brake provides for the system's stability by generating a controllable damping D in order to improve the displayable stiffness by the motor K according to the sampling rate T.

in parallel. The end-effector is linked to a motor which is connected to a brake through an angular spring. Thereby, the brake is used to control the amount of stored energy in the spring while the motor is used to eliminate the error between the desired and applied torques. The avaliable energy is the one provided by the motor plus the energy stored in the spring.

4.1 CONTROLLABLE DAMPING APPROACH

The Colgate's passivity criterion given by (1.10) suggests that the addition of physical a damping increases both the maximum achievable stiffness K or damping B. Using a hybrid system a controlled physical damping D can be applied on the interface using the brake in order to increase the maximal stiffness achieved by the motor. The passivity condition for the simulation of a spring/damper system can be rewritten as:

$$b+D > \frac{KT}{2} + B \tag{1.20}$$

An and Kwon [An et Kwon, 2004] demonstrated that a controllable physical damping provided by a brake can effectively improve the simulated stiffness under stability conditions. The same conclusion is obtained by Campion et al. [Campion *et al.*, 2006] who used eddy current brakes as programmable physical damping to improve both the impedance range and stability. By this means, the impedance presented by the haptic device is both the contribution of the simulated stiffness K and the damping B provided by the brake. In other words, the rendering is based on the active actuator, while the passive one provides for the system's stability. Figure 1.10 illustrates the controllable damping approach.

The translation of (1.20) in the non-dimensional plane viscous friction/stiffness is shown in Figure 1.11 for $B = 0$. The motor simulates the stiffness K. The region $\Re_1$ is the region in which an active interface with a friction coefficient b is stable. If the friction is increased to $b+b_1$ with $b_1 > 0$, the stability region is $\Re_1 \cup \Re_2$. A controllable brake delivering the controllable damping D increases the stability region to $\Re_1 \cup \Re_2 \cup \Re_3$. The maximal impedance depends only on the physical saturation of both actuators.

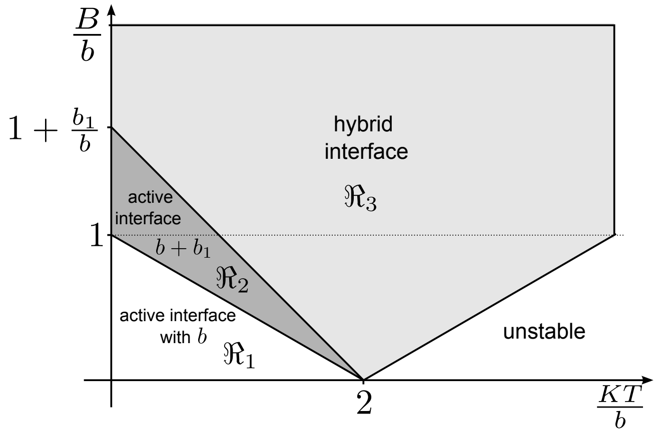

Figure 1.11: Stability map of a hybrid actuator. K is the stiffness simulated by the motor, D is the damping imposed by the brake, b and b_1 are two physical dampings with $b_1 > 0$ and $b > 0$, and T is the sampling rate. The region $\Re_1$ is the region of stability of an active interface. An inherent friction b_1 added to $\Re_1$ results in the stability region $\Re_1 \cup \Re_2$. The stability region of an hybrid interface is $\Re_1 \cup \Re_2 \cup \Re_3$.

In the same way, Baser et al. [Baser *et al.*, 2012a] developed a hybrid system based on a brushless motor and a brake. The reference torque is shared between the actuators and the participation of the brake is increased if instability cycles are detected using an vibration detection system. Another control method consists in using the active actuator to compensate for the inherent friction introduced by the passive actuator which generates the force-feedback. By these means the system remains stable and the transparency is improved. This control method is presented in the following section.

4.2 MOTOR FOR FRICTION COMPENSATION

The previous analysis demonstrated that the upper limit of the displayable impedance range can be improved using a hybrid haptic device. However, due to the intrinsic physical friction of brakes, it can also raise the lower impedance limit. It affects the perception of free motion and damages the transparency of the device. In order to improve transparency, several works addressed active friction compensation using appropriated control laws [Mahvash et Okamura, 2006] [Bi *et al.*, 2004].

Active friction compensation can be summarized into three categories: dither, motion-based cancellation, and force feedback. Dithering [Pervozvanski et Canudas-de Wit, 2002] is characterized by the modulation of a high frequency and low amplitude signals on top of the desired reference signal [Bernstein *et al.*, 2005]. In motion-based cancellation, frictional forces are predicted using a dynamic model [Canudas de Wit *et al.*, 1995] and added to the commanded force. This method does not necessitate force measurement but some motion detection is necessary . Force feedback is the friction compensation category which most directly addresses the transparency goal of haptic devices. The friction forces are measured and

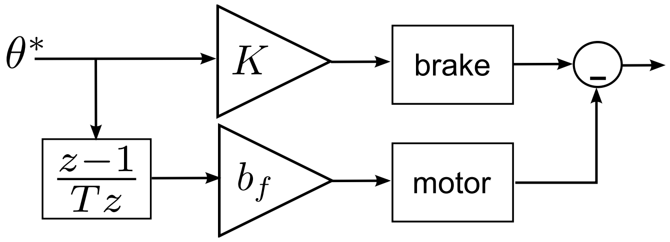

Figure 1.12: Actuation based on the brake using motion based friction compensation. The brake displays the virtual stiffness K while the motor compensates for the inherent viscous friction of the brake b_f according to the sampling rate T.

compensated by the controller. This requires however a minimal detectable inertia.

Since a passive actuator is intrinsically stable, it can display the reflective forces as stiffness and damping while the active actuator provides for the interaction's transparency by compensating for its inherent physical viscous friction. In this approach, the motor can as well be used in order to compensate for the nonlinear behaviour of magnetic brakes due, for example, to hysteresis loops. Nam and Park [Nam et Park, 2007] used a hybrid brake/motor system where the motor compensates for the friction generated by the brake using motion-based friction compensation. The brake is simultaneously used to display the forces of the virtual environment. A schematic representation is given in Fig. 1.12. By these means they obtain a wide-ranged torque device that can provide the sensation of free motion as well as the high output impedance while maintaining stability. A similar approach proposed in [An et Kwon, 2006a] uses the motor to compensate for the inherent friction of the brake (active force feedback), while the brake displays simultaneously a virtual damping (passive force feedback).

Combining the brake and the motor to simulate stiffness necessitates a measure of interaction forces. This is demonstrated in the next section.

4.3 CONTROL USING FORCE SENSING [3]

By contrast to the previous control methods where either the passive or the active actuator are used to display the forces of the virtual environment, the efforts can simultaneously be displayed by both actuators. The question arises as how the controller can determine the activation of the brake and the motor without prior knowledge of the environment model. Actuators are linked in parallel can generate an effort against the motion the brake should be turned off if the interface must restore energy to the operator. In this proposed control method, the controller determines whether the interface has to dissipate or restore energy by observing the velocity, the desired force, and the force applied by the operaotr.

---

[3] This section was reprinted with permission from ©2012 Springer Berlin Heidelberg - C. Rossa, J. Lozada, and A. Micaelli. "Interaction Power Flow Based Control of a 1-DOF Hybrid Haptic Interface" Eurohaptics 2012 Conference, Lecture Notes in Computer Science, Isokoski, Poika, Springare, Jukka, vol 7283, pages 151-156, 12-15 June 2012.

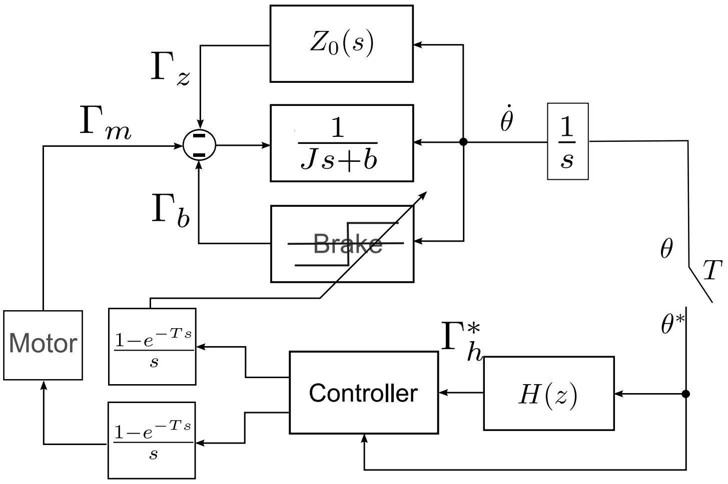

Figure 1.13: Hybrid haptic device control sheme: The reference torque is $\Gamma_h^* = H(z)\theta^*$ and applied in the interface by means of the brake (Γ_b) or the motor (Γ_m) where θ^* is the position and $H(z)$ is the virtual environement model. The torque appleid by the operator $Z_0(s)$ is caleld Γ_z and $\dot{\theta}$ represents the rotational speed. The symbols marked with a star correspond to discrete variables.

Fig. 1.13 presents a block diagram of the 1-DOF rotary force-feedback device. The mechanical device of inertia J and friction b is actuated by a controllable brake, that imposes the torque Γ_b, and a motor in parallel, which applies a torque Γ_m. The human operator is represented by the function $Z_0(s)$ and he imposes a torque Γ_z. The system is controlled by a microcontroller with a sampling period T. The conversion discrete/continuous time domain is modelled by a zero-order-hold function. The virtual environment $H(z)$ calculates the reference torque Γ_h^* as a function of the measured position θ^* so that $\Gamma_h^* = H(z)\theta^*$. The asterisk symbolises discrete variables.

The torque applied by the interface is the sum of the motor's and the brake's torque. If $\dot{\theta}(t)$ is the end-effector velocity, the power delivered by the interface is:

$$\dot{\theta}(t)\left[\Gamma_m(t) + \Gamma_b(t)\right] \geq 0 \tag{1.21}$$

The reference torque Γ_h^* is applied by the device using the brake and/or the motor, thus we cab consider that $\Gamma_h^* = \Gamma_m(s) + \Gamma_b(s)$. The observed power by the controller is:

$$P = \Gamma_h^* \dot{\theta}^* \tag{1.22}$$

Equation (1.22) defines the power flowing in the interface from a control perspective. The reference torque is applied by the interface in negative feedback, therefore if P is positive, the power flows from the operator to the interface. The torque is applied against the velocity and the interface dissipates energy. If the power is negative, the torque is applied in the same direction of the velocity, and the interface restores energy. This suggests that the observed power P can be used to control the haptic device. If the power is positive, the brake must be

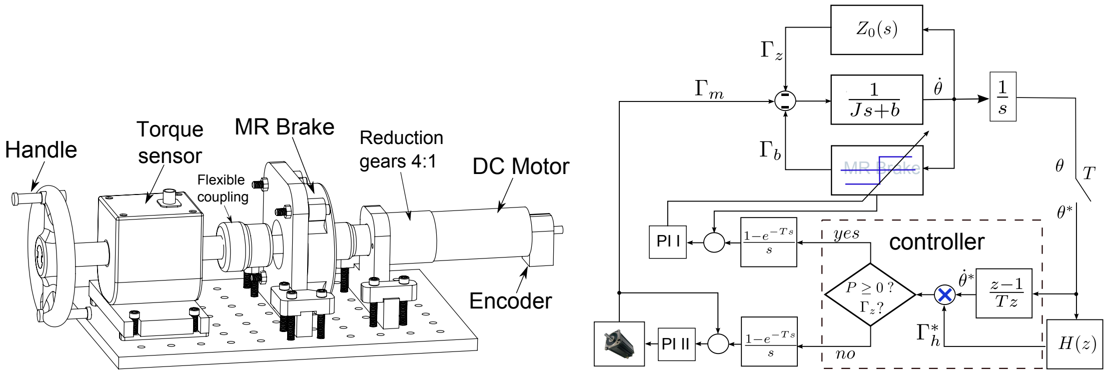

(a) 1-DOF mechanical device **(b)** control loop

Figure 1.14: 1DOF hybrid force feedback device and its respective control loop. A DC motor is connected to a magneto-rheological brake linked to the handle using a torque sensor (a). Each actuator is controlled in force by two PI controllers (b) where Γ_m, Γ_b, Γ_z and Γ_h^* are the torque applied by the motor, by the brake, by the human operator $Z_0(s)$ and the reference torque calculated by the virtual environment $H(z)$ as a function of the position θ^*. The device has an inertia J, a damping b ant the sampling rate is T. The controller is independent of the virtual environment.

activated; if the power is negative, only the active actuator should be enabled. The control law is given by:

$$\begin{pmatrix} \Gamma_m \\ \Gamma_b \end{pmatrix} = \begin{cases} ZOH \begin{pmatrix} 0 \\ \Gamma_h^* \end{pmatrix} & (\Gamma_h^*)\dot{\theta}^* \geq 0 \\ ZOH \begin{pmatrix} \Gamma_h^* \\ 0 \end{pmatrix} & (\Gamma_h^*)\dot{\theta}^* < 0 \end{cases} \tag{1.23}$$

Based on this control method, the behaviour of the system when the velocity is zero cannot be determined. Zero velocity can be due to the torque balance on the handle or because the operator released the handle during the dissipation phase. For instance, consider that the virtual environment simulates an angular spring. The operator moves the handle and a reference torque is calculated in the virtual environment. Using the interaction power based flow method, the brake is used to simulate the compression phase of the spring whereas the motor is used to simulate its decompression phase. At zero velocity, the transition brake/motor should be supervised using a measure of the torque imposed by the operator. When this torque is inferior to the reference torque, the motor should be activated instead of the brake.

Fig. 1.14a shows the 1-DOF interface used as a test bench to validate the control. A DC motor (Maxon RE40) connected to a controllable magnetorheological brake (Lord RD2087, exploited up to 400 mNm) compose the device. A torque transducer (Sensor Developments 01324) is placed between the end-effector and the brake. All these elements are linked together in parallel through flexible couplings. Fig. 1.15b shows its respective control scheme. The

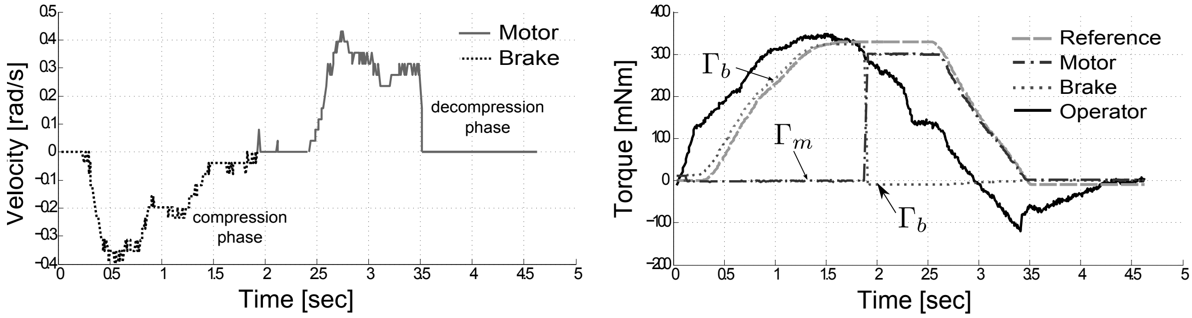

(a) Velocity **(b)** Interaction torques

Figure 1.15: Experimental results using interaction power and torque based control. Γ_m and Γ_b are the torque of the motor and of the brake. During the compression phase of the spring the brake is activated, when the torque imposed by the operator becomes inferior to the reference torque, the motor is used to simulate the decompression phase.

actuator's force is controlled by two custom-made analog proportional-integral controllers (PI). An incremental encoder with 4096 pulses per revolution measures the position. The system is controlled by a microcontroller 8051F120 runing at 99.4MHz.

The virtual environment is assigned as a virtual spring so that $H(z) = K_h$, where K_h is the spring's stiffness. Since passive actuators cannot produce energy, this represents one of the most critical simulation cases using hybrid interfaces.

4.3.1 TORQUE MEASUREMENT BASED CONTROL

This method uses a quantitative measure of the torque imposed by the operator to determine the behaviour of the system when the power is zero. Two conditions are henceforth required to keep the brake activated. The control laws is implemented as:

$$\begin{pmatrix} \Gamma_m \\ \Gamma_b \end{pmatrix} = \begin{cases} ZOH \begin{pmatrix} 0 \\ \Gamma_z^* \mathrm{sgn}(\dot{\theta}) \end{pmatrix} & (\Gamma_h^*)\dot{\theta}^* \geq 0 \; and \; \Gamma_z \geq \Gamma_h \\ ZOH \begin{pmatrix} \Gamma_h^* \\ 0 \end{pmatrix} & otherwise \end{cases} \tag{1.24}$$

This control method is designed to notify the controller when the torque imposed by the user is inferior to the torque calculated by $H(z)$. In this case the motor must be activated to induce a velocity in the same direction of the reference torque. From this point, the power becomes negative. Note that, if motors and brakes do not have the same torque capacity, the measured torque must be compared to the maximum torque of the motor to avoid undesirable vibration at the transition brake/motor.

Fig. 1.15 shows the experimental results. Between t=0 and t=1.8s the operator compresses the spring ($|\Gamma_z| > |\Gamma_h^*|$), the velocity is opposed to the reaction torque, thus the power is positive and the rendering is assured by the brake. At t=1.8s the user begins to release the handle (the torque decreases gradually) and the velocity is zero when $|\Gamma_z| = \left|\Gamma_h^*\right|$. When the imposed torque by the operator is inferior to the applied torque ($|\Gamma_z| < \left|\Gamma_h^*\right|$) (t=1.9s), the desired torque is transferred to the motor and the velocity inverted. Thus, the interface simulates the decompression phase of the spring using the motor (power becomes negative). The difference between the desired and applied torque is due to uncompensated viscous friction.

4.3.2 TORQUE DETECTION BASED CONTROL

By contrast to the previous method, the only information sent to the controller is whether the operator imposes a torque or not, without quantifying it. In this case, the control law becomes:

$$\begin{pmatrix} \Gamma_m \\ \Gamma_b \end{pmatrix} = \begin{cases} ZOH \begin{pmatrix} 0 \\ \Gamma_h^*) \end{pmatrix} & (-\Gamma_h^*)\dot{\theta}^* \geq 0 \; and \; \Gamma_z \neq 0 \\ ZOH \begin{pmatrix} \Gamma_h^* \\ 0 \end{pmatrix} & otherwise \end{cases} \tag{1.25}$$

The experimental results are presented in Fig. 1.16. In this case, we note that a torque detection imposes an inherent delay in the transition brake/motor. The operator compresses the spring until t=2.8s since $|\Gamma_z| > \left|\Gamma_h^*\right|$. At this point the reactive force is equal to the imposed force ($|\Gamma_z| = \left|\Gamma_h^*\right|$) and $\dot{\theta} = 0$. The operator gradually releases the handle and the measured torque decreases, while the brake remains activated and in consequence $\dot{\theta} = 0$. When $\Gamma_z = 0$ at t=4.0s, the brake is turned off, the motor is activated and the handle can turn freely. Note that the observed delay in the activation of the motor depends on the rapidity that the human operator releases the handle.

This method makes the system control independent of the application: a desired torque is converted into two signals to control each actuator. The controller has no prior knowledge of the virtual environment model. Combined with torque measurement, it is possible to determine the behaviour of the system even when the velocity is zero. Torque detection-based method it introduces an inherent delay that may be acceptable for some applications. This detection can be realized using the brake as suggested in [Rossa *et al.*, 2012].

4.4 DISCUSSION

Three control approaches for hybrid actuators are available in the literature. The controllable damping approach is an effective solution to improve the range of displayable stiffness of the motor. However, only the motor can render the stiffness of the virtual environment and as a consequence, the maximal static torque displayable by the device is bounded to the

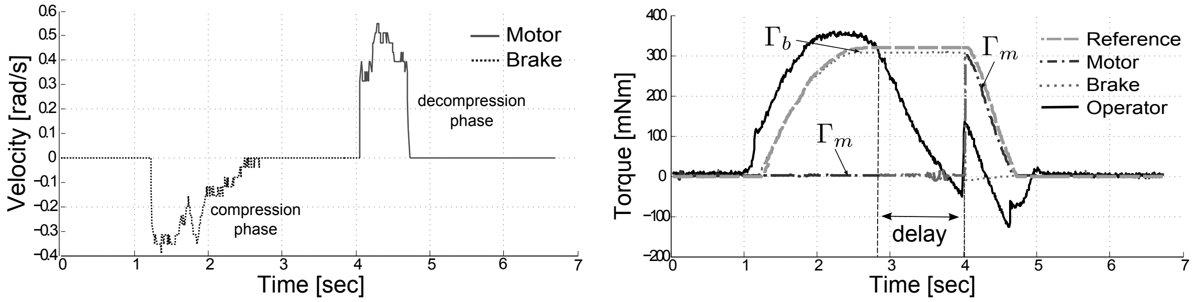

(a) Velocity **(b)** Interaction torques

Figure 1.16: Experimental results using energy flow and torque detection based control. Γ_m and Γ_b are the torque of the motor and of the brake. The system simulates an angular spring. The operator compresses the spring up to t=2.8s and the brake is activated. When the operators torque is zero, the motor is engaged to decompress the spring.

torque capacity of the active actuator. Conversely, the damping cancellation approach bases the haptic rendering on the brake. The motor works simultaneously in order to compensate for the generated friction. Although this approach has been demonstrated as a solution to improve transparency, the rendering is strictly passive and the system is not able to restore any energy to the operator. Though, these control methods turn out to be complementary. In the last method, both actuators are used to display the forces of the virtual environment, the capability of the device to impose dissipative efforts is the contribution of the passive and active torques. Besides, the system can restore some energy to the human operator. The observation of the power flow in the device as an indication of the behaviour of the system, passive or active, is a useful tool to indicate if the active or the passive actuator should be enabled. However, this needs the use of torque traducers to manage the transition brake/motor.

5 CONCLUSION

In order to accurately render the virtual environment forces to the human operator, a haptic device must cover a wide range of achievable impedance while maintaining stability. Several works have dealt with the utilisation of active actuators for haptic rendering. They are inevitably confronted to instability issues due to the sampling rate and imperfection of transducers. It has been demonstrated that the stiffness simulated by any active actuator must be bounded in order to avoid instability. In addition, due to the their relative low torque to volume ratio, active actuators are usually coupled to reduction stages. It dramatically increases the parasitic forces such as inertia and friction reflected to the end-effector and damages the interaction's transparency.

Documented control methods employed in the control of active interfaces are designed to achieve stability with passive based control schemes. Since most virtual environments can be envisaged as passive, and most of the time the haptic device is requested to constrain the motion of the end-effector, the use of a passive actuators instead of passivity-based controller can be justified. High output impedance can be generated using passive actuators with stability and safety. Although such actuators provide relatively good control performance, they are unable to restore energy to the human operator.

The association of passive and active actuators enables the system to combine the advantages of each actuation approach. As demonstrated in the literature, it can effectively improve the range of achievable impedance of haptic devices using either the active actuator to display the efforts while the passive one provides for the interaction's stability, or inversely, where the rendering is assumed by the passive actuator and the active actuator is used to enhance the transparency.

A more efficient passive/active linkage may employ both actuators to display the reflective forces. Generality speaking, the passive actuator can be used to simulate passive elements and the active one to restore some amount of energy. Besides, it also allows the device to combine both actuators to impose an effort against the motion. However, as demonstrated in Section 4.3, if both actuators are mechanically coupled in parallel, the passive actuator dissipates the energy provided by the active one. Using a passive actuator with higher torque capability, the coupled system behaves equivalently as a passive system. This implies the use of torque transducers which are however costly an bulky.

A suitable hybrid actuation system for force feedback interfaces comprises an integrated passive/active mechanical actuator, independent specific control laws, and must meet the following requirements:

1. The active and the passive actuators are mechanically decoupled and can be considered as two independent systems. In order words, the passive actuator is able to impose passive forces without obstructing the actuation of the active one.
2. The control laws are able to respect the reference torque of the virtual environment using the combination of both actuators taking into account to the stability limits and torque capabilities.
3. The control laws do not necessitate any measure of interaction forces.
4. The controller is completely independent of the virtual environment model. The actuation system should be implementable in several different haptic devices.
5. The actuator combines a powerful passive actuator and a small active one in an integrated configuration without reduction stages. It naturally guarantee the operator's safety.

The following Chapters directly address these points. More specifically, in Chapter 2 a new hybrid actuation concept is introduced. It consists of a mechanical configuration using a brake and a motor linked through of an overrunning clutch. By this means the brake can apply a torque only in a defined direction. By controlling the activation of both actuators, the brake does not obstruct the motor. Control laws for stable interaction are subsequently presented in Chapter 3. They share out the reference torque obtained from the virtual environment and bound the energy and the stiffness displayed by the motor. The rest of the document addresses the design and evaluation of an integrated actuator.

A NEW HYBRID ACTUATION APPROACH FOR FORCE-FEEDBACK DEVICES

2

Contents

Partially reprinted, with permission from

©2012 IEEE

C. Rossa, J. Lozada, and A. Micaelli. "A new hybrid actuator approach for force-feedback devices," Intelligent Robots and Systems (IROS), 2012 IEEE/RSJ International Conference on, pp.4054,4059, 7-12 Oct. 2012 doi: 10.1109/IROS.2012.6385784.

A NEW actuation concept based on unidirectional rotary brakes associated to a DC motor is introduced in this chapter. A brief review of mechanical arrangements employed in human-machine interfaces is presented. Inspired from this configurations, several ways can be envisaged to couple active and passive actuators in order to meet the requirements of force feedback interfaces.

A 1-DOF haptic device is developed to validate the actuation approach. A commercial magnetorheological brake and a DC motor compose the actuator. The brake is linked to the motor using an overrunning clutch. Two control methods are proposed to determine the participation of the brake and of the motor following a reference torque. In the first method, the motor is only activated if the velocity is zero and to restore energy. The second method allows for the dissipation of energy using the motor. The brake compensates for the difference between the reference torque and the torque capability of the motor. Experimental results demonstrate the feasibility of the proposed approach.

1 MECHANICAL CONFIGURATIONS

In order to design a hybrid actuator for human-machine interaction, several factors should be taken into consideration. This includes the interaction's safety, bandwidth, torque capability, stability issues and force quality. Frequently, there is a tradeoff between these measures of performance and a compromise should be found. An ideal actuator should possess low inertia, high torque capability, sufficient bandwidth and low power requirements. Several mechanical configurations suitable for human-machine interfaces are available in the literature and they are presented in Section 1.1. Inspired hybrid configurations derived from these approaches can be subsequently envisaged.

1.1 CLASSICAL ACTUATION APPROACHES

Documented actuator arrangements designed for human-machine interaction can be categorized as explicit force feedback, impedance controllable direct drive, series elastic, differential elastic, variable stiffness, variable damper actuators, and micro/nano manipulator approach.

Explicit force feedback actuators are widely employed in haptic devices. It includes a force sensor in series with an actuator such as electric motors and make no use of position measurement. The interaction force is controlled using force feedback [Carignan et Cleary, 2000]. These actuators use admittance control schemes which provides good accuracy in free motion but can result in instability during the interaction with stiff environments [Ott *et al.*, 2010]. According to [Eppinger et Seering, 1987a] [Eppinger et Seering, 1987b], factors as environment stiffness, sensor dynamics and impact forces upon workpiece contact are some of possible sources of instability . Furthermore, the high impedance using active actuators may pose a potential danger to the operator if the system becomes unstable. Besides, this method needs the user of torque transducers.

Impedance controllable direct drive actuators consist in direct driving an actuator connected to a system [Kazerooni et Kim, 1988] [Reyes et Kelly, 2001]. This method eliminates all the transmission mechanisms such as gear boxes and, since the end-effector is directly coupled to the actuator output, a direct-drive manipulator is essentially free of problems caused by transmission mechanisms [Asada et Kanade, 1981] [Bergamasco *et al.*, 1989]. Electric motors for example, are usually low inertia devices and have a well-known current and output force relationship. The main advantage claimed for direct drive actuators are high accuracy and velocity, and light weight [Aghili *et al.*, 2000]. However, because no reduction stage is used, the torque to weight and to volume ratios are relatively small and limit the range of applications.

Series elastic actuators combine a compliant element placed between a high impedance actuator and a force sensor. A classical configuration consist in coupling an angular spring to a geared electric motor [Pratt et Williamson, 1995] [Sensinger et Weir, 2005]. This arrangement decouples the high inertia of the gear-motor system to the inertia of the end-effector. The output force is proportional to the position difference across the series elastic element multiplied by its stiffness. This arrangement offers a number of advantages, including less reflected inertia to the end-effector, shock tolerance, and the capacity to store energy [Sensinger et Weir, 2006] [Wyeth, 2008]. However, at the same time the addition of an elastic element presents several drawbacks, such as the limited bandwidth and stability issues due to the non-collocation of sensors [Vallery *et al.*, 2007]. Due to the fact that the stiffness is usually constant, achieving good force fidelity at both low and high impedance ranges is not trivial.

Differential elastic actuators differ from series elastic actuators by the use of a differential coupling instead of a serial coupling between the power source and the end-effector. This gives to the system a simpler solution with similar performance [Lauria *et al.*, 2008] specially for rotational actuators.

Variable stiffness actuators usually link two non-linear antagonistic springs to provide a physical variation of the output stiffness (see [Bicchi *et al.*, 2005], [Schiavi *et al.*, 2008] and [Migliore *et al.*, 2005]). An example consists on a lever which rotates around a fixed point. Its compliance is due to two attached springs at a variable distance to the pivot. The stiffness adjustment is done through moving the position of the springs along the lever. Another possibility may consist in varying the pretension of the springs at a fixed position [Ham *et al.*, 2007] [Vanderborght *et al.*, 2009] [Choi *et al.*, 2011]. The motors used to regulate the stiffness work against the springs force. Alternatively, variable stiffness actuator take also serial configurations, characterized by the mechanical series geared motor/springs both for linear and rotational implementations. Such actuators suffer however from high mechanical complexity and relative low bandwidth.

Variable damper actuators incorporate a series damper instead of a series elastic component between the actuator and the end-effector [Zhou *et al.*, 2005]. It enables to decouple the inertia and frictions of the actuator to the end-effector with higher bandwidth compared to series elastic actuators [Chew *et al.*, 2004] [Chapuis, 2009]. The output force is obtained by varying the damping coefficient and it is proportional to the relative velocity across the damper. However, the inherent friction of the damper limits the capabilities of the actuator to display small forces.

Micro-Macro manipulator arrangement [Sharon et Hardt, 1984] corresponds to the series association of a small "micro" actuator carried by a large "macro" manipulator, both sharing the same load. This approach divides the torque generation into low-and high-frequency actuators. The high-frequency actuation is typically a low impedance actuator achieved by using a small, low-inertia motor linked to the end-effector through a low-reduction ratio transmission. The low-frequency actuation uses a series elastic actuator [Zinn *et al.*, 2004]. This configuration can improve the achievable flexibility and velocity and reduces the apparent inertia of the system [Sharon *et al.*, 1988] citeSalcudean1989 [Stocco et Salcudean, 1996]. However, the small actuator must be able to bear the whole brunt of the efforts of the end-effector.

1.2 HYBRID ACTUATION ARRANGEMENTS

The related mechanical designs of human-friendly robotics devices commonly employ active actuators. Inspired from these arrangements, several ways can be envisaged to form a hybrid system for haptic interfaces coupling an active and a passive actuator.

Fig. 2.1 summarizes some related mechanical ways to couple a brake and a motor in order to form a hybrid device. In the symbolism, a rectangle, a coil, and a piston represents an inertia, a spring, and a damper respectively. A motor is illustrated by two parallel lines and a brake by a concave line. The mechanical connection using a continuous line represents a common velocity on each side and connections with a dashed line indicates that the velocity is opposed. Half parallel lines or half concave lines symbolises an actuator that can apply a torque only in one rotational direction.

Arrangement **(a)** is the standard configuration where a brake and a motor are directly connected in parallel. Some applications to haptic interfaces can be found in [Walker *et al.*, 2009] [Chen et Liao, 2009] [Baser *et al.*, 2012a] [An et Kwon, 2006b]. This option allows for the use of explicit force feedback configuration [Nam et Park, 2007] or impedance controllable direct drive [Badescu *et al.*, 2002]. In both cases, the efforts provided by each actuator can be added to create resistive forces against the motion of the end-effector, but at the same time the main drawback of this arrangement is that the brake dissipates the active effort of the motor and the system can behave as passive [Kwon et Song, 2006].

Option **(b)** employs the micro/macro manipulator concept. A brake and a motor with similar torque capabilities are linked in series. The brake actuates as a clutch transferring the

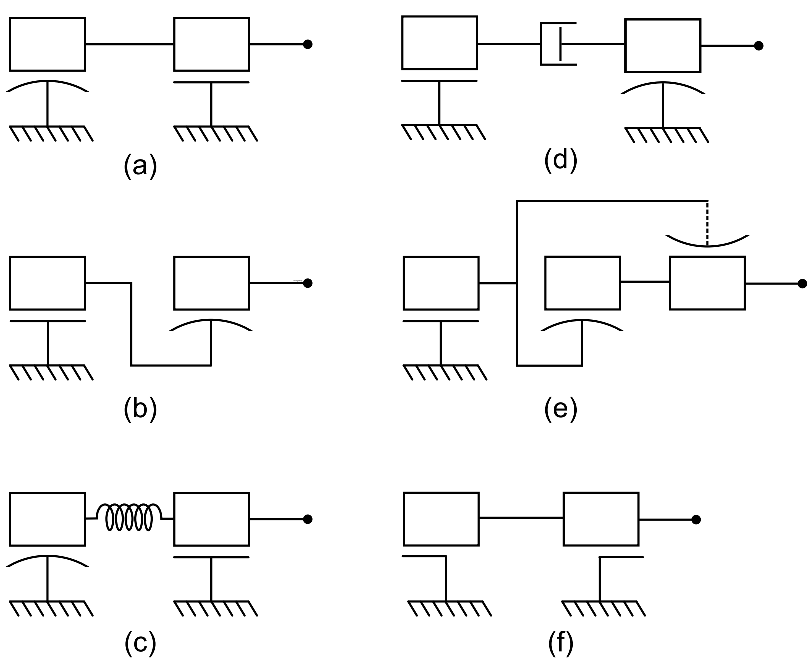

Figure 2.1: Several ways to form a hybrid actuator using a motor and a brake. A rectangle represents an inertia, two parallel lines represent a motor. A concave line represents a brake. A coil and a piston symbolizes a spring and a damping receptively and a circle shows the end-effector. A half line indicates an unidirectional actuators. A mechanical connection indicates that the velocity is the same on each side. Dashed lines indicate velocity inversion. Option (a) links a brake and a motor in parallel, option (b) in series thus the brake actuates as a clutch, arrangement (c) uses a spring to store energy, in (d) a damper decouples the apparent inertia, (e) uses opposite clutches to transfer the motor's torque, and (f) employs unidirectional motor as semi-passive actuators.

motor's torque to the end-effector. Chapuis et al. [Chapuis *et al.*, 2006] present a configuration where an ultrasonic motor (USM) is used as active actuator. Thanks to its high blocking torque, the brake can impose a resistive force when the motor is deactivated. This option however impairs the system to transfer the brake/motor torques to the end effector at the same time.

Configuration **(c)** is inspired from series elastic actuators. As proposed by Conti and Khatib [Conti et Khatib, 2009], the motor and the brake are linked via an angular spring in order to store the energy provided by the operator. Two position encoders are used to measure the relative deformation of the spring in order to calculate the amount of available torque. The motor compensates for the error between the reference torque and the torque of the spring. In a force feedback device, one would rather make the linkage as stiff as possible to keep the natural bandwidth of each actuator [Mohand-Ousaid *et al.*, 2012]. In the same way, option **(d)** couples two stages by a viscous damper in order to decouple the inertia of one actuator to the end-effector. An application using two motors, is related in [Mohand-Ousaid *et al.*, 2012] and [Chew *et al.*, 2004]. The system can be controlled so that it has a linear torque-velocity relationship varying the damping coefficient and the velocity can be inverted without changing the velocity of the motor. The brake can direct apply a torque at the end-effector independently of

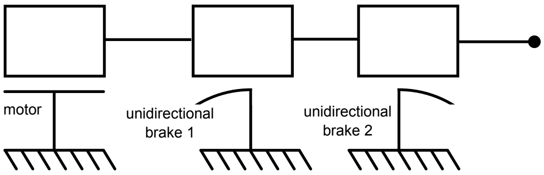

Figure 2.2: Working principle of an unidirectional brake based actuator. Each brake is connected to the shaft through opposite overrunning clutches. The motor is directly connected to the shaft and can impose an effort at the end-effector in both directions. If the operator turns the end-effector in the clutched direction, the brake can impose a resistive torque, in the other direction the end-effector can be turned freely.

the state of the motor, which is an advantage compared to **(b)**.

Alternative **(e)** incorporates two brakes acting as clutches, being driven at the same velocity but in opposite directions by a motor linked in series. The brakes output are connected in parallel [Fauteux *et al.*, 2009]. Each brake then transfers the motor's torque to the end-effector in a defined direction. Since the velocity of the brakes are opposed, the friction reflected at the end-effector is reduced which enables the transmission of very small torques. Furthermore, the motor rotates always in the same direction. When using a USM as power source the system is equivalent to configuration **(b)**. However, the actuator behaves as an active system and the maximal torque is bounded by the torque capability of the motor.

In the actuation approach described in **(f)**, two opposite overrunning clutches are used rather than brakes. Each of them is connected to a motor. Depending on the relative velocity of the motor and of the shaft, the shaft is blocked or not. The rotational velocities determine the maximum clockwise and counterclockwise joint angular velocities which an operator can generate without engaging a clutch. Each motor then can restrict the motion only in one direction and cannot directly drive the shaft [Troccaz et Delnondedieu, 1996] [Troccaz *et al.*, 1998].

1.3 DISCUSSION

Exploring both actuators to simulate controllable stiffness while keeping the natural bandwidth of each actuator may imply the use of solution **(a)** or **(d)**. Arrangement **(d)** employs a viscous damping between the actuator which increases the complexity of the device and may restrain the use of the actuator only to specific applications in which series elements are adaptable. Solution **(a)** is a more generalisable solution which does not contain other elements than the brake and the motor. Nonetheless, the brake blocks the motor and the system can behave as passive. In order to mechanically decouple the motor from the brake, a solution is the use of unidirectional brakes. It is achieved using the combination **(f)** and **(e)**. We obtain an equivalent system as **(a)** but both actuators can be controlled independently. More specifically, this actuation concept combines two unidirectional brakes and a motor in parallel as is illustrated in Fig. 2.2. The brakes are connected to the shaft using opposite overrunning clutches, to apply a

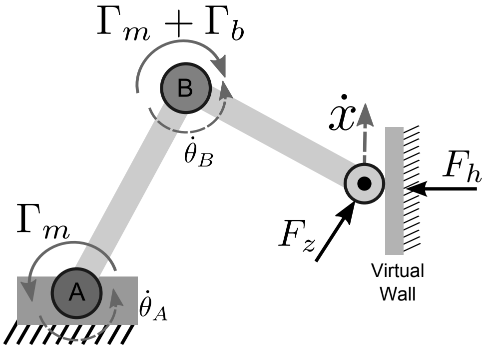

Figure 2.3: A 2DOF device with unidirectional brakes and a motor on each joint. The frictionless virtual wall is simulated with the force F_h. Given the operator's force F_z the resultant velocity $\dot{x}$ is tangential to the wall. This induces a reference torque on both joints A and B actuated by a motor/brake. The motor and the corresponding brake are enabled. In the joint B the reference torque is opposed to the velocity. Both actuators apply a resistive torque. In the joint "A" both a brake and the motor are enabled. Since the torque and the velocity are in the same direction, the braking torque is zero. Γ_m and Γ_b are the motor and brake torques respectively

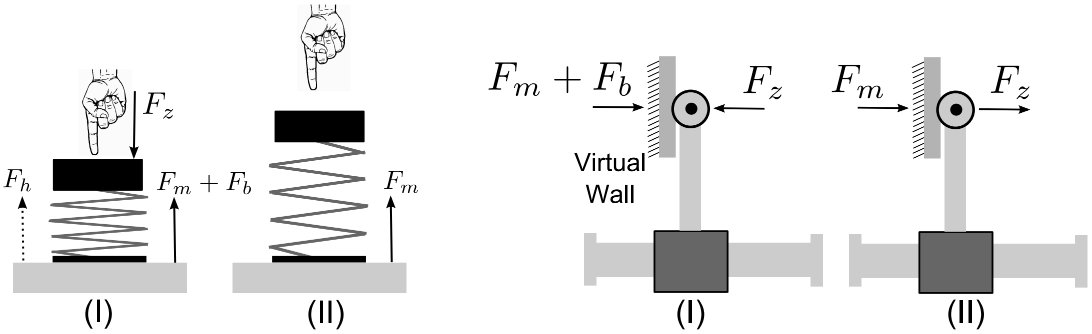

(a) Virtual Spring

(b) Virtual Wall

Figure 2.4: A 1DOF haptic interface with unidirectional brakes. In (a) the simulation of a virtual spring. The user compresses the spring with a force F_z (a I). The motor applies a force F_m and the brake able to generate the force F_b in the direction of F_h is activated. When the operator releases the handle, it gives $F_b = 0$ and the motor is free to decompress the spring (a II). The same behaviour is observed in (b). Both actuators apply a force against the penetration of the wall (b I). When the operator inverses the velocity, the braking force is zero and does not block the motor (b II).

torque only in one defined direction while the motor can apply a torque in both directions.

This configuration has several advantages compared to the classical approaches. The brakes and the motor are rigid coupled and the absence of elastic or viscous elements does not deteriorate the mechanical bandwidth of each actuator. The use of unidirectional brakes enables the system to be controlled using impedance control with no measure of interaction torques. The novelty of the proposed hybrid actuation system lies in the use of controllable unidirectional brakes, in the technologies employed for brakes and the in the associated control laws without a torque transducer.

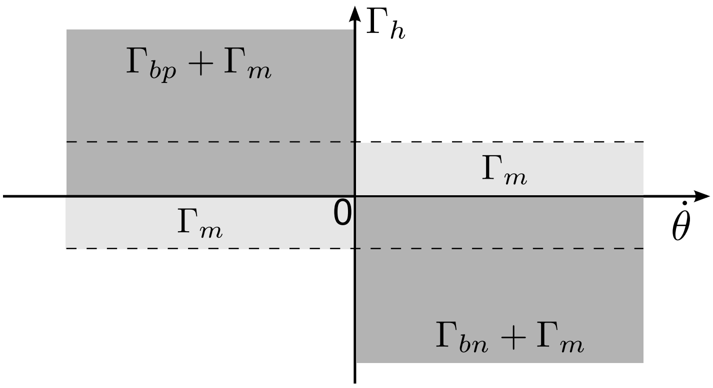

Figure 2.5: Torque capability of an actuator comprising brakes and a motor. The torque of the motor is Γ_m and Γ_{bp} and Γ_{bn} are the torque provided by the positive and by the negative brakes. If the velocity $\dot{\theta}$ is opposed to the reference torque torque Γ_h, both brake and motor can be engaged. Conversely, only the motor can provide a torque.

2 A NEW HYBRID ACTUATION APPROACH

Using two unidirectional brakes, both the brake and the motor can be activated at the same since the brake does not block the motor. The activation of the unidirectional brake can be realised as a function of the reference torque Γ_h^*. We call "positive brake" the brake able to generate a torque $\Gamma_{bp} > 0$ opposed the velocity of the shaft $\dot{\theta} < 0$. If the velocity of the shaft is positive, this brake cannot impose a torque. In complementary way, the "negative brake" can impose a torque $\Gamma_{bn} < 0$ which needs $\dot{\theta} > 0$.

As a function of the desired torque Γ_h^*, the selection of a brake is realised as follows:

$$\begin{pmatrix} \Gamma_{bp} \\ \Gamma_{bn} \end{pmatrix} = \begin{cases} \begin{pmatrix} \Gamma_h^* \\ 0 \end{pmatrix} & \Gamma_h^* > 0 \\ \begin{pmatrix} 0 \\ \Gamma_h^* \end{pmatrix} & \Gamma_h^* < 0 \end{cases} \tag{2.1}$$

By these means, a braking torque is observed only if the velocity is opposed to the reference torque. The torque capability the brake/motor system is shown in Fig. 2.5. When $\text{sgn}(\Gamma_h) \neq \text{sgn}(\dot{\theta})$, the total torque is the contribution of the brake and of the motor, otherwise, only the motor can provide a torque. Therefore, the capability of the system to dissipate energy is greater than its capability to restore energy to the operator.

This actuation approach ensures that the braking torque has always the same sign as the reference torque. Consider the simulation of the virtual wall of Fig. 2.3. The wall is simulated by the normal force F_h. According to the Jacobian characteristics of the manipulator, on the joint A and B a torque in the positive and negative directions respectively are necessary. Thus, the motor and the brake able to generate a torque in these directions are activated. Given the operator's force F_z, the desired resultant velocity $\dot{x}$ is parallel to the wall and induces a respective angular velocity in each joint. In the joint B the reference torque and the velocity have opposite signs. Thus, the motor and the brake can apply a torque. In the joint A, the reference torque is the in positive direction. Since the velocity and the torque have the same sign, the brake is activated but cannot generate a torque due to the overrunning clutch. As a consequence, the motor is free to impose a torque in the desired direction.

Consider the simulation of a virtual spring and the unilateral contact presented in Fig. 2.4. In 2.4a the operator compresses the spring and the reference force F_h can be simulated by a brake and by the motor (I) so that $F_h = F_b + F_m$. The brake able to generate a force in the direction of F_z is activated. When the operator releases the end-effector (II), the braking force is zero, and the motor is free to simulate the decompression of the spring. Likewise, in Fig. 2.4b, unilateral contact is simulated by the combination of the motor and of the brake opposed to the operator's force F_z. The braking force is naturally zero when the operator inverses the motion and the motor can repulse the end-effector out of the wall.

The active actuator that will be employed in the design of the haptic device is a conventional DC motor. DC motors have accurate and a well-known current/torque relationships and a wide range of speed control. Concerning the passive actuator, some potential solution for the design of the hybrid system are presented in the following section.

2.1 PASSIVE ACTUATORS FOR HAPTIC RENDERING

Passive actuators used in the design of haptic devices includes eddy current brakes, friction brakes, electromagnetic clutches, powder brakes, and rheological brakes.

Hysteresis or eddy current brakes have been successfully applied in the design of haptic devices [Gosline et Hayward, 2008] [Campion *et al.*, 2006]. An eddy current brake consists of a conductor moving through a magnetic field. As a result, Foucault's currents are induced and create a resistive force proportional to the relative velocity, according to Lorentz force law. These actuators provide controllable torque with higher accuracy and higher bandwidth compared to particles brakes. However, eddy current brakes cannot generate static torque.

Friction brakes such as piezoelectric-ceramic stack actuators require low power and provide relatively high bandwidth [Gogola et Goldfarb, 1999]. It consists of ceramic material that can be deformed in a particular direction under the application of an electric field. The fundamental component of a piezoelectric stack actuator is a wafer of piezoelectric material placed between two electrodes [Goldfarb et Celanovic, 1997]. An assembling of several of the wafer elements in series has an output force sufficient to create a braking torque that is comparable to commercial brake designs. However, the working principle of these actuators presents inherent difficulties for force-feedback devices including a highly non-linear behaviour [Claeyssen *et al.*, 2001].

Electromagnetic brakes enables the mechanical linkage of two rotation axis by means of magnetic actuation [Chen *et al.*, 2008]. The brake has a coil which can generate a magnetic flux across the different rotary parts. Thanks to the magnetic attraction between the armature and the rotor, the armature is pulled against the rotor and frictional forces are generated at contact [Qian et Kachroo, 1997]. Consequently, the armature is gradually accelerated up to match the velocity of the rotor. However, the amount of transmitted torque cannot be controlled. In order to allow for the control of the transmitted velocity, magnetic particles can be placed between the rotor and the armature [Bica, 2004]. This characterizes the working principle of powder brakes.

Powder brakes contain small magnetic particle powder located in a cavity between the stator and the brake rotor [Eddens, 1982]. The system has an excitation coil which can apply a magnetic field in the powder cavity. When the filed is applied, the resulting magnetic flux tries to bind the particles together, and the powder aligns in the direction of the field. When the current is increased, the binding of the powder becomes stronger. The interaction between the particles create a resistance against motion which slows or stops the relative rotation of the rotor. Such brakes have been successfully implemented in the design of life-sized passive interfaces [Matsuoka et Townsend, 2001] [Hirata *et al.*, 2010] and mini invasive endoscopy devices [Maillard *et al.*, 2008]. However, powder brakes suffer of relative low endurance due to degradation of the powder.

Another category of brakes is the rheological fluid-based brakes. In this case, the particles powder are dispersed in a carrying liquid typically mineral oils, synthetic oils or water. The particles are either of ferromagnetic or non-conducting materials. The rheological properties of such suspensions can be strongly and reversibly modified by the action of an electric field, in the case of an electrorheological fluid (ERF) [Furusho *et al.*, 2002], or by the action of a magnetic field in the case of a magnetorheological fluid (MRF) [Nguyen et Choi, 2010] [Scilingo *et al.*, 2000]. While ERF typically exhibit yield stress up to 5kPa with excitation voltages in the range of a kilovolt, MRF can provide a yield stress up to 100kPa and need relatively low operating currents and voltages, which makes them particularly suitable in the design of human-machine interfaces. Furthermore, MRF have between 20 and 50 times higher control effect than the equivalent ERF [Olabi et Grunwald, 2007].

An MRF-based actuator works as follows. When a magnetic field is applied in the fluid cavity, the micron-sized ferromagnetic particles are magnetized and undergo magnetic interaction forces. This leads to the formation of chain-like structures or aggregates aligned roughly parallel to the magnetic field. As a consequence, MRFs posses the ability to achieve a wide range of apparent viscosity [Klingenberg, 2001]. This is macroscopically manifested, when the fluid is sheared, by the development of a yield stress which increases with the magnitude of the applied field in a fraction of a millisecond. This phenomenon can be exploited for designing controllable brakes. The fluid is confined between two magnetic poles. The chain-like structures then create a resistive force against the pole displacement, which increases with the

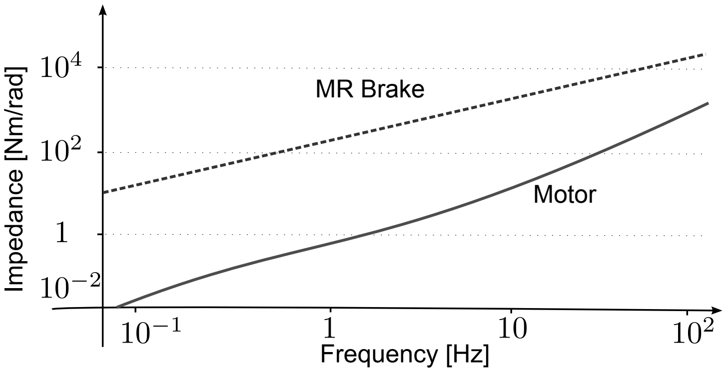

Figure 2.6: Comparative analysis of displacement impedance range of an MR brake (Lord Corp. RD-2068-10, 5Nm,) and a DC motor (Maxon EC-40, 220mNm). The actuators are coupled to a reduction stage in order to obtain 50Nm at the end effector.

magnitude of the applied field. A more detailed description and an extensive model of an MRF brake will be presented in Chapter 4.

MFR based actuators provide high controllability, fast response time, very low power requirements and high torque-to-volume ratio. Thanks to these advantages, they hold great potential in many application requiring variable impedance devices such as controllable clutches (see [Shafer et Kermani, 2011], [Chen et Liao, 2010] and [Fauteux *et al.*, 2009]) or brakes (see [Huang *et al.*, 2002], [J. *et al.*, 2002] and [Saito et Ikeda, 2007]), variable pressure drop valves [Grunwald et Olabi, 2008] [Ai *et al.*, 2006], dampers for vibration control (see [Milecki, 2001], [Dyke *et al.*, 1998] and [Duan *et al.*, 2006]), [Winter et Bouzit, 2007]and passive haptic devices ([Blake et Gurocak, 2009] and [Lozada *et al.*, 2007]).

Compared with a DC motor, MRF brakes have the advantage of a higher torque/volume and torque/mass ratio, and present lower power requirements. Fig. 2.6 presents the impedance range as a function of the frequency, achieved using both a commercial available MRF form Lord corporation (Lord Corp. RD-2068-10), maximal torque 4Nm, and a DC motor Maxon EC-40, nominal torque 220mNm. Both actuators are coupled to a reduction stage with an appropriate reduction ratio in order to obtain 50Nm at the end-effector. The results highlights that the brake can achieve higher impedance compared to the motor [Rhijn, 2011].

Periquet and Lozada [Periquet et J.Lozada, 2010] used MRF for a miniature 1-DOF haptic interface actuator that produces a torque from 0.03Nm to 1.7Nm and consumes 27 Watts. Compared with a commercial DC motor (Maxon RE25), it represents 51 times more torque for the same volume with a ratio torque/power-volume 38 times superior than the motor. A haptic glove, proposed by Blake et al. [Blake et Gurocak, 2009], employs six compacts MRF brakes to generate a haptic feedback in three fingers, allowing the operator to pick up and feel virtual objects. Lozada et al. [Lozada *et al.*, 2007] also used MFR actuators for haptic feedback in musical keyboards. A linear brake applies a resistive force in real-time by dissipating the mechanical energy given by the pianist. Other applications of MRF-based actuators include the conception of joystick for virtual reality [Liu *et al.*, 2006], and rotary knobs for in-vehicle information system control [Periquet et Hafez, 2009] [Han *et al.*, 2009].

In virtue of these attractive features for haptic rendering, an MRF-based brake is adopted in this research. The feasibility of the proposed actuation approach is investigated using a commercial magneto-rheological brake, from Lord Corporation, model RD2078 [1] linked to a Maxon Motor RE40 [2]. Both actuators are associated using an overrunning clutch [3].

3 PROOF OF CONCEPT

The haptic interface prototype is shown in Fig. 2.7. The motor is directly connected to the end-effector while the brake is linked on the shaft via the overrunning clutch placed into the handle. Note that the device is asymmetrical and can work only in one direction. A complete system will require two brakes and one motor. If the operator turns the end-effector in the clutched direction, the brake can impose a resistive torque. If the handle is turned in the other direction, it can move freely.

The motor is exploited up to 54 mNm and is coupled to a reduction gear with a transmission ratio of 4:1. The maximal motor's torque is 216mNm. The braking torque is arbitrarily limited to 400mNm. The overrunning clutch mechanism has 16mm diameter and 23mm length. It can transmit up to 20Nm of torque in its recommended operation range. An incremental encoder with 500 pulses per revolution is used to measure the position of the motor shaft. By definition, the brake can impose a torque only if the velocity of the end-effector is positive.

The overrunning clutch or freewheel mechanism that links the brake and the motor is illustrated in Fig. 2.8. It is composed of two principal parts. The external cylinder **A** over which the motor and the handle are linked, and the inner cylinder **B**, which is connected to the brake. The inner cylinder has rollers pins associated to springs. In the example, when **A** rotates in the counterclockwise direction, the roller slip into the cylinders and the rotation is not transferred to **B**. Thus, even if the brake is activated, the external cylinder can turn freely. When it rotates in the other direction, the rollers lock with the cylinder and the rotation is transferred to **B**. In this case, the brake can impose a resistive force against the rotation of **A**.

An analysis of the power flow in the device is used to control the actuator. By definition, the interface dissipates energy if power flows from the operator to the interface. This condition can be determined by observing the direction of the desired torque Γ_h^* which is applied in negative feedback to the interface. If the calculated torque by the virtual environment has the same sign of the measured velocity $\dot{\theta}^*$, the device should produce a resistive torque against the torque imposed by the operator: the haptic device dissipates energy and the brake must be

---

[1] WO 1998000649 A1 for the patent details

[2] http://uk.misumi-ec.om/eu/ItemDetail/10302273810.html for the DC motor Maxon RE40 datasheet

[3] http://aviton.spb.ru/files/doc/pdf/maxon/082.pdf for the specifications of the overruling clutch

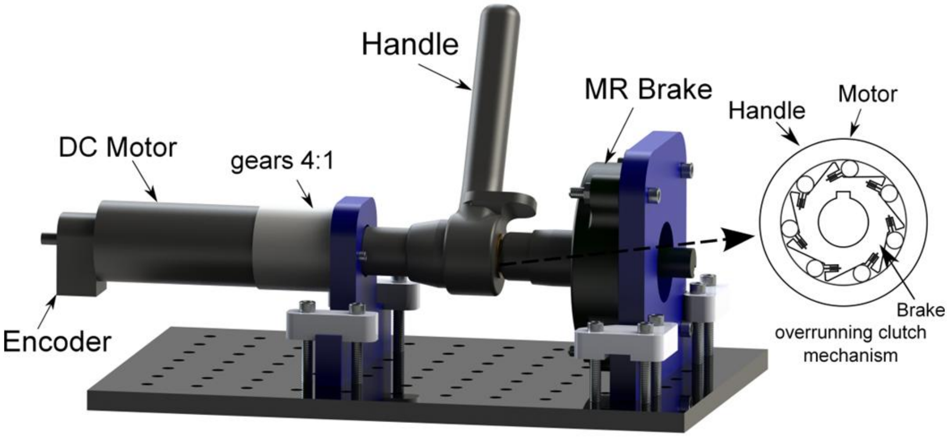

Figure 2.7: Hybrid haptic interface based on an unidirectional MR brake. The end-effector is direct linked to a DC motor and its axis is linked to a magnetorheological brake through an overrunning clutch mechanism. The torque of the brake can henceforth be transferred to the end-effector in only one direction. The position is measured using an incremental encoder.

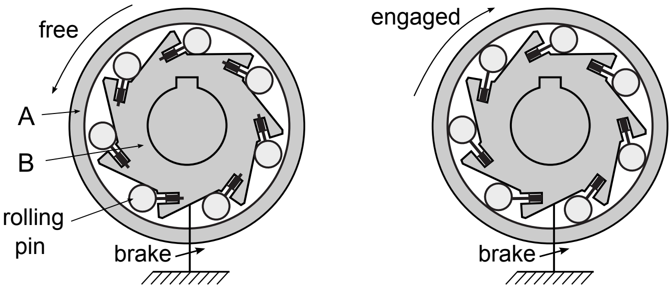

Figure 2.8: Working principle of an overrunning clutch. The mechanism has spring loaded rollers inside a driven cylinder. When the external cylinder **A** rotates in the counterclockwise direction (left figure), the rollers slip inside the cylinder and the rotation of **A** is not transferred to **B**. If **A** rotates in the other direction (right), the rollers lock with the cylinder making it rotate in unison. In the motor/brake system, the brake is linked to **B** and the motor and the handle are mounted on **A**.

activated. However, if the desired torque and the velocity have opposed signs, the haptic device is supposed to restore energy and the motor has to be engaged.

Fig. 2.9 shows the global control scheme. The mechanical device is represented as an inertia J with some viscous friction b. The operator is modelled as an impedance $Z_0(s)$ and his applied torque on the device is denoted Γ_z. Both actuators are controlled in torque by two analog proportional-integral controllers (PI 1 and PI 2) and the overrunning clutch mechanism is represented as a nonlinear unilateral constraint. The global system is controlled by a micro-controller Silabs 8051F120 operating at 99.4MHz. Γ_m and Γ_b are the torques imposed by the brake and motor respectively.

The observed power is given by:

$$P = \Gamma_h^* \dot{\theta}^* \tag{2.2}$$

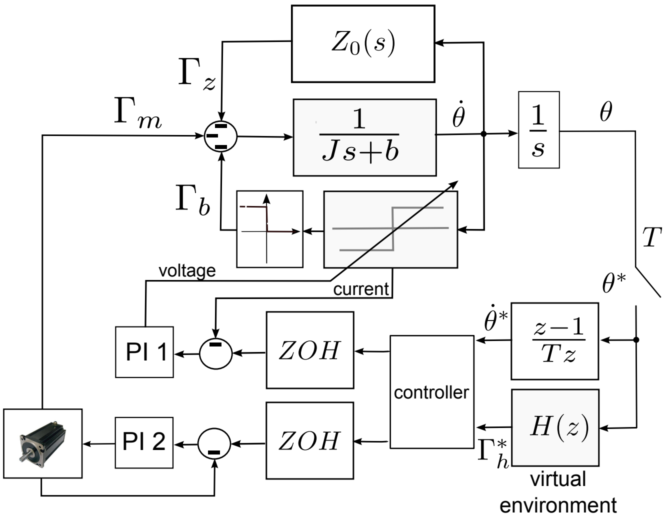

Figure 2.9: Hybrid Actuator control scheme: The position θ is measured. $H(z)$ represents the virtual environment and calculates the desired torque $\Gamma_h^* = H(z)\theta(z)$. The symbols marked with an asterisk are discrete variables. Γ_m, Γ_b and Γ_z are the torque applied by the motor, the brake and the operator $Z_0(s)$ respectively. The system is controlled with a sampling period T and ZOH is the zero order hold operator. Both actuators are controlled by two custom made PI controllers.

Equation 2.3 presents the control law that does not consider the overrunning clutch mechanism.

$$\begin{pmatrix} \Gamma_m \\ \Gamma_b \end{pmatrix} = \begin{cases} ZOH \begin{pmatrix} 0 \\ \Gamma_h^* \end{pmatrix} & P \geqslant 0 \\ ZOH \begin{pmatrix} \Gamma_h^* \\ 0 \end{pmatrix} & P < 0 \end{cases} \tag{2.3}$$

Consider the simulation of a virtual spring using this control method. When the operator compresses the spring, the displacement generates a reference torque in the virtual environment which is opposed to the velocity. Thus, the observed power is negative and the brake is activated to display a torque proportional to the position. To simulate the decompression phase of the spring, the motor is activated when the operator inverses the velocity. However, an indetermination occurs when the velocity is zero. There a two possibilities:

1. The operator has released the handle. Since only the brake is activated, the end-effector stays in the final position although it should turn back. The motor needs to be activated to simulate the spring decompression.
2. There is a force balancing: the torque imposed by the operator and the reaction torque are the same. The brake must not be desactivated.

In order to solve this indetermination, a minimal participation of the motor is necessary. Two main control methods are proposed. The first method minimizes the activation of the

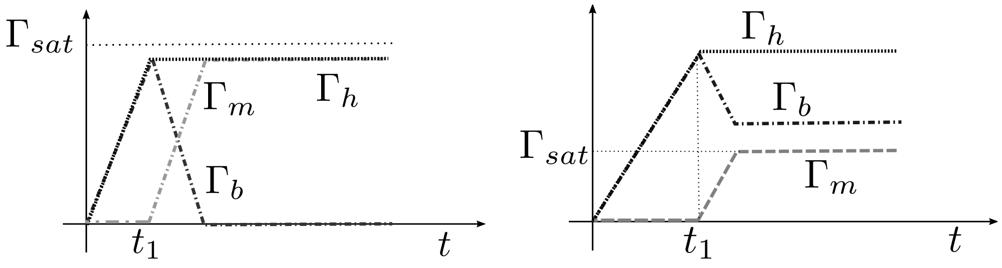

(a) motor not saturated

(b) motor saturated

Figure 2.10: Control method using brake/motor transition: Supposing a passive behavior, at $t = t_1$ the velocity becomes zero. In the first case (a) the desired torque (dotted line) is ensured by the motor (dash-doted line Γ_m), in the second case (b) the motor is saturated and the brake (dashed line Γ_b) is simultaneously engaged.

motor to reduce energy consumption. The motor is used to restore energy with one exception and is activated if velocity becomes zero. In this case the desired torque is simultaneously assumed by the brake and the motor. The motor the can rotate the end-effector if the operator releases the handle. The second method defines a minimum participation of the motor in the applied force and the brake is activated only after this limit being reached. The brake is activated only when this limit is exceeded. This method enables the actuator to display resistive forces in arbitrary directions when this limit is not reached, equivalently to an active device.

The virtual environment has been defined as a simulation of an angular spring ($H(z) = K$, where K is the stiffness of the spring). In both methods, the maximum active torque has been arbitrary fixed at Γ_{sat} =80mNm.

3.1 GRADUAL BRAKE/MOTOR TRANSITION

According to this method, both the brake and motor are activated as long as the velocity is zero. If the desired torque cannot be provided by the motor only, the difference between the desired torque and the maximal torque of the motor is supplied by the brake (in the case of passive behavior). Thanks to the overrunning clutch mechanism, the brake does not block the motor. The handle can turn freely if the user releases it.

The transition brake/motor can generate an error between the desired and provided torque which can induce undesirable vibrations at the handle. Thus, it is necessary to implement a gradual temporal transition controller. As long as $\dot{\theta} = 0$, the brake is gradually turned off, while the active torque is simultaneously and proportionally increased. This transition controller takes the form of a time variant element ζ determined by:

- Whether only the motor is activated: $\zeta = 1$;
- Whether only the brake is activated: $\zeta = 0$;
- During the transition brake/motor: $0 < \zeta < 1$. The ζ variable is increased by ψ at each

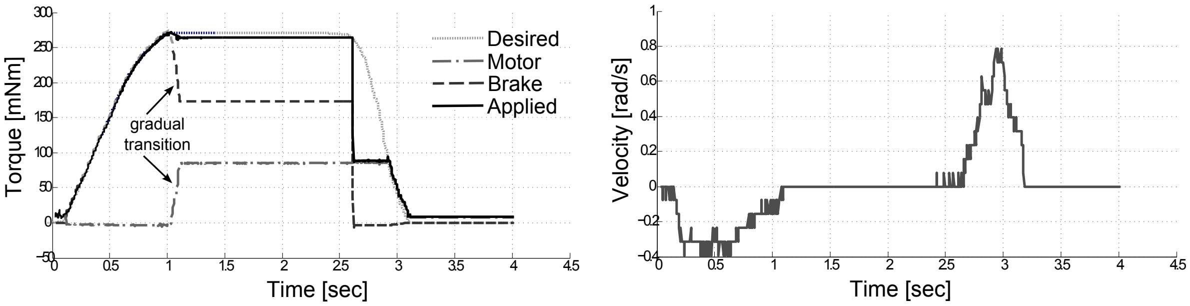

(a) Torques **(b)** Velocity

Figure 2.11: Experimental results using power flow based controller with gradual transition. The operator compresses the spring up to 1.1s and the resistive force proportional to the position is applied by the brake. When the velocity becomes zero, the motor's torque is gradually increased while the braking torque decreases proportionally. When the operator inverses the velocity at 2.4s, the brake is turned off.

period T.

The maximal active torque is $\Gamma_{sat} = i_{max}k_i$, wit i_{max} the maximal admissible current of the motor and k_i its characteristic torque/current constant. Fig. 2.10 shows the theoretical implementation. During the transition, if the reference torque is lower than the maximal torque of the motor ($\Gamma_h^* < \Gamma_{sat}$), the motor's torque gradually increases while the braking tends to zero (Fig. 2.10a). Otherwise, if the motor is saturated, the final torque is the contribution of both the brake and the motor (Fig. 2.10b).

The control law with gradual brake/motor transition controller is given by:

$$\begin{pmatrix} \Gamma_m \\ \Gamma_b \end{pmatrix} = \begin{cases} ZOH\begin{pmatrix} 0 \\ \Gamma_h^* \end{pmatrix} & P > 0 \\ ZOH\begin{pmatrix} \Gamma_h^* \\ 0 \end{pmatrix} & P < 0 \\ ZOH\begin{pmatrix} \zeta\Gamma_h^* \\ \Gamma_h^* - \Gamma_m \end{pmatrix} & P = 0 \end{cases} \tag{2.4}$$

with $-\Gamma_{sat} \leq \Gamma_m \leq \Gamma_{sat}$.

Fig. 2.11 presents the experimental results using the gradual transition. At t =0 the spring is in its initial position. The operator compress the spring inducing a resistive torque in the virtual environement: the power is positive and the compression phase of the spring must be simulated by the brake. The brake follows the desired torque until t =1.1s. At this point, the velocity becomes zero. At this point the motor is activated. Since $\Gamma_h^* > \Gamma_{sat}$ the motor is saturated and the torque difference is provided by the brake making $\Gamma_b = \Gamma_h^* - \Gamma_{sat}$. The transition is managed by the gradual transition controller. Note that in the direction of the compression of the spring, the desired torque is respected. After the gradual transition, if the

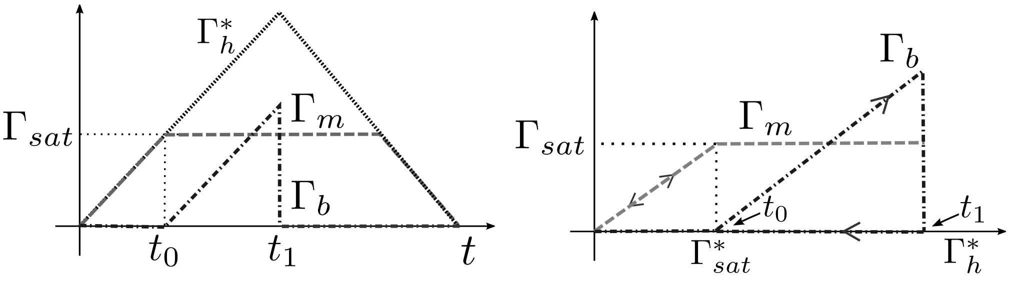

(a) applied torque *vs* time **(b)** applied *vs* desired torque

Figure 2.12: Control method based on the motor: Only the motor is used until its saturation. Supposing a passive behaviour between $0 \leq t \leq t_1$, the desired torque is provided by the motor, at $t = t_0$ the motor is saturated and the brake is simultaneously engaged. At $t = t_1$ the velocity is inverted (power becomes negative), as a consequence the brake is turned off. Γ_{sat} is the maximum torque that can be provided by the motor.

operator releases the handle, or if he imposes an effort inferior to the active torque, the handle can turn back ($\forall t \geq 1.1s$). The velocity remains zero until t =2.4s. At this point the operator turns the handle back and the velocity is inverted;the power becomes negative and the interface is supposed to restore energy. Therefore, the motor simulates the decompression phase of the spring while the brake is off. Durign this phase the torque presented to the operator is limited to Γ_{sat}.

Depending on the interaction velocity the controller may not react fast enough. Thus, the constant ψ can be defined as a non-linear function of the velocity.

3.2 MOTOR SATURATION LIMIT

By contrast to the previous method, this technique allows for the energy dissipation using the motor. To ensure a transparent transition a solution consists in maintaining the motor always activated.

A minimum contribution of the motor in the applied torque is defined. The brake is only activated if the motor reaches its maximal torque caleld Γ_{sat}. If the desired force is inferior to Γ_{sat}, only the motor is activated; if the desired torque is greater than Γ_{sat}, and in the case of passive behaviour ($P > 0$), the brake compensates for the difference between the reference torque and desired torques. In other words, the energy flow controller works only when the motor reaches Γsat. The transition becomes naturally continuous.

The activation of the brake and of the motor is then defined by:

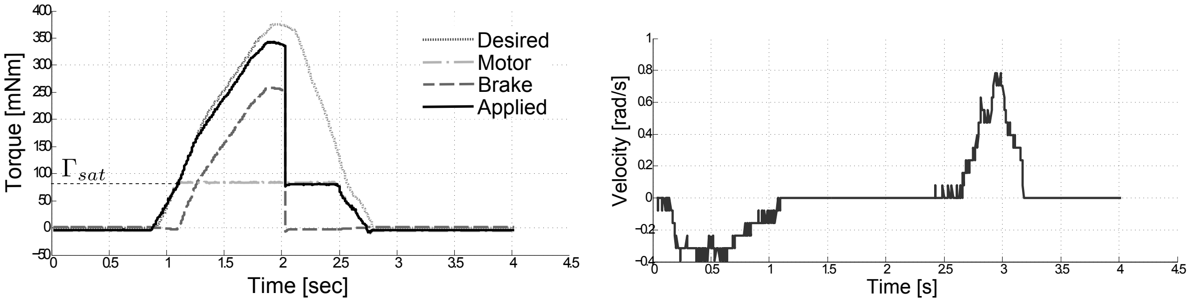

(a) Torques **(b)** Velocity

Figure 2.13: Experimental results exploring the motor up to its saturation. The operator compresses the spring and the interaction torque is assumed by the motor up to its saturation at 1.3s. Beyond this point the brake is activated and compensates for the difference between the reference torque and the saturation torque of the motor Γ_{sat}. When the velocity becomes positive, the brake is tourned off and the motor simulates the decompression phase.

$$\begin{pmatrix} \Gamma_m \\ \Gamma_b \end{pmatrix} = \begin{cases} ZOH \begin{pmatrix} \Gamma_h^* \\ 0 \end{pmatrix} & \begin{cases} \Gamma_h^* < \Gamma_{sat} \text{ or} \\ P < 0 \end{cases} \\ ZOH \begin{pmatrix} \Gamma_{sat} \\ \Gamma_h^* - \Gamma_m \end{pmatrix} & \begin{cases} \Gamma_h^* \geq \Gamma_{sat} \text{ and} \\ P \geq 0 \end{cases} \end{cases} \tag{2.5}$$

Fig. 2.12 shows a working principle of this control method. The brake is activated to display large forces and up to the saturation of the motor, it is maintained off.

The experimental results are presented in Fig. 2.13. At t =0 the spring is in its initial position. The operator moves the handle to compress the spring. It represents a dissipative behaviour. By contrast to the precedent method, the compression phase is simulated by the motor until its saturation at t =1.3s (when $\Gamma_h^* = \Gamma_{sat}$) while the brake remains deactivated. From this point, the difference between the desired torque and the motor's torque is compensated by the brake ($\Gamma_b = \Gamma_h^* - \Gamma_{sat}$). When the velocity is inverted, at t =2.0s, the brake is turned off.

The only difference compared to the gradual transition appears when the interface dissipates energy. In the first method, the interface dissipates energy using only the brake, and in the second case by means of the brake and the motor.

4 CONCLUSION

In this Chapter a new hybrid actuation approach has been introduced and validated with results obtained from a 1-DOF device. This actuation approach is based on a magnetorheological brake combined to a DC motor. Thanks to the overrunning clutch placed between the actuators, the torque of the motor is not influenced by the brake and can be directly transmitted to the operator. Thereby, the actuators can be activated at the same time to exert feedback torques. This enables the system to combine the versatility of electric motor to the stability and high torque capability of brakes.

Experimental results suggest that this configuration can solve the limitation of passive actuators such as stick phenomenon, impossibility to create an active behavior and forces in arbitrary directions. Besides, the actuator design enables the system to combine a powerful brake with a small DC motor. The brake is used to display high torques while the motor exerts a limited active behaviour. Thus, safety concerns can be addressed without damaging the performance of the device.

Two main control strategies have been developed. The first method restricts the motor to impose an active behaviour or to dissipate energy only when the velocity is zero. It is designed to minimize power consumption and can be used in the case of 1-DOF interfaces. In the second method, the motor is always activated to ensure a continuous transition and to assist the device to display forces in arbitrary directions. This method is designed for a multiple DOF haptic interfaces. Furthermore, the motor can dissipate energy and the maximal resistive torque is the sum of the torque of the brake and the motor. Both methods are based only on two basic pieces of information: the measured velocity and the torque calculated by the virtual environment. Thus, the control is independent of the simulation and does not need any measure of interaction torque. As a consequence, the actuator approach and its control methods are adaptable in a large range of force-feedback devices. Using a hybrid system however, the capability of the system to dissipate energy is greater than its capability to restore energy to the human operator.

The control law proposed in this chapter allows for the rendering of the virtual environment impedance using only the motor. Since both actuators can be treated as independent systems thanks to their mechanical linkage, the motor is subjected to the classical stability issues during the simulation of stiff environments.

The following chapter completes the same hybrid approach from a control perspective. A stability criterion is applied to the system and the results enables the development of control laws which bound the stiffness and the energy involving the motor. The brake is used to compensate the difference between the reference torque and the capabilities of the motor.

HYBRID ACTUATOR CONTROL

3

Contents

Partially reprinted, with permission from

©2012 IEEE

Rossa, C.; Lozada, J.; Micaelli, A., "Stable haptic interaction using passive and active actuators,"International Conference on Robotics and Automation (ICRA), 2013, pp.2386,2392, 6-10 May 2013

STABILITY is a key requirement in haptics. This chapter addresses the control of the hybrid system taking into consideration the different stability limits and torque capabilities of the passive and active actuators. The proposed control laws are intended to follow a reference torque while maintaining stability. The stability condition is obtained using two different approaches. The describing function analysis of an active interface controlled in impedance (torque applied in response to a mesured position) demonstrates that there is a maximal control loop gain that leads the system to instability. The same analyis applied to a passive interface highlights that there are no limitation to the control loop gains.

The stability condition of the hybrid interface is subsequently obtained via the passivity condition analysis and highlights that passivity is respected under assumption of a passive virtual environment and if the energy restored by the active actuator is inferior to the energy store in the virtual environement. Two complementary control methods based on the sharing of control loop gains and energy are developed in order to respect these stability criteria. The proposed control laws have been implemented in an 1-DOF device and validated by using the simulation of an active virtual environment and a stiff virtual wall. The experimental results show that the system remains stable even for nonlinear and virtual environments with high control loop gains.

1 MOTIVATION

One of the advantages of using a hybrid actuation approach is the possibility to achieve a wide range of impedance under stability conditions. The displayable impedance depends in particular on the torque capability and on the stability limits of each actuator. The reference torque provided by the virtual environment in response to a measured position or velocity must be provided by the interface using the combination of the passive and active actuators. A virtual environment can however exhibit high levels of impedance and when both actuators are engaged in parallel to display this impedance, it can lead the active actuator to the instability. In a hybrid system, only the impedance displayed by the active actuator must be limited.

As presented in the first chapter, an active device simulating a virtual wall modelled as a spring-damper model with a stiffness K and a damping B needs to respect the following stability criterion [Colgate et Schenkel, 1994]:

$$b > \frac{TK}{2} + B \tag{3.1}$$

Considering only the virtual wall stiffness ($B = 0$), the maximal displayable stiffness by an active interface is $K_{lim} = 2b/T$, where b and T are the viscous friction coefficient and the sampling rate respectivelly. The virtual environment can however suppose higher levels of impedance. Thus, a stiffness bounding algorithm need to implemented in order to limit the stiffness sent to the motor and to compensate for the difference using the brake.

The controller should use only two pieces of information: the reference torque of the virtual environment and the measured position. We propose two control algorithms i.e. energy and stiffness bounding. A passivity condition is obtained for the hybrid system. The first algorithm considers the stability condition via passivity analysis of the coupled system. The controller bounds the interaction energy involving the active actuator and uses the passive one to dissipate energy when the passivity condition is not respected. The second algorithm is based on the stability condition given in 3.1. The controller bounds the stiffness of the active actuator and follow a reference torque using the combination of both actuators.

The control laws are validated using the simulation of an active virtual environment and by the simulation of a stiff virtual wall.

2 PASSIVITY ANALYSIS OF THE COUPLED SYSTEM

This analysis is a heuristic control method used to achieve stability by passivation. It aims to obtain a sufficient criterion for the passivity of the coupled brake/motor system.

Consider a hybrid interface comprising a brake and a motor linked in parallel. The torque calculated by the virtual environment $\Gamma_h(t)$ is applied on the interface by means of the brake, which applies the torque $\Gamma_b(t)$ and by the motor that applies $\Gamma_m(t)$. The operator imposes a torque $\Gamma_z(t)$.

A statement of global passivity of a system is that the maximal extractable energy never be great as the one provided by the operator [Hannaford et Ryu, 2002]. Thus, considering that the virtual environment calculates a torque $\Gamma_h(t)$ is response to a measured velocity $\dot{\theta}(t)$, a sufficient condition for passivity of the virtual environment is:

$$\int_0^t \Gamma_h(t)\dot{\theta}(t)dt \geq 0 \qquad \forall t \geq 0 \tag{3.2}$$

The haptic device is passive if the total energy is never greater than the energy provided by the operator. Considering that the initial energy is zero, this passivity condition is:

$$\frac{1}{2}J\dot{\theta}^2(t) \leq -\int_0^t \Gamma_z(t)\dot{\theta}(t)dtqquad\forall t \geq 0 \tag{3.3}$$

The kinetic energy of the device is the sum of all energies acting on the system, namely the one provided by the motor, brake, operator, and dissipated by linear frictions. The energy balance yields:

$$\frac{1}{2}J\dot{\theta}^2(t) = -\int_0^t \Gamma_z(t)\dot{\theta}(t)dt - \int_0^t \Gamma_m(t)\dot{\theta}(t)dt - \int_0^t \Gamma_b(t)\dot{\theta}(t)dt - \int_0^t b\dot{\theta}^2(t)dt \tag{3.4}$$

Replacing (3.4) in (3.3), the passivity condition is computed as:

$$\int_0^t \Gamma_m(t)\dot{\theta}(t)dt + \int_0^t \Gamma_b(t)\dot{\theta}(t)dt + \int_0^t b\dot{\theta}^2(t)dt \geq 0 \qquad \forall t \geq 0 \tag{3.5}$$

Consider $0 \leq S(t) \leq 1$ a function which determines the sharing of the desired torque between the motor and the brake. If only the motor is activated $S(t) = 1$, whereas if only the brake is enabled $S(t) = 0$. If $0 < S(t) < 1$ the torque calculated by the virtual environment is applied on the interface by the brake and the motor simultaneously. Consider also that the brake is always able to provide the required torque so that $\max(\Gamma_b) \geq \max(\Gamma_h)$. Finally, we denote $0 < \beta(\Gamma_h) \leq 1$ the unsaturation ratio of the motor with respect to the reference torque, which could be physical or implemented in the virtual environment. $\beta(\Gamma_h) = 1$ indicates that the motor can display the reference torque of the virtual environmental, and $\beta(\Gamma_h) = 0.5$ for example, informs that the motor can display only 50% of Γ_h.

The effective torque provided by the motor is:

$$\Gamma_m = \Gamma_h S(t)\beta(\Gamma_h) \tag{3.6}$$

And the torque provided by the brake is:

$$\Gamma_b = \Gamma_h[1 - S(t)] \tag{3.7}$$

The observed power delivered by the device is $P(t) = \dot{\theta}(t)\,[\Gamma_m(t) + \Gamma_b(t)]$. If we consider that $\Gamma_h(t) = \Gamma_m(t) + \Gamma_b(t)$, the power can be defined as the product of the reference torque and the measured velocity $\dot{\theta}(t)$, so that $P(t) = \Gamma_h(t)\dot{\theta}(t)$.

Replacing the brake and the motor's torque as a function of $S(t)$ in (3.5), the passivity condition becomes:

$$\int_0^t S(t)\beta(\Gamma_h)\Gamma_h\dot{\theta}dt + \int_0^t (1 - S(t))\Gamma_h\dot{\theta}dt + \int_0^t b\dot{\theta}^2 dt \geq 0 \quad \forall t \geq 0 \tag{3.8}$$

Since $P(t) = \Gamma_h\dot{\theta}$, the expression yields:

$$\int_0^t S(t)\beta(\Gamma_h)P(t)dt + \int_0^t (1 - S(t))P(t)dt + \int_0^t b\dot{\theta}^2 dt \geq 0 \qquad \forall t \geq 0 \tag{3.9}$$

Regrouping the term $S(t)$ gives the relation:

$$\int_0^t S(t)\beta(\Gamma_h)P(t)dt - \int_0^t S(t)P(t)dt + \int_0^t P(t)dt + \int_0^t b\dot{\theta}^2 dt \geq 0 \qquad \forall t \geq 0 \tag{3.10}$$

This expression, after some mathematical manipulation, can be reformulated as:

$$\int_0^t S(t)\left[\beta(\Gamma_h) - 1\right]P(t)dt + \int_0^t P(t)dt + \int_0^t b\dot{\theta}^2 dt \geq 0 \qquad \forall t \geq 0 \tag{3.11}$$

The term $\int_0^t b\dot{\theta}^2 dt$ represents the energy dissipation due to viscous friction, and is a power-independent variable guaranteed to be always positive. The second term $\int_0^t P(t)dt$ is the energy of the virtual environment defined by (3.2). As we assumed that the virtual environment is passive, this sum is guaranteed to be positive or zero. Finally, a sufficient condition for the passivity of the system is that the first sum is positive or zero $\forall t$.

Let's make the assumption that the sign of the power is constant in the interval $]t_k, t_{k+1}]$ and that the passivity condition is respected in the interval $[0, t_k]$ so that:

$$\int_0^{t_k} S(t)\left[\beta(\Gamma_h) - 1\right]P(t)dt \geq 0 \tag{3.12}$$

To analyse the interaction's passivity, we look for a condition that respects this criterion in the interval $]t_k, t_{k+1}]$ in order to obtain a condition for the whole interval $[0, t_{k+1}]$. Consider the first sum of (3.11) defined between $]t_k, t_{k+1}]$. Two cases must be analysed:

- $P(t) \geq 0 \; \forall \; t_k < t \leq t_{k+1}$. As we assumed, the bake is always able to provide the required torque. Making $S(t) = 0$ the sum is zero for a positive power. The passivity condition is respected.
- $P(t) < 0 \; \forall \; t_k < t \leq t_{k+1}$. If the interface restores energy $S(t) = 1$. Since $\beta(\Gamma_h) < 0$, the sum is positive and the passivity condition is ensured.

Finally, combining this statment with (3.12), we can writte:

$$\int_0^{t_{k+1}} S(t)\left[\beta(\Gamma_h) - 1\right]P(t)dt \; \geq 0 \; \forall \; 0 < t \leq t_{k+1} \tag{3.13}$$

Therefore the interface is guaranteed to be passive under two assumptions:

1. The virtual environment is passive: $\int_0^t P(t)dt \geq 0 \; \forall t \geq 0$.
2. The actuators do not restore all the energy stored in the virtual environment which needs $\beta(\Gamma_h) < 1$.

These results reach the consensus that to achieve stability, some energy dissipation involving the motor is necessary. However, the passivity analysis does not take into consideration the injected energy into the system by the sampling period. Furthemore, we choose to activated the brake only when the motor reaches its maxiamal torque. Although this method enhances the reactivity of the system, the passivity condition may not be ensured since for a positive power we have $S(t) < 0$.

In order to respect the passivity criterion, we propose a controller that monitors the first sum of (3.12). If the energy involving the motor become negative, the motor is turned off and the controller activate the brake to dissipate the created energy. The controller sets $S(t) = 0$ as long as the observed energy is negative. A second algorithm that limits the control loop gains using the motor is combined to this controller.

3 STABLE CONTROL

In this section, two algorithms are proposed to ensure the stability of the coupled system even for nonlinear and virtual environments with high control loop gains. An energy-bounding based control method is implemented to guarantee the passivity of the system and a stiffness-bounding based control able to limit the stiffness sent to the motor is combined to the this method.

The control laws are based on the following premises:

1. Since the hybrid actuator combines a brake with higher torque capability than the motor, the participation of the motor is maximized;
2. The stiffness simulated by the motor is bounded to avoid instability. The reference torque of the virtual environment is respected using the combination of the brake and motor;
3. The interaction energy with the motor is bounded to respect passivity (the interface does not create energy).

3.1 ENERGY-BOUNDING ALGORITHM DEFINITION

In order to determine the sharing of efforts between the brake and the motor, the observation of the power is used to determine whether the interface is expected to dissipate or restore energy.

By definition, the interface dissipates energy if the torque applied by the interface on the operator is opposed to the velocity. The observed power is then positive. In other words, the power flows from the operator to the interface. Thus, if $P < 0$, the controller sets $S(t) = 1$ and $P \geq 0 \therefore 0 \leq S(t) \leq 1$.

In order to obtain a transparent transition between the brake and the motor, and to maximize the reactivity of the system, the actuation approach works as follows. The motor is activated up to its saturation $\forall t$. Beyond this point, and in the case of a dissipative behaviour, the torque is compensated by the brake so that $\Gamma_b = \Gamma_h - \Gamma_{sat}$ if $|\Gamma_h| > |\Gamma_{sat}|$, where Γ_{sat} is the maximal torque of the motor.

The physical unsaturation ratio of the motor $\beta(\Gamma_h)$ as a function of the desired torque can be computed as follows:

$$\beta(\Gamma_h) = \frac{\min(|\Gamma_h|, |\Gamma_{sat}|)}{|\Gamma_h|} \tag{3.14}$$

As a result the variable $S(t)$ should be set to $\beta(\Gamma_h)$ for a dissipative behaviour and to 1 when the interface restores energy. In order to implement this control method, a power-sign dependent variable $\sigma(P) = 0$ if $P(t) \geq 0$ and $\sigma(P) = 1$ if $P(t) < 0$, is defined as:

$$\sigma(P) = \frac{1}{2}[\mathrm{sgn}(P) - 1]\,\mathrm{sgn}(P) \tag{3.15}$$

Thus, the variable $S(t)$ can be computed as follows:

$$S(t) = \beta(\Gamma_h)(1 - \sigma(P)) + \sigma(P) \tag{3.16}$$

The torque provided by the motor can then be redefined as $\Gamma_{mh} = ZOH[S(t)\Gamma_h^*]$ while the brake's torque remains $\Gamma_b = ZOH[(1 - S(t))\Gamma_h^*]$.

The passivity condition is not respected if the virtual environment is not passive. Furthermore, the ZOH function injects energy into the system in an amount proportional to the displayable stiffness. It may cause the violation of the stability criterion. However, the passivity of the system can be assured by the controller if a limitation of the active torque is implemented.

Since the brake cannot inject energy into the system, the energy-bounding algorithm is defined only as a function of the energy provided by the motor. Its energy is defined as $E(n) = T\sum_{k=1}^{n}\Gamma_{mh}(k)\dot{\theta}(k)$, where T is the sampling delay. Another possibility may consist in considering the energy of the coupled system $E_c(n) = T\sum_{k=1}^{n}[\Gamma_{mh}(k) + \Gamma_b(k)]\dot{\theta}(k)$ as the passivity observer. However, if the brake has a greater torque capability than the motor, the energy observer stores a high value of energy and the motor will not be constrained to display a passive behaviour up to the restitution of the total stored energy.

If the observed energy becomes negative, it means that the interface is not passive. The reference torque Γ_h is then transferred to the brake instead of the motor and the created energy is dissipated. As long as the energy is negative, the brake is activated if the observed power is negative by setting $S(t) = 0$. If the observed power is positive, the motor also be activated making $S(t) = \beta(\Gamma_h)$.

The energy observer is defined as a function of the energy involving the motor, and the dissipated energy using the brake if the observed power is negative. The energy observer is:

$$E(n) = T\sum_{k=1}^{n}[\Gamma_{mh}(k) + \Gamma_b(k)\sigma(P)]\dot{\theta}(k) \tag{3.17}$$

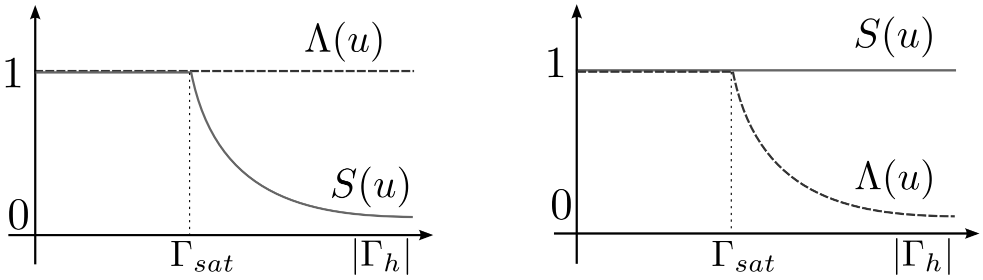

(a) Energy dissipation **(b)** Energy restitution

Figure 3.1: Time-variant control variable $S(t)$ and the unsaturation ratio of the system $\Lambda(t)$. For a dissipative behavior both actuators are engaged and the system can display the requiered torque ($\Lambda(t) = 1$). For an active behavior the motor is only enabled if $E \geq 0$, the saturation of the system depends on the torque capacity of the motor.

The energy-bounding based control takes the following formulation:

$$S(t) = \begin{cases} \beta(\Gamma_h)(1-\sigma(P)) + \sigma(P) & if \quad E \geq 0 \\ \beta(\Gamma_h)(1-\sigma(P)) & otherwise \end{cases} \tag{3.18}$$

The capability of the system to respect the reference torque, supposing that the braking torque is not limited, can be expressed by $\Lambda(t)$, which represents the unsaturation ratio of the device computed as follows:

$$\Lambda(t) = \sigma(P)(\beta(\Gamma_h) - 1) + 1 \tag{3.19}$$

The variable $\Lambda(t)$ indicates the capacity of the system to respect the reference torque. The evolution of the variables $S(t)$ and $\Lambda(t)$ are presented in Fig. 3.1. The interface dissipates energy when $P(t) \geq 0$. Only the motor is activated up to its saturation by setting $S(t) = 1$. Beyond this point, the brake compensates for the difference between the reference torque and the saturation of the motor. Thus, both actuators are engaged at the same time and the braking the torque increases as $S(t)$ decreases. The system is able to dissipate all the energy of the virtual environment and $\Lambda(t) = 1$. When $P(t) < 0$ the interface restores energy to the operator. In this case only the motor can be engaged and $S(t)$ is set to 1. The system displays the reference torque only up to the saturation of the motor ($\Lambda(t) = 1$ if $\Gamma_h < \Gamma_{sat}$). Beyond this point the system becomes saturated and $\Lambda(t)$ decreases as a function of the reference torque.

Using this control method, the brake and the motor can be treated as two independent actuators. The total stiffness of the system is the contribution both of the stiffness of the motor and the brake. The only constraint is that if the energy of the motor is negative, the brake is enabled instead of the motor.

3.2 STIFFNESS-BOUNDING ALGORITHM DEFINITION

According to the proposed control method, only the motor is engaged until its saturation. During this phase, the maximal stiffness K_{lim} under stability condition is $K_{lim} = 2b/T$. The controller then compares the variation of the torque calculated by the virtual environment with the variation of the measured position called $\delta\theta^* = \theta^*_{(k)} - \theta^*_{(k-1)}$ observed between two samples. The index (k) represents the current value of the variable and $(k-1)$ is the value at the previous sampling time. By these means the controller deduces the instantaneous stiffness of the virtual environment. If the stiffness violates the stability criterion, the effective torque sent to the motor $\Gamma_{sb(k)}$ should be recalculated and the difference sent to the brake. A schematic of the stiffness bounding algorithm is shown in Fig. 3.2.

The stiffness of the virtual environment K_h at the sampling k can be calculated as:

$$K_{h(k)} = \frac{\Gamma_{h(k)} - \Gamma_{sb(k-1)}}{\delta\theta^*} \tag{3.20}$$

with $K_{h(k)} = K_{h(k-1)}$ if $\delta\theta^* = 0$. The stiffness bounding algorithm then takes the following formulation:

$$\Gamma_{sb(k)} = \begin{cases} \Gamma_{h(k)} & if \quad K_{h(k)} \leq K_{lim} \\ K_{lim}\delta\theta^* + \Gamma_{sb(k-1)} & otherwise \end{cases} \tag{3.21}$$

After recalculation, the torque Γ_{sb} sent to the motor ensures that the stability criterion is respected. For a dissipative behaviour, the brake can be used to compensate for the difference between the motor's torque and the reference torque so that $\Gamma_{b(k)} = \Gamma_{h(k)} - \Gamma_{sb(k)}$. Stating that $\Gamma_b = (1 - S(t))\Gamma_h$, it gives the relation $\Gamma_h - \Gamma_{sb} = (1 - S(t))\Gamma_h$. Therefore, making $S(t) = \Gamma_{sb}/\Gamma_h$ is a sufficient condition for respecting the reference torque using the brake. Taking into consideration the bounded torque of the motor Γ_{sb}, $S(t)$ respects this conditions by redefining $\beta(\Gamma_h)$ as:

$$\beta(\Gamma_h) = \frac{\min(|\Gamma_{sb}|, |\Gamma_{sat}|)}{|\Gamma_h|} \tag{3.22}$$

The unsaturation ratio of the motor then depends both on its hardware and software limitations. Note that the algorithm is implemented in the controller and thereby the virtual environment is not altered.

4 EXPERIMENTAL RESULTS

A test bench composed of a geared Maxon motor RE40 with a maximal torque limited to 0.302Nm, linked in parallel to a Lord Corporation magnetorheological brake RD2078, maximal torque 2Nm, was used to validate the developed algorithms (Fig. 3.3a). There is no overruning clutch in this experiment. The system is controlled by a microcontroller (Silicon

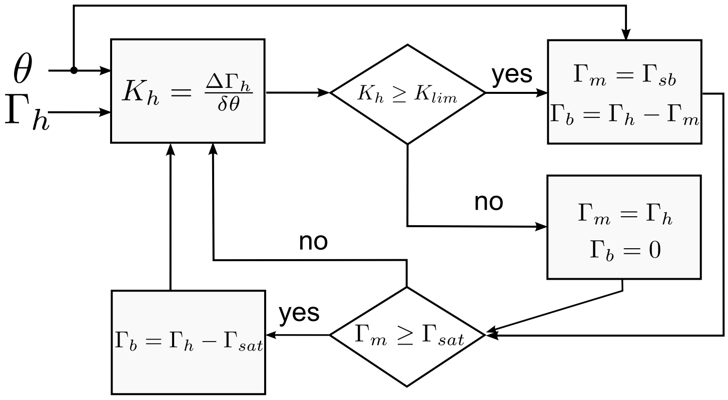

Figure 3.2: Schematic representation of the stiffness bounding algorithm. Where Γ_h, Γ_b and Γ_m are the reference torque, and the torque of the brake and motor respectively. The maximal torque and stiffness delivered by the motor are Γ_{sat} and K_{lim}. The virtual environment stiffness K_h is obtained as the ratio of reference torque variation $\delta\Gamma_h$ to measured position variation $\delta\theta$. The bounded active torque to limit the stiffness is $\Gamma_{sb(k)} = \delta\theta K_{lim} + \Gamma_{sb(k-1)}$.

Lab. C8051F120) operating at 99.4MHz with a sampling rate of $T = 200\mu$s. The angular position is measured using an incremental encoder with 500 pulses per revolution. Fig. 3.3b shows the control loop. The control laws are implemented in the controller and are independent of the virtual environment.

Two tests were conducted. In the first case the passivity condition is obtained using the energy-bounding algorithm and in the second experiment the passivity condition is respected using the stiffness-bounding algorithm. To validate the control laws, the virtual environment has been defined as an active simulation and a virtual obstacle with high stiffness for each test respectively, as shown in (Fig. 3.4).

4.1 ENERGY-BOUNDING ALGORITHM RESULTS

The first virtual environment designed to validate the control laws simulates a variable-stiffness angular spring (Fig. 3.4a). The stiffness K_2 during the decompression phase ($P < 0$) is higher than the stiffness K_1 during the compression phase ($P > 0$). Considering that the spring moves forward from the initial position θ_0 to a position θ_1 and then returns to the initial position, the mechanical energy is:

$$E_{ve} = \int_{\theta_0}^{\theta_1} K_1 \theta d\theta + \int_{\theta_1}^{\theta_0} K_2 \theta d\theta \qquad (3.23)$$

As $K_2 > K_1$ thus $E_{ve} < 0$ and the passivity condition is not be respected: the virtual environment creates energy and the amount of created energy is $-E_{ve}$. It enables the simulation for observing the impact of an active virtual environment on the interaction's stability. Consider

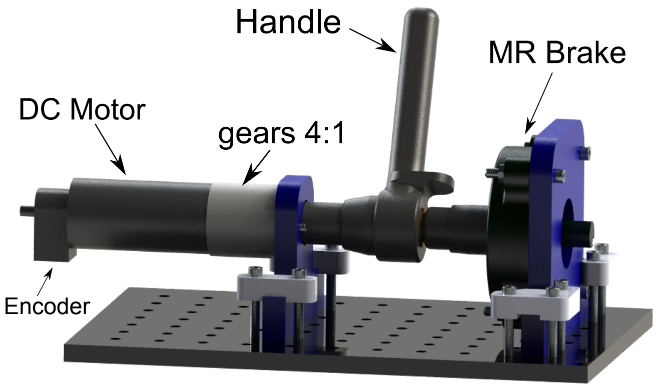

(a) Haptic device

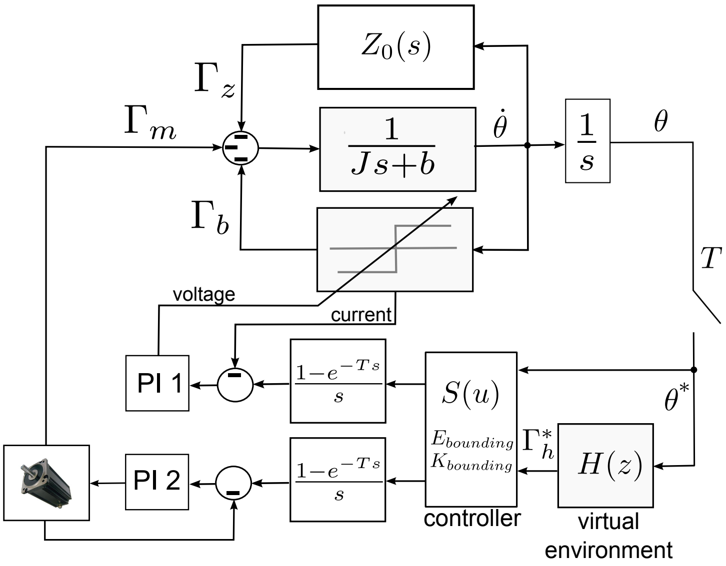

(b) Hybrid interface control-loop

Figure 3.3: 1-DOF test bench used to validate the control laws (3.3a) comprising an MR brake and a motor and its control scheme (3.3b). Both the brake, the motor and the handle are rigid coupled. There is no overrunning clutch in this experiment. The current of both actuators are regulated by two analog proportional-integral controllers (PI 1 and PI 2). The device has an inertia J and a damping b, the operator $Z_0(s)$ applies a torque Γ_z. The motor and brake's torque are Γ_m and Γ_b. The sampling rate is T. The virtual environment $H(z)$ calculates the reference torque as a function of the position θ^*. The velocity is called $\dot{\theta}$.

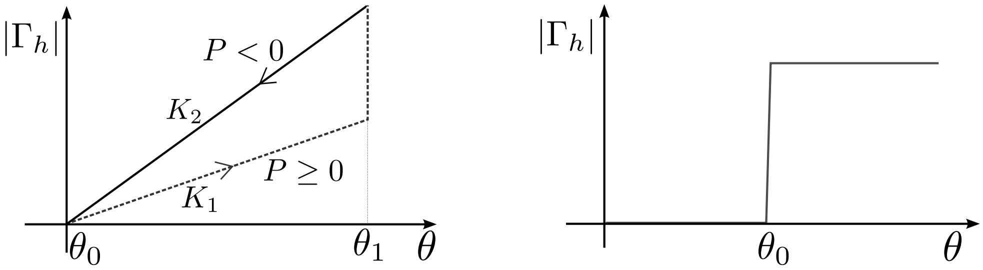

(a) Active environment **(b)** Virtual obstacle

Figure 3.4: Virtual environments designed to validate the control algorithms: In 3.4a an active virtual spring used to validate the energy bounding algorithm. The stiffness K_1 during the compression phase is inferior to the stiffness K_2 during the decompression phase. In 3.4b the high stiffness virtual wall model used to validate the stiffness-bounding algorithm.

$K_2 = 10K_1$.

The experimental result is shown in Fig. 3.5. The end-effector reaches θ_0 at $t = 0.38$s (A). The virtual environment calculates a torque resulting in a dissipative behaviour ($P > 0$). The motor follows the reference torque until its saturation (from (A) to (B) as shown in 3.5b). When the motor reaches its maximal torque Γ_{sat}, the brake compensates for the difference between the reference torque and the saturation of the motor (B). At $t = 1.41$s the velocity is inverted and the power becomes negative (3.5d). The brake is turned off (C) and the motor simulates the decompression phase according to the second stiffness (from C to D). At $t = 2.12$s, the observed energy becomes negative (D in Fig. 3.5e). The motor is turned off and the torque is transferred to the brake until the total dissipation of the created energy (E). A zoomed view of the torque in this region is shown in Fig. 3.5c. Note that if the operator tries to compress the spring again, the motor is activated since it represents a dissipative behaviour. As a result, the observed energy is maintained positive or zero and the interface is guaranteed passive despite the active virtual environment.

The considered simulation is a critical case in which the virtual environment is highly active. The use of the brake instead of the motor can destruct the perception of the virtual environment. However, in the case of a passive model, the use of the brake can effectively eliminate oscillations due to the instability.

4.2 STIFFNESS-BOUNDING ALGORITHM RESULTS

In the second experiment the virtual environment is assigned as a high-stiffness angular spring (K_h=85Nm/rad) (Fig. 3.4b). This stiffness overtakes the maximal stiffness displayed by the motor fixed at K_{lim}=25Nm/rad. Thus, the algorithm limits the motor's stiffness and the brake compensates for the difference.

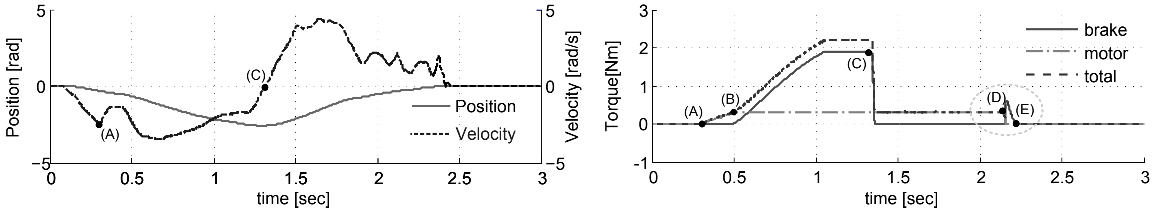

(a) Position and velocity

(b) Applied torque

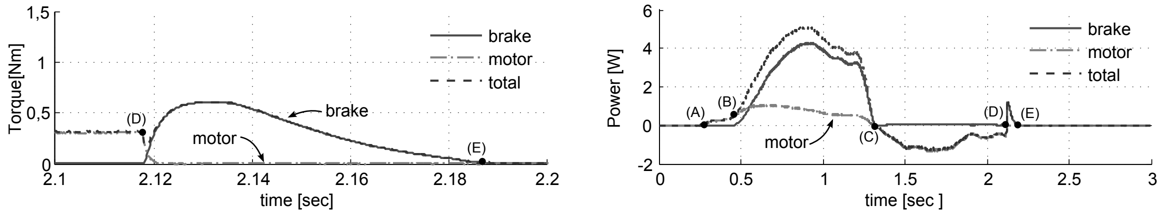

(c) Applied torques with negative energy

(d) Power flow

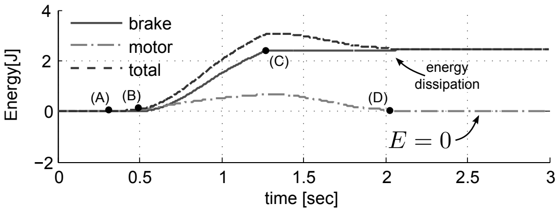

(e) Energy flow

Figure 3.5: Experimental results using the energy-bounding algorithm. The virtual spring is simulated by the motor (3.5b) from (A) to (B) followed by the brake after (B). The velocity is inverted at (C) and the stiffness of the spring increases. The brake is turned off and reactivated when the energy becomes negative (3.5c) to dissipated the created energy. Thus, the interaction is maintained passive (3.5e).

Fig. 3.6 shows the experimental result. The end-effector attains the wall at 0.26rad (A). The algorithm calculates the virtual stiffness and bounds the stiffness sent to the motor to 25Nm/rad (from (A) to (B) in Fig. 3.6b). The difference between the motor's torque and the desired torque is sent to the brake which then displays a stiffness of 60Nm/rad until the saturation of the motor (B). Beyond this point the total stiffness (85Nm/rad) is transferred to the brake. The reference torque is respected using the contribution of the brake and of the motor.

5 USER EVALUATION

The objective of the experiment is to evaluate the performance of the device as experienced by users and to demonstrate the feasibility of this actuation approach using the asymmetric system. For this purpose, a virtual environment has been defined as passive and nonlinear, which is usually the case for haptic interaction.

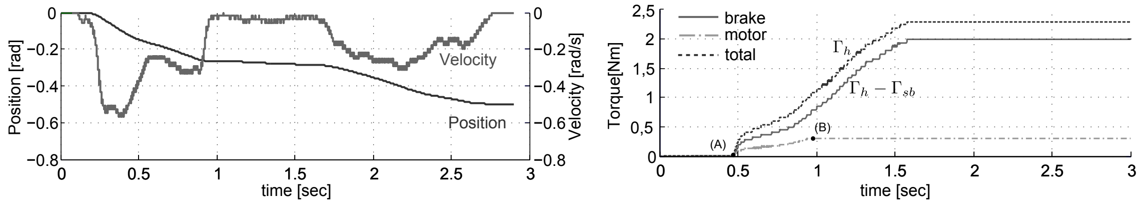

(a) Position and velocity

(b) Applied torque *versus* time

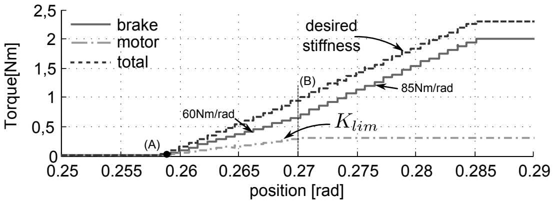

(c) Applied torque *versus* position

Figure 3.6: Simulation of a 85Nm/rad stiff virtual wall. Experimental results using the stiffness-bounding algorithm. The end-effector attains the wall at 0.5s. Before the saturation of the motor, it displays 25Nm/rad. The actuators are engaged with different stiffness values. The maximal stiffness of the motor is bounded to 25Nm/rad. The segmentation is due to the resolution of the controller to calculate $\beta(\Gamma_h)$. Γ_h, Γ_{sb} are the reference torque and the torque sent to the motor.

The virtual environment is composed of a mass-spring system as shown in Fig. 3.7. The user controls the vertical position of the end-effector y using the haptic device (represented by a rectangle **A**). When the end-effector touches the mass m, the user is able to push it up. A reaction torque $\Gamma_h^* = mg/r + K_h\theta^*$, proportional to the mass displacement $y = \theta^* r$ is applied to the handle. θ^*, r, K_h and g are the position of the end-effector, the radius of the handle, the stiffness of the spring and the gravity respectively. When the mass reaches the virtual wall, the system simulates an obstacle by setting $K_h \to \infty$.

The measured reaction torque, determined using the reference current sent of each actuator independently, is presented in Fig. 3.8. At the initial contact with the mass the reference torque is $\Gamma_h^* = mg/r$. Without the stiffness bounding algorithm the motor's torque should sudden vary form zero to mg/r and this torque variation violates the maximal stiffness of the motor leading the interface to oscillation cycles. The torque at the initial contact is then assumed by the brake giving to the operator the illusion of unilateral contact. From this point the controller detects that the reference stiffness can be displayed by the motor and the reference torque is assumed by the contribution of the brake and of the motor following the stiffness K_h. The active torque remains constant when the motor reaches the saturation. This amount of torque gives to the user the sensation of elasticity. When the end-effector touches the virtual wall, the brake is activated up to its maximal torque. The rest position of the mass is at 20° and the virtual wall is placed at 100°.

The experiment consisting in detecting the rest position of the mass and the position of the

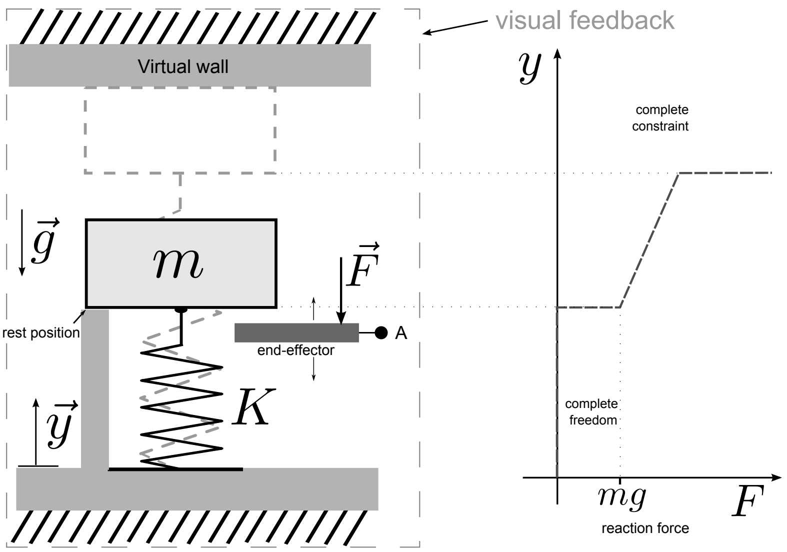

Figure 3.7: Schematic view of the virtual environment: The model simulates a mass-spring system of a mass m and stiffness K. The operator moves the mass using the end-effector. A torque $\Gamma_h^* = mg/r + k\theta^*$ is applied on the handle where g is the constant of gravity and r is the radius of the handle. The user can control the point A using the end-effector. The visual feedback given to users is represented by the dashed rectangle.

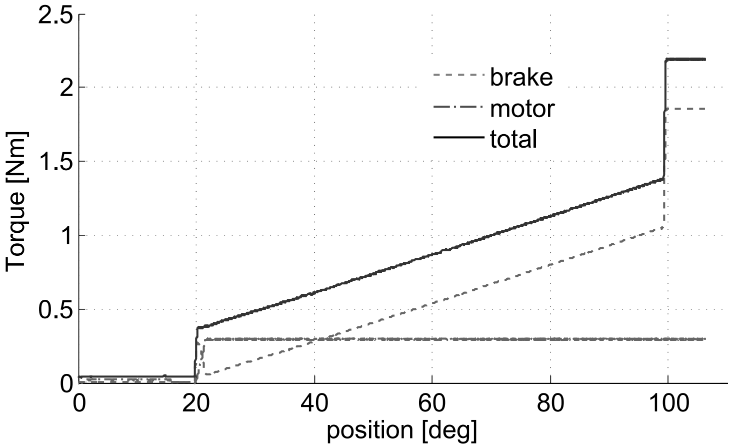

Figure 3.8: Reaction torque of the simulation. The variation of the torque is non-linear and at the contact with the mass and the wall, the stiffness violate the stability criteria of the motor. The initial contact is ensured by the brake, thanks to the stiffness bounding algorithm, and the reference torque is followed by the combination of the brake and of the motor. The contact with the wall is simulated by the brake. The torque provided by the motor gives to the user the sensation of stiffness and gravity.

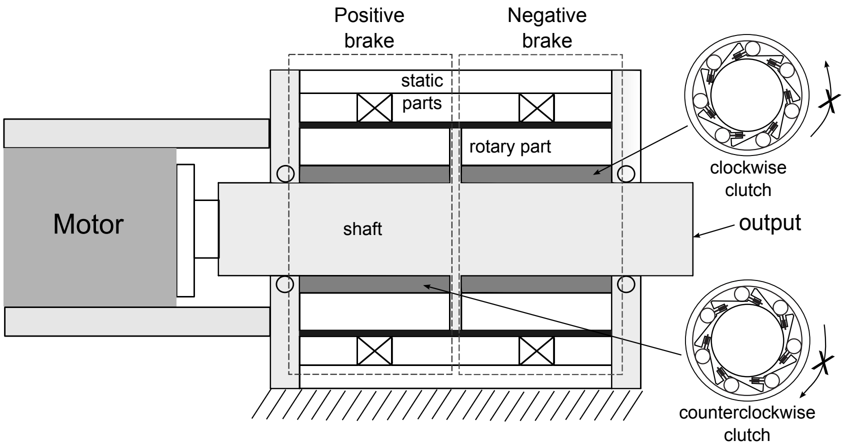

Figure 3.9: Working principle of the unidirectional brake based actuator. Two identical brakes are mounted on the same shaft using an overrunning clutch. By this means a brake can impose a force only in one defined direction. A motor is connected to the same shaft and can apply a torque in both directions.

virtual wall without visual feedback has been performed.

Participants: Twenty users (4F, 16M) aged 22 to 56 volunteered to participate in the experiment. All but one were right-handed. None of them had prior knowledge about the device used in the experiment. The device was hidden and participants only had access to the handle.

Procedure: Participants did not know the nature of the simulation and they were asked to interact with the end-effector without visual feedback of the simulation and try to describe the virtual environment. Subsequently, the simulation model was explained to the participants. They were requested to find the position of the mass and of the virtual wall using both devices and keep the end-effector in the respective positions. The final position and the time to complete the task were recorded and the errors between the real and the estimated position of the mass and of the wall are then calculated.

The relative error in the estimation of the rest position of the mass is 0.28° ±0.14°. Users spend on average 1.02s ± 0.13s to realize the task. The position of the wall is estimated with an error of 0.33° ± 0.22°. These results suggests that the rendering given to the operator by means of the stiffness bounding algorithm (initial contact with the mass) or by the brake only (contact with the wall), are equivalent from a perception perspective. Furthermore, the torque provided by the motor combined to the passive torque gives to the operator the illusion of gravity and stiffness though most of the time the simulated stiffness is presented by the brake.

6 CONCLUSION

In view of ensuring the interaction's stability, this chapter introduced a control method for a system comprising a passive and an active actuator. The sharing of efforts is obtained as a function of the power flow. If the interface dissipates energy, the motor is engaged until its saturation and the brake compensates for the error between the virtual torque and the motor's torque. When the interface restores energy to the operator, the brake is turned off. Each actuator behaves as an independent system.

A sufficient condition for the hybrid system's stability is that the virtual environment is passive, and that the active actuator does not restore all the energy store in the virtual environment. From these results, an energy-bounding based control was implemented to ensure the passivity of the system even for highly stiff and nonlinear virtual environments. A second stability analysis, via describing function, shows that the stiffness sent to the motor should be limited in order to ensure the stability of the system. Therefore, a stiffness-bounding algorithm was implemented, which adjusts the simulated stiffness by each actuator in real time following the reference torque.

These algorithms work simultaneously. The first one was validated using an active virtual environment. The experimental results demonstrate that the system remains passive. The second one was tested using the simulation of a virtual obstacle. The experimental results demonstrate that the stiffness of the coupled system can be improved under stability constraints. This control method enables for the simulation of nonlinear and highly stiff virtual environments and remains independent of the virtual environment model.

In this experiment the brake and the motor are rigidly coupled. There is no overrunning clutch in order to allow for the energy dissipation using the brake in both directions. A complete system based on the unidirectional brakes approach requires two brakes and a motor as illustrated in Fig. 3.9. In this integrated configuration, identical brakes are mounted in opposition on the shaft by means of overrunning clutches. The direction of the braking torque is then determined by the choice of the brake.

Design considerations for the development of the passive actuator in view of forming the hybrid actuator are presented in **Chapter** 4. The fabrication, characterisation and implementation of the control laws to the complete system are presented in Chapter 5.

DESIGN CONSIDERATIONS FOR MAGNETORHEOLOGICAL BRAKES

4

Contents

At the time of the writing, this chapter was accepted for publicaiton on IEEE/ASME Transactions on Mechatronics under the title: C. Rossa, A. Jaegy, J. Lozada, and A. Micaelli "Design Considerations for Magnetorheological Brakes" doi: 10.1109/TMECH.2013.2291966

Designing a passive actuator for human-friendly robotics application is a nontrivial task. A versatile device should possess high torque capability and high torque per volume ratio, high displayable impedance range, high bandwidth and low power requirements. In the case of magnetorheological based actuators, all these measures of performance are interconnected and some tradeoffs need to be established. Furthermore, designing an MR actuator implies dealing with inherent non-linearities introduced by the fluid behaviour and the magnetic saturation of the magnetic circuit. This chapter presents a comprehensive analysis of the interdependence of the measures of performance characterising an actuator suitable for high transparency force feedback devices.

An extensive magnetostatic model of different brake geometries is proposed. The model highlights the existent design tradeoffs and enables for a comparison of different brake configurations. In order to avoid the magnetic saturation of the fluid, the model specifies a maximal admissible induction in the fluid gap. Knowing the fluid surface and the maximal induction, the maximal magnetic flux can be calculated. Then, the power supply is determined and the coil dimensions can be deducted. In the same way, if we attribute a maximal induction in the ferromagnetic path, its cross section can be calculated. The analytical models are validated using finite element analysis and will constitute the basis for the optimization of a hybrid actuator.

1 INTRODUCTION

Magnetorheological (MR) fluids have been successfully employed in a wide range of high fidelity actuators within the context of human-machine interfaces during the past two decades. Such devices provide fast response time, high force per volume ratio with low power requirements, making them particularly suitable for the design of compact systems.

An MR fluid is an active material composed of a suspension of soft ferromagnetic micron-sized particles (typically 1 to 10 microns) dispersed in a carrying liquid (mineral oils, synthetic oils or water) [Gedik *et al.*, 2012][Melle et Martin, 2003]. Their volume concentration in the fluid may range typically between 20% and 40% [Fang *et al.*, 2005]. The rheological properties of these materials can be strongly and reversibly modified by the action of an external magnetic field. Generally speaking, the apparent viscosity of the fluid can be controlled by adjusting the intensity of the applied magnetic field.

Fig. 4.1 shows a schematic view of the evolution of an MR fluid suspension placed between two ferromagnetic plates. The ferromagnetic particles are initially homogeneously placed in a carrier liquid (Fig. 4.1a). When a magnetic field $\vec{H}$ is applied across the plates, the particles are magnetized and possess henceforth a magnetic moment aligned in the direction of the magnetic field (Fig. 4.1b) [Jolly *et al.*, 1998] [Li *et al.*, 2002] [Bossis *et al.*, 2002]. The magnetization of each particle depends on the applied field and on the disturbance fields emanating from the neighbouring magnetized particles [Kittipoomwong *et al.*, 2005]. The mag-

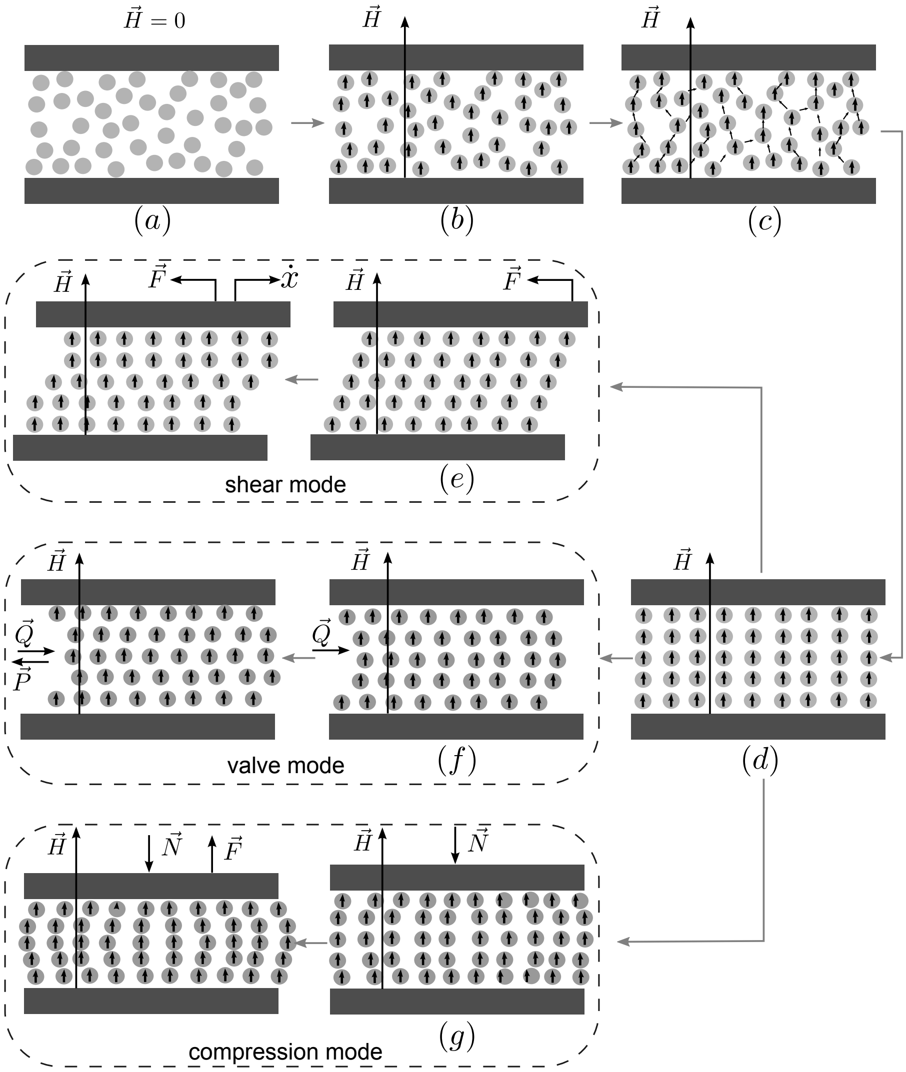

Figure 4.1: Rheological effect in a magnetorheological suspension and typical utilisation modes. The particles are homogeneously distributed in the carrier liquid (a). When a magnetic field $\vec{H}$ is applied (b) the particles are magnetized and behave as a magnetic dipoles (c). Therefore, they form chain-like structures or agreagates roughly aligned in parallel to the field (d), arrangement corresponding to the minimum energy. This phenomenon can be exploited according to there operation modes. In the shear mode (e) the fluid creates a resistive force $\vec{F}$ against the relative velocity of the poles $\dot{x}$. When the poles moves, the chain structures are stretched, broken, and immediately reconstituted. In the valve mode (f) the fluid flow $\vec{Q}$ generates a pressure drop ΔP which can be controlled by the magnetic field intensity. In the compression mode (g), a force $\vec{N}$ is applied perpendicularly to the poles and the fluid resists against the displacement of the poles generating the force $\vec{F}$.

netic interaction between the particles induces a magnetic force which is proportional to their relative position and orientation to the external field and the magnetic permeability of the carrier fluid [Joung et See, 2008]. The particles then behave as magnetic dipoles that undergo magnetic interaction forces (Fig. 4.1c). Hence, this mutual interaction amongst the particles causes the formation of chain-like structures or fibrils, roughly aligned parallel to the applied field (Fig. 4.1d). If the magnetic poles are considered as a magnetic potential surface, the interaction between a particle and the pole can be modelled as equivalent to the interaction of the particle and the dipole images of all other particles reflected about the surface [Kittipoomwong *et al.*, 2005]. The formation of the chain-like structures is macroscopically perceived as a change in the viscous characteristics of the suspension, thereby restricting the displacement of the fluid. The necessary mechanical energy to break these structures increases with the strength of the applied magnetic field resulting in a field dependent yield stress. This is macroscopically manifested when the fluid is sheared by the development of a yield stress which increases with the magnitude of the applied field in a fraction of a millisecond [Mohammadi *et al.*, 2010].

This phenomenon can be exploited in the design of passive actuators according to three operation modes: shear mode, valve mode and compression mode [Carlson et Jolly, 2000] [Olabi et Grunwald, 2007]. In the shear mode (Fig. 4.1e), a relative displacement of the poles is induced. Since the particles, when close to the wall, acquire the same translational velocity than the pole, the chain-like structures create a resistive force $\vec{F}$ against the velocity of the poles $\dot{x}$. The chains are subsequently continuously broken and immediately reconstituted due to the field across the poles and due to the pole displacement. In the valve mode (Fig. 4.1f) the poles are immobilized and the magnetic field is adjusted to control the pressure drop ΔP between the input and the output and therefore the resistance against the fluid flow $\vec{Q}$. In the compression mode, a force $\vec{N}$ is imposed perpendicularly to the poles. The compression of the fluid generates a force $\vec{F}$ against the imposed force $\vec{N}$.

Furthermore, the behavior of MR fluids when in the "off" state is also non-Newtonian and temperature dependent, however it deviates little enough for the fluid to be ultimately considered as a Bingham plastic for a simple analysis.

The behavior of MR fluids in the absence of a magnetic field is non-Newtonian and temperature depenent. This deviation is however very small. For a simple analysis, we consider the MR fluid as Newtonian for zero field. In the presence a magnetic field, MR fluids display both a pre-yield regime, characterized by an elastic response, and a post-yield regime characterized by a viscous response [Jolly *et al.*, 1996]. The transition point occurs when the shear rate $\dot{\gamma}$ is almost zero [Weiss *et al.*, 1994]; this point is called yield point and denoted $\tau_z(H)$. The Herschel-Bulkley [Lee et Wereley, 2000] and Bingham models [Lindler et Wereley, 2003] are the commonly plastic models employed to describe the non-linear behaviour of MR fluids as a function of the magnetic field. The Herschel-Bulkley model allows a non-linear post-yield

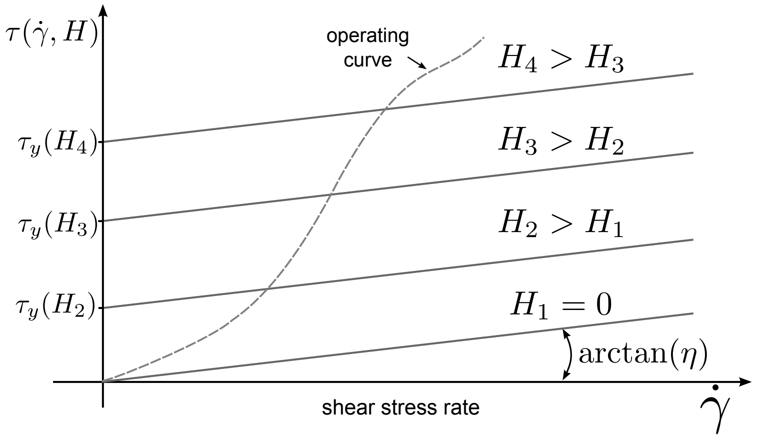

Figure 4.2: MR fluid behaviour according to the Bingham plastic model. The fluid shear stress $\tau(\dot{\gamma},H)$ is a function of the shear stress rate $\dot{\gamma}$ and of the field dependent yield point $\tau_y(H)$, where H_n is the magnetic field strength and η is the fluid viscosity coefficient. It is possible to follow almost any curve on this plan by controling the magnetic field. This is the case of the dashed line which represents a fluid with a variable viscosity coefficient.

behaviour while the Bingham model assumes a linear behaviour. The constitutive formulation of the Bingham model is presented in (4.1). $\tau(\dot{\gamma},H)$ is shear stress, and η the fluid viscosity coefficient. The fluid yield stress $\tau_y(H)$ is a function of the external magnetic field H.

$$\begin{cases} |\tau(\dot{\gamma},H)| = \tau_y(H) + \eta|\dot{\gamma}| & |\tau(\dot{\gamma},H)| \geqslant \tau_y(H) \\ \dot{\gamma} = 0 & |\tau(\dot{\gamma},H)| < \tau_y(H) \end{cases} \tag{4.1}$$

Fig. 4.2 presents the evolution of the fluid shear stress as a function of the magnetic field according to the Bingham plastic model. The pre-yield regions are shortened as the magnetic field increases. During the pre-yield regime, the chain structures present an elastic behaviour with some stiffness. When the fluid deforms beyond the yield point ($\tau(\dot{\gamma},H) \geq \tau_y(H)$), its response can satisfactorily be described by the Bingham model.

Usually, rotary brakes are based on the shear mode and take the form of disc or cylindrical housings as shown in Fig. 4.3 [Kikuchi et Kobayashi, 2011]. In disc brakes (Fig. 4.3a) the fluid is contained in a disc volume perpendicular to the rotation axis and the magnetic flux is applied orthogonally against the fluid shear. In cylindrical brakes (Fig. 4.3b), the fluid is in a cylindrical gap around the rotation axis. In both cases, the tangential force generated between the magnetic poles is calculated by the integration of the tangential traction of $\tau(H)$ with respect to the fluid shearing area. This shearing area S is called "active surface", which comprises for any fluid surface employed to create a controllable torque. Taking into account the radius R between the fluid surface and the rotation axis, the total torque Γ is given by:

$$\Gamma = \int\int R\tau(H)dS \tag{4.2}$$

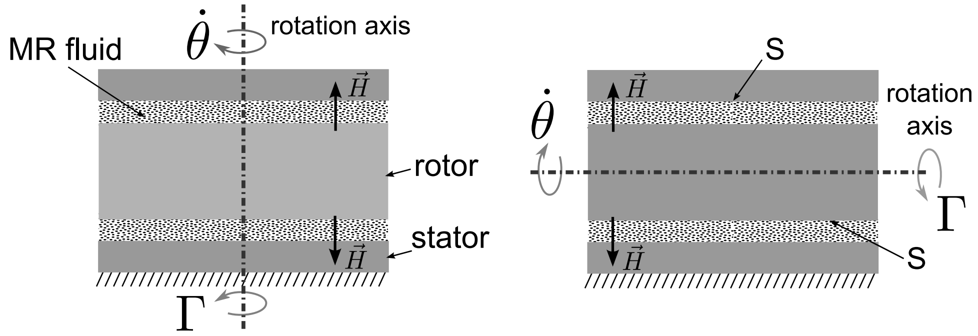

(a) Disc brake **(b)** Cylindrical brake

Figure 4.3: Schematic view of cylindrical and disc brake configurations. The fluid is placed between two discs for the disc type (a) and three concentric cylinders in the drum brake (b). The braking torque Γ against the velocity $\dot{\theta}$ is generated over the active surface S, and controlled by a magnetic field H.

This equation highlights that the braking torque strongly depends on the brake geometry. Several ways can be envisaged to increase the fluid shearing surface and as a consequence the braking torque.

1.1 DOCUMENTED BRAKE DESIGNS

Disc-type brakes are widely used in a large range of applications. An example is the system proposed by McDaniel [McDaniel, 2011] composed of a clutch and a brake linked in series. Li and Du [Li et Du, 2003] designed a high-efficiency single disc brake and conclude that the uncontrollable viscous torque increases strongly with the rotary velocity. Li et al. [Li *et al.*, 2007] used a disc brake to develop a 2-DOF joystick for virtual reality applications. Karakoc et al. [Karakoc *et al.*, 2008] present an automotive MR brake which provides 23Nm at 1.8A. Assadsangabi et al. [Assadsangabi *et al.*, 2011] report the optimization and design of disc-type brakes in terms of maximum torque.

Cylindrical-brakes, on the other hand, can, according to [Kikuchi et Kobayashi, 2011], effectively transduce the MR effect in braking torque with lower inertia compared to disc brakes. [Huang *et al.*, 2002] develop a theoretical design method of a cylindrical MR brake using the Bingham model and determine parameters of the fluid gap when the mechanical power, velocity, and dynamic range are specified. [Shiao et Chang, 2011] optimize a cylindrical brake by increasing the active chaining areas using a multiple-pole configuration. Avraam et al. [Avraam *et al.*, 2008] develop a portable passive rehabilitation device with optimized volume and mass. [Rosenfeld et Wereley, 2004] demonstrate the optimization of a cylindrical valve with constrained volume and concluded that small changes in the fluid gap drastically affects its performance. Nguyen et al. describe a hybrid brake combining a disc and cylinder based in a T-shaped and U-shaped ferromagnetic core which combines the use of discs and cylinders

[Nguyen et Choi, 2012].

Multiple-layered brakes composed of several elementary discs or cylinders constitute an efficient way to improve performance. Multiple-layered disc brakes, for example, are commonly employed in the design of electrorheological (ER) actuators [Nikitczuk *et al.*, 2007] [Carlson et Duclos, 1990]. Several works have reported their implementation in high torque applications using MR fluids too as proposed in [Park *et al.*, 2006], [Gudmundsson *et al.*, 2010], and [Fauteux *et al.*, 2009]. Nguyen and Choi [Nguyen et Choi, 2010] use a tooth-shaped automotive disc brake able to display 1025Nm for an with limited dimensions and optimized weight. In [Shafer et Kermani, 2011] and [Kikuchi *et al.*, 2009], a multiple-disc based high torque clutch for human-robot interaction is chosen. Guo and Liao [Guo et Liao, 2011] report the optimization of multiple-disc clutch/brake comparing models with different configurations of inner coils. Nikitczuk et al. [Nikitczuk *et al.*, 2007] report on the conception of a multi-layered cylindrical brake using ER fluid for rehabilitation devices. Periquet and Lozada [Periquet et J.Lozada, 2010] chose a multiple cylinder configuration for a 1.7Nm miniature MR brake and achieve high performance in terms of torque density and power consumption.

1.2 SELECTION OF A BRAKE DESIGN

Four main configurations comprising single cylinder and single disc brakes and their extension using multi-layered design can be identified. Nguyen and Choi [Nguyen et Choi, 2012] use finite element analysis to compare different geometries in terms of maximum torque and volume ratio. Their results suggest that disc-shaped brakes produce more torque than cylindrical brakes for small values of radius/length ratio. To our knowledge, no author has focused on an analysis of multiple layered and single brakes that takes into consideration the measures of performance such as torque, volume, power consumption, bandwidth, viscous torque, etc.

In this Chapter an analytic model for the usual brake geometries is developed. This analysis allows for the identification of tradeoffs on the design of a brake. Thus, knowing the evolution of the performance as a function of the geometry, different brake designs can be compared according to different criteria.

2 EVALUATION CRITERIA FOR MR BRAKES

Most of the available works dealing with the design and optimization of MR fluid actuators predominantly focusses on torque optimization. For instance, [Karakoc *et al.*, 2008] present the design of an automotive brake using a multiphysics optimization method to maximize the controllable torque. A cost function is defined including the braking torque and weight. In the same way, using finite element analysis, [Park *et al.*, 2008] define cost functions to maximize to the torque-to-weight ratio while keeping a minimal required braking torque. In

[Gudmundsson *et al.*, 2010], a multi-objective optimization method for a prosthetic knee brake in terms of controllable torque, including also the off-state torque and weight is proposed. The autors consider an optimization parameter as a constraint in the modelling, or as an additional objective function. [Zhang *et al.*, 2006] focus on a finite element analysis of the magnetic circuit saturation of an MR-based damper. [Yang *et al.*, 2008] investigate the feasibility of an MR valve considering the relation of the volume fraction to yield stress, response time of the coils and electric power losses. [Nguyen *et al.*, 2011] present an optimized design of a motorcycle brake where the required braking torque, maximal temperature, mass and geometric dimensions are defined as optimization constraints. In some approaches, the goal of the optimization is to increase the magnetic flux in the MR fluid as much as possible [Assadsangabi *et al.*, 2011]. However, the necessary coil volume and power supply increase if the fluid becomes saturated.

On the design of an MR brake, all parameters are interconnected and may have the opposite influence on performance. According to [Fauteux *et al.*, 2009], a versatile actuator possess a high torque density, sufficient bandwidth and very low output impedance. Here we define as measures of performance, the torque density, efficiency, controllability and electrical bandwidth.

2.1 TORQUE DENSITY

The torque density is obtained by dividing the maximum torque Γ_{max} by the total volume V_t. The maximal torque corresponds to the achieved torque when a specified magnetic flux density B_{sat} is reached in the fluid surface. The torque density ρ is obtained as:

$$\rho = \frac{\Gamma_{max}}{V_t} \tag{4.3}$$

2.2 EFFICIENCY

The efficiency is defined as the ratio between the torque Γ_{max} and the power supply P_{max}. A linear relationship can be reached if the saturation of the magnetic circuit and of the fluid is avoided [Guo *et al.*, 2003]. Ideally, the magnetic induction of the fluid and of the ferromagnetic circuit should reach their saturation at the same electric power corresponding to P_{max} [Liu *et al.*, 2006]. The efficiency E is then defined as:

$$E = \frac{\Gamma_{max}}{P_{max}} \tag{4.4}$$

2.3 CONTROLLABILITY

The controllability is defined as the ratio between the controllable torque Γ_{max} and the viscous friction coefficient. According to (4.1), the shear stress depends also on the shear strain rate. It represents an uncontrollable viscous torque Γ_f which depends on the rotational velocity $\dot{\theta}$. To overcome this dependence, we consider the ratio viscous-torque-to-velocity $\Gamma_v = \Gamma_f / \dot{\theta}$. The controllability K, then represents the relation between the controllable and uncontrollable torque coefficient and is given by:

$$K = \frac{\Gamma_{max}}{\Gamma_v} \tag{4.5}$$

2.4 REACTIVITY

The reactivity depends on the necessary time that the brake need to deliever the desired torque. It comprises by the electrical time of the electromagnetic circuit δt_c and the response time of the fluid. An MR fluid needs less than 1ms shifting from fluid to semi-solid state [Zhu, 2007]. Thus, the response time of the fluid is negligible compared to the electromagnetic response time which depends of the coil design and the magnetic reluctance [Koo *et al.*, 2006]. The coil is concentric to the rotation axis and is dimensioned to support the power supply P_{max}. The ratio torque/eletrical time-constant then characterizes the reactivity of the brake δt_c in terms of Nm/s, for a step-type voltage excitation, and is computed as:

$$\delta t = \frac{\Gamma_{max}}{\delta t_c} \tag{4.6}$$

Section 3 presents a modelling of these criteria for the two basic brake configurations.

3 BASIC ROTARY BRAKE GEOMETRIES

The indexes "d" and "c" refer to a disc and to a cylindrical brake respectively.

In the following models the magnetic circuit is dimensioned to deliver a desired magnetic flux density over the smallest fluid surface. This enables the brake to maintain the fluid under its saturation point in order to guarantee a linear current-torque relationship and to minimize the power supply. Fig. 4.4 present graphs of the yield stress as a function of the magnetic field for some typical fluids from Lord Corporation obtained from product datasheets [1]. For a given fluid, a maximal induciton is specified before its magnetic or mechanical saturaion. For example, in the case of the MR fluid 132EG, we can assume that the maximal field dependent yield stress $\tau_y(H)$ in the linear range is 39kPa (see Fig. 4.4b]). Beyond this point the fluid saturates. In order to guarantee that the brake operates in the linear range, the magnetic field across the

---

[1] http://www.lord.com/products-and-solutions/magneto-rheological-(mr)/mr-products.xml

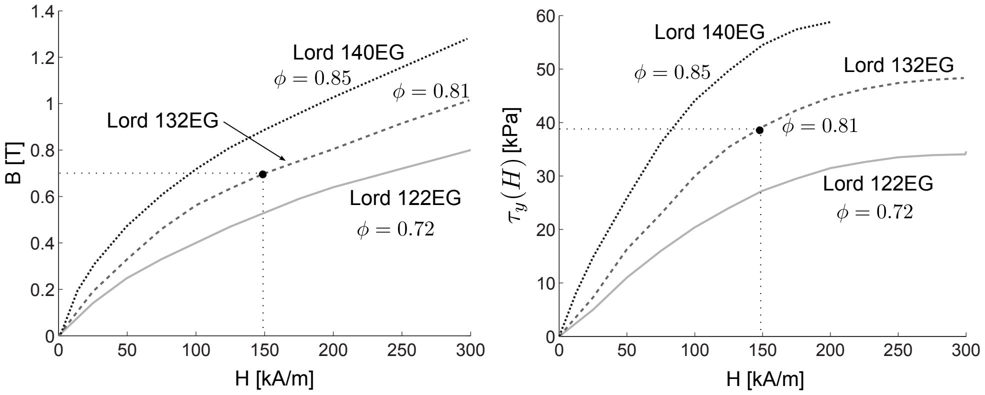

(a) Yield stress **(b)** B-H curves

Figure 4.4: Characteristics of commercial MR fluids from Lord Corporation. In 4.4a the fluid yield stress as a function of the magnetic field. In 4.4b the respective induction curves. ϕ is the particle weight fraction for each fluid formulation. The black point defines the linearity limit of the fluid used in the proposed model. Figures adaped from [Avraam, 2009].

Table 4.1: Linear model parameters

term	value	unit	parameter
B_{sat}	0.7	T	desired induction in the smallest fluid gap
B_{fer}	1.4	T	maximal admissible induction of the path
μ_{mr}	$16\pi 10^{-7}$	H/m	fluid absolute permeability
μ_{fer}	∞	H/m	path absolute permeability
α	0.22	Pa.m/A	fluid magnetic field to yield stress constant
η	61.10^{-3}	Pa.s	fluid viscosity coefficient
ν	6.10^{6}	A/m^2	coil wire current to section ratio
κ	17.10^{-9}	Ω/m	coil wire linear resistivity
S_w	$4.9.10^{-}8$	m^2	wire section
χ	70%	-	coil fill rate

fluid cannot exceed 150kA/m. Thus, the maximal induction called B_{sat} to be speficied in the model is 0.7T (see Fig. 4.4a).

In the same way, considering a maximal admissible induction attributed on the ferromagnetic path, the circuit is designed so that the fluid and the path reach their saturation for the same magnetic flux. By these means the volume of the brake can be optimized.

The parameters considered in the evaluation of different brakes throughout this chapter are listed in Table 4.1. The fluid is Lord Corporation MFR-122EG [Corporation,].

3.1 DISC-SHAPED BRAKES

A disc-shaped brake is illustrated in Fig 4.5. The magnetic flux $\Phi(t)$ generated by a coil having N turns and by a current $i(t)$ is given by $\Phi(t) = Ni(t)/\mathscr{R}$ where $\mathscr{R}$ is the magnetic reluctance. The relative permeability of commercial MR fluids may range from 4 to 6.5 [Company,]

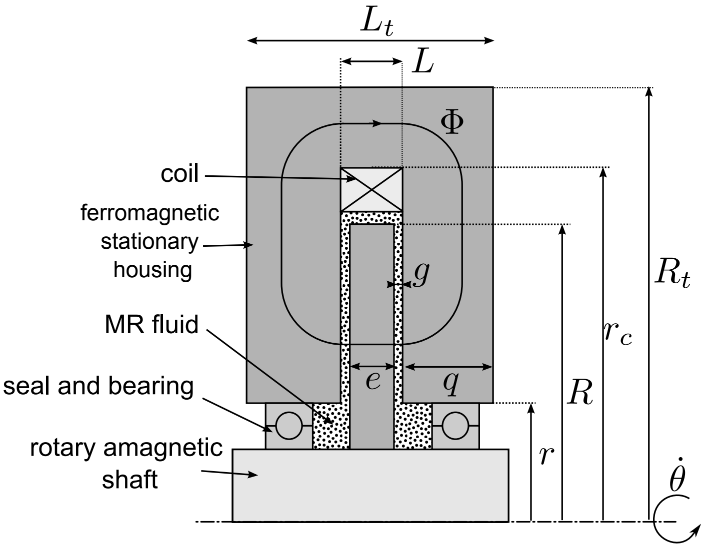

Figure 4.5: Cross view of a single disc brake. An excitation coil, concentric to the axis, with an external radius r_c, generates the magnetic flux Φ. The fluid gap depth is noted g, the disc width is e and the outer and inner radius of the fluid are R and r respectively. The length of the disc and the gaps is called L, R_t and L_t are the external dimensions of the brake taking into consideration all ferromagnetic paths. The total volume is $V_{td} = \pi R_t^2 L_t$. The velocity of the rotary shaft is denoted $\dot{\theta}$.

[Corporation,]. On average, the permeability of the ferromagnetic path made in iron is 2000 times superior. For the usual brake dimensions, the ferromagnetic reluctance can be neglected compared to the reluctance of the fluid. If we note g, μ_{mr}, r, and R the fluid gap depth, the absolute permeability of the fluid, the inner and external radius of the fluid gap respectively, the active surface is $S = 2\pi(R^2 - r^2)$. The reluctance is then computed as [Karakoc *et al.*, 2008]:

$$\mathscr{R}_d = \sum_{k=1}^{n} \frac{g}{\mu_{mr} S} = 2\frac{g}{\pi \mu_{mr}(R^2 - r^2)} \tag{4.7}$$

with n the number of fluid gaps. Since the reluctance of the ferromagnetic path is neglected, the induction of the fluid can be considered as homogeneous along the gap. Considering a linear relationship between the magnetic field $H(t)$ and the magnetic flux density $B(t) = \mu_{mr} H(t)$, the magnetic field on the fluid gap is $H(t) = Ni(t)/\mu_{mr} S \mathscr{R}_d$. The relation between the magnetic field and the field dependent yield stress $\tau(H)$ is typically denoted $\tau_z(H) = \alpha H(t)^{\beta}$ where α and β are two constant characteristics of the fluid [Li et Du, 2003]. Considering a linear behaviour ($\beta = 1$) and using the Bingham plastic model, the total controllable torque is $\Gamma_{maxd} = 4\pi(R^3 - r^3) N \alpha i_{max}/3 S \mathscr{R}_d \mu_{mr}$.

The electromagnetic circuit is designed to develop a desired induction value B_{sat} across the fluid surface S. For a given fluid, B_{sat} is set at the maximal induction of fluid before its magnetic or mechanical saturation. The torque written as a function of B_{sat} is:

$$\Gamma_{maxd} = \frac{4\pi}{3}(R^3 - r^3)\frac{\alpha}{\mu_{mr}} B_{sat} \tag{4.8}$$

Note that the proposed modeling is only valid for $\beta = 1$. The magnetic flux that gives B_{sat} is $\Phi = B_{sat}S$. It defines the magneto-motive force $Ni = \Phi\mathscr{R}$ which can be correlated to the power supply. Calculated by Joule's losses, the power is $P = i^2R_e$ where R_e is the electric resistance of the coil given by $R_e = 2\pi r_b \kappa N/S_w$ with κ the resistivity of the coil wire, r_b the mean radius of the coil, and S_w the section of the wire. Given a maximum current-to-surface ratio ν (A/m^2), we obtain the relation $i = S_w\nu$. The power as a function of Ni then is $P = 2\pi r_b \nu\kappa Ni$.

As a function of B_{sat}, the power is expressed as $P_{maxd} = 2\pi\kappa\nu r_b B_{sat} S\mathscr{R}$. In the case of the single disc, it can be simplified to:

$$P_{maxd} = 4\pi g \frac{1}{\mu_{mr}} r_b \kappa \nu B_{sat} \tag{4.9}$$

Considering only the reluctance of the fluid gap, note that, for a disc brake, the power supply does not depend on the fluid surface length $(R-r)$.

The coil volume can be expressed as $V_{coil} = 2\pi r_b S_w N/\chi$ where χ is the coil fill rate. The volume of the coil as a function of the required power is $V_{coil} = P_{maxd}/\nu^2\kappa\chi$. Combining this Equation with (4.9) and considering that the width of the coil is $L = 2g + e$, with e the disc width, the external radius of the coil r_c can be deduced.

Considering the coil as a RL circuit, the electrical time constant, proportional to the magnetic reluctance [Yang *et al.*, 2008] [Koo *et al.*, 2006] is given by:

$$\delta t_c = \frac{N^2}{R_e \mathscr{R}_d} = \frac{S}{2\pi\kappa\nu r_b} B_{sat} \tag{4.10}$$

The ferromagnetic circuit should support the magnetic flux without saturation. It requires a minimal cross section S_{fer} of the ferromagnetic path, so that $S_{fer} = B_{fer}/\Phi$ where B_{fer} is the saturation point of the ferromagnetic material. The ferromagnetic cross section can be calculated as a funcion of the fluid surface. If we call $c_{sat} = B_{sat}/B_{fer}$ the maximal induction ratio of the ferromagnetic circuit and of the fluid, the ferromagnetic cross section is $S_{fer} = c_{sat}S$, so that the ferromagnetic path and the fluid reach their saturation for the same flux. In this way, the minimal width q on both sides is $q = (R^2 - r^2)/2c_{sat}R$ and the minimal external radius R_t, taking into account the position of the coil is $R_t = \sqrt{(R^2 - q^2)c_{sat} + r_c^2}$.

Therefore, when the fluid surface and the desired field are defined, all other dimensions can be optimally calculated. The total volume is $V_{td} = \pi R_t^2 L_t$ where R_t and L_t are the external radius and length and can be calculated as:

$$V_{td} = \pi[(R^2 - r^2)c_{sat} + r_c^2]\left[2g + e + \frac{(R^2 - r^2)c_{sat}}{r}\right] \tag{4.11}$$

Considering η the fluid viscosity coefficient and $\dot{\theta}(t)$ the rotational velocity, the viscous torque Γ_f generated on the active surface is [Li et Du, 2003]:

$$\Gamma_f = 2 \int_r^R (2\pi r_p^2) \left(\frac{\dot{\theta}(t)\eta}{g} r_p \right) dr_p \tag{4.12}$$

Thus, the viscous torque coefficient $\Gamma_{vd} = \Gamma_f / \dot{\theta}(t)$ is given by $\Gamma_{vd} = \pi\eta(R^4 - r^4)/g$.

The measures of performance can henceforth be determined. The efficiency computed as $E_d = \Gamma_{max}/P_{max}$ is:

$$E_d = \alpha \frac{1}{3} \frac{(R^3 - r^3)}{g} \frac{1}{r_b \kappa \nu} \tag{4.13}$$

The efficiency is directly dependent on the fluid characteristics, on the fluid gap depth and on the design of the coil. Equation 4.13 demonstrates also that the coil radius should to be as small as possible in order to minimize its electric resistance.

The reactivity is $\delta t_d = \Gamma_{maxd}$ in terms of Nm/s is:

$$\delta t_d = \frac{8\pi}{3} \frac{\alpha}{\mu_{mr}} r_b \kappa \nu \frac{R^3 - r^3}{R^2 - r^2} \tag{4.14}$$

According to Equation 4.14, the reactivity depends on the fluid characteristics and on the design of the coil. The response time can be reduced by increasing the coil radius but it increases also the electric resistance and, as consequence, the power supply.

The torque density ρ_d is:

$$\rho_d = \frac{4\alpha}{3\mu_{mr}} \frac{(R^3 - r^3)}{[(R^2 - r^2)c_{sat} + r_c^2][2g + e + (R^2 - r^2)c_{sat} r^{-1}]} B_{sat} \tag{4.15}$$

The controllability $K_d = \Gamma_{maxd}/\Gamma_{vd}$ is expressed as:

$$K_d = \frac{4}{3} \frac{\alpha}{\mu\eta} g \frac{(R^3 - r^3)}{(R^4 - r^4)} B_{sat} \tag{4.16}$$

This equation shows that K_d is proportional to the gap depth, inversely proportional to the radius and depends on the characteristics of the fluid. A large gap generates less viscous torque but increases the power. Fig. 4.6 presents a graphic representation of all performance criteria as a function of the dimensions.

To design a disc brake with optimized torque density, only the fluid surface radius and the gap should be specified. Increasing the radius improves the efficiency, the resistivity and the maximal torque. However, the viscous torque increases faster and the controllability decreases. A controllability/torque tradeoff is then governed by the radius. Since the reluctance of the ferromagnetic path is neglected, the length L has no effect on performance. For a given power, a small fluid gap g increases the maximal torque but the viscous torque increases too. A tradeoff between controllability and maximal torque and controllability/efficiency is set by the gap depth.

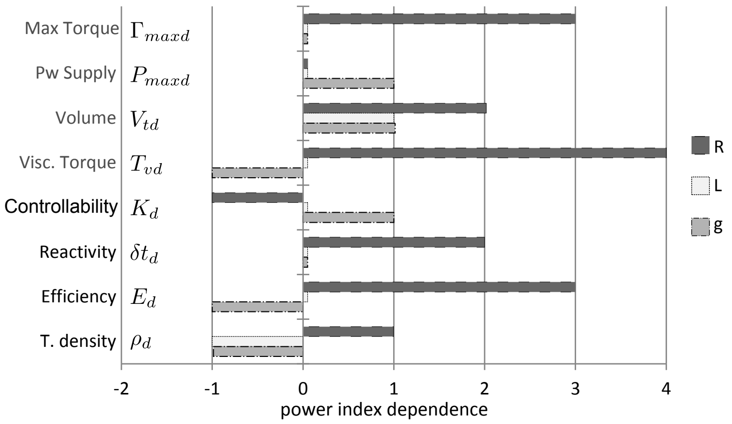

Figure 4.6: Graphic representation of the evolution of the interdependent measure of performance as a function the brake dimensions. The coordinates of the graphic represent the highest polynomial power index dependence of each criterion as a function of the radius *R*, of the length *L* and of the depth *g* of the fluid gap. For example, the efficiency depends on the cube of the radius, thus, it is represented buy the index 3 when the radius is changed.

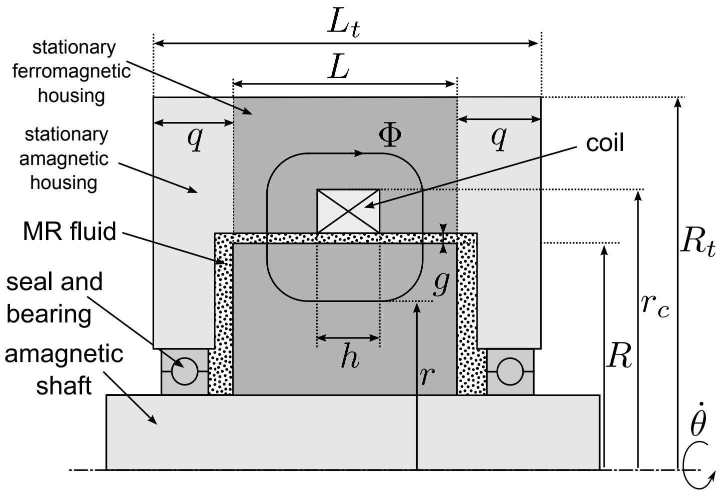

Figure 4.7: Single cylinder brake. The radius and length of the fluid gap are called *R* and *L*. The inner radius is *r*. An excitation coil with external radius r_c and height *h* provides the magnetic flux Φ. The active surface is $2\pi R(L-h)$. The magnetic flux Φ is supposed to be homogeneous along the fluid gap *g* and the total volume is $V_{tc} = \pi R_t^2 L_t$. The rotary shaft velocity is $\dot{\theta}$. The width of the lateral supports is denoted *q*.

For brakes with large L_t/R_t ratio, the design tends to cylindrical brake, which corresponds to the second basic geometry presented in the following section.

3.2 CYLINDER-SHAPED BRAKES

The second elementary brake type consists of cylindrical shaped brakes also called drum-brakes. A schematic cross view is presented in Fig. 4.7.

If *R* is the fluid gap inner radius and *r* is the radius of the inner section crossed by the flux, the reluctance is given by the integral of the reluctance of fluid gap from the cylinder *R* up to

$R+g$ along a radius r_p computed as:

$$\mathscr{R}_c = \int_{R}^{R+g} \frac{2}{\mu_{mr}(2\pi R(L-h))} dr_p = \frac{ln(1+\frac{g}{R})}{\pi\mu_{mr}(L-h)} \tag{4.17}$$

with h the height of the coil. Considering $R >> g$, the reluctance can satisfactorily be approximated as $\mathscr{R}_c = g/\left[\pi\mu_{mr}(L-h)R\right]$. Combining (4.2) with the equation of the induction on the fluid, the controllable torque is $\Gamma_{maxc} = 2\pi R^2(L-h)\alpha Ni/S\mathscr{R}_c\mu_{mr}$, which can be rewritten as a function of B_{sat} as:

$$\Gamma_{maxc} = 2\pi R^2(L-h)\frac{\alpha}{\mu_{mr}}B_{sat} \tag{4.18}$$

By contrast to disc-brakes, the maximal torque is proportional to the length. The necessary power P_{maxc} is obtained using the same procedure employed for the disc-type. The efficiency is then obtained computing $E_c = \Gamma_{maxc}/P_{maxc}$:

$$E_c = \alpha\frac{1}{2}\frac{R^2(L-h)}{g}\frac{1}{r_b\kappa\nu} \tag{4.19}$$

Considering only the fluid surface and $R >> g$, the viscous torque can be approximated by (4.20) [Nguyen et Choi, 2011]. A complete viscous model is presented in [Huang *et al.*, 2002].

$$\Gamma_f = \int_0^{2\pi}\int_0^{L-h} R\tau d\theta dS = \int_0^{L} R\frac{\eta R\dot{\theta}(t)}{g}2\pi R dl \tag{4.20}$$

Thus, the viscous torque to velocity coefficient $\Gamma_{vc} = 2\pi\eta(L-h)R^3/g$ suggests that the viscous torque depends mainly on the cylinder radius and of the fluid gap depth. The controllability $K_c = \Gamma_{maxc}/\Gamma_{vc}$ is then computed as follows:

$$K_c = \frac{\alpha}{\mu_{mr}\eta}\frac{g}{R}B_{sat} \tag{4.21}$$

The controllability is proportional to the fluid gap, inversely proportional to the radius and independent of the thickness L. Thus, in order to improve Γ_{maxc} without altering the controllability, the thickness should be increased instead of the radius.

The fluid surface crossed by the magnetic flux is $S = \pi R(L-h)$. The magnetic flux is given by $\Phi = SB_{sat}$. For the same flux the induction at the top of the coil is $B_{fer} = \Phi/S_{fer}$ with $S_{fer} = \pi(R_t^2 - r_c^2)$. Combining these equations gives the required outer radius $R_t = \sqrt{c_{sat}R(L-h)+r_c^2}$ to avoid the saturation of the ferromagnetic path, where r_c is the coil radius which can be determined using the coil volume. In the same way, the section at the bottom of the coil is $S_b = \pi(R^2 - r^2)$. The minimal inner radius can therefore be written as $r = \sqrt{R^2 - c_{sat}R(L-h)}$. Note that the inner radius specifies also the maximal length of the fluid gap.

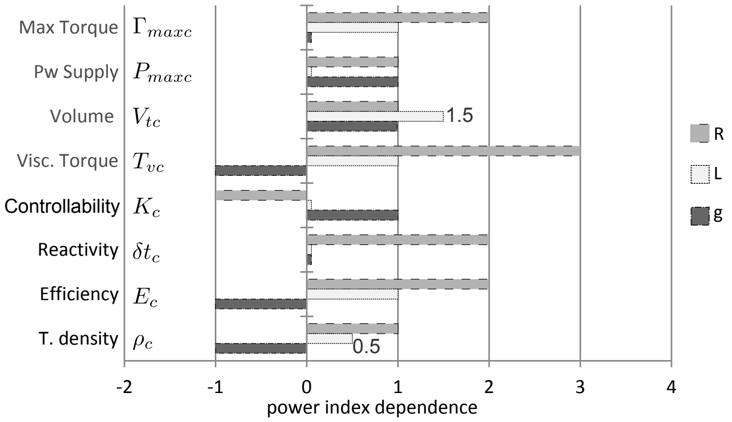

Figure 4.8: Cylindrical brake performance as a function of its external dimension variation. Where L, L and g are the fluid gap radius, length and depth respectively.

The volume of the brake is given by $V_{tc} = \pi L_t R_t$ and the torque density $\rho_c = \Gamma_{maxc}/V_{tc}$ is:

$$\rho_c = \frac{\alpha}{\mu_{mr}} \frac{2R^2(L-h)}{[c_{sat}(L-h)R + r_c^2](2q+e)} B_{sat} \tag{4.22}$$

The response time of the brake is obtained combining (4.10) with (4.17), and is given by $\delta t_r = B_{sat}(L-h)R/[2\kappa\nu r_b]$. The reactivity, in terms of Nm/s, is:

$$\delta t_c = 4\pi\kappa\nu r_b R \frac{\alpha}{\mu_{mr}} \tag{4.23}$$

Fig. 4.8 presents the evolution of all parameters as a function of L and R. Increasing the radius improves the maximal torque, the efficiency, and the reactivity but the controllability is reduced, increasing the thickness L improves the efficiency and of the maximal torque. The same tradeoffs between torque and controllability and between reactivity and power are observed.

3.3 FINITE ELEMENT MODELLING

The magnetostatic models have been simulated by finite elements using FEMM[2] software. The model is solved with the same geometry in Matlab and with FEMM. The fluid is Lord Corp. MFR-122EG [Corporation,] (see Fig. 4.4). The variables assumed as constant in the analytical model have been listed in Table 4.1. For the FEA, the B-H curves (flux density versus magnetic field) for the fluid and for the ferromagnetic path (Telar 57S), are obtained from the manufacturer's specifications. The same procedure is employed to obtain the variable $\alpha(H)$ (magnetic field to yield stress constant).

To design a brake, only three variables need to be specified: the magnetic flux density over the fluid B_{sat}, the fluid gap g depth and its radius R. All other dimensions can optimally be

---

[2] Finite Element Method Magnetics: www.femm.info

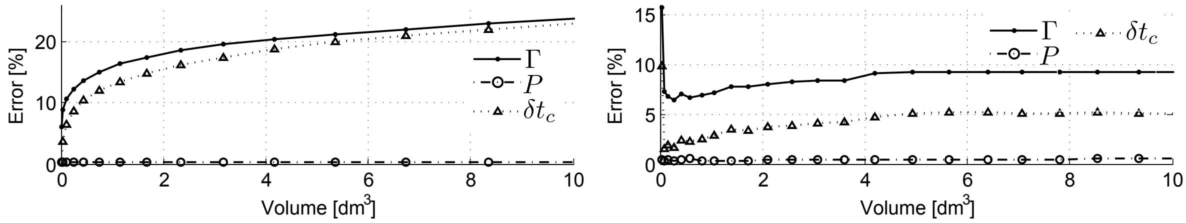

(a) Single disc brake **(b)** Single cylinder brake

Figure 4.9: Relative error between the analytical model and the FEA for the single disc (top) and the single cylinder brake (bottom). Where Γ, P and δt_c are the torque, the power and the electrical time constant respectively.

deduced. The fluid gap is 0.5mm. The radius varies from 10mm to 170mm for the cylinder brake and from 10mm to 250mm for the disc brake in order to achieve an equivalent volume.

The relative errors between the analytical model and the FEA as a function of the brake volume are presented in Fig. 4.9. The difference in terms of power is less than 0.5%.

The reluctance obtained in the analytical model is inferior than with the FEA, which directly affects the response time, as presented in Eq. 4.14. Considering the power calculated in the analytical model, the magnetic flux in the FEA is not sufficient to achieve B_{sat}. This has an impact of reducing the maximal torque. For the disc and the cylinder brake respectively, the maximal torque error are 23% and 9.8% and in terms of response time are 23% and 8.7%. These errors are however attained of a 10dm^3 volume, which represents a uncommon size for an MR brake (a cube with 373mm space diagonal or a 500mm diameter disc brake).

These errors increase with the brake volume. If the FEA neglects the reluctance of the ferromagnetic path, they are reduced to 3.1% and 1.9% for the torque and to less than 1% for electrical time constant. The error depends also on the fluid gap depth. For example, for g=0.3mm, the torque error for the disc and for the cylinder rises to 31.1% and 13.8%. For g=0.75mm, the error are reduced to 18.8% and 6.5%.

In the FEA, the maximal magnetic flux density observed in the ferromagnetic path is 1.38T. As predicted by the model, the ferromagnetic path is maintained under the saturation point of the material specified at 1.4T.

3.4 DISCUSSION

The measure of performance obtained by FEA for each brake are presented in Fig. 4.10. For the cylinder brake, the lateral support are arbitrary fixed to $q = 2$mm. Both brakes exhibit an equivalent torque density for a given volume. The results show that disc brakes possess a better efficiency compared to cylindrical brakes and generate less viscous friction. Conversely, cylindrical brakes react faster.

The proposed model allows for an optimal design of both brake types in terms of torque

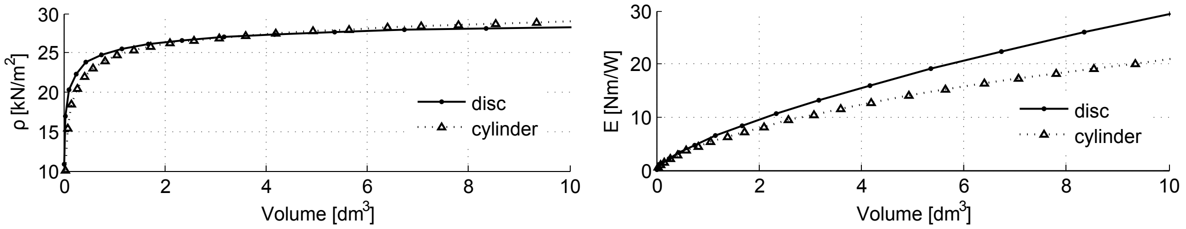

(a) Torque density **(b)** Efficiency

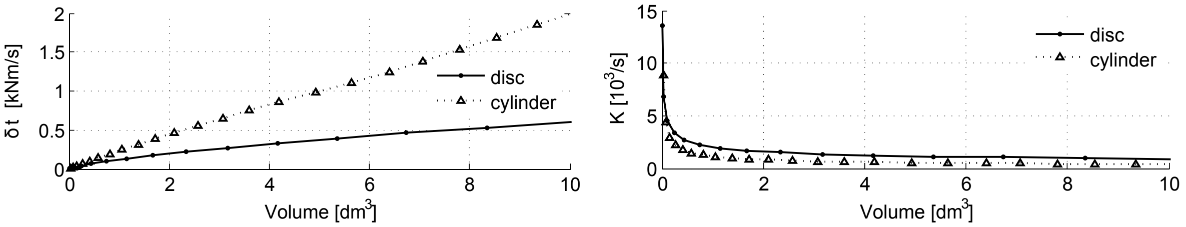

(c) Reactivity **(d)** Controllability

Figure 4.10: Measures of performance as a function of the volume obtaiend by FEA. The results present the optimised torque density ρ for a given L_t/R_t ratio. The efficiency E is higher in a disc brake for L_t/R_t <0.48 but the reactivity δt is inferior than cylinder brakes. Disc brakes present higher controllability K.

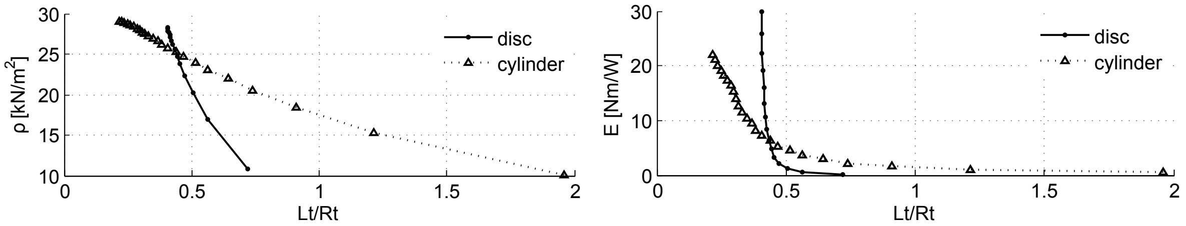

(a) Torque density **(b)** Efficiency

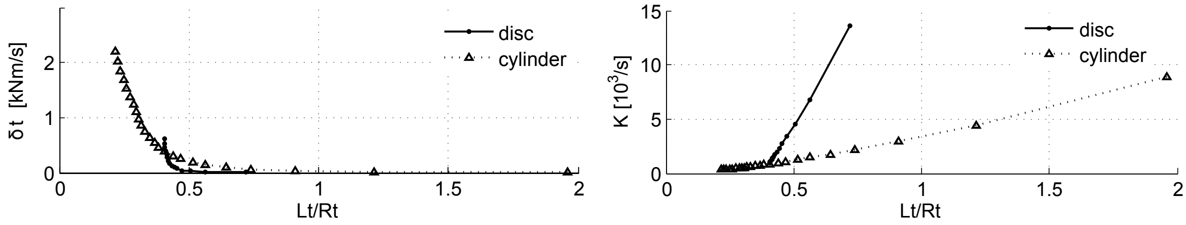

(c) Reactivity **(d)** Controllability

Figure 4.11: Measures of performance as a function of the L_t/R_t ratio. The results present the maximal torque density that can be achieved for a given geometrical form.

density when only the fluid surface and the desired flux density are specified. The other dimensions can be calculated to provide the required field and to avoid the saturation of the ferromagnetic path.

In the case of a disc brake, when the radius R is defined, an optimal length L_t can be calculated to support the magnetic flux so that $L_t = c_{cat}(R^2 - r^2)/R + 2g + e$. The minimum external radius R_t to accommodate the coil and the flux over the coil is a function of R. For a

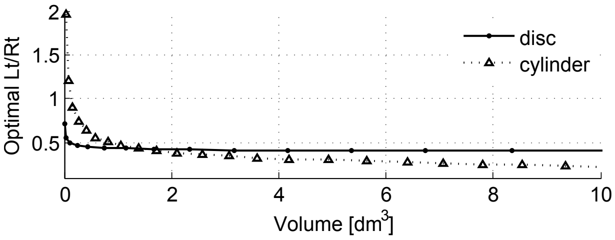

Figure 4.12: Optimal geometry form ratios that maximize the torque density for single disc and single cylinder brakes as a function of the external volume.

cylinder brake, the relation length/radius is $L_t = (R^2 - r^2)/2Rc_{cat} + h + 2q$. Therefore, for a given volume, there is an optimal L_t/R_t ratio that minimizes the volume and as a consequence maximises the torque density. For convenience, the ratio L_t/R_t is called "geometric form ratio".

These optimal geometric form ratios are presented in Fig. 4.12. In the volume range of 0.03dm^3 to 10dm^3, the optimal ratio for a disc brake varies from 0.40 to 0.72 and for a cylinder brake from to 0.21 to 1.96. This highlights that disc brakes present external flat forms while cylinder brakes can take more varied forms. The choice of brake design then depends on the available volume geometric form.

The measures of performance as a function of the optimal geometric form ratios are shown in Fig. 4.11. Since the length of a disc brake has no influence on the torque, for large L_t/R_t ratio, cylinder shaped brakes provide more torque density.

In order to improve the maximal torque, many elementary brakes can be combined in parallel. Section 4 investigates the performance of both brakes types in this case.

4 MULTIPLE-LAYERED BRAKES

We turn now our focus to the design of multiple cylinder and disc in parallel. This configuration improves the torque density of both brakes.

4.1 MULTIPLE-DISC BASED BRAKES

A schematic representation of a multiple disc brake is presented in Fig. 4.13. Consider m the number of fluid gaps. Note that a disc possesses two fluid gaps. When the thickness of the brake is augmented, a new repetition can be added since $L = gm + e(m-1)$.

The total reluctance is expressed as a sum of the reluctance $\mathscr{R}_d$ of a single disc k, as given by (4.7), as:

$$\mathscr{R}_{md} = \mathscr{R}_d \frac{m}{2} \tag{4.24}$$

The torque Γ_{md} of a muti-disc expressed as a function of the torque of a single disc Γ_{maxd}

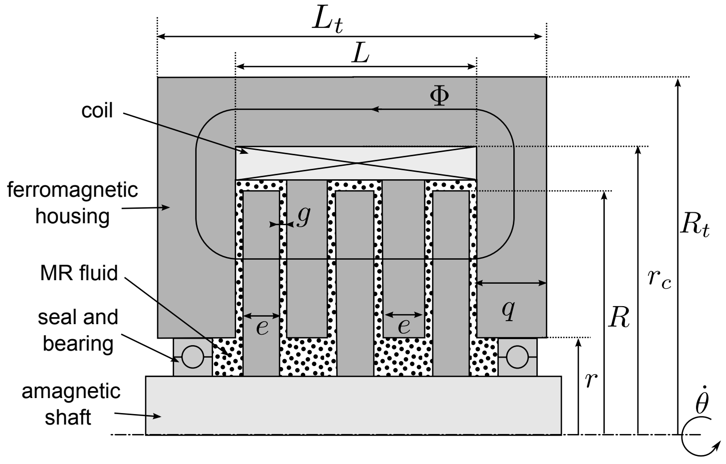

Figure 4.13: Multilayered disc-based brake comprising three elementary discs and six gaps ($m = 6$) in parallel. Each disc k possesses a inner radius r, a fluid gap radius R and a thickness e. A coil with a outer radius r_c generates the flux Φ. The total radius and length are denoted R_t and L_t.

and the number of fluid gaps is:

$$\Gamma_{md} = \Gamma_{maxd} \frac{m}{2} \tag{4.25}$$

The necessary power supply P_{md} to achieve this torque, if only the reluctance of the fluid is considered is:

$$P_{md} = P_{maxd} \frac{m}{2} \tag{4.26}$$

It can be concluded that the efficiency E_{md} of the brake is independent on the number of fluid gaps.

The viscous torque coefficient Γ_{vmd} is given by:

$$\Gamma_{vmd} = \Gamma_{vd} \frac{m}{2} \tag{4.27}$$

The controllability K_{md} is also constant and does not depend on the number of fluid gaps.

The volume of the brake is $V_{md} = \pi R_t^2 L_t$ where $L_t = c_{cat}(R^2 - r^2)/R + mg + e(m-1)$ and $R_t = \sqrt{c_{sat}(R^2 - r^2) + r_c^2}$. The torque density ρ_{md} then is:

$$\rho_{md} = \frac{2\alpha}{3\mu_{mr}} \frac{c_2(R^3 - r^3)}{[L + (R^2 - r^2)c_{sat} r_c^{-1}][(R^2 - r^2)c_{sat} + r_c^2]} m B_{sat} \tag{4.28}$$

with $c_2 = 2\alpha B_{sat}/3\mu_{mr}$ and $L = gm + e(m-1)$. The torque density is proportional to the number of fluid gaps. Finally, the reactivity as a function of the reactivity of a single disc is:

$$\delta t_{md} = \delta t_d \frac{m}{2} \tag{4.29}$$

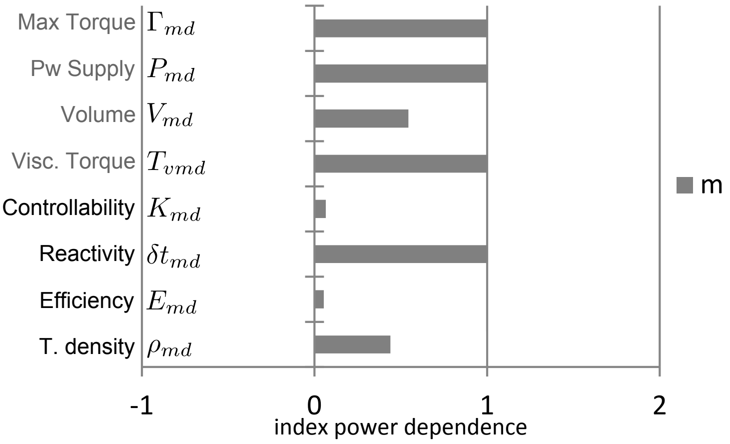

Figure 4.14: Multilayered disc brake performance as a function of the number of fluid gaps

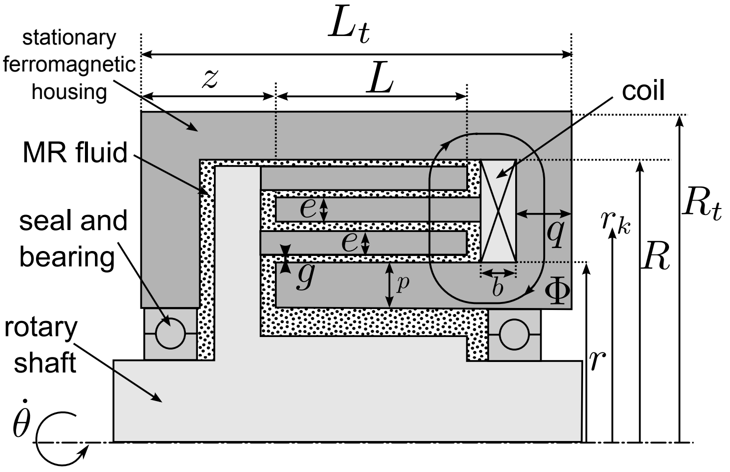

Figure 4.15: Multiple cylinder brake with m fluid gaps. The radius of the smallest and the largest fluid surfaces are r and R. The external length and radius are L_t and R_t. Each cylinder k separated by a gap g has a thickness e, radius r_k and a length L. The width of the coil and of the path on its right side are b and q respectively. The thickness of the path under the smallest fluid surface is p and z is the width of the lateral supports. The velocity of the shaft is $\dot{\theta}$.

The evolution of all measures of performance as a function of the number of fluid gaps is synthesized in Fig.4.14. The reactivity and the torque density increases with m. The efficiency and the controllability remain constant.

4.2 MULTIPLE-CYLINDER BASED BRAKE

Consider the multiple-cylinder brake presented in Fig. 5.1. The external radius of the fluid chamber R is proportional to the number of fluid gaps. The relation between the measures of performance and the number of gaps is non-linear.

The radius R of the largest fluid surface as function of number of fluid gaps m is $R =$

$r+gm+e(m-1)$ where r is the radius of the smallest one. The surface of each fluid gap k is $S_k = 2\pi L r_k^2$ where $r_k = r+(k-1)(e+g)$. Thus, the reluctance can be calculated as:

$$\mathscr{R}_{mc} = \frac{1}{2\pi\mu_{mr}L}\int_r^R \frac{dr}{r} = g\frac{ln\left(1+m\frac{e+g}{r}\right)}{2\pi\mu_{mr}L(g+e)} \tag{4.30}$$

For a given magnetic flux the smallest surface saturates before the others. Thus, the magnetic circuit is designed to provide the desired field B_{sat} over this surface. The controllable torque is the sum of the torque provided by each cylinder and can be expressed as a function of B_{sat} as :

$$\Gamma_{mc} = 2\pi r^2 L\frac{\alpha}{\mu_{mr}}\left[m+\frac{(m-1)(R-r)}{2r}\right]B_{sat} \tag{4.31}$$

Note that if $m=1 \therefore r=R$, therefore the torque collapses to the single cylinder. Replacing the reluctance in (4.9), the power is given by:

$$P_{mc} = \pi\frac{\nu\kappa}{\mu_{mr}}\frac{(r+R)rg}{e+g}ln\left(1+\frac{m(e+g)}{r}\right)B_{sat} \tag{4.32}$$

Increasing the number of fluid gaps requires more power supply. The coil width b then can be deduced from the coil volume so that $b = P_{mc}/\pi(R^2-r^2)\nu^2\kappa\chi$ or clearer: $b = gB_{sat}(R-r)ln[1+(e+g)r^{-1}]/\nu\mu_{mr}(e+g)(R^2-3r^2)$. The efficiency $E_{mc} = \Gamma_{mc}/P_{mc}$ yields:

$$E_{mc} = \frac{\alpha}{\nu\kappa}\frac{L(e+g)[2rm+b(m-1)]}{g(2r+R-r)ln\left[1+m(e+g)r^{-1}\right]} \tag{4.33}$$

This equation highlights that the efficiency increases as the number of fluid gaps. The viscous torque coefficient, as the sum of the torque for each cylinder is:

$$\Gamma_{vmc} = 2\pi\eta\frac{L}{g}\sum_{k=1}^{m}[r+(k-1)(e+g)]^3 \tag{4.34}$$

This expression can be approximated by:

$$\Gamma_{vmc} = 2\pi\frac{\eta L r^3}{g}\left[1+\frac{3}{2}\left(\frac{e+g}{r}\right)(m-1)\right]m \tag{4.35}$$

Subsequently, the controllability is obtained by:

$$K_{mc} = \frac{\alpha}{\mu\eta}\frac{g}{r}\left[\frac{2r+(m-1)(e+g)}{2r+3(m-1)(e+g)}\right]B_{sat} \tag{4.36}$$

The minimal external radius, taking into consideration the saturation of the path on the top of the coil, is $R_t = \sqrt{2rLc_{sat}+R^2}$. The width on the right side of the coil is $q = Lc_{sat}$. We assume that the lateral support z has the same width than the magnetic path so that $z=q$. The total length is $L_t = 2q+L+b$. The torque density yields:

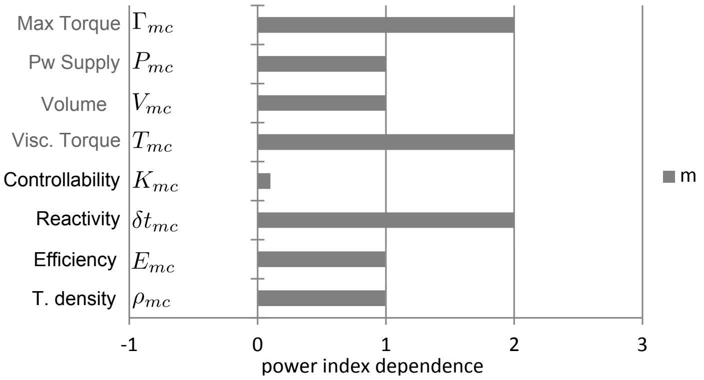

Figure 4.16: Measure of performance of a multiple cylinder layered brake as a function of the cylinders number.

$$\rho_{mc} = \frac{\alpha}{\mu_{mr}} \frac{rL[2rm+(m-1)(R-r)]}{(2rLc_{sat}+R^2)[L(2c_{sat}+1)+b]} B_{sat} \tag{4.37}$$

The analysis of this equation demonstrates that the torque density increases with the number of fluid gaps.

Finally, the electrical time constant is $\delta t_c = 2RLB_{sat}/\nu\kappa(2R+L)$. The reactivity is computed as follows:

$$\delta t_{mc} = \pi \frac{\alpha\nu\kappa}{\mu_{mr}} r(R-r)\left[m + \frac{(m-1)(R-r)}{2r}\right] \tag{4.38}$$

Since the reluctance increases with the number of gaps, the electrical time constant decreases and the reactivity is improved. Fig. 4.16 presents a synthesized representation of all performances criterion as a function of *m*. Increasing the number of fluid gaps for a cylindrical brake improves the efficiency, the reactivity as well as the torque density.

4.3 FINITE ELEMENT MODELLING

Both brakes have been evaluated using FEA. The characteristics of the coil, of the fluid and of the ferromagnetic material are the same that those employed in the previous section.

In the case of the disc brake, the inner radius is arbitrary fixed to R=50mm, and for the cylinder we attribute r=35mm. The maximal length of the fluid gaps then is $L = r/2c_{sat}$. In both cases, the width of a cylinder and of a disc are 1mm. The number of fluid gaps *m* varies from 2 to 20.

The relative error between the analytical model and the FEA is presented in Fig. 4.17. In the disc brake, the relative error can be assumed as constant a function of the number of gaps. The average is proportional to the volume of the brake as presented in the previous section. For the multiple cylinder, the power error is constant while in terms of torque, it decreases with *m*.

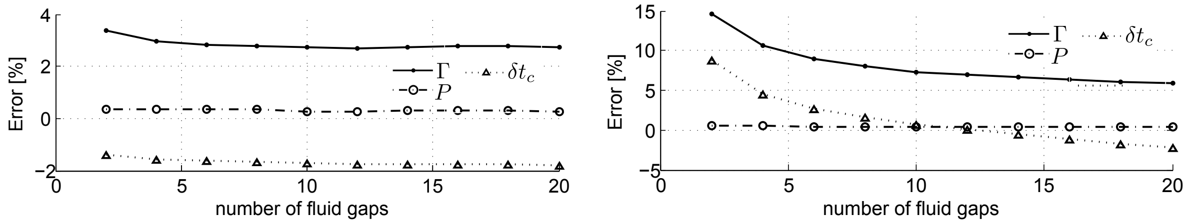

(a) Multiple disc brake

(b) Multiple cylinder brake

Figure 4.17: Relative error between the analytical model and the FEA for the mutiple disc (top) and the multiple cylinder brake (bottom) as a function of the number of fluid gaps. Where Γ, P and δt_c are the torque, the power and the electrical time constant respectively.

4.4 DISCUSSION

The model of the multiple layered brakes demonstrates that the association of many elementary cylinders or discs in parallel is an effective way to improve the global performance, in particular the torque density.

The addition of these repetitions gives to the model an additional parameter: In the case of a multi-disc brake, the radius, the fluid gap depth and the number m of fluid surfaces are the geometrical model inputs. All other dimensions can be calculated accordingly. The length of the brake is proportional to m. The torque density is therefore proportional to the radius and to the number of fluid gaps. The measures of performance are listed in Fig. 4.18.

In the case of a multiple cylinder the model input corresponds to the radius of the smallest fluid surface r, the fluid gap depth and the number of fluid gaps m. The length L of the fluid surface can be determined in order to optimize the torque density and depends on the radius so that $L < rc_{sat}$. The measures of performance are presented in Fig. 4.19.

With a maximal number of fluid gaps $m = 20$, the optimal L_t/R_t ratio for a given volume is presented in Fig. 4.20. When the number of fluid gaps is fixed, the evolution of the measure of performance is similar to a single fluid gap brake.

In next the section, the influence of the fluid characteristics is addressed.

5 INFLUENCE OF THE MR FLUID AND MATERIALS

Whether for the disc-type or cylinder-type, the influence of some intrinsic parameters of the fluid and of the housing materials are the same. Generally, performance is improved if the fluid possesses a high field-to-stress constant α and a low viscosity coefficient η. However, in the available commercial MR fluid, α and η depends on the ferromagnetic particle density. As a consequence the choice of a fluid establishes some compromises, in particular between the maximum torque and zero-field torque.

The power supply depends on the reluctance while the electrical time constant in inversely

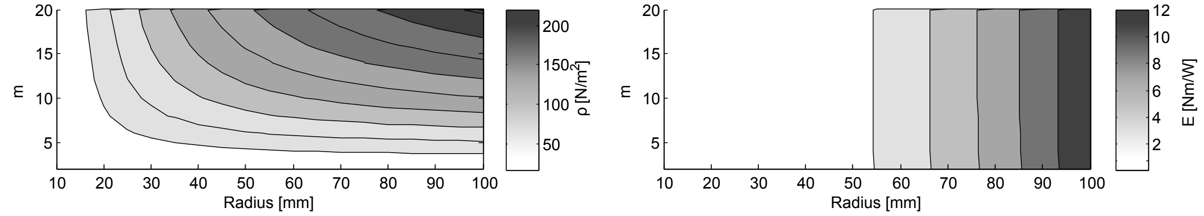

(a) Torque density **(b)** Efficiency

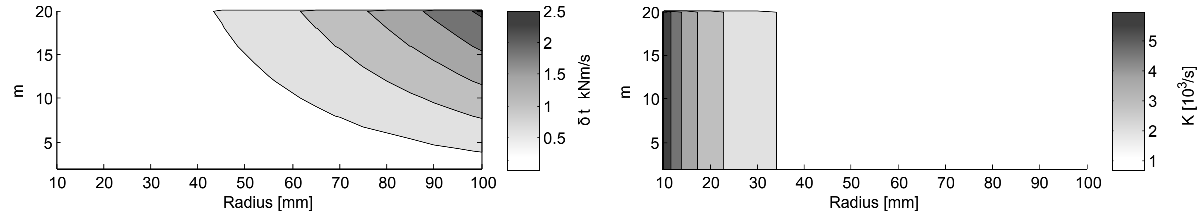

(c) Reactivity **(d)** Controllability

Figure 4.18: Multiple disc brake performance as a function of the number of fluid gaps *m* and the radius of the fluid gap *R*.The torque density ρ and the reactivity δt are proportional to the number of fluid gaps while the controllability *K* and the efficiency *E* are independent of *m*.

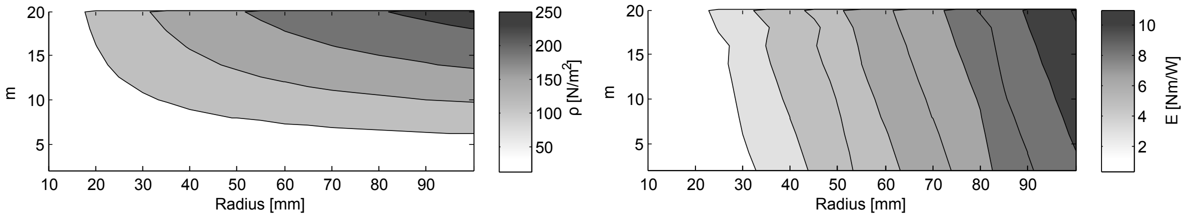

(a) Torque density **(b)** Efficiency

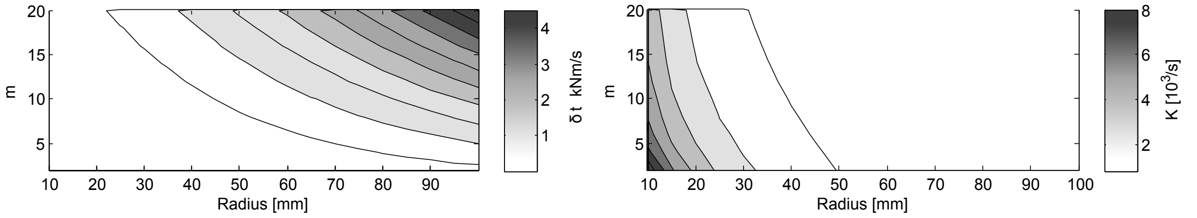

(c) Reactivity **(d)** Controllability

Figure 4.19: Multiple cylinder brake performance as a function of the number of fluid gaps *m* and the radius *R* of the smallest fluid surface. The torque density ρ, the efficiency *E* and the reactivity δt increases with the number of gaps *m* while the controllability *K* monotonically decreases.

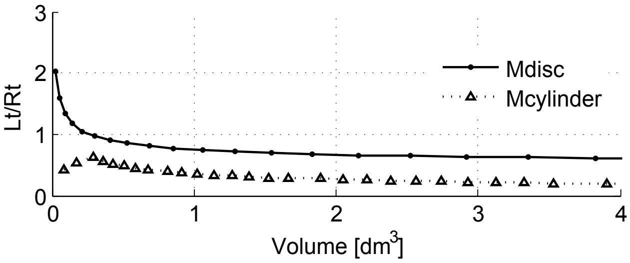

Figure 4.20: Obtained L_t/R_t ratio as a function of the volume for 20 fluid gaps.

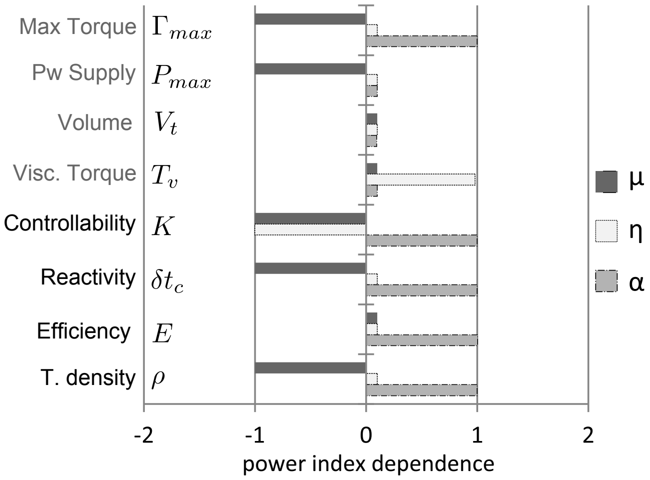

Figure 4.21: Influence of fluid intrinsic parameters in the performances.The magnetic permeability of the magnetic circuit, the viscosity coefficient and the field-to-yield stress constant are μ, η , and α respectively .

proportional to it. Therefore, the relative permeability μ_{mr} of the fluid has a dual effect: an increasing-permeability reduces the power supply but reduces also the reactivity of the brake. The permeability of the ferromagnetic path has the same influence on the performance. The material should possess a high permeability (or low reluctance) to guide and focus the magnetic flux into the MR fluid gap and minimize flux leakages. The power supply is proportional to the reluctance observed by the coil, thus high permeability reduces the volume of the coil and the total volume of the brake.

The influence the fluid properties and of the permeability of the ferromagnetic path on the measure of performance are presented in Fig. 4.21.

In the proposed model, the magnetic circuit is designed to provide B_{sat} over the fluid surface. This field can correspond to the saturation point of the fluid which bounds the linearity range of the brake. The torque density is strongly improved if B_{sat} is increased as presented in Fig. 4.22. The maximal admissible induction of the housing material B_{fer} affects only the volume of the brake, and as a consequence, the torque density. A high B_{fer} allows the minimization of the ferromagnetic path as well as the width of ferromagnetic cylinder or discs.

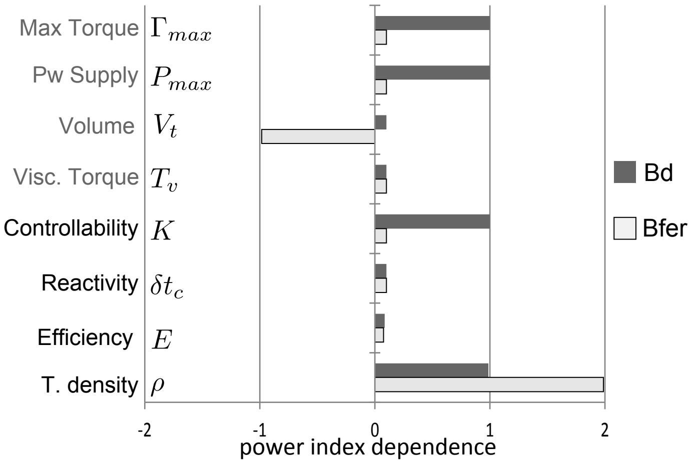

Figure 4.22: Influence of the maximal admissible inductions of the fluid B_{sat} and of the housing material B_{fer} on the brake performance.

6 CONCLUSION

The proposed magnetostatic model is specified to provide a required induction over the smallest active fluid surface. When its radius and the gap depth are defined, the power and the geometrical dimensions can be deduced. The model shows that all evaluation criteria are interdependent.

The length of a single disc brake has no considerable influence on its performance while increasing the radius improves the efficiency, the reactivity and the torque density. The results highlight that to improve the torque density, a disc brake is suitable for external dimensions ratio between 0.4 and 0.72.

By contrast, for a single cylindrical brake, both the length and the radius have an influence on performance. The torque density and the efficiency are proportional to them. Given a radius, the optimal length of the fluid gap can be determined to improve the torque density. The external dimensions are interdependent but the cylinder brake can assume more variate forms than the disc brake (0.21 to 1.96 for a volume inferior to 10dm^3).

In an optimal configuration, the results demonstrate that as a function of the volume, both brakes exhibit an equivalent torque density. Cylindrical brakes however are more reactive but consume more energy than disc brakes. For high L_t/R_t ratios, drum brakes have higher torque density.

FEA has been used to strengthen the models. The error between the model and the FEA is proportional to the volume. For an uncommon volume of 10dm^3 the torque difference attains 23% and 9% for a disc and a cylinder brake respectively. These difference is due to the fact that in the analytic model the reluctance of the ferromagnetic path is considered as infinite.

For multiple-layered brakes, the maximal torque, the torque density and the reactivity rise with the number of fluid gaps. The controllability and the efficiency remain constant. The performance depends also on the brake radius, which should be specified and follows the same dependence as presented for single brakes.

The fluid gap depth has an important role on performance. Large gaps requires high power supply and large coil volume. The viscous torque however is reduced. The fluid gap depth represents the compromise between controllability and efficiency.

The choice of a brake type remains dependent on the application and on the compromises between the different measures of performance.

The results highlights that a multiple cylinder configuration has the highest torque density for small number of fluid gaps. For the development of the hybrid device, the passive actuator will be based on a multiple cylinder configuration.

5

INTEGRAL DESIGN OF THE HYBRID ACTUATOR

Contents

At the time of the writing , the first part of this chapter was submitted to Smart Materials and Structures Journal under the title: C. Rossa, J. Lozada, and A. Micaelli "Development of a wide ranged torque magnetorheological brake".

PERFORMANCE of force feedback devices are directly dependent on the treadoffs observed in the design of the actuator. These tradeoffs have been identified in the modelling of the passive actuator performed in the previous chapter. The complete model of a multiple cylinder magnetorheological brake is employed in this chapter to develop the brakes in view of forming the hybrid actuator. An algorithm is used to optimize the dimension of the brake with respect to a minimal torque and maximal volume. Subsequently, two identical brakes associated to overrunning clutches are connected to a DC motor to constitute the complete hybrid actuator. The control laws proposed in **Chapter** 3 are subsequently implemented to the system.

1 INTRODUCTION

An actuator suitable for human-machine interaction can be evaluated with regard to torque density, controllability and reactivity. Torque density is the ratio torque-to-volume and characterizes the optimization of the brake volume, the controllability is the maximum torque to minimum torque ratio which quantifies the ability of the actuator to vary from low to high output impedance, and the reactivity is the torque-to-time constant ratio measured for a step-type excitation.

In order to maximize the torque provided by the magnetorheological brake, the association of many elementary discs or cylinders in parallel is an efficient way for achieving high levels of torque. While in a multiple disc brake the relation between the number of discs and the torque is linear, the torque displayed by a multiple cylinder increases with the square of the radius of each cylinder. A multiple cylinder configuration is chosen as passive actuator for the hybrid system.

This chapter is organized in two parts. The first part presents the development of the MR brake from analytical modelling to prototyping and characterisation. The magnetostatic model is applied to a multiple cylinder brake and optimized using finite element analysis. The optimized brake has been built and characterized. The final dimensions are 60mm diameter, 39mm width with a hollow shaft of 12mm diameter. The torque varies from 0.03Nm to 5.3Nm and the brake consumes 20W. This gives a torque density of 48kN/m^2, a controllability of 176.6 and a reactivity ratio of 176.6 Nm/s. This results make the actuator amply adaptable for high transparency human-machine interfaces design.

The second part deals with the integration of the brakes with a DC motor to form the hybrid actuator and the implementation of stable control laws. The complete system, comprising two brakes and the motor, has a torque density 7.9 times higher than when using the motor only. Quantitative results demonstrate that the proposed device exhibits less parasitic torques and inertia than a torque equivalent motor associated to an ideal transmission. However the active torque that can be provided by the hybrid actuator is 27.5 times inferior to its passive torque.

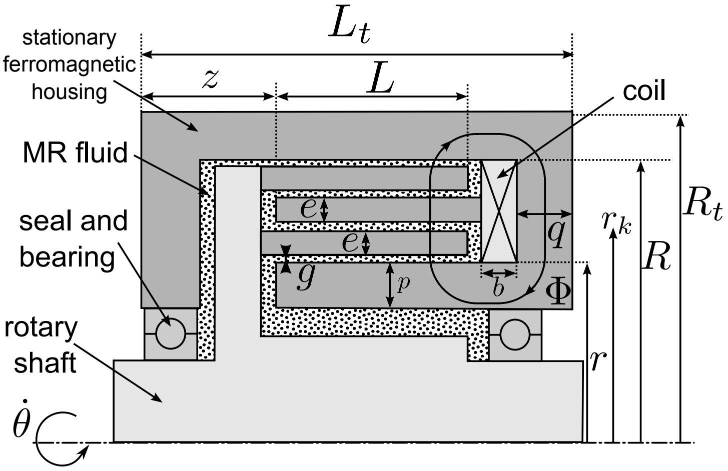

Figure 5.1: Multilayered cylindrical brake with 4 active fluid gaps: The external length and radius are L_t and R_t. Each cylinder separated by a gap g has a thickness e and an radius r_k. The radius of the smallest fluid gap is called r and the radius of the largest one is $r_4 = R$. L is the gap length, b the height of the coil and q the width of the ferromagnetic path on the right side of the coil, in-where the magnetic flux Φ loops. The width of the ferromagnetic section under the gaps is denoted p and of the lateral supports width is z. The shaft rotates according to a velocity $\dot{\theta}$.

2 SINGLE BRAKE DESIGN

The analytical model of a multiple cylinder brake is implemented in an optimization algorithm and solved with respect to some geometric constrains.

2.1 MAGNETOSTATIC MODEL SUMMARY

The following formulations are a reminder of the magnetostatic model developed in the previous chapter.

The brake shown in Fig. 5.1 is composed of m fluid gaps. The total radius and length are R_t and L_t respectively. We denote g the fluid gap depth, e the thickness of each cylinder, r_k the inner radius of the fluid gap k, so that $1 \leq k \leq m$ with $k \in \mathbb{N}^*$, with $r_m = R$ and $r_1 = r$ the inner radius of the largest and of the smallest fluid surface respectively, b the coil width, q the width of the ferromagnetic path on the right side of the coil, and p the ferromagnetic path width below the gaps.

The controllable braking torque Γ as a function of the desired induction B_{sat} of the smallest fluid gap is:

$$\Gamma = 2\pi r^2 L \frac{\alpha}{\mu_{mr}} \left[m + \frac{(m-1)(R-r)}{2r} \right] B_{sat} \tag{5.1}$$

where α is the yield stress to magnetic field constant of the fluid and μ_{mr} is its absolute permeability. The viscous torque is:

$$\Gamma_v(t) = 2\pi\frac{\eta L r^3}{g}m\left[1+\frac{3}{2}\left(\frac{e+g}{r}\right)(m-1)\right]\dot{\theta}(t) \tag{5.2}$$

With $\dot{\theta}$ and and η the rotational velocity and the fluid viscosity coefficient respectively. The necessary power to obtain B_{sat} is:

$$P = \pi\frac{\nu\kappa}{\mu_{mr}}g\frac{r_b r}{e+g}ln\left[1+\frac{m(e+g)}{r}\right]B_{sat} \tag{5.3}$$

The power is expressed as a function of the resistivity of the coil wire κ, the mean radius of the coil r_b and the current-to-surface ratio of the coil wire ν. The coil has a time constant δt_c expressed as:

$$\delta t_c = 2\frac{rL}{\kappa\nu(R+r)}B_{sat} \tag{5.4}$$

The total volume of the brake considering all the ferromagnetic path is:

$$V = \pi\left[2rLc_{sat}+R^2\right]\left[z+b+L(1+c_{sat})\right] \tag{5.5}$$

with z the width of the lateral supports, $c_{sat} = B_{sat}/B_{fer}$ the induction ratio considering the maximal admissible induction B_{fer} of the ferromagnetic path, and b the coil width given by:

$$b = \frac{g(R-r)}{\mu_{mr}\nu\chi(e+g)(R^2-3r^2)}ln\left[1+\frac{m(e+g)}{r}\right]B_{sat} \tag{5.6}$$

where χ is the coil fill rate. From these equations are defined the cost functions further used in the optimization of the brake.

2.1.1 EVALUATION CRITERIA

The cost functions for the optimization of the brake focus on the maximization of:

1. Torque density, in terms of N/m^2 given by $\rho = \Gamma/V$ as:

$$\rho = \frac{\alpha}{\mu_{mr}}\frac{rL[2rm+(m-1)(R-r)]}{(2rLc_{sat}+R^2)[L(c_{sat}+1)+b+z]}B_{sat} \tag{5.7}$$

2. Controllability defined as $K = \Gamma/\Gamma_v(t)\dot{\theta}(t)$ [1]:

$$K = \frac{\alpha}{\mu\eta}\frac{g}{r}\left[\frac{2r+(m-1)(e+g)}{2r+3(m-1)(e+g)}\right]B_{sat} \tag{5.8}$$

3. Reactivity, in terms of Nm/s given by $\delta t = \Gamma/\delta t_c$:

$$\delta t = \pi\frac{\alpha\nu\kappa}{\mu_{mr}}r(R-r)\left[m+\frac{(m-1)(R-r)}{2r}\right] \tag{5.9}$$

---

[1] In this Chapter the presented values for the controllability are given for $\dot{\theta}(t) = 1$ rad/s. We also added the Couloumb friction to the obtained viscous torque. Thus, the controllability is here a dimensionless quantity.

Table 5.1: Analytic model constant parameters

term	value	unit	parameter
B_{sat}	0.7	T	desired induction on the smallest fluid gap
B_{fer}	1.5	T	maximal admissible induction of the path
μ_{mr}	$16\pi 10^{-7}$	H/m	fluid absolute permeability
μ_{fer}	10^{6}	H/m	ferromagnetic path absolute permeability
α	0.22	Pa.m/A	fluid magnetic field to yield stress constant
η	61.10^{-3}	Pa.s	fluid viscosity coefficient
ν	5.10^{6}	A/m^2	coil wire current to section ratio
κ	17.10^{-9}	Ω/m	coil wire linear resistivity
χ	70%	-	coil fill rate

The efficiency of the brake will not be considered as a direct cost function since power consumption is not a particular constraint for the hybrid actuator. The power consumption of the brake is considerably inferior to a torque equivalent commercial DC motor.

2.2 OPTIMIZATION IMPLEMENTATION

The magnetostatic model has been implemented with Matlab and a finite element analysis (FEA) using FEMM software [2] is used to strengthen the analytical approach.

The employed fluid is the MRF122EG from Lord Corporation [Corporation,]. The ferromagnetic path is made of pure iron (Telar 57).

Table 5.1 lists the parameters of the fluid, the ferromagnetic path and the coil adopted in the simulations. In the analytical model the absolute permeability of the fluid μ_{mr} and the field-to-yield stress constant α are assumed as constant. The permeability of the ferromagnetic path μ_{fer} is considered as infinite. The same parameters are used in the FEA except the B-H curves (magnetic flux density *versus* induced field) of the fluid and of the ferromagnetic material which are acquired from the datasheets of each material. In the same way, by contrast to the analytical model, in the FEA the fluid yield stress $\tau_y(H)$ is obtained as a non-linear function of the magnetic field.

The design specifications, the geometrical constraints and the optimisation variables used in the optimization algorithm are listed in the following sections.

2.2.1 DESIGN REQUIREMENTS

The minimal required controllable braking torque is $\hat{\Gamma}$=3.2Nm. This corresponds to the maximal average torque exertion of the human hand using a circular shaped handle with a diameter comprised between 30mm and 35mm [Kong et Lowe, 2005][Shih et Wang, 1996].

In order to place the overrunning clutches into the inner core, a hollow shaft of 6mm radius must be predicted. The external radius R_t is arbitrary limited to 30mm. Due to manufacturing

---

[2] Finite Element Method Magnetics: www.femm.info

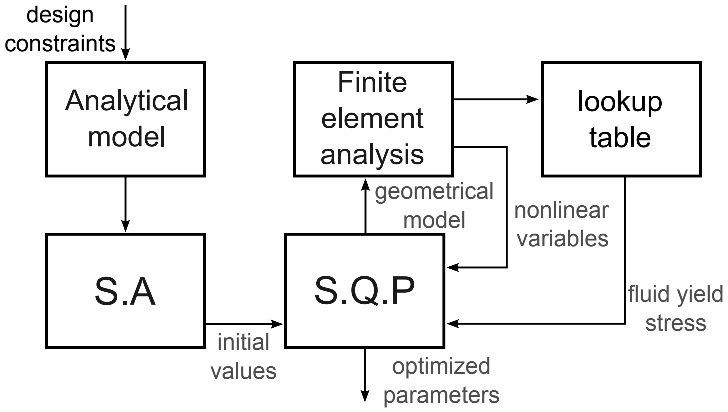

Figure 5.2: Representation of the optimization algorithm. The geometrical constrains are implemented in the analytic model. An initial solution is found using the simulated annealing (SA) algorithm. The SA minimizes the function $(\Gamma - \hat{\Gamma})/\hat{\Gamma}$ in order to guarantee a required torque $\hat{\Gamma}$. The initial solution provided by the SA is sent to the sequential quadratic programming (SQP) algorithm which generates a finite element analysis to calculate nonlinear behaviours. The materials characteristics are taken in account using a lookup table. The SQP maximizes the torque density.

limitations, the thickness of each cylinder is fixed to e =1mm. The time constant should not exceed 2.5ms. The emplacement of commercial bearings and seal imposes:

$$r - q \geq 13mm \tag{5.10}$$

2.2.2 FERROMAGNETIC PATH DESIGN

In order to avoid saturation of the ferromagnetic path, the following geometric constraints must be respected. To avoid saturation at the top of the coil:

$$R_t \geq \sqrt{2rLc_{sat} + R^2} \tag{5.11}$$

On the adjacent section of the coil the minimal width is:

$$q \geq c_{sat}L \tag{5.12}$$

Finally, the ferromagnetic path at the bottom of the gaps necessitates:

$$p \geq r - \sqrt{r^2 - 2Lc_{sat}} \tag{5.13}$$

2.2.3 OPTIMISATION VARIABLES

The following parameters are the model variables: the number of fluid gaps m, the inner radius r of the smallest fluid gap, the fluid gap depth g, the length L of each fluid gap, and the means radius of the coil r_b.

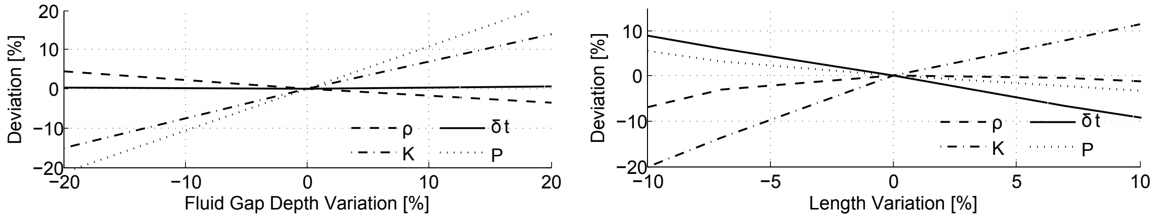

(a) Influece of the fluid gap depth **(b)** Influece of the fluid gap length

Figure 5.3: Influence of the fluid gap depth g and of the fluid gap length L on the evaluation criteria. A compromise between ρ and K can be observed. If the fluid gap is increased from 0.5mm to 0.6mm (+20%), K increases by 14%. In the second figure, for $L = 7$mm, ρ reaches its maximum value. For a length variation superior to +7%, the ferromagnetic path on the right side of the coil is saturated. For variation inferior to -11%, a 6mm radius hollow shaft can not be built.

2.2.4 DESIGN TRADEOFFS

Two critical parameters for optimising the brake are the fluid gap depth g and the number of fluid gaps m. The reactivity and the torque density are maximized when m tends to infinite. However, in order to maximize the controllability, m tends to zero. In the same way, the functions ρ, K, and δt do not meet an optimal value as a function of g as shown in Fig. 5.3a. Maximising the torque density necessitates minimization of the fluid gap depth, while maximising the controllability implies a large fluid gap. Consequently, g determines the compromise controllability *versus* power supply and controllability *versus* torque density. Hence, g is set at 0.5mm and optimisation will focus on the maximization of the torque density. Increasing the length improves the torque but also the necessary power supply and the dimensions of the magnetic path. An optimal fluid gap length that maximizes the torque density can be found as presented in Fig. 5.3b. A small change on these dimensions affects strongly the performance. The parameters used in this simulation of Fig. 5.3 are those obtained in the following section.

2.3 OPTIMIZATION ALGORITHM AND RESULTS

The optimization algorithm represented in Fig. 5.2 comprises two successive steps. In the first step, a solution with respect to the geometric specifications and torque objective is obtained using a "simulated annealing algorithm" (SA). It consists of a random search algorithm which statistically guarantees the convergence of the model to the required torque $\hat{\Gamma}$ after a finite number of iterations. The SA minimizes the following function:

$$f(\Gamma) = \frac{|\Gamma - \hat{\Gamma}|}{\hat{\Gamma}} \tag{5.14}$$

The results provided by the SA are used in the "sequential quadratic programming" (SQP)

Table 5.2: Optimized brake dimensions

term	value	unit	parameter
m	4	-	number of fluid gaps
r	22.5	mm	smallest fluid gap radius
r_2	24	mm	second fluid gap radius
r_3	25.5	mm	third fluid gap radius
r_4	27	mm	fourth fluid gap radius
L	7	mm	fluid gap length
g	0.5	mm	fluid gap depth
r_b	23.5	mm	coil mean radius
R_t	30	mm	outer radius

algorithm which searches for an optimal solution that maximises the torque density. The solution provided by the SA ensures that the SQP does not converge to a local minimum.

In order to maximize the torque density for a given number of fluid gaps, the SQP minimizes the function $g(\rho)$:

$$g(\rho) = \frac{1}{\rho} \tag{5.15}$$

The SQP communicates with the FEA software in order to take into account the magnetic saturation and non-linearities. The magnetic field is monitored for 10 levels of current strength varying from 0A to 1A. As a results were obtained four fluid gaps. The dimensions of the optimized brake are listed in Table 5.2.

The design of the brake is shown in Fig. 5.4. The final external dimensions are 39mm width, 30mm radius with 6mm hollow shaft radius. The rotary hollow shaft (1) is connected to the stationary ferromagnetic inner core (2) where the coil is built using two bearings (3). A bearing cap (4) constraints their motion along the axis. Around the shaft (1) is placed a thin rotary disc (5) which supports the rotary cylinders (7) of the fluid chamber. The rotary parts are (1) and (5). All but (2)(6)(7) and (8) are non magnetic parts. By this means the magnetic flux is guided into the fluid gaps minimizing flux leakages.

The brake is designed to work with a maximum required magnetic flux density $B_{sat} = 0.7$T over the smallest fluid surface S_1. Figure 5.5 shows the evolution of the mean induction over S_1 as a function of the current. According to the analytical model, the desired induction is reached for a magnetomotive force of Ni_{max} =232 A.turn. It is achieved with N=475 turns of 0.25mm diameter wire and a current of i_{max}=0.49A. Beyond this point, the fluid is expected to saturate. Therefore, this is the limit of validity of the analytical model. Using the FEA model, the desisted induction is reached at Ni_{max}=247A.turn or rather 475 turns of wire and 0.52A. This represents an error of +6% compared to the analytical model (or 6% less torque for Ni_{max} =232).

Fig. 5.6 presents the simulation results using the FEA. The magnetic flux density B across the ferromagnetic circuit for Ni_{max}=247A.turn is show in Fig. 5.6a. The fluid and the ferro-

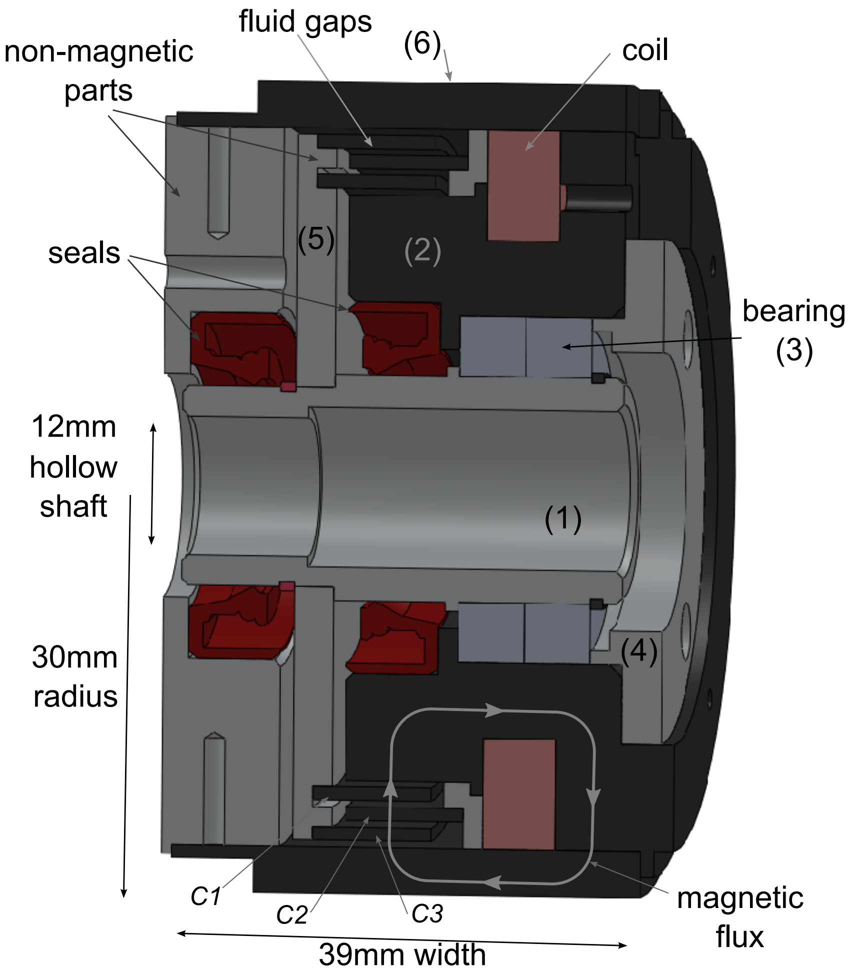

(a) Cross-view of the MRF-brake

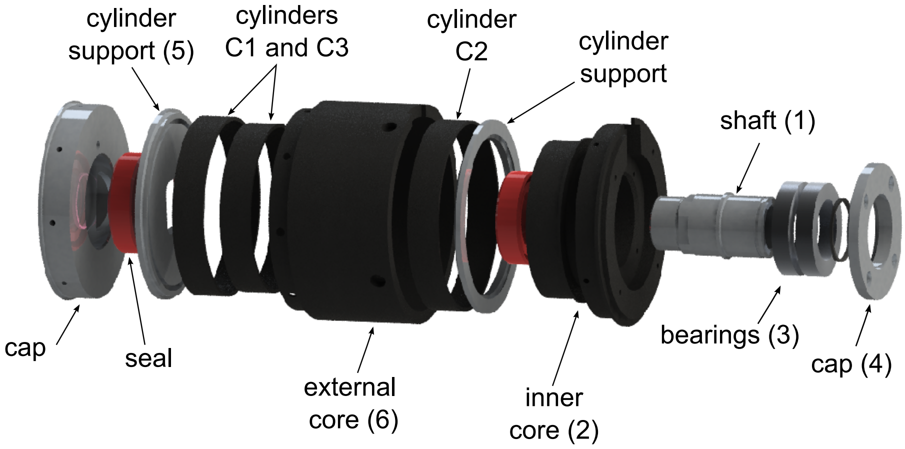

(b) Exploded view of the MRF-brake

Figure 5.4: CAD view of the MRF-brake. Attached to the hollow rotary shaft (1) a thin non-magnetic disc (5) supports two ferromagnetic cylinders which compose the fluid chamber. The shaft is connected the inner core by the bearings (3). The coil is built in the inner core (2) and thanks to the external housing (6) the magnetic flux is guided across the fluid gaps. A non-magnetic lateral support (4) blocks the translation of the axis and bearings. The brake has 30mm radius with a 6mm radius hollow shaft and 39mm length. The expected torque in the linear range is 3.4Nm.

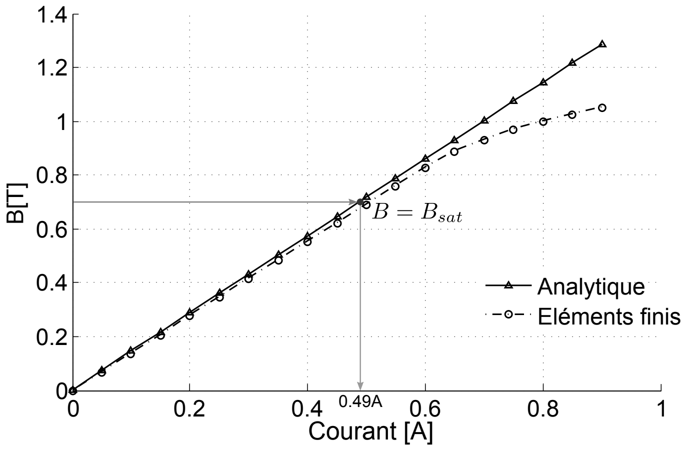

Figure 5.5: Magnetic flux density over the smallest fluid surface as a function of the current. In the analytical model, the surface reaches the desired induction of 0.7T at 0.49A and using FEA at 0.52A.

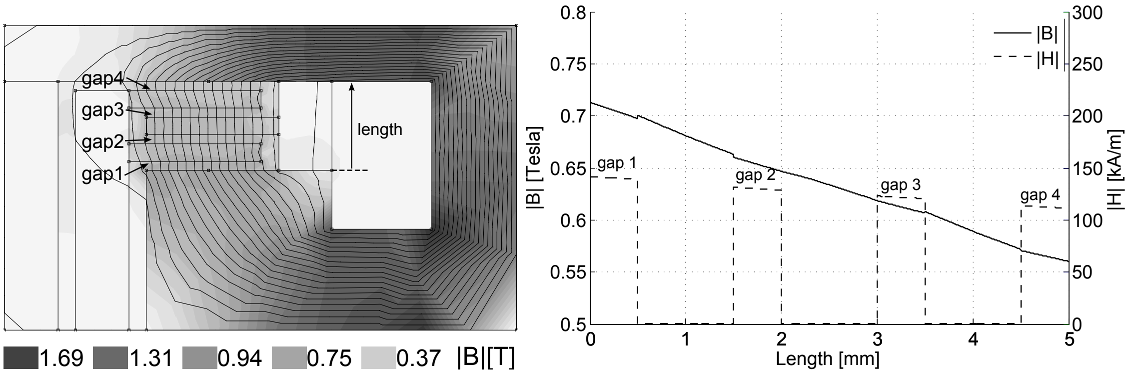

(a) Finite element simulation **(b)** Magnetic field and flux density

Figure 5.6: Simulation results using finite element analysis. In (a) the magnetic flux density in the ferromagnetic path. The ferromagnetic path and the fluid reach their saturation at the same magnetic flux. The evolution of the induction across the fluid gaps is shown in (b). The fluid is exploited up to the desired induction of 0.7T at 0.52A.

magnetic path reach the inductions B_{sat} and B_{fer} respectively at the same magnetomotive force. Fig 5.6b presents the induction and the field over each fluid surface. The expected torque using the FEA combined to the Bingham model is 3.2Nm, which corresponds to the reference torque used in the optimization. Using the analytical model, the estimated torque is 3.4Nm. According to the FEA, the largest surface reaches its saturation at 0.92A.

Considering the obtained parameters, the brake has been built and characterized using aluminium for the non-magnetic parts and pure iron (Telar 57) for the magnetic path. The brake is presented in Fig. 5.7. The sealing of the fluid is ensured using low-friction radial shaft seals without spring compressors. The experimental results are presented in the next section.

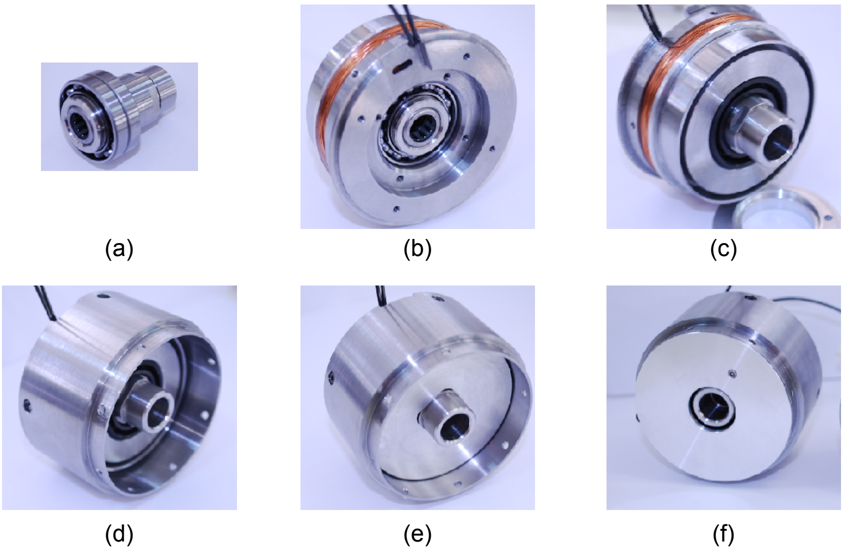

Figure 5.7: Assembly sequence of the MR brake. On the hollow shaft are mounted two identical bearings (a). The assembly is placed in the inner core which contains the coil (b). A radial shaft seal is situated in the inner core and two fluid gaps are formed by the addition of a thin cylinder (c). The inner core is placed in the external ferromagnetic housing (d). Two other concentric cylinder are placed on the inner core (e) before bringing the fluid, finally a non-magnetic sealing cap which contains a second radial seal closes the fluid chamber (f).

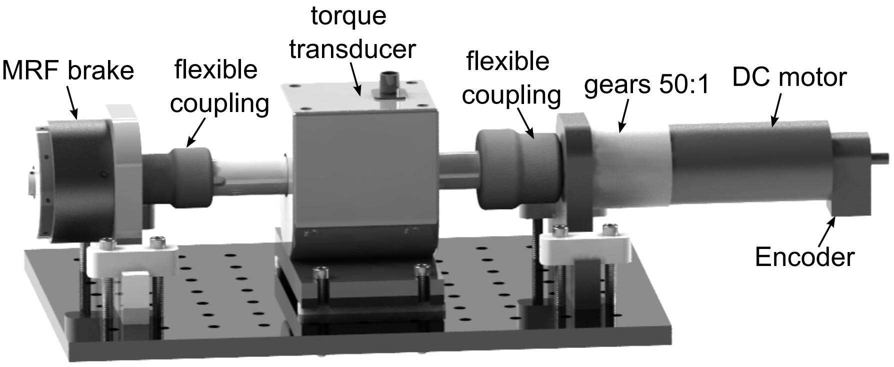

Figure 5.8: Experimental test bench. The brake is connected to an excitation motor Maxon RE-40 through a torque transducer Sensors Development 01324. The motor is connected to a reduction stage with a reduction ratio of 50:1 and can apply a torque of 6Nm. The position is measured using an incremental encoder with 500 ppr.

3 SINGLE BRAKE CHARACTERISATION

3.1 MECHANICAL CHARACTERISTICS

The test bench of Fig. 5.8 is used to characterise the brake. A Maxon motor RE-40 linked to a reduction stage of 50:1 that can apply up to 6Nm is used to generate a velocity. The gearmotor is connected to the brake through a torque transducer Sensor Development (model 01324). Fig. 5.9 shows the measured viscous torque of the test bench and the torque generated

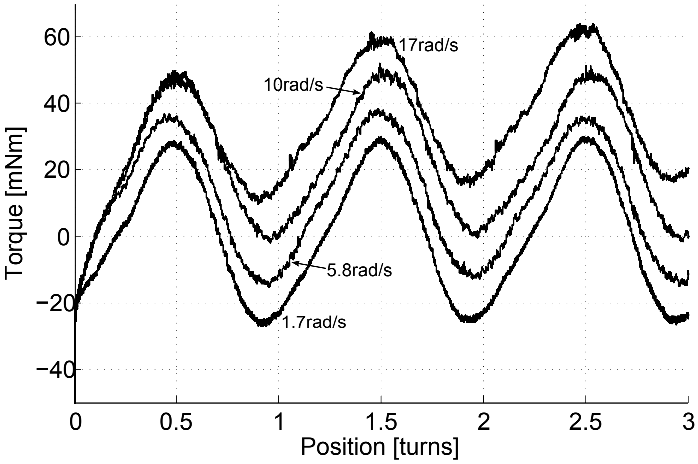

Figure 5.9: Influence of the flexible coupling on the measured torque. The figure present the measured torque when the actuator is off for different excitation velocity. The result comprises the viscous torque of the torque transducer. The torque asymmetry is due to the flexible coupling.

by the flexible coupling. The position of the shaft is measured using an incremental encoder with 500 pulses per revolution. The brake and the motor are controlled by a discrete controller (Silabs 8051F120) with a sampling frequency of 16kHz and a linear power amplifier. The braking torque, the current and the position of the shaft are recorded at 2.5kHz.

Fig. 5.10 presents the measured and estimated braking torques. The motor is activated by the controller and an excitation current is sent to the brake. The current calculated by the controller has a triangular form 0A-920mA-0A according to slope of 1mA/10ms. The measured torque at the desired induction of the fluid according to the analytical and finite element models at 0.49A and 0.52A are 3.6Nm and 3.8Nm respectively. When the largest surface reaches B_{sat} (at 0.92A) the measured torque is 5.3Nm. The torque at zero current is 30mNm.

As predicted by the rheological model of the fluid behaviour, the viscosity of the fluid generates an uncontrollable torque. In Fig. 5.11, the influence of the velocity on the braking torque is presented. The brake is activated with constant currents ranging from 0A to 0.9A with 0.15A steps. The motor velocity is then gradually increased. At low velocity, the influence of the viscous torque is negligible compared to the controllable torque.

3.2 ELECTROMAGNETIC RESPONSE

The measured resistance of the coil is 24Ω. At the maximal current of 0.92A, the power consumption is 20.31W with corresponds to an efficiency of 0.26Nm/W. The torque to power consumption efficiency is presented in Fig. 5.12.

The electric response of the coil is presented by its bode diagram in Fig. 5.13. The bode diagram is obtained using an excitation sinusoidal voltage of 12V with a sweep frequency

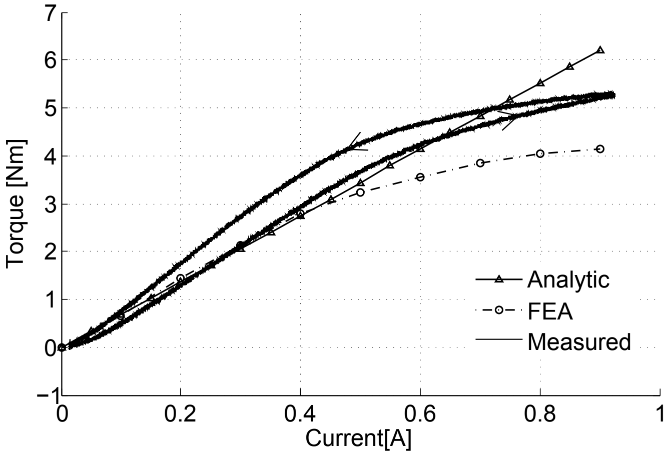

Figure 5.10: Measured braking torque with its hysteresis loop. The expected torque and the measured torque when the fluid reaches the desired induction are 3.4Nm and 3.6Nm respectively according to the analytical model. Using the FEA, the expected torque is 3.2Nm and the measured torque is 3.8Nm. The experimental results overreach theory by +5.5% and +15.7% compared to the analytical and to the FEA models respectively. When the largest fluid surface reaches B_{sat}, the torque is 5.3Nm.

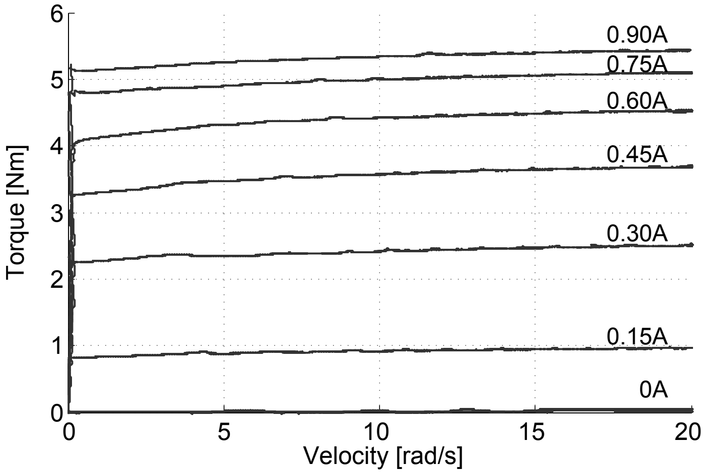

Figure 5.11: Influence of the velocity on the braking torque. The brake is activated according to different current strengths varying from 0A to 0.9A. For each current, the velocity of the motor is gradually increased using the controller.

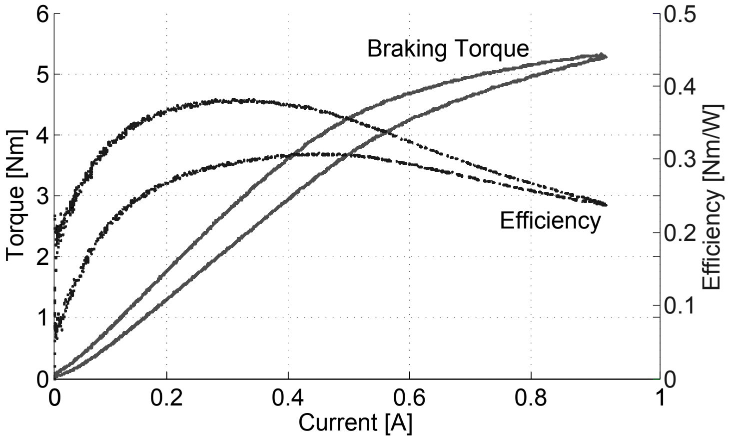

Figure 5.12: Torque efficiency of the brake. The power is calculated by Joule's losses considering an electric coil resistance of 24Ω. The maximal power consumption is 20W.

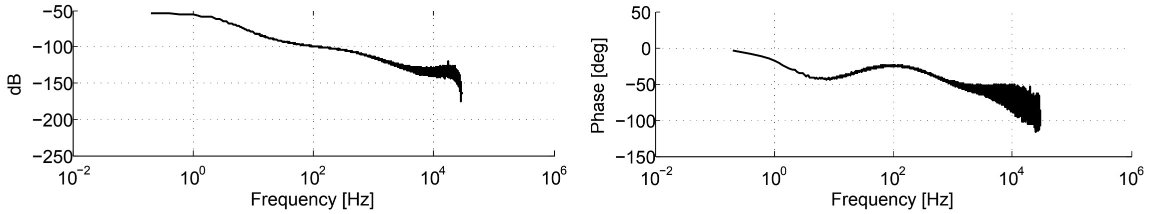

(a) Voltage to current gain

(b) Voltage to current phase

Figure 5.13: Electrical frequency response of the brake. A 10s sinusoidal sweep frequency of a 12V varing from 0.1Hz to 30kHz is sent to the brake and the current is measured by a shunt resistance of 1Ω. The observed cut frequency is 18Hz.

form 0.1Hz to 30kHz and by measuring the induced current with a shunt resistance of 1Ω. The observed cut frequency at $\pi/4$rad out of phase is 18Hz.

3.3 ELECTROMECHANICAL RESPONSE

The observed electromagnetic bandwidth of the brake is given by an step time excitation voltage. In Fig. 5.14a the mechanical response for a 5V excitation voltage with a frequency of 1Hz in open-loop is presented. The observed electromechanical response time is 200ms. This result comprises the response time of the fluid and the measuring scheme. In order to improve the reactivity of the brake, a custom designed proportional-integral PI controller is used to directly control the current.

The electromechanical response for a 0.2mA square ware form of 1Hz is shown in Fig. 5.14b. The observed response time decreases to 30ms.

To determine the maximal observed stiffness K_b deliverable by the brake, consider ppr the number of pulses-per-revolution of the position encoder. The minimal detectable position variation is $\theta_m = 2\pi/4ppr$ radians and the position variation during the leading edge pulsing

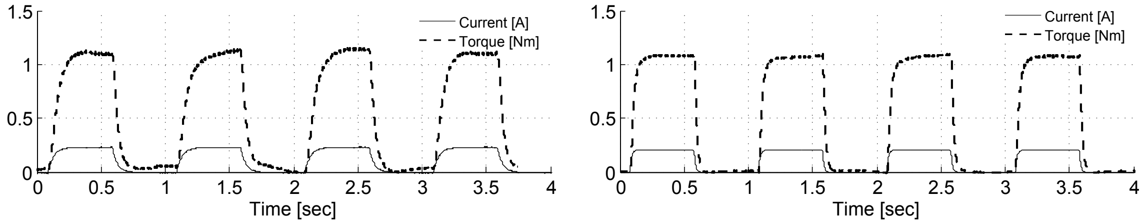

(a) Respose to a step-type voltage excitation

(b) Respose to a step-type current excitation with PI controller

Figure 5.14: Influence of the PI controller on the torque response. In (a) the brake response for 1Hz a step-type voltage excitation using a linear amplifier. In (b) the response for a step-type current excitation with a PI controller. The response time for a voltage step is 200ms and for a current step using the PI controller is 30ms.

time of the brake is $\delta t \dot{\theta}(t)$, where δt is the response time of the brake in closed-loop (30ms). The maximal observed stiffness is:

$$K_b = \begin{cases} \frac{\Gamma}{\delta t \dot{\theta}} & if \quad \dot{\theta}(t) > \frac{\theta_m}{\delta t} \\ \frac{\Gamma}{\theta_m} & otherwise \end{cases} \tag{5.16}$$

Using an incremental encoder with ppr=500, the maximal displayable stiffness is 1687 Nm/rad for interaction velocities inferior to 0.1 rad/s.

3.4 EXPERIMENTAL RESULTS ANALYSIS

The torque calculated by the analytical model when the smallest fluid surface reaches the desired induction, corresponding to 0.49A, is 3.4Nm. For the same current, the measured torque is 3.6Nm. This result overreaches the theory by +5.5%. After this point, the fluid is supposed to saturate and the analytical model is not valid. According to the FEA, the smallest fluid surface reaches B_{sat} at 0.52A and the expected torque is 3.2Nm, which corresponds to the desired torque in the optimization algorithm. The measured torque at this current is 3.8Nm. It represents a deviation of +15% compared to the FEA.

The deviation can be attributed to three main phenomena:

1. It has been shown in Fig. 5.3 that the fluid gap depth has a strong influence on the power supply. A variation of 10% of the gap depth implies a change of 11% in the power. Therefore, a small variation of the fluid gap strongly alters the necessary magnetomotive force Ni_{max} to achieve the desired induction B_{sat}. Due to the dimensional tolerance of the cylinders as well as assembly imprecisions, the reluctance may be lower than expected. For example, an imprecision in the positioning of the cylinders, that increases the fluid gap length of 2% (0.1mm), leads a decrease of 1.27% on the total reluctance which results in 1.42% more torque.

2. The analytical model assumes a homogeneous magnetic field over a fluid gap. However, the FEA results presented in Fig. 5.6b highlight that the magnetic flux density is not constant and is stronger in the vicinity of the coil as compared to elsewhere. As a consequence, the fluid reacts with different yield stress in different locations within the same fluid gap which contributes to the observed deviation.

3. At 0.92A, the largest fluid surface reaches B_{sat}. The torque calculated by the FEA is then 4.14Nm. Compared to the measured torque, a deviation of 47% is observed. The deviation between the FEA and the measured torque increases as the induction goes beyond the magnetic saturation point of the fluid. In the proposed magnetostatic model, the torque as well as the power supply are strongly dependent on the permeability of the fluid as shown in Equations 5.1 and 5.3 respectively. Therefore, this deviation may be due to imprecisions of the permeability of the fluid beyond the saturation point as well as the estimation of field dependent yield stress as a function of the applied field. The estimated yield stress $\tau_y(H)$ is given by the fluid's manufacturer as guidelines only.

4 SINGLE BRAKE DESIGN CONCLUDING REMARKS

An MR brake has been developed on the basis of the proposed magnetostatic model. The magnetic circuit is dimensioned to deliver a desired magnetic flux density over the smallest fluid surface. This enables the brake to maintain the fluid under its saturation point in order to guarantee a linear current-torque relationship and to minimize the power supply. In addition, considering a maximal admissible induction attributed on the ferromagnetic path, the circuit is designed so that the fluid and the path reach their saturation for the same magnetic flux.

The considered evaluation criteria are the torque density, the controllability and the reactivity, as a function of the number of fluid gaps and the shearing surface dimensions. The analytical model highlights that the torque density and the reactivity increase with the number of fluid gaps, while the controllability is inversely dependent to it. It can be concluded that there is a optimal value for the fluid gap length that maximizes the torque density for a given fluid gap radius. In particular, the fluid gap depth plays an important role with regards to the controllability/torque density and controllability/power supply tradeoffs. These compromises have been established by setting the fluid gap to 0.5mm and by focusing the optimization on the torque density with respect to a minimal required torque.

According to the analytical model, the fluid reaches the desired induction at 232A.turn and the expected torque is 3.4Nm. The measured torque at this point overreaches the theory by +5.5%. The FEA indicates that the fluid reaches the required induction at 247A.turn to display 3.2Nm. The measured torque of 3.8Nm yields a deviation of 15%. When exploited up to its complete saturation, it can generate 5.3Nm and the power consumption is 20W. This repre-

Table 5.3: Specifications of the proposed brake and comparision to other documented results.

	unit	Designed brake	Lord Corp. RD-2078-1	Senkal and Gurocak	Liu et al.	Guo and Liao	Nam et al.
Max. Torque	Nm	5.3	4.0	10.9	7	0.48	4.2
Off-state	mNm	30	400	100	500	50	-
Length	mm	39	35.7	89.7	21	18	38
Radius	mm	30	96.6	31.75	78	25	60
Power	W	19	15	20	-	-	52
Time Const	ms	50	10	60	-	25	33
Torque/Vol	kN/m^2	48.1	12.5	38.3	17.4	13.6	9.8
Efficiency	mNm/W	280	260	540	-	-	80
Controll.	-	176	10	109	14	9.6	-
Reactivity	kNm/s	106	400	108	-	19.2	127

sents 48.1 kNm/m^2 torque density. The obtained maximum-to-minimum torque ratio, taking also into consideration the off-state torque due to Coulomb friction, is 176 and a response time is 200ms. The response time is 10 times superior to the maximal time constant specified in the optimization algorithm. The obtained performace are listed in Table 5.3. For comparison purposes, a commercial MRF brake from Lord Corporation (RD-2078-01) has a torque range varying from 0.4 to 4Nm. It represents a torque density of 12.5kN/m^2. In other words, the proposed brake generates 23% more torque for a volume 76% inferior. The table also present some documented results available in [Senkal et Gurocak, 2010], [Liu *et al.*, 2006], [Guo et Liao, 2011], and [Nam *et al.*, 2008].

The developed magnetostatic model needs only three inputs to completely define the brake: the number of fluid gaps, the inner radius of the smallest fluid gap and the fluid gap depth. All other dimensions can be calculated accordingly in order to accurately guide the magnetic flux into the gaps without saturation.

The relatively low differences observed between the model and the experimental results in the linear range indicates that this method is sufficient to design a multiple cylinder MR brake. Moreover, the high controllability and torque capability make the actuator amply adaptable for high transparency human-machine interfaces design.

The hybrid actuator comprising two MR brakes is presented in the next section.

5 HYBRID ACTUATOR DESIGN

Two identical modular brakes and a DC motor Maxon RE40-1148877 form the hybrid actuator illustrated in Fig. 5.15. While the motor is directly linked to the through-axis, each brake is connected to it by means of an overrunning clutch placed in the hollow shaft of each brake. By this means a brake can apply a torque only in one defined direction corresponding to the clutched direction of the overrunning clutch. In the other direction the shaft can turn freely

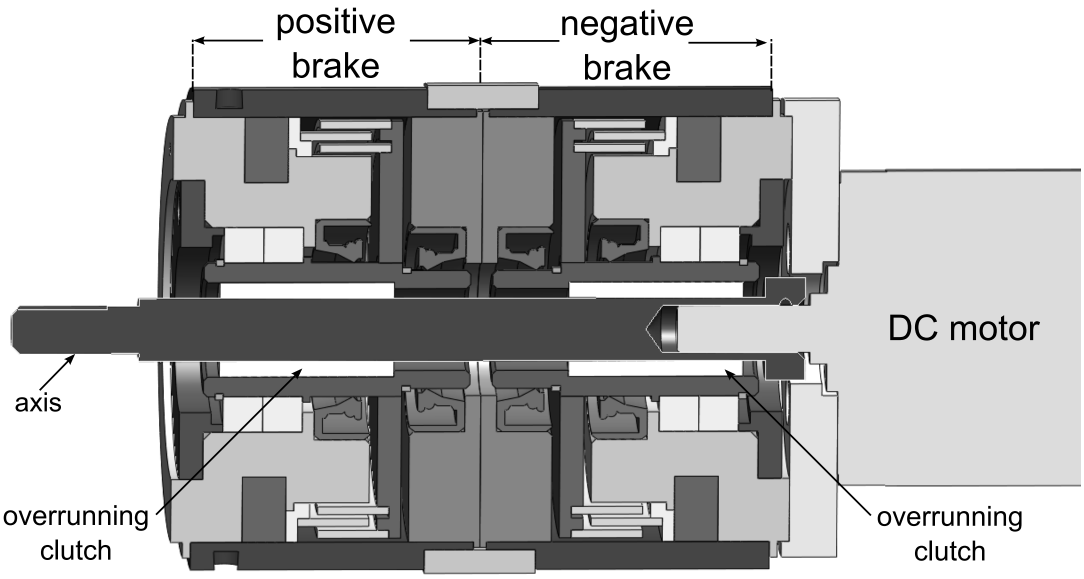

Figure 5.15: CAD representation of the dual unidirectional brake based hybrid actuator. Two identical brakes are mounted in opposition on the axis through an overrunning clutch. By these means a brake can apply a torque only in a defined direction. A DC motor Maxon RE40 is directly connected to the axis. The position is measured using an incremental encoder with 500 pulses per revolution.

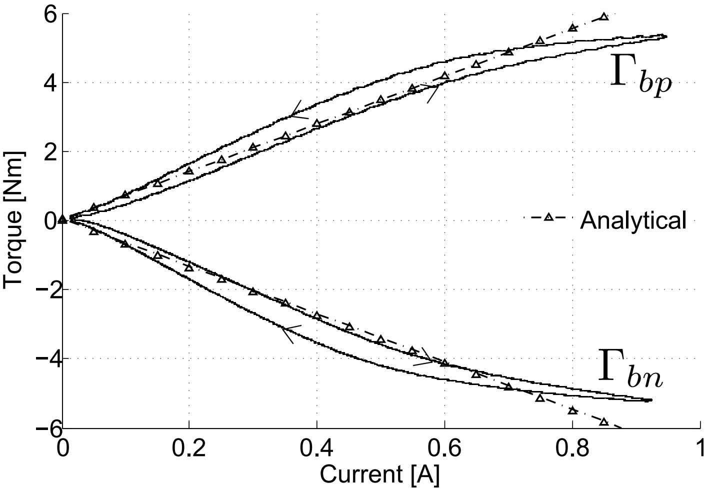

Figure 5.16: Measured braking torques and their hysteresis loops. A triangular current slop is sent to the brakes and a DC motor is used as velocity source. The maximal measured braking torque is 5.3 Nm at 0.92A.

even the brake is activated. If both brakes are simultaneously engaged, the shaft is braked in both directions.

By definition "positive brake" is the brake able to generate a torque $\Gamma_{bp} > 0$ in the positive direction, or rather opposed the velocity of the shaft $\dot{\theta} < 0$, and "negative brake" is the brake that can impose a torque $\Gamma_{bn} < 0$ which needs $\dot{\theta} > 0$.

The assembled hybrid actuator was mounted in the same test bench used to characterize the brakes (as presented in Fig. 5.8). Fig. 5.16 presents the measured braking torques as a function of the current strength in both directions. The braking torque as a function of the current is submitted to an hysteresis loop. It can be compensated using a subhysteretic loop model [Liu *et al.*, 2006]. However, when the actuator is used to simulate a virtual obstacle, in contrast to the motor, the braking torque is zero when the velocity is inverted according to the proposed control laws as presented in Chapter 3. In this case, in most of the time, only the first subhysteretic loop of each brake is exploited. The relation braking torque to current can be satisfactory approximated using two different linear regions. Considering the first subhysteretic loop, the torque as a function of the current i is:

$$\begin{bmatrix} \Gamma_{bp} \\ \Gamma_{bn} \end{bmatrix} = \begin{cases} \begin{bmatrix} 6.96i \\ 6.55i \end{bmatrix} & 0 \leq i \leq 0.61A \\ \begin{bmatrix} 3.25i + 2.26 \\ 4.13i + 1.47 \end{bmatrix} & 0.61A < i \leq 0.92A \end{cases} \tag{5.17}$$

When the motor of the hybrid actuator is engaged and the brakes are desactivated, the no load current of the motor is i_0=2.23A. Given the motor's torque constant k_i =60.3mNm/A, this represents a no load torque, calculated as $i_0 k_i$ of 134mNm. The reached velocity in this case is $\dot{\theta}_0$=182rad/s. The estimated viscous torque coefficient $b = i_0 k_i / \dot{\theta}_0$ thereby corresponds to 732μNms. Using the same torque/velocity step response, the inertia of the hybrid system has graphically been deduced and the result corresponds to the CAD model. The estimated rotor inertia of the hybrid actuator is 418gcm^2.

The addition of the overrunning clutches generates a mechanical slash between the shaft and the rotary parts of the brake. Fig. 5.17 presents the necessary torque to be applied to the actuator in order to generate a displacement when both brakes are activated. Considering the minimal position resolution of the encoder, i.e. 3.14mrad, the necessary torque to detect a position variation is 0.3Nm. The mechanical slash cannot be perceived by the user.

6 HYBRID ACTUATOR CONTROL

An overview of the global control-loop of the hybrid actuator is presented in Fig. 5.18. Each brake is associated to an overrunning clutch modelled as an unilateral constraint. The brake 1 and the brake 2 apply a torque Γ_{bp} and Γ_{bn} respectively. The electromechanical behaviour of the brake is represented as a transfer function $B(s)$. The brake current is controlled by an analog proportional-integral controller (PI 1 and PI 2). The electromechanical transfer function of the motor is called $M(s)$. As the case of brakes, a voltage is applied by the PI controller and the current is monitored. The global system is operated by a microcontroller Silicon

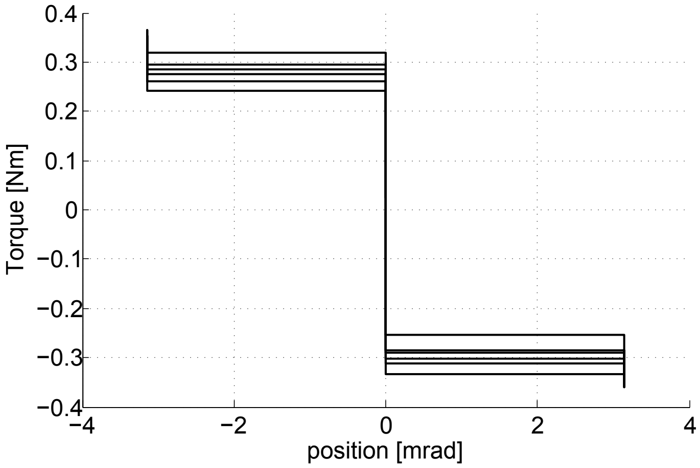

Figure 5.17: Mechanical slash between the brakes due to the clutches. The necessary torque to detect a position variation when both brakes are activated is 0.3Nm.

Labs C8051F120 running at 99.4 MHz. The conversion between the discrete and continuous domain is obtained by a zero-order hold function according to a sample period T of 200μs. A human operator represented as a passive impedance $Z_0(s)$ interacts with the device and applies a torque Γ_z. The virtual environment is the discrete function $H(z)$, linear or not, which calculates the reference torque Γ_h^* as a function of the measured position θ^*. The rotational velocity is called $\dot{\theta}$. Note that the control scheme is independent of the virtual environment. The asterisk identifies variables in discrete domain.

The stiffness K_h of the virtual environment observed by the controller is:

$$K_{h(k)} = \frac{\Gamma^*_{h(k)} - \Gamma^*_{sb(k-1)}}{\theta^*_{(k)} - \theta^*_{(k-1)}} \tag{5.18}$$

The index (k) represents the actual value of the variable, $(k-1)$ is the value at the previous sampling, and Γ^*_{sb} is the maximal torque that can be provided by the motor. If $\theta^*_{(k)} - \theta^*_{(k-1)} = 0$ the controller considers that the stiffness does not change, therefore $K_{h(k)} = K_{h(k-1)}$.

Since the nominal power of the motor is nine times superior to the brake, an efficient way to reduce consumption is avoiding the activation of the motor. Furthermore, during the simulation of virtual obstacles, for example, the high stiffness requested by the virtual environment represents in fact the simulation of a passive obstacle. Therefore, the controller incorporates a stiffness threshold which differentiates the simulation of elasticity or obstacles. Up to the defined threshold, called K_p, the controller assumes that the virtual environment intents to simulate elastic elements. This requires an active torque, thus the motor and the brake are activated. If the virtual environment stiffness is superior to this threshold, the controller considers that the system simulates a virtual obstacle, which requires a passive force. In this case only the brake is activated. Obviously, low stiffness observed by the controller may come from the simulation of a viscous model, however in this context the controller is not able to determine

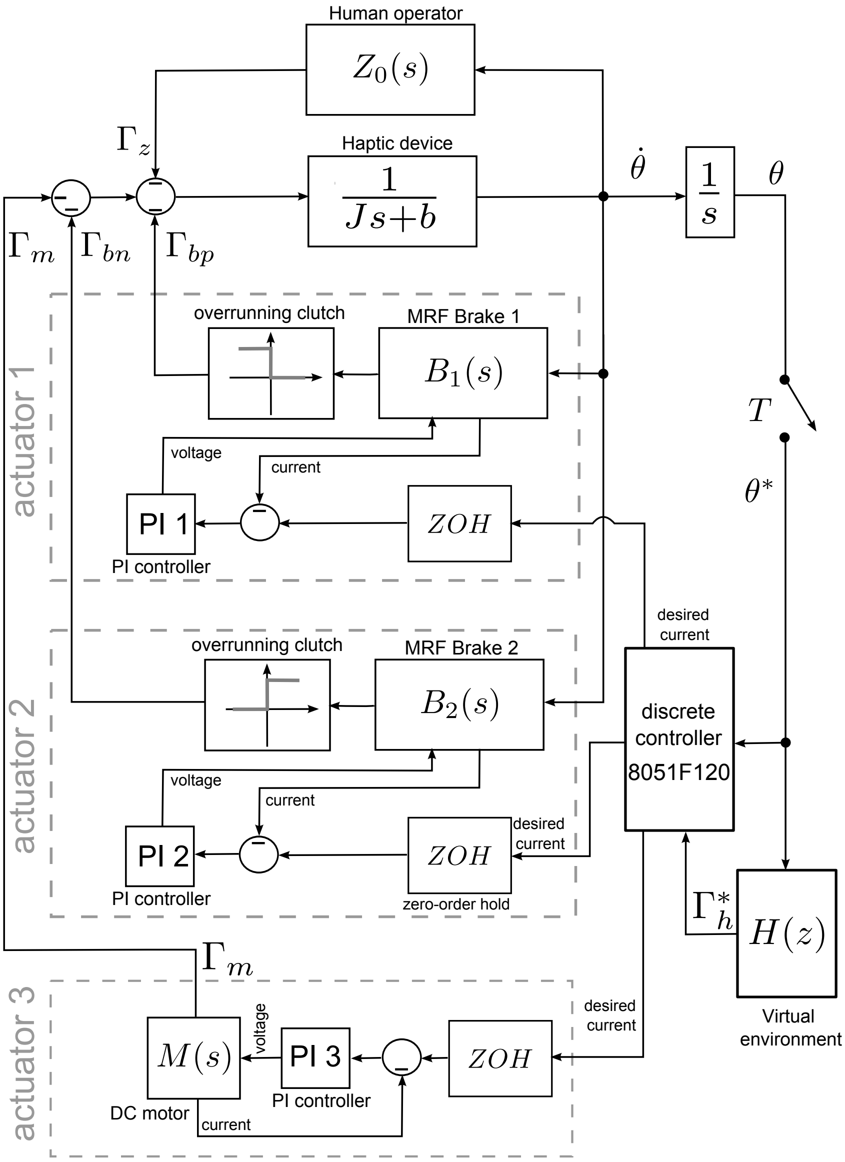

Figure 5.18: Haptic display impedance control-loop. The haptic device is modelled as an inertia J and a damping b. The human operator $Z_0(s)$ applies a torque Γ_z. The torque of the motor, and of the brakes are called Γ_m, Γ_{bp}, and Γ_{bn} respectively. The virtual environment $H(z)$ calculates the desired torque Γ_h^* as a function of the measured position θ^*. It is sent to the controller (Silabs 8051F120) that determines the sharing of efforts. The asterisk represents discrete variables and the conversion to continuous domain is obtained by a zero-order hold function ZOH with a sample rate $T = 200\mu$s. A voltage is applied to each actuator and the current controlled in using an analog-proportional controller (PI). The electromechanical transfer function of the motor and of each brake are called $M(s)$, $B_1(s)$ and $B_2(s)$ respectively.

the nature of the simulation. Indeed, the participation of both actuators in parallel cover both possibilities. K_p is defined as the ratio maximal torque to position resolution, which yields $K_p = 5.3\text{Nm}/4ppr = 29.4\text{kN/rad}$.

Considering the maximal stiffness displayable by the motor K_{lim} and the stiffness threshold characterizing a virtual obstacle K_p, the torque that can be sent to the motor Γ^*_{sb} is computed as:

$$\Gamma^*_{sb(k)} = \begin{cases} 0 & if \quad K_h > K_p \\ K_{lim}(\theta^*_{(k)} - \theta^*_{(k-1)}) + \Gamma^*_{sb(k-1)} & if \quad K_{lim} \leq K_h \leq K_p \\ \Gamma^*_{h(k)} & otherwise \end{cases} \tag{5.19}$$

Considering Γ_{sat} the maximal torque of the motor, its unsaturation ratio, represented by the variable $\beta(\Gamma_h)$, considering also the bounded torque Γ^*_{sb}, yields:

$$\beta(\Gamma_h) = \frac{\min\left(\left|\Gamma^*_{sb}\right|, \left|\Gamma_{sat}\right|\right)}{\left|\Gamma^*_h\right|} \tag{5.20}$$

By these means the motor is guaranteed to not overtake the maximal displayable stiffness under stability condition and is not activated in the case of the simulation of a virtual obstacle.

The observed interaction power is $P = (\Gamma^*_h)\dot{\theta}^*$ where the measured velocity is $\dot{\theta}^* = \theta^*(1-z)/Tz$. A power-sign dependent variable $\sigma(P) = 0$ if $P \geq 0$ and $\sigma(P) = 1$ if $P < 0$, is specified as follows:

$$\sigma(P) = \frac{1}{2}\left[\text{sgn}(P) - 1\right]\text{sgn}(P) \tag{5.21}$$

Dissipative behaviour then yields $\sigma \geq 0$ and active behaviour implies $\sigma < 0$. The control variable $S(u)$ is then introduced to determine the sharing of Γ^*_h into Γ_b and Γ_m so that: if $S(u) = 1$ only the motor is enabled; if $0 < S(u) < 1$, the reference torque is applied using both actuators. Considering the stiffness limitation, $S(u)$ can be set to $\beta(\Gamma_h)(1-\sigma(P)) + \sigma(P)$ and the torque of the brake and the motor are defined by $\Gamma_b = \Gamma^*_h(1-S(u))$ and $\Gamma_m = \Gamma^*_h S(u)$ respectively.

The observed energy of the motor is $E(n) = T\sum_{k=1}^{n}\Gamma_m(k)\dot{\theta}(k)$. If this energy becomes negative the created energy $-E(n)$ is transferred to the brake instead of the motor. Thereby, the energy observer $E_o(n)$ is defined as a function of the torque provided by the motor and the energy dissipated in the brake when the power is negative:

$$E_o(n) = T\sum_{k=1}^{n}\left[\Gamma_m(k) + \Gamma_b(k)\sigma(P)\right]\dot{\theta}(k) \tag{5.22}$$

Taking into consideration the limitation of stiffness and energy, $S(u)$, takes the following formulation:

$$S(u) = \begin{cases} \beta(\Gamma_h)(1-\sigma(P)) + \sigma(P) & if \quad E_o(n) \geq 0 \\ \beta(\Gamma_h)(1-\sigma(P)) & otherwise \end{cases} \tag{5.23}$$

Finally, the torque that can be applied by the motor under stability and global passivity condition is:

$$\Gamma_m = ZOH[\Gamma_h^* S(u)] \tag{5.24}$$

Using this formulation implies that Γ_h is first transferred to the motor. The reference braking torque then compensates for the saturation of the motor making $\Gamma_b^* = \Gamma_h^* - \Gamma_m^*$. To respect the passivity condition the braking torque to be applied is:

$$\Gamma_b = ZOH[\Gamma_h^*(1-S(u))] \tag{5.25}$$

The selection of the brake then can be realized independently of the velocity. The activation of the positive brake as a function of the reference braking torque is:

$$\Gamma_{bp} = \frac{1}{2}\Gamma_b\left[1+\operatorname{sgn}(\Gamma_b)\right] \tag{5.26}$$

Thanks to the overrunning clutch, $\Gamma_{bp} = 0$ if the velocity is positive. The torque of the negative brake is:

$$\Gamma_{bn} = \frac{1}{2}\Gamma_b\left[1-\operatorname{sgn}(\Gamma_b)\right] \tag{5.27}$$

The torque provided by the positive brake is zero if the velocity is negative.

6.1 VIRTUAL ENVIRONMENT EXAMPLE

Consider the example of the virtual environment presented in Fig. 5.19. The environment simulates an unilateral contact with a virtual obstacle, which has a stiffness K_h as shown in (a) as a function of the position θ. The obstacle is placed in the position θ_1. When the end-effector touches the virtual obstacle at the right or left side, the virtual environment calculates a torque which should be opposed to the penetration of the obstacle. The reaction torque Γ_h is shown in (b). If the operator closes the obstacle on the left, the reaction torque is positive and on right side the torque is negative.

Using the unidirectional brakes, the effective torque provided by the positive and negative brake is shown in Fig. 5.19 (c) and (d) respectively. If the operator touches the obstacle on the left with a negative velocity, the reaction torque is positive. Thus the positive brake is engaged. If the operator inverses the velocity, the brake remains activated by since the velocity becomes positive, the resultant braking torque is zero. The other brake is used to simulate the contact with the obstacle on the right.

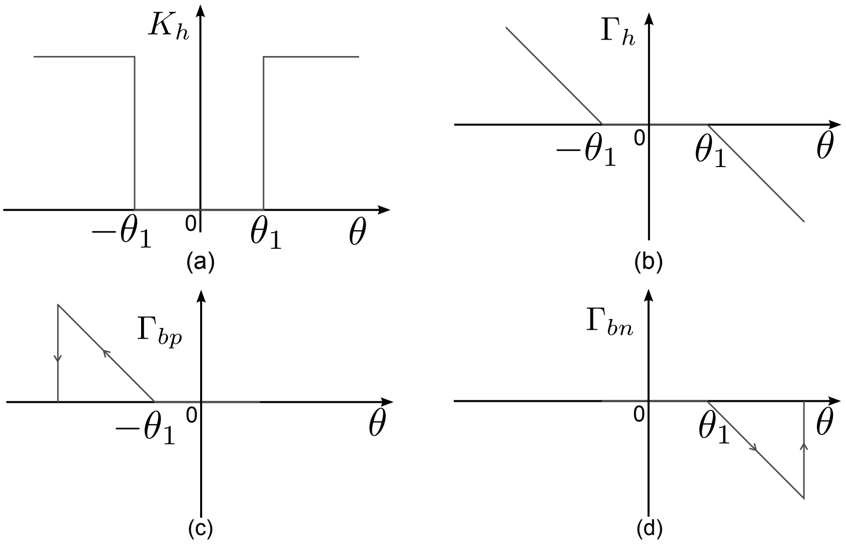

Figure 5.19: Example of a virtual environment implementation. The environment simulates an unilateral contact under the form of an obstacle with a stiffness K_h as a function of the position θ. The reaction torque Γ_h then depends on veloctiy of approach of the end-effector . The effective torque provided by each brake Γ_{bp} and Γ_{bn} are indicated in (c) and (d) receptively of according to the velocity signalized by the arrows.

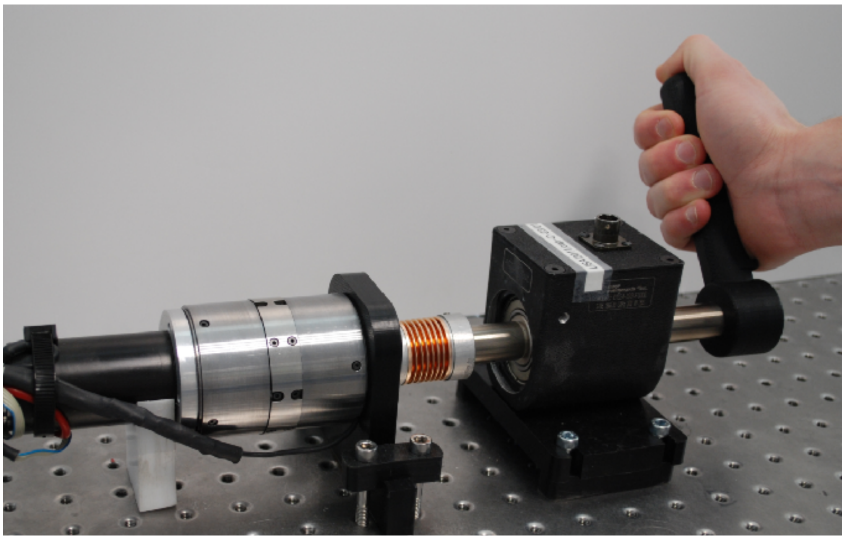

Figure 5.20: User interaction with the hybrid actuator. A torque transducer is used to measure interaction forces. The torque measure is not required by the control.

The implementation of the virtual environment remains independent of the actuation system. The control laws automatically ensure that the reference torque is respected using the combination of the brake and the motor.

7 EXPERIMENTAL RESULTS

To demonstrate the feasibility of the control approach applied to the complete actuator, three simulations are presented. The first corresponds to the simulation of the virtual obstacle presented in the previous section, the second and the third are the simulation of soft a stiff virtual spring. In all cases, the virtual environment is only modelled as a stiffness K_h. Only the reference torque of the virtual environment and the measured position are used by the controller.

The maximal stiffness supported by the motor is fixed at $K_{lim} = 6.8$Nm/rad and the stiffness threshold characterizing a virtual obstacle is $K_p = 29$kNm/rad. Fig 5.20 shows the hybrid actuator during the test.

7.1 VIRTUAL OBSTACLE SIMULATION

In order to simulate the unilateral contact the stiffness of the virtual environment is assigned to $K_h = 10^6$Nm/rad. The obstacle is placed at ± 0.1rad.

The experimental results is shown in Fig. 5.21. The operator turns the end-effector toward the obstacle on the right side. The controller calculates the desired stiffness of the virtual environment. When the operator touches the wall at 0.1rad (Fig. 5.21a) the calculated stiffness is superior to the threshold K_p. The controller deduces that the virtual environment simulates an obstacle and only the negative brake is used to constrain the motion (Fig. 5.21b). The brake is thereby activated up to its maximal torque. The operator then turns the end-effector in the other direction. When in contact with the obstacle on the left side, the positive brake is activated to simulate the unilateral contact.

7.2 SOFT VIRTUAL SPRING SIMULATION

In this simulation the virtual environment simulates a soft virtual spring. The stiffness K_h corresponds to the maximal stiffness supported by the motor $K_{lim} = 6.8$Nm/rad.

Fig. 5.22 presents the experimental result. The end-effector attains the spring at 0.5rad. The controller determines the stiffness of the virtual environment and since $K_h \leq K_{lim}$, the torque sent to the motor is not bounded and $\beta = 1$. As a consequence only the motor is activated. At the point (A), the motor attains it maximal torque. Thus, β decreases gradually. The difference between the reference torque and the maximal motor's torque then is compensated

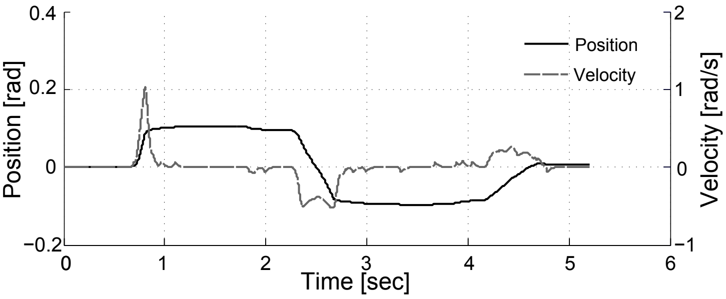

(a) Position and velocity

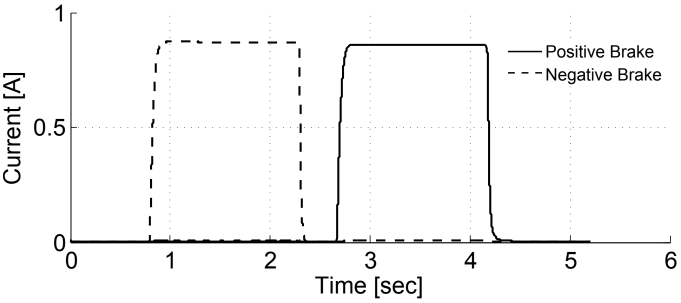

(b) Brakes current

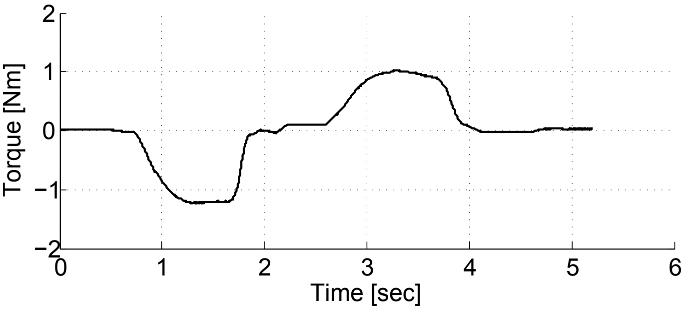

(c) Torque imposed by the operator

Figure 5.21: Virtual obstacle simulation. The virtual environemnt is assigned as an unilateral constrain placed at ±0.1rad. In (a) the operator turns the end-effector toward the obstacle with a positive velocity, thus when he touches the wall the negative brake is activated (b). Since the observed stiffness is superior to the stiffness threshold, the motor is not activated. When the operator reaches the second obstacle at -0.1rad, the positive brake is activated. The torque imposed by the operator is shown in (c).

by the brake which displays 6.8Nm/rad. The viscous and coulomb frictions are not compensated.

7.3 STIFF VIRTUAL SPRING SIMULATION

Consider now the simulation of a stiff virtual spring with $K_h >> K_{lim}$. According to the control laws, the controller should be able to bound the stiffness sent to the motor and compensate the difference using the brakes.

Fig. 5.23 shows the experimental results of the simulation of a 60Nm/rad stiff virtual spring. The end-effector attains the spring at 0.5rad. The virtual environment calculates the desired torque and the controller deduces the stiffness. Since $K_h >> K_{lim}$ the torque sent to the motor is therefore bounded to 6.8Nm/rad. The motor can assume only 11% of the total torque as shown in 5.23b. The difference (53.2Nm/rad) is sent to the brake up to the mechanical saturation of the motor at the point (A). After this point $\beta \rightarrow 0$ and all the desired stiffness is sent to the brake and it displays a stiffness of 60Nm/rad.

When the user inverses the force, the brakes are turned off and the system can display the maximal stiffness of the motor with a maximal torque of 0.2Nm. During the compression phase of the spring the reference torque of the virtual environment is respected under stability conditions.

7.4 PERFORMANCE EVALUATION

To evaluate the performance of the proposed system, the hybrid actuator will be compared to a classical system comprising the same DC motor and a reduction stage. In its recommended operating range the motor generates up to 200mNm, thus the maximal torque of the hybrid actuator is 5.5Nm. To achieve this torque without the brakes, the motor needs to be associated to a reduction stage with a ratio of 27.5:1. For comparison purposes, consider an hypothetical ideal capstan transmission which has no inertia, no friction and an no mechanical looses.

The no load current given in the datasheet of the DC motor is 69mA and the torque constant is 60.3mNm/A. This corresponds to a off-state torque of 4.16mNm. The no load velocity of the motor is 793rad/s, it yields a viscous torque coefficient of 5.24μNms. The inertia of the motor is 134gcm^2.

Each brake possesses a torque density of 48kN/m^2 and consumes 20W. When compared to the motor, a brake has a torque capacity 21 times superior. The torque density of the complete hybrid actuator is 7.9 times higher than the motor.

The performance of the motor, of the motor with capstan transmission, of a single brake, and of the complete hybrid actuator are listed in Table 5.4. The inertia of the motor with capstan is 241 times superior to the hybrid actuator, while the viscous torque is 5 times inferior.

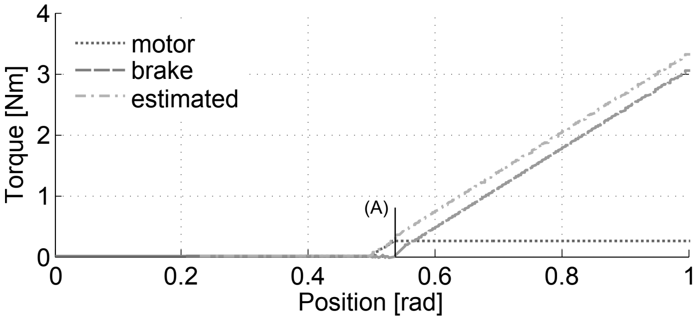

(a) Interaction torques

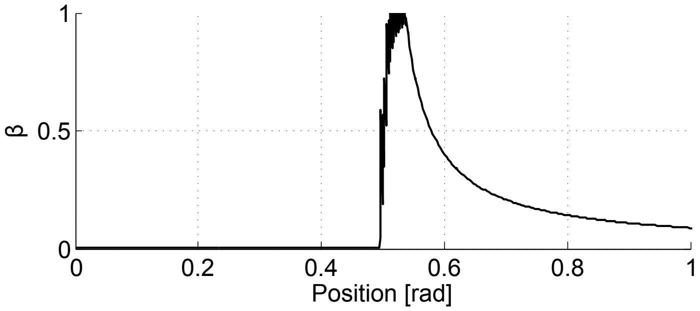

(b) Unsaturation ratio of the motor

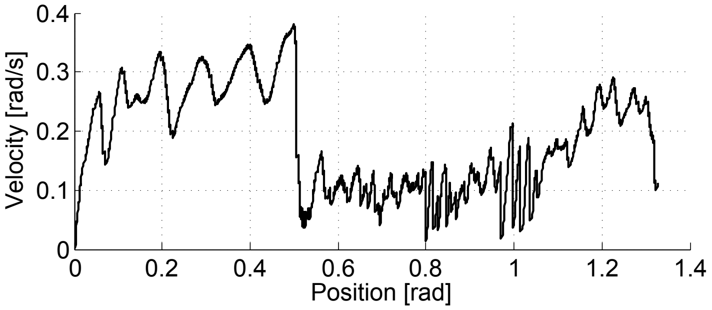

(c) End-effector velocity

Figure 5.22: Simulation of a soft virtual spring. The stiffness corresponds to the maximal stiffness supported by the motor. The end-effector attains the spring at 0.5rad. Since the stiffness can be displayed by the motor, the reference torque is sent to the motor and $\beta = 1$. When the motor attains its maximal torque, the brake is activated to compensate for the difference between the reference torque and the torque of the motor and $\beta \to 0$. The estimated torque refers to the sum of the calculated torque using the brake and motor's current. The viscous friction of the brake is not compensated.

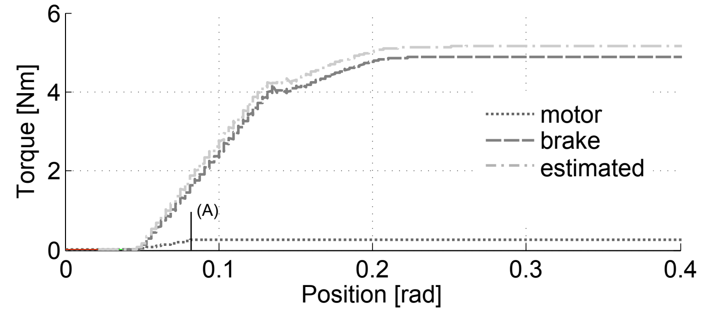

(a) Interaction torques

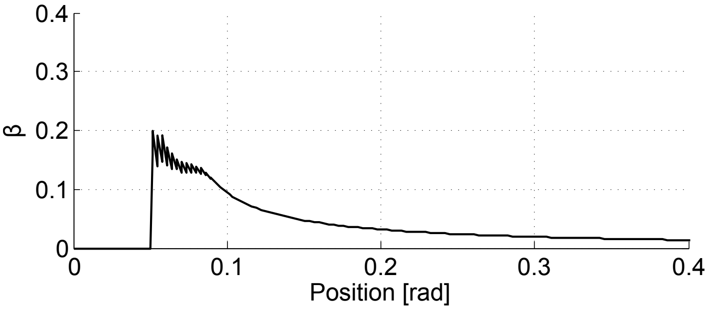

(b) Unsaturation ratio of the motor

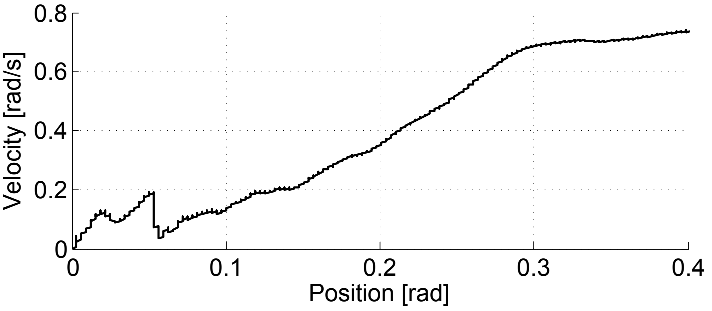

(c) End-effector velocity

Figure 5.23: Simulation of 60Nm/rad stiff virtual spring. The torque sent to the motor is bounded according to its maximal stiffness of 6.8Nm/rad. The difference, 53.2 Nm/rad is then sent to the brake up to the saturation of the motor at the point (A). This saturation can be observed in the evolution of β. Before the saturation of the motor $\beta = 6.8/60$, after this point $\beta \to 0$. Subsequently, all the reference stiffness is sent to the brake, which displays 60Nm/rad. There is no compensation of viscous torque.

Table 5.4: Comparison between the hybrid actuator and a DC motor

	Maxon RE40 direct driven	Maxon RE40 with capstan	Single MRF brake	Hybrid actuator	unit
Reduction ratio	1	27.5	1	1	-
Passive Torque	0.2	5.5	5.3	5.5	Nm
Active Torque	0.2	5.5	0	**0.2**	Nm
Power Consumption	150	150	20	170	W
Rotor Inertia	134	101k	279	418	gcm^2
Viscous torque coefficient	5.24	144	567	732	μNms
Off-state torque	4.16	114.4	25.8	30	mNm
Torque density	2.24	-	48.1	17.75	kN/m^2

However, the off-state torque is 4.43 times higher. The necessary rotational velocity to attains the same parasitic torques in both devices (viscous plus off-state torque) is 142rad/s. In other words, the hybrid actuator exhibits less parasitic torque up to 22.7 tours/sec. Velocities superior to this value are rarely the case of haptic interactions.

Although these evidence demonstrate that the hybrid actuator provides more transparency than a torque equivalent motorreductor, the torque capability of the actuator to restore energy is 27.5 times inferior than its maximal passive torque. The energy restitution is limited to the torque capability of the motor.

8 CONCLUSION

This chapter addressed the mechanical design, fabrication, evaluation and control of the hybrid actuator.

The first part focussed on the design of a single brake. The cost function defined to optimize the performance deal with the controllability, reactivity and torque density. The obtained large dynamic range makes it suitable to high transparency haptic devices. The measured mechanical response time for a voltage step-time excitation is 200ms in the linear range. When controlled in current by a PI controller, the response time is reduced to 30ms.

A particular concern using MR actuators is their inherent hysteresis loops. It implies in a non-linear torque-to-current relation which should be integrated in the controller by using appropriated subhysteretic curves. Erol et al. [Liu *et al.*, 2006] demonstrated that directly controlling the magnetic field instead of the current, can effectively reduce the hysteresis. In the same way, the viscous and coulomb frictions should be integrated in the control laws to improve the accuracy of the displayed torque by the brake.

Two identical brakes associated to overrunning clutches form the hybrid actuator. The use of opposite unidirectional brakes in parallel enables the system to be controlled with impedance control without torque measurement. The application of the proposed control laws developed in **Chapter** 3 allows for the simulation of high stiffness virtual environments while maintaining stability. In addition, the control incorporates an algorithm to determine if the virtual environment simulates a virtual obstacle rather than elastic elements. In this case only the brakes are used to generate a passive torque which reduces the power consumption.

The complete system, comprising two brakes and the motor, has a torque density 7.9 times higher than when using the motor only. Quantitative results demonstrate that the proposed device exhibits less parasitic torques and less inertia than a motor associated to an ideal transmission. However, since the system combine brakes and a motor, its capability to dissipate energy is superior than its capability to restore energy to the human operator. The limitation of the active torque has antagonistic goals. High interaction torques can be displayed with safety and stability. On the other hand, the active torque is 27.5 times inferior than the active torque. Since most virtual environment as assumed as passive, the use of such a system may be justified. Besides, the system need two brakes, but there are many virtual environments that can be envisioned which passive forces only in single direction. In this case, only a motor and a brake are necessary.

The limitation of the active torque could affect the perception of elastic elements by the human operator. In order to evaluate the influence of this torque asymmetry, an user experiment is performed in the following chapter.

6

EVALUATION OF THE PASSIVE/ACTIVE TORQUE CAPABILITY ASYMMETRY

Contents

UNDERSTANDING human perceptual mechanisms is a key point to guide the design of high-performance haptic interfaces and the associated software solutions. These human capabilities have to be taken into consideration in the integral design of the actuators used to render haptic stimuli. The proposed hybrid device combines a powerful brake and a small DC motor. As a consequence, its capability to dissipate energy is considerably superior to its capability to restore energy to the human operator. This chapter aims to identify the implication of this asymmetry on the perception of stiffness by human operators. This represents the worst application case in one degree of freedom for the proposed device. The motor is associated to a capstan transmission so that the maximal torque of the brakes and the motor are the same. The asymmetry is controlled by setting the participation of the brake and of the motor.

Seventeen participants took part in the experiment consisting in interacting with a virtual spring and try to identify if the spring restores all the provided energy. Experimental results obtained from nine participants indicate that when the stiffness during the compression of the spring is less than 80% of the stiffness during the compression, users perceived the asymmetry in 80% of trials. Further results from other eight participants show that springs were assumed as asymmetrical when the maximal torque presented to the user to decompress the spring were inferior to 60% of the necessary torque to compress the spring. These results highlight that some interaction energy can be dissipated without affecting the perception of stiffness.

1 MOTIVATION

Knowledge of how humans interact with haptic devices is a crucial point in the design of force-reflecting interfaces. Three commonly used psychophysical tasks to evaluate haptic interaction are stimuli detection, discrimination and identification [Tan, 1997]. Detection deals with the smallest human perceptible kinaesthetic stimulus. Differential thresholds reveal the minimal difference in the intensity of two stimuli that leads to an alteration in perception [Vicentini *et al.*, 2010]. Identification refers to the human ability to categorize dissimilar parameters.

The integration of these characteristics in the design of human-machine interfaces will make the resolution of such devices in terms of force, bandwidth, displacement detection and magnitude, response time, adapted to human perceptual kinaesthetic thresholds.

In the case of a haptic device, a particular concern is the system's ability to generate virtual stiffness. In most virtual environments, object surfaces supposed to be rigid are frequently modelled as passive elastic elements with some stiffness and damping [Tan *et al.*, 1994]. For Rosenberg and Adelstein [Rosenberg et Adelstein, 1993], three sequential perceptual components compose the basic percept of a rigid surface, i.e. the initial dynamic contact, the static interaction and the final release. The initial contact with the surface can effectively be displayed by either a damper or spring while the dynamic interaction and release needs to be

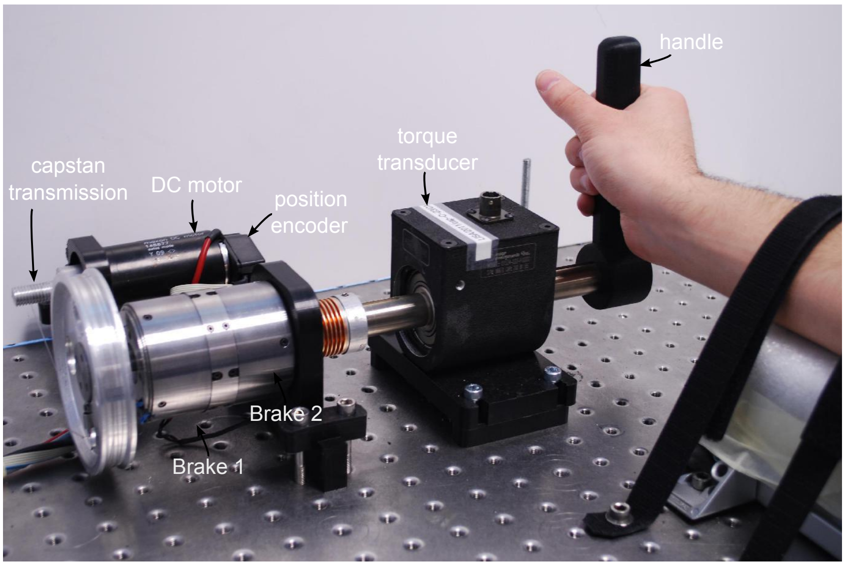

Figure 6.1: Haptic feedback apparatus and the experimental setup. Two unidirectional controllable brakes and a motor Maxon compose the device. The brakes are directly connected to the handle shaft and linked to the motor thorugh a 7:1 capstan transmission. Each actuator can apply up to 1.2Nm to the handle and the interaction torque is monitored using a torque transducer. The position of the motor's shaft is measured using an incremental encoder with 500 pulses per revolution. The participant's front arm is attached to the mount and he claps the handle in the vertical position.

simumated as a spring.

The perception of stiffness is presumably based on the perception of both force and displacement [Jones et Hunter, 1990]. Several works have dealt with factors affecting human perception of forces. The just-noticeable-difference (JND) is one of the most common measures of forces discrimination. For instance, Jones and Hunter [Jones et Hunter, 1993] related a JND of 15% for forces applied to the hand-arm system. Hurmuzlu et al. [Hurmuzlu *et al.*, 1998] found values varying from 6% to 50% during the interaction with a pneumatic robotic arm. The JND in length found by Tan et al. [Tan *et al.*, 1994] was roughly 1mm for a length of 10-20mm and 2.2mm for a length of 80mm. Past studies using the discrimination paradigm have established a fraction of 5-10% for force magnitude [Pang *et al.*, 1991], 13% for torque [Woodruff et Helson, 1967] and 3-10% for length [Durlach *et al.*, 1989]. Cholewiiak et al. [Cholewiak *et al.*, 2008] studied the haptic identification of stiffness magnitude in the range of 0.2-3N/mm and force magnitude ranging between 0.1N and 5N. Their results indicate that users are only able to correctly identify 2.8 stiffness levels and 2.9 force magnitudes. In an absolute identification paradigm presented by Forrest et al. [Forrest *et al.*, 2009], users were able to identify 2 levels of stiffness among 5 levels in the range of 0.2-5N/mm.

When interacting with a haptic device, users may perceive rigidity on the basis of a terminal force or mechanical work rather than stiffness [Tan *et al.*, 1995]. Differential thresholds for stiffness perception are suspected to be greater compared to force and position thresholds.

In this sense, the human ability to discriminate stiffness depends on the exploration technique [Koccak *et al.*, 2011].

The proposed haptic device combines brakes and motors, thus its capability to dissipate energy is greater than its capability to restore the energy provided by the operator. As a consequence, an asymmetry is observed between the dissipation and the restitution of energy, in terms of maximal stiffness and torque capabilities of the actuator. High levels of asymmetry, however, may damage the perception of an elastic virtual environment.

To our knowledge, no data exist on the human ability to perceive asymmetry originating from torque or stiffness difference, during energy dissipation and restitution phases, when the user interacts with the hybrid device. Therefore, the goal of the present study is to analyze the users capability to identify asymmetry in the simulation of virtual springs.

Two environments were used in the experiment. In the first one, the spring was softer during the decompression phase, and in the second the maximal torque restored to the user was bounded. For each environment, eleven levels of symmetry were assigned to the spring ranging from 0% (complete asymmetry, no force feedback during the decompression phase) to 100% (complete symmetry). Nine participants participated in the experiment based on stiffness asymmetry and other eight participants participated in the experiment based on torque asymmetry. Experimental results indicate that when the decompression stiffness is inferior to 80% of the compression stiffness, users can perceive the asymmetry. For the second environment, the spring were assumed as asymmetrical when the maximal torque presented to the operator to decompress the spring were inferior to 60% of the necessary torque to compress the spring. The results highlights that some amount of the energy provided by the operator can be dissipated in the virtual environment without affecting the perception of stiffness.

2 GENERAL METHODS

In this study, users interact with a compliant virtual environment, modelled as a virtual angular spring, using the proposed feedback device. The only difference is that the motor is associated to a capstan transmission. The virtual environment is assumed to be symmetric if it restores exactly the same amount of energy given by the user.

The environments presented to the user are:

- **Asymmetric stiffness spring**: refers to a pring with a relative stiffness difference between the compression and decompression interaction phases. In other words, the spring is softer during the decompression phase than during the compression phase.
- **Asymmetric torque spring**: refers to a pring with a relative difference between the compression and the decompression phase of the spring in terms of maximal torque. It means that the maximal torque imposed by the device to simulate the decompression phase of the spring is inferior to the torque provided by the user to compress the spring.

Users were requested to interact with the virtual environment and try to identify if the virtual environment is symmetrical or asymmetrical.

2.1 APPARATUS

The hybrid actuator is used in this experiment as presented in Fig. 6.1. It includes the same Maxon motor RE40 and the brakes. The motor-reducto can apply a torque of 1.2Nm. The maximal torque applied by the brakes is limited to 1.2Nm. A torque transducer is used to monitor interaction torques. The position of the motor's shaft is measured using an incremental encoder with 500 pulses per revolution. Each actuator is controlled in force by two analog proportional-integral regulators. A microcontroller 8051F120, operating at 99.4MHz, calculates the reference torque with sampling frequency of 5kHz.

The device simulates a virtual spring. The necessary torque to turn the handle is proportional to its position according to the assigned stiffness.

2.2 PARTICIPANTS

A total of 17 participants (4F, 13M) aged from 21 to 32, (average age of 23 years) volunteered to participate in the experiments. All but four were right-handed. None of them had prior knowledge about the device used in the experiment. They had no known medical neuromuscular problems. The participants were divided into two different groups of, respectively, 9 and 8 participants. The first group realized tests with stiffness asymmetry environment and the second group used torque asymmetry environment.

2.3 ENVIRONMENT

The environments presented to the participants represent a virtual spring. The reference torque is proportional to the position and the proportionality constant represents the stiffness of the spring. In the case of an ideal spring, the reaction torque in a given position is the same during the compression or the decompression phase. In order to create an asymmetrical virtual environment, the restored energy is bounded according to two different kind of environments.

For the first environment, the stiffness of the spring changes during the compression and decompression phase while for the second one, the stiffness is constant but the maximal torque presented to the user during the decompression phase is bounded.

1) Asymmetric stiffness environment: The torque as a function of the handle position is illustrated in Fig. 6.2. When the user turns the handle to compress the spring, both the brake and the motor apply a torque against the motion of the handle. The torque presented to the user is the sum of the brake and of the motor and follows the first slope which characterizes the

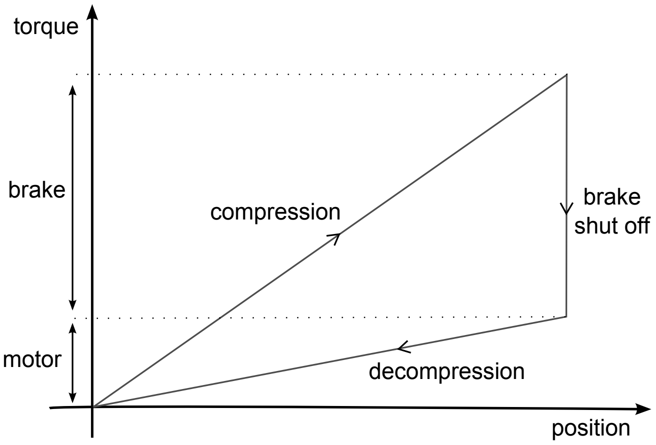

Figure 6.2: Asymmetric stiffness environment. During the compression phase of the spring, both brake and motor generate a torque against the motion which is proportional to the position of the handle. During the decompression phase, the brake is turned of and only the motor applies a torque in the same direction of the motion. The spring is stiffer during its compression phase. The participation of the brake defines the asymmetry level of the spring.

compression stiffness. When the user turns the handle back, the brake is turned off and only the motor remains activated. This represents the decompression stiffness.

Thus, the compression and decompression stiffness are not the same. The asymmetry is observed along the total displacement of the handle. This asymmetry can be controlled by the participation ratio of the brake. Eleven levels of asymmetry were defined starting from 0% up to 100% with constant intervals of 10%. When the symmetry ratio is 100%, only the motor is activated and the spring is symmetric. For a symmetry ratio of 0%, only the brake is activated and there is no force feedback during the decompression phase. In this case, the rendering presented to the user is similar to a virtual damping. A symmetry ratio of 50% indicated that the torque is equivalently shared between the brake and the motor. In other words, the decompression stiffness is equal to the one half of the compression stiffness.

2) Asymmetric torque environment: In the second environment category, the motor is used to simulate the same stiffness either during the compression or the decompression phase. The asymmetry is generated by limiting the maximal displayed torque by the motor. Fig. 6.3 systematizes the evolution of the torque as a function of the position. The motor displays the stiffness up to the maximal torque. When this point is reached, the torque of the motor is maintained constant and the brake is subsequently activated to compensate for the difference between the maximal motor's torque and the reference torque that simulates the spring. When the user turns the handle back, the brake is turned off. The torque provided by the motor remains at the maximal attributed value. When the reference torque is inferior to the maximal torque, the torque becomes proportional to the position of the handle and stimulates again the spring stiffness.

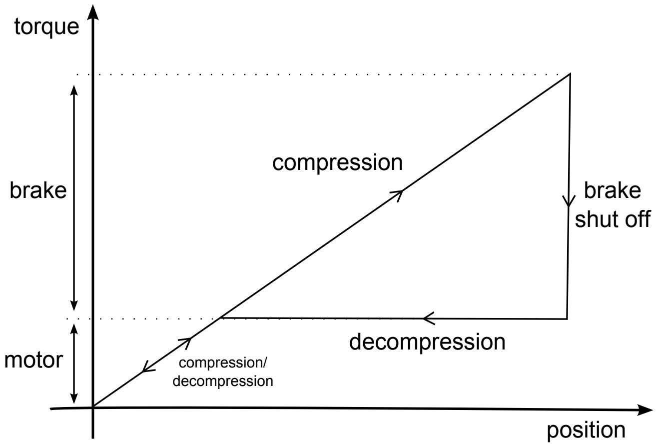

Figure 6.3: Asymmetric torque environments. The motor is activated to simulate the compression and the decompression of the spring with the same stiffness in both direction. The maximal torque imposed by the motor is however bounded. When the motor reaches the assigned desired torque, the brake is activated and compensates for the difference between the desired torque and the maximal motor's torque. The brake is turned off during the decompression phase.

By contrast to the previous environment, the asymmetry is observed only when the motor has reached its specified maximal torque. This point can be modified in order to control the asymmetry ratio of the spring. For a symmetry ratio of 100% the stiffness is displayed by the motor during all the displacement of the handle for the compression and decompression phases. For a symmetry ratio of 0% only the brake is used and there is no force feedback during the decompression phase. An symmetry ratio of 50% means that only the motor is used during one half of the total displacement of the handle. It can apply a maximal torque corresponding to one half of the total torque. The brake compensates for the difference when this torque is reached. By these means only 50% of the maximal torque imposed by the user is restored.

For both environments, two levels of reference stiffness are defined, corresponding to 4.5Nm/rad and 2.9Nm/rad. The lowest stiffness was chosen after preliminary user tests and corresponds to the smallest perceptible stiffness using the device. In addition, for each stiffness level, two maximal angular displacements of the handle were defined, corresponding to 15° and 30°. Thus, 44 different environments could be composed by the combination of the symmetry levels to the defined stiffness and displacement.

Taking into account the four sets and the number of participants, each stiffness asymmetry ratio was presented 360 times and each torque asymmetry ratio was presented 320 times.

2.4 PROCEDURE

The participant was comfortably seated in front of the device and his front arm was attached to the mount, so that his hand clamps the handle in the vertical position. The haptic device was hidden and the participants had no visual feedback. Each participant was allowed to get acquainted with the device, before the actual tests, by interacting as long as he desired with virtual environments with known stiffness and asymmetry level.

Nine participants realized test with stiffness asymmetry and eight others participants with torque asymmetry environments. Each participant realized four sets of 110 tests with constant stiffness and maximal displacement. Each asymmetry level was presented 10 times. A set employed one of four possible combinations: 4.5Nm/rad and 30°, 4.5Nm/rad and 15°, 2.9Nm/rad and 30° or 2.9Nm/rad and 15°. The sequence in which the four sets were realised was determined randomly. After a set, a break of 2 minutes was accorded to the participant.

For each test, an asymmetry level was randomly assigned to the virtual environment. Subjects were instructed to firmly hold the end-effector and to turn it in the direction of the virtual spring and then come back to the initial position. Three degrees before the respective end position, a buzzer triggered. The end position was indicated by a second buzzer. The participants were instructed to turn the handle back before the second signal.

After each test, the participants were asked to classify the environment as symmetrical or asymmetrical. They were allowed to compress and decompress the virtual spring at most two times.

3 RESULTS: STIFFNESS ASYMMETRY

Fig. 6.4a shows the average rate of environments perceived by the participants as symmetric, as a function of the symmetry ratio of the virtual spring for each set. Fig. 6.4b presents the average of all environments for each of the four sets and the relative standard deviation for all symmetry ratio.

The rate of environments considered as symmetric seems to be equivalent for all sets. Given the relative standard deviation, it cannot be concluded that the displacement or the stiffness has an impact on the perception of asymmetry.

With regard to Fig. 6.4b, the results demonstrate that for environments with symmetry levels inferior to 50%, participants perceived the virtual spring as asymmetrical in 80% of the tests. Conversely, for environments with symmetry ratio superior to 80%, in average 80% of environments were considered as symmetrical.

Since the stiffness was not constant during the compression and the decompression phase of the spring, the asymmetry in terms of force presented to the user was observed during the total displacement of the handle. Users could then base the discrimination on two aspects, i.e. the force perceived when they reverse the motion at the final position, or the force at initial position during the decompression phase. For a low stiffness, the initial force could be very low and imperceptible. Therefore, the participants classified the spring as asymmetrical. This may partly explain the low discrimination threshold of 50%.

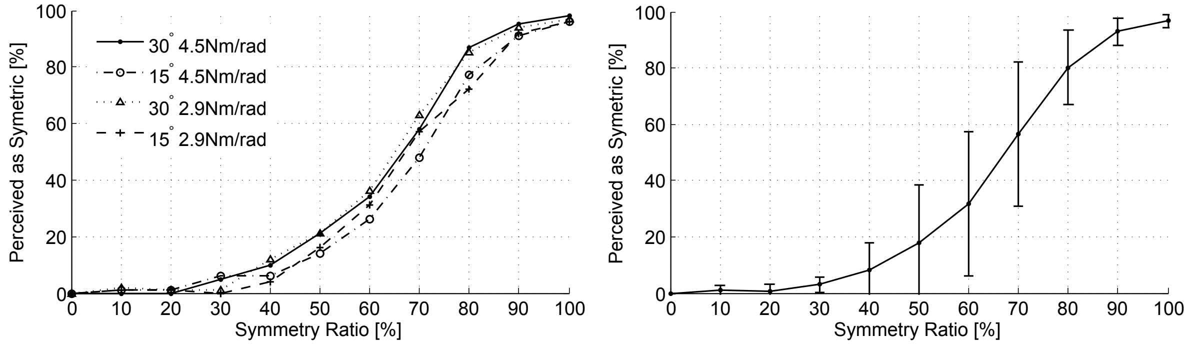

(a) Environments perceived as symetric for each set of tests

(b) Global average of environments perceived as symetric

Figure 6.4: Experimental results using stiffness asymmetry environment. The environments average rate perceived as symmetric, as a function of the asymmetry ratio, is presented for each set of tests (a). In (b) the global average and standard deviation for the four sets. In total, each symmetry ratio was presented 360 times.

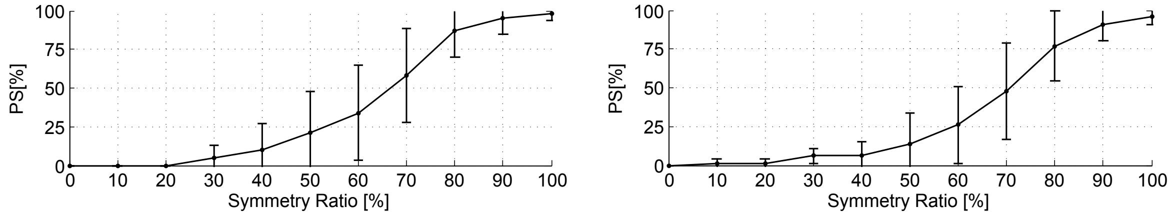

(a) 30° with 4.5Nm/rad

(b) 15° with 4.5Nm/rad

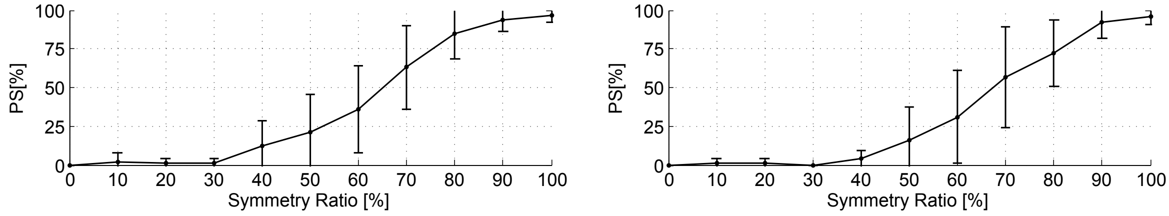

(c) 30° with 2.9Nm/rad

(d) 15° with 2.9Nm/rad

Figure 6.5: Average and standard deviation of environments perceived as symetric (PS) as a function of the stiffness asymmetry ratio for each set of stiffness and displacement.

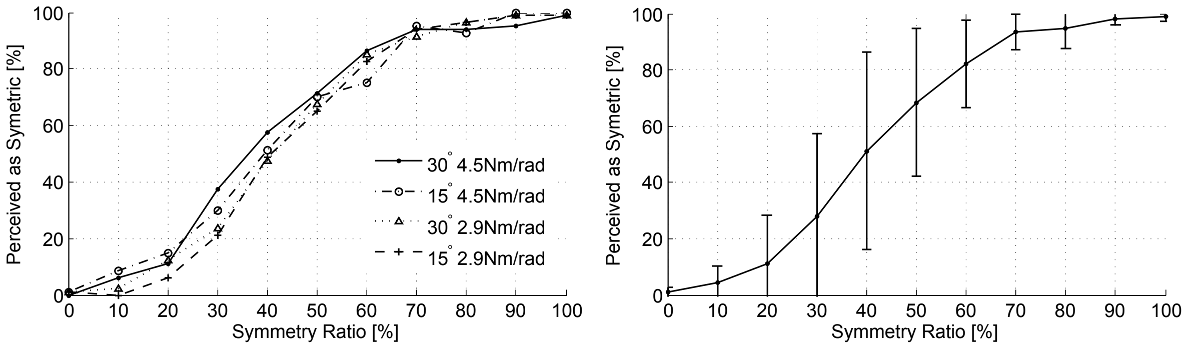

(a) Environments perceived as symetric for each set of tests

(b) Global average of environments perceived as symetric

Figure 6.6: Experimental results using torque asymmetry environments. The rate of environments perceived as symmetric as a function of the asymmetry ratio is presented for each combination of stiffness and displacement (a). In (b) the average and standard deviation of the four sets.

The average and the relative standard deviation for each set of tests are presented in Fig. 6.5. The standard deviation are equivalent for each set. The observed high standard deviation may be due to the randomly sequence in which the symmetry ratios are presented to the users.

4 RESULTS: TORQUE ASYMMETRY

Fig. 6.6a presents the rate of environments considered by the participants as symmetrical, as a function of the symmetry level of the spring for each set of tests. The total average and the relative standard deviation for the 320 test of each symmetry ratio is shown in Fig. 6.6b.

The tendency of the plots is the same whatever the stiffness or the displacement. For a symmetry ratio inferior to 20%, 87% of the environments were considered as asymmetrical. On the other extremity, for an asymmetry ratio superior to 60%, 81% of environments were perceived as symmetrical.

The asymmetry in this case is due to the limitation of the maximal torque. This means that there is a region in which the forces are the same during the compression or decompression phases. For example, considering the case when a symmetry ratio of 50% is attributed the spring with a total displacement of 30°. Up to 15°, the torque in both directions is the same, and only between 15° and 30°, the asymmetry can be observed.

By contrast to the stiffness environments, users cannot base their discriminations on the basis of perceived force close to the initial position. The asymmetry is observed in terms of maximal force only. This may partly explain the high threshold perception limit of 60%.

The average and standard deviation for each set of test is presented in Fig. 6.7. The standard deviation are equivalent for each set.

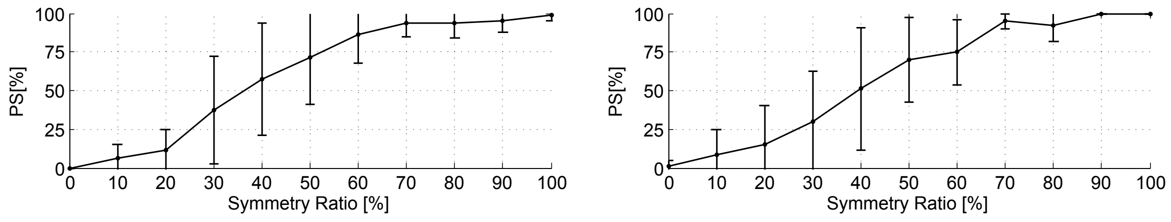

(a) 30° with 4.5Nm/rad **(b)** 15° with 4.5Nm/rad

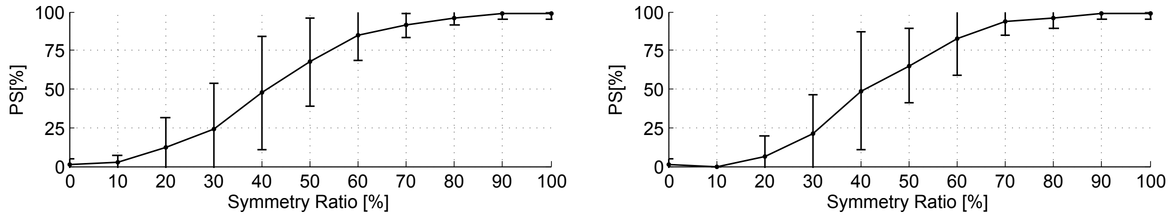

(c) 30° with 2.9Nm/rad **(d)** 15° with 2.9Nm/rad

Figure 6.7: Average and standard deviation of environments perceived as symetric (PS) as a function of the stiffness asymmetry ratio for each set of tests.

5 CONCLUDING REMARKS

The environments used in this experiment bound the energy restore by the virtual spring. When using variable stiffness, the asymmetry is observed during the total displacement of the handle. The minimal threshold under which the environments were considered as asymmetrical is 50% of symmetry ratio. When using torque asymmetry, the initial contact force is the same during the compression or decompression phase. The minimal threshold is 20%. This evidence suggests that users perceive the asymmetry on the basis of the initial contact force rather than on the final force.

As for the maximal thresholds, the spring is considered as symmetrical for a symmetry ratio superior to 80% and 60% for stiffness and torque asymmetry respectively. This suggests that users can effectively detect stiffness difference but have more difficulties to identify asymmetry when only the final force is bounded. The rigidity is perceived on the basis of mechanical work rather than stiffness.

The observed high standard deviation may be due to the randomly sequence in which the symmetry ratios are presented to the users. The response of the participant can be influenced by the previous environment. For example, a symmetry ratio of 60% is rather classified as symmetrical when it comes after a 20% symmetry ratio environment. Conversely, participants may potentially classify a environment as asymmetrical if it follows a symmetry ratio of 80%. In addition participants expected to perceive more asymmetrical than symmetrical environments. When in doubt, they classified a environment as asymmetrical.

These results indicate that a virtual environment can be perceived as symmetrical by properly controlling the initial force. In other words, the device does not need to restore exactly the same amount of energy provided by the operator. It allows the system to bound the restore energy as a consequence improving the interaction's safety and stability.

GENERAL CONCLUSIONS AND PERSPECTIVES

7

THE research reported in this thesis describes the development of a new hybrid actuation approach for force feedback devices, from mechanical design to control and user evaluation. The proposed actuator combined to its specific control laws forms an actuation system independent of any application, allowing for the implementation of such a system in many different haptic devices. The following point have previously been treated:

1. Identification of key requirements for high fidelity haptic devices design and how conventional actuation approaches meet these points;
2. Factors affecting performance in haptic rendering using either active and passive actuators, namely, stability limits, control issues and range of displayable haptic rendering;
3. Analysis of several state-of-the-art mechanical arrangements combining active, passive and semi-passive actuators and how the potential arrangements could respect the requirement obtained in (1) while avoiding the limitations observed in (2). Finally, the choice of the passive actuation technology has been investigated.

The conclusions drawn from these analyses suggested the proposed configuration combining two unidirectional brakes and a motor in parallel, and the development of specific control laws. This work then can be divided into two main parts. The first dealing with the mechanical design of the actuator and the second dealing with its control. The contribution emerged from this work are listed in the following.

1 CONTRIBUTIONS

The main contributions of this work address (1) the development of stable control laws for the hybrid actuator regardless the virtual environment model, taking into consideration the stability limits of each actuator as well as its torque capabilities; (2) the magnetostatic model that describes the tradeoffs in the design of magnetorheological brakes; (3) the concept of unidirectional brakes actuation, and (4) the results drawn from the user perception evaluation of the asymmetry generated by the intrinsic characteristics of the proposed actuation approach.

1.1 ACTUATOR CONTROL

The proposed control laws consider each actuation independently. A stability analysis gives the stability limits of each actuator via describing function and via global passivity criteria. Considering the case of one degree of freedom, the brake can be considered as intrinsically stable. The stiffness simulated by the brake depends only on its response time. On the other hand, the state-of-the-art stability condition applied to the motor demonstrated that the simulated stiffness needs to be bounded to avoid instability. The analysis highlighted also that the system is guaranteed to be passive if the virtual environment is also passive, and assuming that the active actuator does not restore all the energy stored in the virtual environment. In addition to the different stability limits, the actuator possesses different torque capabilities.

From these statements, two control approaches have been developed based on impedance control. As a function of the variation of the measured position and of the reference torque calculated by the virtual environment, the controller calculates in real time the instantaneous stiffness required by the simulation. (1) The stiffness is then shared between the brake and the motor with regard to the maximal stiffness that can be assumed by the motor as well as its maximal torque, the brake is then employed to compensate for the difference between the reference torque and the torque provided by the motor. This control method imposes a minimal participation of the motor which improves the reactivity of the system but increases the energy consumption. (2) The interaction energy involving the motor is limited to no more than the energy provided by the human operator. By these means the system is guaranteed to be passive. If some amount of energy is created due to sampling effects or due to a non-passive virtual environment, the reference torque is sent to the brake instead of the motor up to the complete dissipation of the created energy. Both algorithms work in parallel.

By contrast to current methods employed in the control of hybrid actuator for haptic feedback, both actuators are direct used to improve the simulated stiffness. It enables the system to combine the torque of both actuators, improving in consequence the range of achievable impedance.

Although these algorithms have been developed for the control of a hybrid device comprising passive and active actuators, the implementation of the stiffness bounding algorithm holds great potential in several applications using only active actuators too. Besides, the design of the controller is independent of the virtual environment model as well as the nature of the actuators employed to convey the reflective forces.

1.2 ACTUATOR DESIGN

An intrinsic characteristic of passive actuators is their limitation to generate forces only against the motion. This phenomenon introduces some drawbacks in the control of haptic devices using either passive or hybrid actuation approaches, namely, the stick phenomenon in the simulation of virtual walls and the impossibility to control the direction of the resultant force in multiple degrees of freedom. Thus, in the hybrid configuration, the active and the passive actuators are mechanically decoupled so that each actuator can be treated independently. By these means, the brake does not block the motor and does not dissipate its energy. This is achieved by the linkage of the brake to the motor using an overrunning clutch. By these means, each actuator can be treated as an independent system. Such system can be controlled without measure of interaction torques.

In order to optimize the passive actuator design taking into consideration the requirements for haptic interfaces, a modelling approach for magnetorheological brakes has been performed. The model considers the torque density, the controllability and the reactivity of the actuator, as a function of different brake geometries. The model is intended to provide a specific magnetic induction over the fluid in order to maintain the brake behaviour in a linear range. In addition, considering a maximal admissible induction in the ferromagnetic path, the circuit is designed so that the fluid and the path reach their saturation for the same magnetic flux. By these means the volume of the path is optimized. This model needs only three inputs to completely define the brake: the number of fluid gaps, the inner radius of the smallest fluid gap and the fluid gap depth. All other dimensions can be calculated in consequence. The relatively low differences observed between the model and the experimental results indicates that this method is sufficient to design a multiple cylinder MR brake.

The capability of the proposed system to dissipate energy is superior than its capability to restore energy to the human operator. High interaction torques can be displayed with safety and stability and, since most virtual environment are assumed as passive, the use of such a system may be justified. Besides, the system needs two brakes, but there are many virtual environments that can be envisioned with passive forces only in a single direction. In this case, only a motor and a brake are necessary.

1.3 ACTUATION EVALUATION

The use of passive actuator can replace the reduction stage commonly associated to the motor. A tradeoff between transparency and active torque is therefore established using impedance control. Although it has been shown that the proposed actuation approach possesses less inertia and friction than a torque equivalent motor with an ideal transmission, the active torque of the system is 27.5 times inferior than the passive torque.

The user's perception evaluation of virtual springs asymmetry simulated by a hybrid actuator suggests that users perceive the asymmetry on the basis of the initial contact force rather than on the final force. Virtual springs are considered as symmetric when the stiffness during the decompression phase is at least 80% of the stiffness during the compression phase. With regard to torque limitations, this threshold is reduced to 60%. It means that by setting the initial contact with the spring, the system can give the illusion of symmetry even if the restore energy is only a fraction of the energy provided by the operator. Furthermore, it has been demonstrated in the literature that passive devices used together with visual feedback, can provide the operator with a pseudo-haptic feedback [Lecuyer *et al.*, 2000] [Pusch *et al.*, 2008]. It allows the system to bound the restore energy as a consequence improving the interaction's safety and stability.

2 FUTURE WORK

In view of enhancing the performance of the system, some points should be considered further. The main challenge using the hybrid device is its implementation in multiple degrees of freedom interfaces. It requires the precise control of the braking force. Thus, the hysteretic behaviour of the brake should be compensated or eliminated. Besides, application in single degrees of freedom can be implemented by other means, for example, by detecting applied torques using the actuator itself.

The implementation of passive actuators in multiple degrees of freedom systems is a non-trivial task. Brakes can only generate a torque against the motion. The principal difficulty comes from the fact that it is impossible to know the user's intention, and yet, the resultant torque provided by a brake depends on the user's force. It implies that their utilisation depends on the mechanism configuration of the system, as well as the reference forces of the virtual environment. Classical approaches consists in measuring the interaction forces and then deactivate brakes on the joints where the resultant velocity and the reference torque in the controller (applied in negative feedback) have opposite signs [Kwon et Song, 2006], or in controlling the braking force intensity to minimize the error between the desired force and the braking force [Cho *et al.*, 2004]. In the case of the proposed hybrid device, undesirable braking forces which could deviate the resultant force are automatically avoided thanks to the overrunning clutches and the associated control laws.

Configurations in which brakes can be used can be obtained by the manipulability ellipsoid of the device. It gives a map of achievable forces and velocities in the workspace taking into account the Jacobian characteristics of the mechanism [Yoshikawa, 1985]. By attempting to increase the use of brakes, two possibilities came out. The first deals with the modification of the Jacobian characteristics of the system. Modifying the mechanism leads to the change of the ellipsoid and therefore to the change of the resultant braking forces. Such modification improves the utilisation of the brake in one velocity direction, but may deteriorate the performance of another direction. For wider range of forces, redundancy is necessary. The second solution then introduces more actuators than the number of degree-of-freedom. Question is, how many brakes should be incorporated in a given system. The dexterity of the mechanism increases with the number of redundant actuators per degree of freedom [Davis et Book, 1997]. Therefore, each system needs to be investigated to seek the best fitted number of brakes and the best configuration of the system. The application of the hybrid actuator in multi degrees of freedom implies also dealing with the different torque capabilities of the brake and of the motors. In regions where the brakes can not generate forces in the requested direction, the torque capability of the system corresponds to the characteristics of the motor.

As the case of numerous electromagnetic actuators, the brakes undergo an inherent hysteresis loop. The hysteresis is generated from the fact that the magnetic field is indirectly controlled by the current applied to the coil. This phenomenon not only induces important non-linearities but also may induces a residual magnetic field which increases the off-state torque exhibited by the brake. Erol et al. [Liu *et al.*, 2006] demonstrated that directly controlling the magnetic field instead of the current can effectively reduce the hysteresis of MR actuators. With this perspective in mind, an location for an hall effect sensor can predicted in the inner core during the initial design.

Considering a brake-based actuator, it has been demonstrated in the **Chapter** 1, 4.3, that a torque detection can partially avoid the stick-phenomenon induced by brakes. In this context, the possibility to detect the application and release of external forces by the actuator itself can be considered. [1] [2]

For an MR brake, based on the assumption that a relative displacement of the poles stretches the fluid chains, the magnetic reluctance of the fluid gap in modified by an external force. This hypothesis can be analytically developed using an elementary group of ferromagnetic particles placed in a non-magnetic carrier liquid. It can be theoretical concluded that when the chains operating in shear mode are stretched, the separation between the particles by the non-magnetic liquid has the effect of increasing the magnetic reluctance of the fluid gap. Thus, considering that the magnetic poles interact with the particles, when an external force induces the displacement of a magnetic pole, the chains are stretched according to the motion. Therefore, the reluctance can be associated to the external torque. Since the inductance of the coil is inversely proportional to the reluctance, a measure of the impedance perceived by the coil can be employed to validated the reluctance variation assumption. Similar to strain gauge-based torque transducers, the working principle of this method is based on the detection of a

---

[1] C. Rossa, J. Lozada, and A. Micaelli - "Magnetic flux analysis on magnetorheological actuators can detect external force variation," Sensors Conference, 2012 IEEE , vol., no., pp.1,4, 28-31 Oct. 2012 doi: 10.1109/ICSENS.2012.6411116.

[2] C. Rossa, L. Eck, A. Micaelli, and J. Lozada,. "On a novel torque detection technique for magnetorheological actuators" Sensors Journal, IEEE, doi: 10.1109/JSEN.2013.2287730.

displacement generated by a torque. Indeed, the interaction forces between the particles need to be superior to the parasitic forces characterized by viscous or coulomb friction in the rotor. Otherwise the interaction forces are not sufficient to generate a rotor displacement when it is released. Thus, parasitic torques due to bearings and seal should be eliminated.

There are several ways to obtain an actuator with similar functionalities than the actual configuration. An inconvenience of the actual implementation is the need of two identical unidirectional brakes for one degree of freedom. In order to obtain an unidirectional braking system in both direction using only one brake, an intuitive solution consists in replacing the second brake by a gear-box or a reversible mechanical system able to inverse the rotation of the brake shaft. In the hybrid configuration, the motor remains direct connected to the end-effector. Only the rotation transmitted to the brake can be inverted by the speed inverter system. This necessitates however a mechanical system and mobile mechanical parts, thus a supplementary response time is added to the system.

In view of optimizing the control and of improving the autonomy of the system, a self calibration algorithm could be implemented. It consist in determining the maximal stiffness that can be displayed by the motor in a particular application. In fact, the instability of the system depends on the viscous friction observed by the actuator. Instability due to the simulation of high stiffness are manifested under the form of oscillations. Using the discrete Fourier transform of the interaction velocity, it is possible to detect the possible oscillations of the end-effector and adjust the maximal control loop gains or increase the participation of brakes to eliminate the instability.

3 FINAL SCOPE

This thesis work has resulted in an actuation system comprising the mechanical actuator and the control laws. In the current configuration, the system input is a reference torque. The control laws determine the activation of both actuator to respect the reference torque. The complete system is independent of any application, and can be adaptable in existent haptic devices. The obtained wide dynamic range makes it also suitable for applications requiring variable impedance involving high torque capability, low power consumption and interaction safety.

PUBLICATIONS

1. C. Rossa, J. Lozada, and A. Micaelli. "*Interaction Power Flow Based Control of a 1-DOF Hybrid Haptic Interface*" Eurohaptics 2012 Conference, Lecture Notes in Computer Science, Isokoski, Poika, Springare, Jukka, vol 7283, pages 151-156, 12-15 Tampere, Finland, June 2012.
2. C. Rossa, J. Lozada, and A. Micaelli. "*A new hybrid actuator approach for force-feedback devices*" Intelligent Robots and Systems (IROS), 2012 IEEE/RSJ International Conference on, pp. 4054, 4059, 7-12 Oct. 2012 Vila Moura, Portugal, October 2012.
3. C. Rossa, J. Lozada, and A. Micaelli. "*Magnetic flux analysis on magnetorheological actuators can detect external force variation*" Sensors, 2012 IEEE, Taipei, Taiwan, 28-31 October 2012.
4. C. Rossa, J. Lozada, and A. Micaelli. "*Actionneur hybride pour interface à retour d'effort*" Conférence des jeunes chercheurs en génie électrique – SEEDS/JCGE 2013, Saint Nazaire, June 2013.
5. C. Rossa, J. Lozada, and A. Micaelli. "*Stable haptic interaction using passive and active actuators*" International Conference on Robotics and Automation (ICRA), pp. 2386, 2392, Karlsruhe, Germany, July 2013.
6. C. Rossa, L. Eck, A. Micaelli, and J. Lozada,. "*On a novel torque detection technique for magnetorheological actuators*" Sensors Journal, IEEE, doi: 10.1109/JSEN.2013.2287730. 2013.
7. C. Rossa, A. Jaegy, J. Lozada, and A. Micaelli. "*Design considerations for magnetorheological brakes*" IEEE/ASME Transactions on Mechatronics doi: 10.1109/TMECH.2013.2291966. 2013.
8. C. Rossa, A. Jaegy, A. Micaelli, and J. Lozada. "*Development of a multilayered wide-ranged torque magnetorheological brake*" Smart Materials and Structures, vol. 23 pp. 025028, doi:10.1088/0964-1726/23/2/025028. 2014
9. C. Rossa, A. Jaegy, J. Lozada, and A. Micaelli. "*Dual unidirectional hybrid actuation system for haptic feedback interfaces*" Transactions on Robotics (in progress).

10. C. Rossa, J. Lozada, and A. Micaelli. "*Actuator with hybrid actuation for a force-feedback interface*. International patent, WO2013189946.

BIBLIOGRAPHY

[Adachi *et al.*, 1995] ADACHI, Y., KUMANO, T. et OGINO, K. (1995). Intermediate representation for stiff virtual objects. *In Virtual Reality Annual International Symposium, 1995. Proceedings.*, pages 203–210. (page 7)

[Adams et Hannaford, 1999] ADAMS, R. et HANNAFORD, B. (1999). Stable haptic interaction with virtual environments. *Robotics and Automation, IEEE Transactions on*, 15(3):465 –474. (page 12)

[Aghili *et al.*, 2000] AGHILI, F., BUEHLER, M. et HOLLERBACH, J. (2000). Development of a high performance direct-drive joint. *In Intelligent Robots and Systems, 2000. (IROS 2000). Proceedings. 2000 IEEE/RSJ International Conference on*, volume 3, pages 2151–2158 vol.3. (page 33)

[Ai *et al.*, 2006] AI, H. X., WANG, D. H. et LIAO, W. H. (2006). Design and modeling of a magnetorheological valve with both annular and radial flow paths. *Journal of Intelligent Material Systems and Structures*, 17(4):327–334. (page 41)

[An et Kwon, 2006a] AN, J. et KWON, D. (2006a). Virtual friction display of hybrid force feedback interface with actuators comprising DC motor and magnetorheological brake. *In IEEE Industrial Electronics, IECON 2006 - 32nd Annual Conference on*, pages 3997 –4002. (page 22)

[An et Kwon, 2002] AN, J. et KWON, D.-S. (2002). Haptic experimentation on a hybrid active/passive force feedback device. *In Robotics and Automation, 2002. Proceedings. ICRA 02. IEEE International Conference on*, volume 4, pages 4217 – 4222 vol.4. (page 19)

[An et Kwon, 2004] AN, J. et KWON, D.-S. (2004). In haptics, the influence of the controllable physical damping on stability and performance. *In Intelligent Robots and Systems, 2004. (IROS 2004). Proceedings. 2004 IEEE/RSJ International Conference on*, volume 2, pages 1204 – 1209 vol.2. (page 20)

[An et Kwon, 2006b] AN, J. et KWON, D.-S. (2006b). Stability and performance of haptic interfaces with active/passive actuatorsâ€"theory and experiments. *The International Journal of Robotics Research*, 25(11):1121–1136. (page 34)

[Asada et Kanade, 1981] ASADA, H. et KANADE, T. (1981). Design of direct-drive mechanical arms. (page 33)

[Assadsangabi *et al.*, 2011] ASSADSANGABI, B., DANESHMAND, F., VAHDATI, N., EGHTESAD, M. et BAZARGAN-LARI, Y. (2011). Optimization and design of disk-type mr brakes. *International Journal of Automotive Technology*, 12:921–932. (pages 75 and 77)

[Astley et Hayward, 2000] ASTLEY, O. et HAYWARD, V. (2000). Design constraints for haptic surgery simulation. *In Robotics and Automation, 2000. Proceedings. ICRA '00. IEEE International Conference on*, volume 3, pages 2446–2451 vol.3. (page 6)

[Avraam, 2009] AVRAAM, M. (2009). *MR-fluid brake design and its application to a portable muscular rehabilitation device*. Thèse de doctorat, Ph. D. thesis, Université Libre de Bruxelle, Bruxelle, Belgium. (page 79)

[Avraam *et al.*, 2008] AVRAAM, M., HORODINCA, M., LETIER, P. et PREUMONT, A. (2008). Portable smart wrist rehabilitation device driven by rotational MR-fluid brake actuator for telemedecine applications. *In Intelligent Robots and Systems, 2008. IROS 2008. IEEE/RSJ International Conference on*, pages 1441 –1446. (page 75)

[Badescu *et al.*, 2002] BADESCU, M., WAMPLER, C. et MAVROIDIS, C. (2002). Rotary haptic knob for vehicular instrument controls. *In Haptic Interfaces for Virtual Environment and Teleoperator Systems, 2002. HAPTICS 2002. Proceedings. 10th Symposium on*, pages 342 –343. (pages 19 and 34)

[Baser *et al.*, 2012a] BASER, O., KONUKSEVEN, E. et GUROCAK, H. (2012a). Stability and transparency improvement in haptic device employing both mr-brake and active actuator. *In RO-MAN, 2012 IEEE*, pages 12 –18. (pages 21 and 34)

[Baser *et al.*, 2012b] BASER, O., KONUKSEVEN, E. I. et GUROCAK, H. (2012b). Transparency improvement in haptic devices with a torque compensator using motor current. *In Haptics: Perception, Devices, Mobility, and Communication*, pages 37–46. Springer. (page 15)

[Bergamasco *et al.*, 1989] BERGAMASCO, M., SALSEDO, F. et DARIO, P. (1989). A linear sma motor as direct-drive robotic actuator. *In Robotics and Automation, 1989. Proceedings., 1989 IEEE International Conference on*, pages 618–623 vol.1. (page 33)

[Bernstein *et al.*, 2005] BERNSTEIN, N., LAWRENCE, D. et PAO, L. Y. (2005). Friction modeling and compensation for haptic interfaces. *In Eurohaptics Conference, 2005 and Sympo-*

sium on Haptic Interfaces for Virtual Environment and Teleoperator Systems, 2005. World Haptics 2005. First Joint, pages 290–295. (page 21)

[Bi *et al.*, 2004] BI, D., LI, Y., TSO, S. et WANG, G. (2004). Friction modeling and compensation for haptic display based on support vector machine. *Industrial Electronics, IEEE Transactions on*, 51(2):491–500. (page 21)

[Bica, 2004] BICA, I. (2004). Magnetorheological suspension electromagnetic brake. *Journal of Magnetism and Magnetic Materials*, 270(3):321 – 326. (page 40)

[Bicchi *et al.*, 2005] BICCHI, A., TONIETTI, G., BAVARO, M. et PICCIGALLO, M. (2005). Variable stiffness actuators for fast and safe motion control. *In* DARIO, P. et CHATILA, R., éditeurs : *Robotics Research*, volume 15 de *Springer Tracts in Advanced Robotics*, pages 527–536. Springer Berlin Heidelberg. (page 33)

[Blake et Gurocak, 2009] BLAKE, J. et GUROCAK, H. (2009). Haptic glove with mr brakes for virtual reality. *Mechatronics, IEEE/ASME Transactions on*, 14(5):606 –615. (pages 15 and 41)

[Bossis *et al.*, 2002] BOSSIS, G., LACIS, S., MEUNIER, A. et VOLKOVA, O. (2002). Magnetorheological fluids. *Journal of Magnetism and Magnetic Materials*, 252(0):224 – 228. <ce:title>Proceedings of the 9th International Conference on Magnetic Fluids</ce:title>. (page 71)

[Brown, 1998] BROWN, J. M. (1998). *Passive implementation of multibody simulations for haptic display*. Thèse de doctorat, Northwestern University. (pages 8, 9, and 12)

[Campion *et al.*, 2006] CAMPION, G., GOSLINE, A. et HAYWARD, V. (2006). Initial results using eddy current brakes as fast turn-on, programmable physical dampers for haptic rendering. *In Haptic Interfaces for Virtual Environment and Teleoperator Systems, 2006 14th Symposium on*, pages 73–74. (pages 20 and 39)

[Canudas de Wit *et al.*, 1995] Canudas de WIT, C., OLSSON, H., ASTROM, K. J. et LISCHINSKY, P. (1995). A new model for control of systems with friction. *Automatic Control, IEEE Transactions on*, 40(3):419–425. (page 21)

[Carignan et Cleary, 2000] CARIGNAN, C. R. et CLEARY, K. R. (2000). Closed-loop force control for haptic simulation of virtual environments. *Haptics-e*, 1:01–1. (page 32)

[Carlson et Jolly, 2000] CARLSON, J. et JOLLY, M. R. (2000). Mr fluid, foam and elastomer devices. *Mechatronics*, 10(4–5):555 – 569. (page 73)

[Carlson et Duclos, 1990] CARLSON, J. D. et DUCLOS, T. G. (1990). Electrorheological fluid force transmission and conversion device. U.S. Classification: 192/21.5 International Classification: : F16D 2700. (page 76)

[Chapuis, 2009] CHAPUIS, D. (2009). *Application of ultrasonic motors to MR-compatible haptic interfaces*. Thèse de doctorat, Ecole Polytechnique Federale de Lausanne. (page 34)

[Chapuis *et al.*, 2006] CHAPUIS, D., GASSERT, R., BURDET, E. et BLEULER, H. (2006). Hybrid ultrasonic motor and electrorheological clutch system for mr-compatible haptic rendering. *In Intelligent Robots and Systems, 2006 IEEE/RSJ International Conference on*, pages 1553 –1557. (pages 19 and 35)

[Chapuis *et al.*, 2007] CHAPUIS, D., MICHEL, X., GASSERT, R., CHEW, C.-M., BURDET, E. et BLEULER, H. (2007). A haptic knob with a hybrid ultrasonic motor and powder clutch actuator. *In EuroHaptics Conference, 2007 and Symposium on Haptic Interfaces for Virtual Environment and Teleoperator Systems. World Haptics 2007. Second Joint*, pages 200 –205. (page 19)

[Chen *et al.*, 2008] CHEN, G., YANG, Y., ZOU, K. et SUN, Y. (2008). Electromagnetic clutch based high-low carpet jacquard control system. *In Intelligent Information Technology Application Workshops, 2008. IITAW '08. International Symposium on*, pages 176–179. (page 40)

[Chen et Liao, 2009] CHEN, J. et LIAO, W.-H. (2009). Design and testing of assistive knee brace with magnetorheological actuator. *In Robotics and Biomimetics, 2008. ROBIO 2008. IEEE International Conference on*, pages 512 –517. (pages 19 and 34)

[Chen et Liao, 2010] CHEN, J. Z. et LIAO, W. H. (2010). Design, testing and control of a magnetorheological actuator for assistive knee braces. *Smart Materials and Structures*, 19(3):035029. (page 41)

[Chew *et al.*, 2004] CHEW, C.-M., HONG, G.-S. et ZHOU, W. (2004). Series damper actuator: a novel force/torque control actuator. *In Humanoid Robots, 2004 4th IEEE/RAS International Conference on*, volume 2, pages 533–546 Vol. 2. (pages 34 and 35)

[Cho *et al.*, 2004] CHO, C., KIM, M. et SONG, J.-B. (2004). Direct control of a passive haptic device based on passive force manipulability ellipsoid analysis. *International Journal of Control Automation and Systems*, 2:238–246. (page 146)

[Cho *et al.*, 2007] CHO, C., SONG, J.-B. et KIM, M. (2007). Energy-based control of a haptic device using brakes. *Systems, Man, and Cybernetics, Part B: Cybernetics, IEEE Transactions on*, 37(2):341 –349. (pages 15 and 17)

[Choi *et al.*, 2011] CHOI, J., HONG, S., LEE, W., KANG, S. et KIM, M. (2011). A robot joint with variable stiffness using leaf springs. *Robotics, IEEE Transactions on*, 27(2):229–238. (page 33)

[Cholewiak *et al.*, 2008] CHOLEWIAK, S., TAN, H. et EBERT, D. (2008). Haptic identification of stiffness and force magnitude. *In Haptic interfaces for virtual environment and teleoperator systems, 2008. haptics 2008. symposium on*, pages 87–91. (page 133)

[Claeyssen *et al.*, 2001] CLAEYSSEN, F., LE LETTY, R., BARILLOT, F., LHERMET, N., FABBRO, H., GUAY, P., YORCK, M. et BOUCHILLOUX, P. (2001). Mechanisms based on piezoactuators. pages 225–233. (page 39)

[Colgate et Brown, 1994] COLGATE, J. et BROWN, J. (1994). Factors affecting the z-width of a haptic display. *In , 1994 IEEE International Conference on Robotics and Automation, 1994. Proceedings*, pages 3205 –3210 vol.4. (page 8)

[Colgate *et al.*, 1993] COLGATE, J., GRAFING, P., STANLEY, M. et SCHENKEL, G. (1993). Implementation of stiff virtual walls in force-reflecting interfaces. *In Virtual Reality Annual International Symposium, 1993., 1993 IEEE*, pages 202–208. (pages 11 and 14)

[Colgate *et al.*, 1996] COLGATE, J., PESHKIN, M. et WANNASUPHOPRASIT, W. (1996). Nonholonomic haptic display. *In Robotics and Automation, 1996. Proceedings., 1996 IEEE International Conference on*, volume 1, pages 539 –544 vol.1. (pages 17 and 18)

[Colgate et Schenkel, 1994] COLGATE, J. et SCHENKEL, G. (1994). Passivity of a class of sampled-data systems: application to haptic interfaces. *In American Control Conference, 1994*, volume 3, pages 3236 – 3240 vol.3. (pages 10, 14, and 52)

[Colgate *et al.*, 1995] COLGATE, J., STANLEY, M. et BROWN, J. (1995). Issues in the haptic display of tool use. *In 1995 IEEE/RSJ International Conference on Intelligent Robots and Systems 95. 'Human Robot Interaction and Cooperative Robots', Proceedings*, volume 3, pages 140 –145 vol.3. (page 12)

[Company,] COMPANY, B. T. C. http://www.inorganics.basf.com. (page 79)

[Conti et Khatib, 2009] CONTI, F. et KHATIB, O. (2009). A new actuation approach for haptic interface design. *The International Journal of Robotics Research*, 28(6):834–848. (pages 19 and 35)

[Corporation,] CORPORATION, L. http://www.lord.com/products-and-solutions/magneto-rheological-(pages 79, 80, 85, and 103)

[Cui *et al.*, 2003] CUI, J., TOSUNOGLU, S., ROBERTS, R., MOORE, C. et REPPERGER, D. W. (2003). A review of teleoperation system control. *In Proceedings of the 2006 Florida conference recent advances in robotics (FCRAR), Florida Atlantic University, FL.* (page 6)

[Davis et Book, 1997] DAVIS, H. et BOOK, W. (1997). Torque control of a redundantly actuated passive manipulator. *In American Control Conference, 1997. Proceedings of the 1997*, volume 2, pages 959–963 vol.2. (page 147)

[Diolaiti *et al.*, 2005] DIOLAITI, N., NIEMEYER, G., BARBAGLI, F. et SALISBURY, J. (2005). A criterion for the passivity of haptic devices. *In Robotics and Automation, 2005. ICRA 2005. Proceedings of the 2005 IEEE International Conference on*, pages 2452 – 2457. (page 8)

[Duan *et al.*, 2006] DUAN, Y. F., NI, Y. Q. et KO, J. M. (2006). Cable vibration control using magnetorheological dampers. *Journal of Intelligent Material Systems and Structures*, 17(4): 321–325. (page 41)

[Durlach *et al.*, 1989] DURLACH, N., DELHORNE, L., WONG, A., KO, W., RABINOWITZ, W. et HOLLERBACH, J. (1989). Manual discrimination and identification of length by the finger-span method. *Perception & Psychophysics*, 46(1):29–38. (page 133)

[Dyke *et al.*, 1998] DYKE, S. J., JR, B. F. S., SAIN, M. K. et CARLSON, J. D. (1998). An experimental study of mr dampers for seismic protection. *Smart Materials and Structures*, 7(5):693. (page 41)

[Eddens, 1982] EDDENS, G. R. (US Patent 4.350.91 septembre 1982). Magnetic particle devices. (page 40)

[Eppinger et Seering, 1987a] EPPINGER, S. et SEERING, W. (1987a). Introduction to dynamic models for robot force control. *Control Systems Magazine, IEEE*, 7(2):48–52. (page 32)

[Eppinger et Seering, 1987b] EPPINGER, S. et SEERING, W. (1987b). Understanding bandwidth limitations in robot force control. *In Robotics and Automation. Proceedings. 1987 IEEE International Conference on*, volume 4, pages 904–909. (page 32)

[Fang *et al.*, 2005] FANG, C., ZHAO, B. Y., CHEN, L. S., WU, Q., LIU, N. et HU, K. A. (2005). The effect of the green additive guar gum on the properties of magnetorheological fluid. *Smart Materials and Structures*, 14(1):N1–N5. (page 71)

[Fauteux *et al.*, 2009] FAUTEUX, P., LAURIA, M., LEGAULT, M.-A., HEINTZ, B. et MICHAUD, F. (2009). Dual differential rheological actuator for robotic interaction tasks. *In Advanced Intelligent Mechatronics, 2009. AIM 2009. IEEE/ASME International Conference on*, pages 47 –52. (pages 36, 41, 76, and 77)

[Forrest *et al.*, 2009] FORREST, N., BAILLIE, S. et TAN, H. (2009). Haptic stiffness identification by veterinarians and novices: A comparison. *In EuroHaptics conference, 2009 and Symposium on Haptic Interfaces for Virtual Environment and Teleoperator Systems. World Haptics 2009. Third Joint*, pages 646–651. (page 133)

[Furusho *et al.*, 2002] FURUSHO, J., SAKAGUCHI, M., TAKESUE, N. et KOYANAGI, K. (2002). Development of er brake and its application to passive force display. *Journal of Intelligent Material Systems and Structures*, 13(7-8):425–429. (page 40)

[Gedik *et al.*, 2012] GEDIK, E., KURT, H., RECEBLI, Z. et BALAN, C. (2012). Two-dimensional cfd simulation of magnetorheological fluid between two fixed parallel plates applied external magnetic field. *Computers & Fluids*, (0):–. (page 71)

[Gillespie et Cutkosky, 1996] GILLESPIE, R. B. et CUTKOSKY, M. R. (1996). Stable user-specific haptic rendering of the virtual wall. *In Proceedings of the ASME International Mechanical Engineering Congress and Exhibition*, volume 58, page 397–406. (page 14)

[Gogola et Goldfarb, 1999] GOGOLA, M. et GOLDFARB, M. (1999). Design of a pzt-actuated proportional drum brake. *Mechatronics, IEEE/ASME Transactions on*, 4(4):409–416. (page 39)

[Goldfarb et Celanovic, 1997] GOLDFARB, M. et CELANOVIC, N. (1997). Modeling piezoelectric stack actuators for control of micromanipulation. *Control Systems, IEEE*, 17(3):69–79. (page 39)

[Gonenc et Gurocak, 2012] GONENC, B. et GUROCAK, H. (2012). Haptic interface with hybrid actuator for virtual needle insertion and tissue cutting. *In Haptics Symposium (HAPTICS), 2012 IEEE*, pages 451 –455. (page 19)

[Gosline et Hayward, 2008] GOSLINE, A. et HAYWARD, V. (2008). Eddy current brakes for haptic interfaces: Design, identification, and control. *Mechatronics, IEEE/ASME Transactions on*, 13(6):669 –677. (page 39)

[Grunwald et Olabi, 2008] GRUNWALD, A. et OLABI, A. (2008). Design of magneto-rheological (mr) valve. *Sensors and Actuators A: Physical*, 148(1):211 – 223. (page 41)

[Gudmundsson *et al.*, 2010] GUDMUNDSSON, K. H., JONSDOTTIR, F. et THORSTEINSSON, F. (2010). A geometrical optimization of a magneto-rheological rotary brake in a prosthetic knee. *Smart Materials and Structures*, 19(3):035023. (pages 76 and 77)

[Guo et Liao, 2011] GUO, H. et LIAO, W.-H. (2011). Optimization of a multifunctional actuator utilizing magnetorheological fluids. *In Advanced Intelligent Mechatronics (AIM), 2011 IEEE/ASME International Conference on*, pages 67 –72. (pages 76 and 115)

[Guo *et al.*, 2003] GUO, N., DU, H. et LI, W. (2003). Finite element analysis and simulation evaluation of a magnetorheological valve. *The International Journal of Advanced Manufacturing Technology*, 21:438–445. 10.1007/s001700300051. (page 77)

[Ham *et al.*, 2007] HAM, R. V., VANDERBORGHT, B., DAMME, M. V., VERRELST, B. et LEFEBER, D. (2007). Maccepa, the mechanically adjustable compliance and controllable equilibrium position actuator: Design and implementation in a biped robot. *Robotics and Autonomous Systems*, 55(10):761 – 768. (page 33)

[Han *et al.*, 2009] HAN, Y.-M., KIM, C.-J. et CHOI, S.-B. (2009). A magnetorheological fluid-based multifunctional haptic device for vehicular instrument controls. *Smart Materials and Structures*, 18(1):015002. (page 42)

[Hannaford et Ryu, 2002] HANNAFORD, B. et RYU, J.-H. (2002). Time-domain passivity control of haptic interfaces. *Robotics and Automation, IEEE Transactions on*, 18(1):1 – 10. (pages 12, 13, and 53)

[Hayward et Astley, 2000] HAYWARD, V. et ASTLEY, O. R. (2000). Performance measures for haptic interfaces. *In Robotics Research*, pages 195–206. Springer. (page 6)

[Hayward *et al.*, 2004] HAYWARD, V., ASTLEY, O. R., CRUZ-HERNANDEZ, M., GRANT, D. et ROBLES-DE-LA-TORRE, G. (2004). Haptic interfaces and devices. *Sensor Review*, 24(1):16–29. (pages 6 and 7)

[Hirata *et al.*, 2010] HIRATA, Y., SUZUKI, K. et KOSUGE, K. (2010). Motion control of passive haptic device using wires with servo brakes. *In Intelligent Robots and Systems (IROS), 2010 IEEE/RSJ International Conference on*, pages 3123–3129. (page 40)

[Hogan, 1989] HOGAN, N. (1989). Controlling impedance at the man/machine interface. *In Robotics and Automation, 1989. Proceedings., 1989 IEEE International Conference on*, pages 1626–1631. IEEE. (page 7)

[Huang *et al.*, 2002] HUANG, J., ZHANG, J., YANG, Y. et WEI, Y. (2002). Analysis and design of a cylindrical magneto-rheological fluid brake. *Journal of Materials Processing Technology*, 129(1–3):559 – 562. The 10th International Manufacturing Conference in China (IMCC 2002). (pages 41, 75, and 84)

[Hurmuzlu *et al.*, 1998] HURMUZLU, Y., EPHANOV, A. et STOIANOVICI, D. (1998). Effect of a pneumatically driven haptic interface on the perceptional capabilities of human operators. *Presence: Teleoperators and Virtual Environments*, 7(3):290–307. (page 133)

[J. *et al.*, 2002] J., H., J.Q., Z., Y., Y. et Y.Q., W. (2002). Analysis and design of a cylindrical magneto-rheological fluid brake. *Journal of Materials Processing Technology*, 129(1):559–562. (page 41)

[Jolly *et al.*, 1998] JOLLY, M. R., BENDER, J. W. et CARLSON, J. D. (1998). Properties and applications of commercial magnetorheological fluids. *In* DAVIS, L. P., éditeur : *Smart Structures and Materials*, volume 3327, pages 262–275. SPIE. (page 71)

[Jolly *et al.*, 1996] JOLLY, M. R., CARLSON, J. D. et MUÑOZ, B. C. (1996). A model of the behaviour of magnetorheological materials. *Smart Materials and Structures*, 5:607. (page 73)

[Jones et Hunter, 1990] JONES, L. et HUNTER, I. (1990). A perceptual analysis of stiffness. *Experimental Brain Research*, 79(1):150–156. (page 133)

[Jones et Hunter, 1993] JONES, L. A. et HUNTER, I. W. (1993). A perceptual analysis of viscosity. *Experimental Brain Research*, 94:343–351. 10.1007/BF00230304. (page 133)

[Joung et See, 2008] JOUNG, C. et SEE, H. (2008). The influence of wall interaction on dynamic particle modelling of magneto-rheological suspensions between shearing plates. *Rheologica Acta*, 47:917–927. 10.1007/s00397-008-0282-3. (page 73)

[Karakoc *et al.*, 2008] KARAKOC, K., PARK, E. J. et SULEMAN, A. (2008). Design considerations for an automotive magnetorheological brake. *Mechatronics*, 18(8):434 – 447. (pages 75, 76, and 80)

[Kazerooni et Kim, 1988] KAZEROONI, H. et KIM, S. (1988). A new architecture for direct drive robots. *In Robotics and Automation, 1988. Proceedings., 1988 IEEE International Conference on*, pages 442–445 vol.1. (page 33)

[Kikuchi *et al.*, 2009] KIKUCHI, T., IKEDA, K., OTSUKI, K., KAKEHASHI, T. et FURUSHO, J. (2009). Compact MR fluid clutch device for human-friendly actuator. *Journal of Physics: Conference Series*, 149:012059. (page 76)

[Kikuchi et Kobayashi, 2011] KIKUCHI, T. et KOBAYASHI, K. (2011). Development of cylindrical magnetorheological fluid brake for virtual cycling system. *In Robotics and Biomimetics (ROBIO), 2011 IEEE International Conference on*, pages 2547 –2552. (pages 74 and 75)

[Kikuchi *et al.*, 2007] KIKUCHI, T., XINGHAO, H., FUKUSHIMA, K., ODA, K., FURUSHO, J. et INOUE, A. (2007). Quasi-3-dof rehabilitation system for upper limbs: Its force-feedback mechanism and software for rehabilitation. *In Rehabilitation Robotics, 2007. ICORR 2007. IEEE 10th International Conference on*, pages 24–27. (page 7)

[Kim et Ryu, 2004a] KIM, J.-P. et RYU, J. (2004a). Energy bounding algorithm based on passivity theorem for stable haptic interaction control. *In Haptic Interfaces for Virtual Environment and Teleoperator Systems, 2004. HAPTICS '04. Proceedings. 12th International Symposium on*, pages 351–357. (page 14)

[Kim et Ryu, 2004b] KIM, J.-P. et RYU, J. (2004b). Stable haptic interaction control using energy bounding algorithm. *In Intelligent Robots and Systems, 2004. (IROS 2004). Proceedings. 2004 IEEE/RSJ International Conference on*, volume 2, pages 1210 – 1217 vol.2. (page 14)

[Kittipoomwong *et al.*, 2005] KITTIPOOMWONG, D., KLINGENBERG, D. J. et ULICNY, J. C. (2005). Dynamic yield stress enhancement in bidisperse magnetorheological fluids. *Journal of Rheology*, 49(6):1521–1538. (pages 71 and 73)

[Klingenberg, 2001] KLINGENBERG, D. J. (2001). Magnetorheology: Applications and challenges. *AIChE Journal*, 47(2):246–249. (page 40)

[Koccak *et al.*, 2011] KOCCAK, U., PALMERIUS, K. L., FORSELL, C., YNNERMAN, A. et COOPER, M. (2011). Analysis of the jnd of stiffness in three modes of comparison. *In*

Proceedings of the 6th international conference on Haptic and audio interaction design, HAID'11, pages 22–31, Berlin, Heidelberg. Springer-Verlag. (page 134)

[Kong et Lowe, 2005] KONG, Y.-K. et LOWE, B. D. (2005). Evaluation of handle diameters and orientations in a maximum torque task. *International Journal of Industrial Ergonomics*, 35(12):1073 – 1084. (page 103)

[Koo *et al.*, 2006] KOO, J.-H., GONCALVES, F. D. et AHMADIAN, M. (2006). A comprehensive analysis of the response time of mr dampers. *Smart Materials and Structures*, 15(2):351. (pages 78 and 81)

[Kwon et Song, 2006] KWON, T.-B. et SONG, J.-B. (2006). Force display using a hybrid haptic device composed of motors and brakes. *Mechatronics*, 16(5):249 – 257. (pages 19, 34, and 146)

[Lauria *et al.*, 2008] LAURIA, M., LEGAULT, M.-A., LAVOIE, M.-A. et MICHAUD, F. (2008). Differential elastic actuator for robotic interaction tasks. *In Robotics and Automation, 2008. ICRA 2008. IEEE International Conference on*, pages 3606–3611. (page 33)

[Laycock et Day, 2003] LAYCOCK, S. D. et DAY, A. M. (2003). Recent developments and applications of haptic devices. *Computer Graphics Forum*, 22(2):117–132. (page 6)

[Lecuyer *et al.*, 2000] LECUYER, A., COQUILLART, S., KHEDDAR, A., RICHARD, P. et COIFFET, P. (2000). Pseudo-haptic feedback: can isometric input devices simulate force feedback? *In Virtual Reality, 2000. Proceedings. IEEE*, pages 83–90. (page 146)

[Lee et Wereley, 2000] LEE, D. et WERELEY, N. M. (2000). Analysis of electro- and magneto-rheological flow mode dampers using Herschel-Bulkley model. *Proceedings of SPIE*, 3989(1):244–255. (page 73)

[Lee et Lee, 2004] LEE, K. et LEE, D. Y. (2004). Multirate control of haptic interface for stability and high fidelity. *In Systems, Man and Cybernetics, 2004 IEEE International Conference on*, volume 3, pages 2542–2547. IEEE. (page 14)

[Lee et Lee, 2003] LEE, M. H. et LEE, D. Y. (2003). Stability of haptic interface using nonlinear virtual coupling. *In Systems, Man and Cybernetics, 2003. IEEE International Conference on*, volume 4, pages 3420–3424 vol.4. (page 14)

[Li et Du, 2003] LI, W. et DU, H. (2003). Design and experimental evaluation of a magnetorheological brake. *The International Journal of Advanced Manufacturing Technology*, 21:508–515. (pages 75, 80, and 81)

[Li *et al.*, 2007] LI, W., LIU, B., KOSASIH, P. et ZHANG, X. (2007). A 2-dof mr actuator joystick for virtual reality applications. *Sensors and Actuators A: Physical*, 137(2):308 – 320. (page 75)

[Li *et al.*, 2002] LI, W. H., DU, H., CHEN, G., YEO, S. H. et GUO, N. Q. (2002). Nonlinear rheological behavior of magnetorheological fluids: step-strain experiments. *Smart Materials and Structures*, 11(2):209. (page 71)

[Lindler et Wereley, 2003] LINDLER, J. et WERELEY, N. M. (2003). Quasi-steady bingham plastic analysis of an electrorheological flow mode bypass damper with piston bleed. *Smart Materials and Structures*, 12(3):305–317. (page 73)

[Liu *et al.*, 2006] LIU, B., LI, W. H., KOSASIH, P. B. et ZHANG, X. Z. (2006). Development of an MR-brake-based haptic device. *Smart Materials and Structures*, 15(6):1960–1966. (pages 42, 77, 115, 117, 128, and 147)

[Lozada *et al.*, 2007] LOZADA, J., HAFEZ, M. et BOUTILLON, X. (2007). A novel haptic interface for musical keyboards. *In Advanced intelligent mechatronics, 2007 IEEE/ASME international conference on*, pages 1 –6. (page 41)

[MacLean et Roderick, 1999] MACLEAN, K. E. et RODERICK, J. B. (1999). Smart tangible displays in the everyday world: a haptic door knob. *In Advanced Intelligent Mechatronics, 1999. Proceedings. 1999 IEEE/ASME International Conference on*, pages 203–208. IEEE. (page 6)

[Mahvash et Hayward, 2003] MAHVASH, M. et HAYWARD, V. (2003). Passivity-based high-fidelity haptic rendering of contact. *In Robotics and Automation, 2003. Proceedings. ICRA'03. IEEE International Conference on*, volume 3, pages 3722–3728. IEEE. (page 7)

[Mahvash et Okamura, 2006] MAHVASH, M. et OKAMURA, A. (2006). Friction compensation for a force-feedback telerobotic system. *In Robotics and Automation, 2006. ICRA 2006. Proceedings 2006 IEEE International Conference on*, pages 3268–3273. (page 21)

[Maillard *et al.*, 2008] MAILLARD, P., FLACTION, L., SAMUR, E., HELLIER, D., PASSENGER, J. et BLEULER, H. (2008). Instrumentation of a clinical colonoscope for surgical simulation. *In Engineering in Medicine and Biology Society, 2008. EMBS 2008. 30th Annual International Conference of the IEEE*, pages 70–73. (page 40)

[Matsuoka et Townsend, 2001] MATSUOKA, Y. et TOWNSEND, B. (2001). Design of life-size haptic environments. *In* RUS, D. et SINGH, S., éditeurs : *Experimental Robotics VII*, volume 271 de *Lecture Notes in Control and Information Sciences*, pages 461–470. Springer Berlin Heidelberg. (pages 15 and 40)

[McDaniel, 2011] MCDANIEL, A. J. (2011). Magneto-rheological brake-clutch apparatuses and methods. U.S. Classification: 192/12.00A. (page 75)

[Melle et Martin, 2003] MELLE, S. et MARTIN, J. E. (2003). Chain model of a magnetorheological suspension in a rotating field. *The Journal of Chemical Physics*, 118(21):9875–9881. (page 71)

[Migliore *et al.*, 2005] MIGLIORE, S., BROWN, E. et DEWEERTH, S. (2005). Biologically inspired joint stiffness control. *In Robotics and Automation, 2005. ICRA 2005. Proceedings of the 2005 IEEE International Conference on*, pages 4508–4513. (page 33)

[Milecki, 2001] MILECKI, A. (2001). Investigation and control of magneto–rheological fluid dampers. *International Journal of Machine Tools and Manufacture*, 41(3):379 – 391. (page 41)

[Miller *et al.*, 2000] MILLER, B. E., COLGATE, J. E. et FREEMAN, R. A. (2000). Guaranteed stability of haptic systems with nonlinear virtual environments. *Robotics and Automation, IEEE Transactions on*, 16(6):712–719. (page 14)

[Mills et Goldenberg, 1989] MILLS, J. K. et GOLDENBERG, A. A. (1989). Force and position control of manipulators during constrained motion tasks. *Robotics and Automation, IEEE Transactions on*, 5(1):30–46. (page 7)

[Minsky *et al.*, 1990] MINSKY, M., MING, O.-y., STEELE, O., BROOKS, Jr., F. P. et BEHENSKY, M. (1990). Feeling and seeing: issues in force display. *In Proceedings of the 1990 symposium on Interactive 3D graphics*, I3D '90, pages 235–241, New York, NY, USA. ACM. (page 7)

[Mohammadi *et al.*, 2010] MOHAMMADI, N., MAHJOOB, M., KAFFASHI, B. et MALAKOOTI, S. (2010). An experimental evaluation of pre-yield and post-yield rheological models of magnetic field dependent smart materials. *Journal of Mechanical Science and Technology*, 24:1829–1837. 10.1007/s12206-010-0607-x. (page 73)

[Mohand-Ousaid *et al.*, 2012] MOHAND-OUSAID, A., MILLET, G., RÉGNIER, S., HALIYO, S. et HAYWARD, V. (2012). Haptic interface transparency achieved through viscous coupling. *The International Journal of Robotics Research*, 31(3):319–329. (pages 14 and 35)

[Munir *et al.*, 1999] MUNIR, S., TOGNETTI, L. et BOOK, W. (1999). Experimental evaluation of a new braking system for use in passive haptic displays. *In American Control Conference, 1999. Proceedings of the 1999*, volume 6, pages 4456–4460. IEEE. (page 7)

[Nam *et al.*, 2008] NAM, Y.-J., MOON, Y.-J. et PARK, M.-K. (2008). Performance improvement of a rotary mr fluid actuator based on electromagnetic design. *Journal of Intelligent Material Systems and Structures*, 19(6):695–705. (page 115)

[Nam et Park, 2007] NAM, Y.-J. et PARK, M.-K. (2007). A hybrid haptic device for wide-ranged force reflection and improved transparency. *In Control, Automation and Systems, 2007. ICCAS'07. International Conference on*, pages 1015–1020. IEEE. (pages 14, 22, and 34)

[Nguyen et Choi, 2011] NGUYEN, P. et CHOI, S. (2011). A new approach to magnetic circuit analysis and its application to the optimal design of a bi-directional magnetorheological brake. *Smart Materials and Structures*, 20(12):125003. (page 84)

[Nguyen et Choi, 2010] NGUYEN, Q. H. et CHOI, S. B. (2010). Optimal design of an automotive magnetorheological brake considering geometric dimensions and zero-field friction heat. *Smart Materials and Structures*, 19(11):115024. (pages 40 and 76)

[Nguyen et Choi, 2012] NGUYEN, Q. H. et CHOI, S. B. (2012). Selection of magnetorheological brake types via optimal design considering maximum torque and constrained volume. *Smart Materials and Structures*, 21(1):015012. (page 76)

[Nguyen *et al.*, 2011] NGUYEN, Q. H., JEON, J. C. et CHOI, S. B. (2011). Optimal design of an hybrid magnetorheological brake for Middle-Sized motorcycles. *Applied Mechanics and Materials*, 52-54:371–377. (page 77)

[Nikitczuk *et al.*, 2007] NIKITCZUK, J., WEINBERG, B. et MAVROIDIS, C. (2007). Control of electro-rheological fluid based resistive torque elements for use in active rehabilitation devices. *Smart Materials and Structures*, 16(2):418. (page 76)

[Olabi et Grunwald, 2007] OLABI, A. et GRUNWALD, A. (2007). Design and application of magneto-rheological fluid. *Materials & Design*, 28(10):2658 – 2664. (pages 40 and 73)

[Ott *et al.*, 2010] OTT, C., MUKHERJEE, R. et NAKAMURA, Y. (2010). Unified impedance and admittance control. *In Robotics and Automation (ICRA), 2010 IEEE International Conference on*, pages 554 –561. (pages 15 and 32)

[Pang *et al.*, 1991] PANG, X., TAN, H. et DURLACH, N. (1991). Manual discrimination of force using active finger motion. *Perception & Psychophysics*, 49(6):531–540. (page 133)

[Park *et al.*, 2008] PARK, E. J., da LUZ, L. F. et SULEMAN, A. (2008). Multidisciplinary design optimization of an automotive magnetorheological brake design. *Computers & Structures*, 86(3–5):207 – 216. <ce:title>Smart Structures</ce:title>. (page 76)

[Park *et al.*, 2006] PARK, E. J., STOIKOV, D., Falcao da LUZ, L. et SULEMAN, A. (2006). A performance evaluation of an automotive magnetorheological brake design with a sliding mode controller. *Mechatronics*, 16(7):405–416. (page 76)

[Periquet et J.Lozada, 2010] PERIQUET, F. et J.LOZADA (2010). A miniature 1-dof mr fluid based haptic interface. *12th International Conference on New Actuators*, pages 541–544. (pages 41 and 76)

[Periquet et Hafez, 2009] PERIQUET, F., L. J. R. S. P. R. A. M. et HAFEZ, M. (2009). Mr-drive: A new 1-dof mr fluid based haptic interface. European Mechatronics Meeting (EMM 2009). (page 42)

[Pervozvanski et Canudas-de Wit, 2002] PERVOZVANSKI, A. A. et Canudas-de WIT, C. (2002). Asymptotic analysis of the dither effect in systems with friction. *Automatica*, 38(1):105–113. (page 21)

[Pesgens *et al.*, 2006] PESGENS, M., VROEMEN, B., STOUTEN, B., VELDPAUS, F. et STEINBUCH, M. (2006). Control of a hydraulically actuated continuously variable transmission. *Vehicle System Dynamics*, 44(5):387–406. (page 7)

[Pratt et Williamson, 1995] PRATT, G. et WILLIAMSON, M. (1995). Series elastic actuators. *In Intelligent Robots and Systems 95. 'Human Robot Interaction and Cooperative Robots', Proceedings. 1995 IEEE/RSJ International Conference on*, volume 1, pages 399–406 vol.1. (page 33)

[Pusch *et al.*, 2008] PUSCH, A., MARTIN, O. et COQUILLART, S. (2008). Hemp-hand-displacement-based pseudo-haptics: A study of a force field application. *In 3D User Interfaces, 2008. 3DUI 2008. IEEE Symposium on*, pages 59–66. (page 146)

[Qian et Kachroo, 1997] QIAN, M. et KACHROO, P. (1997). Modeling and control of electromagnetic brakes for enhanced braking capabilities for automated highway systems. *In Intelligent Transportation System, 1997. ITSC '97., IEEE Conference on*, pages 391–396. (page 40)

[Reyes et Kelly, 2001] REYES, F. et KELLY, R. (2001). Experimental evaluation of model-based controllers on a direct-drive robot arm. *Mechatronics*, 11(3):267–282. (page 33)

[Rhijn, 2011] RHIJN, J. V. (2011). *Contribution a l'etude et au developpement des systemes adaptables pour les robots reconfigurables: application a la corobotique*. Thèse de doctorat, INSA Rennes. (page 41)

[Rosenberg et Adelstein, 1993] ROSENBERG, L. et ADELSTEIN, B. (1993). Perceptual decomposition of virtual haptic surfaces. *In Virtual Reality, 1993. Proceedings., IEEE 1993 Symposium on Research Frontiers in*, pages 46–53. (pages 11 and 132)

[Rosenfeld et Wereley, 2004] ROSENFELD, N. C. et WERELEY, N. M. (2004). Volume-constrained optimization of magnetorheological and electrorheological valves and dampers. *Smart Materials and Structures*, 13(6):1303–1313. (page 75)

[Rossa *et al.*, 2012] ROSSA, C., LOZADA, J. et MICAELLI, A. (2012). Magnetic flux analysis on magnetorheological actuators can detect external force variation. *In Sensors, 2012 IEEE*, pages 1–4. (page 26)

[Ryu *et al.*, 2004a] RYU, J.-H., KWON, D.-S. et HANNAFORD, B. (2004a). Stability guaranteed control: Time domain passivity approach. *Control Systems Technology, IEEE Transactions on*, 12(6):860–868. (pages 13 and 14)

[Ryu *et al.*, 2004b] RYU, J.-H., KWON, D.-S. et HANNAFORD, B. (2004b). Stable teleoperation with time-domain passivity control. *Robotics and Automation, IEEE Transactions on*, 20(2):365–373. (pages 13 and 14)

[Saito et Ikeda, 2007] SAITO, T. et IKEDA, H. (2007). Development of normally closed type of magnetorheological clutch and its application to safe torque control system of Human-Collaborative robot. *Journal of Intelligent Material Systems and Structures*, 18(12):1181–1185. (page 41)

[Sakaguchi et Furusho, 1998] SAKAGUCHI, M. et FURUSHO, J. (1998). Force display system using particle-type electrorheological fluids. *In Robotics and Automation, 1998. Proceedings. 1998 IEEE International Conference on*, volume 3, pages 2586–2591 vol.3. (page 7)

[Salisbury *et al.*, 1995] SALISBURY, K., BROCK, D., MASSIE, T., SWARUP, N. et ZILLES, C. (1995). Haptic rendering: programming touch interaction with virtual objects. *In Proceedings of the 1995 symposium on Interactive 3D graphics*, I3D '95, pages 123–130, New York, NY, USA. ACM. (page 6)

[Samur *et al.*, 2008] SAMUR, E., FLACTION, L., SPAELTER, U., BLEULER, H., HELLIER, D. et OURSELIN, S. (2008). A haptic interface with motor/brake system for colonoscopy simulation. *In Haptic interfaces for virtual environment and teleoperator systems, 2008. haptics 2008. symposium on*, pages 477–478. (page 19)

[Schiavi *et al.*, 2008] SCHIAVI, R., GRIOLI, G., SEN, S. et BICCHI, A. (2008). Vsa-ii: a novel prototype of variable stiffness actuator for safe and performing robots interacting with humans. *In Robotics and Automation, 2008. ICRA 2008. IEEE International Conference on*, pages 2171–2176. (page 33)

[Scilingo *et al.*, 2000] SCILINGO, E., BICCHI, A., DE-ROSSI, D. et SCOTTO, A. (2000). A magnetorheological fluid as a haptic display to replicate perceived biological tissues compliance. *In Microtechnologies in Medicine and Biology, 1st Annual International, Conference On. 2000*, pages 229–233. (page 40)

[Senkal et Gurocak, 2010] SENKAL, D. et GUROCAK, H. (2010). Serpentine flux path for high torque mrf brakes in haptics applications. *Mechatronics*, 20(3):377 – 383. (page 115)

[Sensinger et Weir, 2005] SENSINGER, J. et WEIR, R. (2005). Design and analysis of a non-backdrivable series elastic actuator. *In Rehabilitation Robotics, 2005. ICORR 2005. 9th International Conference on*, pages 390–393. (page 33)

[Sensinger et Weir, 2006] SENSINGER, J. et WEIR, R. (2006). Improvements to series elastic actuators. *In Mechatronic and Embedded Systems and Applications, Proceedings of the 2nd IEEE/ASME International Conference on*, pages 1–7. (page 33)

[Sevcik *et al.*, 2007] SEVCIK, K. S., KOPP, E. et O'MALLEY, M. K. (2007). Improved haptic fidelity via reduced sampling period with an fpga-based real-time hardware platform. *In Proc. of ASME International Mechanical Engineering Congress and Exposition*. (page 14)

[Shafer et Kermani, 2011] SHAFER, A. et KERMANI, M. (2011). On the feasibility and suitability of mr fluid clutches in human-friendly manipulators. *Mechatronics, IEEE/ASME Transactions on*, 16(6):1073–1082. (pages 41 and 76)

[Sharon et Hardt, 1984] SHARON, A. et HARDT, D. (1984). Enhancement of robot accuracy using endpoint feedback and a macro-micro manipulator system. *In American Control Conference, 1984*, pages 1836–1845. (page 34)

[Sharon *et al.*, 1988] SHARON, A., HOGAN, N. et HARDT, D. (1988). High bandwidth force regulation and inertia reduction using a macro/micro manipulator system. *In Robotics and Automation, 1988. Proceedings., 1988 IEEE International Conference on*, pages 126–132 vol.1. (page 34)

[Shiao et Chang, 2011] SHIAO, Y. J. et CHANG, C. Y. (2011). Design of an innovative High-Torque brake. *Advanced Materials Research*, 339:84–87. (page 75)

[Shih et Wang, 1996] SHIH, Y.-C. et WANG, M.-J. J. (1996). Hand/tool interface effects on human torque capacity. *International Journal of Industrial Ergonomics*, 18(2–3):205 – 213. <ce:title>Towards a New Ergonomics Age in the Pan-Pacific Region</ce:title>. (page 103)

[Srikanth *et al.*, 2008] SRIKANTH, M. B., VASUDEVAN, H. et MUNIYANDI, M. (2008). Dc motor damping: A strategy to increase passive stiffness of haptic devices. *In Haptics: Perception, Devices and Scenarios*, pages 53–62. Springer. (page 14)

[Srinivasan et Basdogan, 1997] SRINIVASAN, M. A. et BASDOGAN, C. (1997). Haptics in virtual environments: Taxonomy, research status, and challenges. *Computers & Graphics*, 21(4):393 – 404. Haptic Displays in Virtual Environments and Computer Graphics in Korea. (page 6)

[Stocco et Salcudean, 1996] STOCCO, L. et SALCUDEAN, S. (1996). A coarse-fine approach to force-reflecting hand controller design. *In Robotics and Automation, 1996. Proceedings., 1996 IEEE International Conference on*, volume 1, pages 404–410 vol.1. (page 34)

[Tan *et al.*, 1994] TAN, H., RADCLIFFE, J., GA, B. N., TAN, H. Z., EBERMAN, B., SRINIVASAN, M. A. et CHENG, B. (1994). Human factors for the design of force-reflecting haptic interfaces. (pages 132 and 133)

[Tan, 1997] TAN, H. Z. (1997). Identification of sphere size using the phantom: towards a set of building blocks for rendering haptic environment. *In Proceedings of the 6th International Symposium on Haptic Interfaces for Virtual Environment and Teleoperator Systems*, volume 61, pages 197–203. (page 132)

[Tan *et al.*, 1995] TAN, H. Z., DURLACH, N. I., BEAUREGARD, G. L. et SRINIVASAN, M. A. (1995). Manual discrimination of compliance using active pinch grasp: The roles of force and work cues. *Perception & psychophysics*, 57(4):495–510. (page 133)

[Troccaz et Delnondedieu, 1996] TROCCAZ, J. et DELNONDEDIEU, Y. (1996). Semi-active guiding systems in surgery. a two-dof prototype of the passive arm with dynamic constraints (padyc). *Mechatronics*, 6(4):399 – 421. Mechatronics in Surgery. (page 36)

[Troccaz *et al.*, 1998] TROCCAZ, J., PESHKIN, M. et DAVIES, B. (1998). Guiding systems for computer-assisted surgery: introducing synergistic devices and discussing the different approaches. *Medical Image Analysis*, 2(2):101 – 119. (page 36)

[Vallery *et al.*, 2007] VALLERY, H., EKKELENKAMP, R., van der KOOIJ, H. et BUSS, M. (2007). Passive and accurate torque control of series elastic actuators. *In Intelligent Robots and Systems, 2007. IROS 2007. IEEE/RSJ International Conference on*, pages 3534–3538. (page 33)

[Van der Linde *et al.*, 2002] Van der LINDE, R. Q., LAMMERTSE, P., FREDERIKSEN, E. et RUITER, B. (2002). The hapticmaster, a new high-performance haptic interface. *In Proc. Eurohaptics*, pages 1–5. (page 7)

[Vanderborght *et al.*, 2009] VANDERBORGHT, B., TSAGARAKIS, N., SEMINI, C., VAN HAM, R. et CALDWELL, D. (2009). Maccepa 2.0: Adjustable compliant actuator with stiffening characteristic for energy efficient hopping. *In Robotics and Automation, 2009. ICRA '09. IEEE International Conference on*, pages 544–549. (page 33)

[Vasudevan *et al.*, 2007] VASUDEVAN, H., SRIKANTH, M. B. et MUNIYANDI, M. (2007). Rendering stiffer walls: a hybrid haptic system using continuous and discrete time feedback. *Advanced Robotics*, 21(11):1323–1338. (page 14)

[Vicentini *et al.*, 2010] VICENTINI, M., GALVAN, S., BOTTURI, D. et FIORINI, P. (2010). Evaluation of force and torque magnitude discrimination thresholds on the human hand-arm system. *ACM Trans. Appl. Percept.*, 8(1):1:1–1:16. (page 132)

[Walker *et al.*, 2009] WALKER, D., THOMA, D. et NIEMEYER, G. (2009). Variable impedance magnetorheological clutch actuator and telerobotic implementation. *In Intelligent Robots and Systems, 2009. IROS 2009. IEEE/RSJ International Conference on*, pages 2885 –2891. (pages 19 and 34)

[Weir *et al.*, 2008] WEIR, D. W., COLGATE, J. E. et PESHKIN, M. A. (2008). Measuring and increasing z-width with active electrical damping. *In Haptic interfaces for virtual environment and teleoperator systems, 2008. Haptics 2008. Symposium on*, pages 169–175. IEEE. (page 14)

[Weiss *et al.*, 1994] WEISS, K. D., CARLSON, J. D. et NIXON, D. A. (1994). Viscoelastic properties of magneto-and electro-rheological fluids. *Journal of Intelligent Material Systems and Structures*, 5(6):772–775. (page 73)

[Winter et Bouzit, 2007] WINTER, S. et BOUZIT, M. (2007). Use of magnetorheological fluid in a force feedback glove. *Neural Systems and Rehabilitation Engineering, IEEE Transactions on*, 15(1):2–8. (page 41)

[Woodruff et Helson, 1967] WOODRUFF, B. et HELSON, H. (1967). Torque sensitivity as a function of knob radius and load. *The American Journal of Psychology*, 80(4):558–571. (page 133)

[Wyeth, 2008] WYETH, G. (2008). Demonstrating the safety and performance of a velocity sourced series elastic actuator. *In Robotics and Automation, 2008. ICRA 2008. IEEE International Conference on*, pages 3642–3647. (page 33)

[Yang *et al.*, 2008] YANG, L., DUAN, F. et ERIKSSON, A. (2008). Analysis of the optimal design strategy of a magnetorheological smart structure. *Smart Materials and Structures*, 17(1):015047. (pages 77 and 81)

[Yoshikawa, 1985] YOSHIKAWA, T. (1985). Dynamic manipulability of robot manipulators. *In Robotics and Automation. Proceedings. 1985 IEEE International Conference on*, volume 2, pages 1033–1038. (page 146)

[Zhang *et al.*, 2006] ZHANG, H. H., LIAO, C. R., CHEN, W. M. et HUANG, S. L. (2006). A magnetic design method of mr fluid dampers and fem analysis on magnetic saturation. *Journal of Intelligent Material Systems and Structures*, 17(8-9):813–818. (page 77)

[Zhou *et al.*, 2005] ZHOU, W., CHEW, C.-M. et HONG, G.-S. (2005). Inverse dynamics control for series damper actuator based on mr fluid damper. *In Advanced Intelligent Mechatronics. Proceedings, 2005 IEEE/ASME International Conference on*, pages 473–478. (page 34)

[Zhu, 2007] ZHU, C. (2007). The response time of a magnetorheological fluid squeeze film damper rotor system. (page 78)

[Zinn *et al.*, 2004] ZINN, M., KHATIB, O., ROTH, B. et SALISBURY, J. (2004). Playing it safe [human-friendly robots]. *Robotics Automation Magazine, IEEE*, 11(2):12–21. (page 34)

Résumé : Cette thèse aborde la conception et la commande d'un nouveau système d'actionnement pour interface à retour haptique. Nous proposons un dispositif hybride comprenant un moteur à courant continu et deux freins magnétorhéologiques. Chaque frein étant associé à une roue libre, son couple de freinage ne peut être transmis que dans une seule direction. De ce fait, lorsqu'un frein et le moteur sont activés en même temps, le frein ne bloque pas le moteur, ce qui permet de combiner les avantages de chaque d'actionneur et d'améliorer la qualité du rendu haptique. L'actionneur peut générer 5.5Nm, avec un couple par unité de volume de 17.75kN/m2. Les résultats démontrent que l'actionneur hybride présente moins de frottement et moins d'inertie comparé à un moteur électrique seul connecté à un réducteur de vitesse idéal. Une nouvelle approche de commande basée sur le partage d'impédance est proposée. Les gains d'asservissement relatifs à la raideur simulée par chaque actionneur sont ajoutés en temps réel de manière à respecter les consignes et les critères de stabilité. Ces lois de commandes sont indépendantes de l'environnement virtuel et permettent l'utilisation de l'actionneur dans une large gamme de dispositifs à retour de forces.

Abstract: The design and control of a 5.5Nm maximal torque, 17.75kN/m2 torque density hybrid actuator for haptic feedback devices are presented. The system employs two unidirectional magneto-rheological fluid based brakes and a DC motor. The brakes are coupled to opposite overrunning clutches. By these means, each brake can generate a torque only in a defined direction. Thus, when both a brake and a motor are engaged to constrain the motion of the end-effector, the brake does not block the motor. Theoretical results demonstrate that the system generates less friction and presents less inertia compared to a DC motor associated to an ideal capstan transmission. The proposed control laws determine the shear of efforts between the brakes and the motor in terms of stiffness and energy of the virtual environment, in order to achieve high torque capability while maintaining stability and safety. The control laws do not necessitate a measure of interaction forces. Besides, the design of the actuator and the control laws are completely independent of the virtual environment allowing for the implementation of the system in many different haptic feedback devices.